Self-interacting scalar field dark matter : From gravitational drag to gravitational wave predictions

Alexis Boudon

To cite this version:

Alexis Boudon. Self-interacting scalar field dark matter : From gravitational drag to gravitational wave predictions. Cosmology and Extra-Galactic Astrophysics [astro-ph.CO]. Université Paris-Saclay, 2023. English. NNT : 2023UPASP083 . tel-04266194

HAL Id: tel-04266194
https://theses.hal.science/tel-04266194

Submitted on 31 Oct 2023

Self-interacting scalar field dark matter: From gravitational drag to gravitational wave predictions

Matière noire scalaire auto-interagissante : Du freinage gravitationnel aux prédictions sur les ondes gravitationnelles

Thèse de doctorat de l'université Paris-Saclay

École doctorale n° 564, Physique en Île-de-France (PIF)
Spécialité de doctorat : Physique
Graduate School : Physique. Référent : Faculté des Sciences d'Orsay

Thèse préparée dans l'unité de recherche **Institut de physique théorique** (Université Paris-Saclay, CNRS, CEA), sous la direction de **Patrick VALAGEAS**, Directeur de recherche

Thèse soutenue à Paris-Saclay, le 28 Septembre 2023, par

Alexis BOUDON

Composition du jury

Membres du jury avec voix délibérative

Danièle STEER Professeure des universités, Astroparticule et Cosmologie, Université Paris Cité, CNRS	Présidente
Julien LAVALLE Directeur de recherche, Laboratoire Univers et Particules de Montpellier, Université de Montpellier	Rapporteur & Examinateur
David Fonseca MOTA Professeur, Institute of Theoretical Astrophysics, Oslo University	Rapporteur & Examinateur
Yann MAMBRINI Directeur de recherche, Laboratoire de Physique Théorique, Université Paris-Saclay	Examinateur

THESE DE DOCTORAT

NNT : 2023UPASP083

université
PARIS-SACLAY

ÉCOLE DOCTORALE
Physique en
Île-de-France (PIF)

Titre : Matière noire scalaire auto-interagissante : Du freinage gravitationnel aux prédictions sur les ondes gravitationnelles

Mots clés : matière noire, champ scalaire, auto-interaction quartique, accrétion de masse, friction dynamique, ondes gravitationnelles

Résumé : L'absence d'observations directes de la matière noire froide motive une meilleure compréhension des scénarios alternatifs. En particulier, les scénarios impliquant des bosons ultralégers de masse inférieure à 1 eV ont connu un regain d'intérêt ces dernières années. Ils préservent les succès du modèle standard de matière noire froide à grande échelle, mais altèrent la dynamique aux échelles galactiques. L'ajout d'auto-interactions à de tels scénarios confère à la matière noire un comportement semblable à celui d'un fluide avec une pression effective non négligeable, la distinguant de la matière noire ultralégère conventionnelle. Nous avons étudié l'accrétion et la friction dynamique appliquée sur un trou noir se déplaçant dans un nuage de matière noire, tant dans le régime subsonique que supersonique. Nos résultats révèlent que si le régime subsonique implique principalement l'accrétion, le régime supersonique introduit une friction dynamique supplémentaire caractérisée par un terme similaire à celui obtenu par Chandrasekhar dans le cas de particules sans collisions. Néanmoins, dans les deux régimes, l'intensité de la force d'accrétion et de la friction dynamique reste inférieure à celle observée pour la matière noire froide ou ultra-légère sans collisions. En utilisant ces résultats, nous avons analysé les effets de ces forces sur les signaux d'ondes gravitationnelles émis par des binaires de trous noirs se trouvant à l'intérieur d'un nuage de matière noire scalaire auto-interagissant. En première approximation, des termes de correction aux ordres -4PN et -5.5PN apparaissent, exerçant une influence sur la phase du signal d'ondes gravitationnelles. Les observations prospectives de LISA et de B-DECIGO ont le potentiel de détecter ces effets sur un large spectre de masses scalaires et de couplages d'auto-interactions. Bien que des détecteurs tels que ET et Advanced LIGO puissent également identifier ces effets, leurs capacités de détection sont limitées à un espace de paramètres plus restreint. Notre analyse démontre que les cas où la détection de ces effets est la plus probable sont les Inspirales à Rapport de Mass Extrême (EMRIs) observées par LISA. Actuellement, cette approche est la seule permettant de contraindre la matière noire scalaire auto-interagissante ayant des nuages de dimensions inférieures à 0,1 pc.

ÉCOLE DOCTORALE
Physique en
Île-de-France (PIF)

Title: Self-interacting scalar field dark matter: From gravitational drag to gravitational wave predictions

Keywords: dark matter, scalar field, quartic self-interactions, dynamical friction, mass accretion, gravitational waves

Abstract: The absence of direct observations of cold dark matter particles calls for a better understanding of alternative scenarios. In particular, scenarios involving ultralight bosons with a mass below 1 eV have experienced a resurgence of interest in recent years. They preserve the successes of the standard cold dark matter model at large scales but alter the dynamics at galactic scales. Including self-interactions to such scenarios endows dark matter with fluid-like behavior with non-negligible effective pressure, distinguishing it from the conventional ultralight dark matter. We investigated the accretion and dynamical friction applied on a black hole moving in a dark matter cloud, both in subsonic and supersonic regimes. Our findings reveal that while the subsonic regime primarily involves accretion, the supersonic regime introduces additional dynamical friction characterized by a term similar to the one obtained by Chandrasekhar for collisionless particles. Nonetheless, in both regimes, the magnitude of the accretion force and dynamical friction remains lower than that observed for cold or collisionless ultralight dark matter. In this framework, we analyzed the effects of these forces on the gravitational-wave signals emitted by binary black holes inside a self-interacting scalar field dark matter cloud. To a fist approximation, correction terms at -4PN and -5.5PN orders appear, exerting an influence on the phase of the gravitational-wave signal. Prospective observations by LISA and B-DECIGO have the potential to detect these effects across a broad spectrum of scalar masses and self-interaction couplings. Our analysis demonstrates that the instances in which the detection of these effects is most probable are Extreme Mass Ratio Inspirals (EMRIs) observed by LISA. Presently, this approach stands as the sole means to constrain self-interacting scalar dark matter with clouds smaller than 0.1 pc.

Aknowledgements

First and foremost, I would like to express my deepest appreciation to Patrick Valageas, my thesis supervisor, and Philippe Brax for their continuous mentorship and unwavering commitment. Their expertise, patience, and availability have been instrumental in shaping the direction of my research, contributing to its successfulness. Their guidance during the COVID-19 pandemic, which significantly impacted the early stage of my thesis, is particularly noteworthy.

In addition to my supervisors, I extend my gratitude to the members of the laboratory, especially the fellow PhD and postdoctoral students. Among them, Raquel Galazo Garcia deserves special mention, as we embarked on our thesis journeys simultaneously. Her unwavering presence and invaluable emotional support have been indispensable as we faced similar challenges and made progress. I am truly grateful for her companionship and encouragement. I would also like to express my appreciation to Massimiliano Maria Riva, whose positive influence and presence significantly enriched my overall experience during the first year of my thesis. I am thankful to Leong Khim Wong, who collaborated with me on a research paper included in this thesis, Natalie Hogg and Petter Taule for their assistance and for fostering a vibrant environment at the IPhT. I am grateful to Pierre Fleury and Filippo Vernizzi for their willingness to offer assistance and their efforts in creating a lively laboratory atmosphere. Their presence and support were greatly appreciated. Moreover, I am thankful for the enlightening conversations and shared experiences with all individuals, both within the laboratory and at conferences.

My family holds a special place in my heart, and their unwavering support has been a constant source of motivation throughout my academic journey. I am forever indebted to my parents, Thierry and Viviane, for their continuous love and encouragement. Their presence has been indispensable. I would also like to express my gratitude to my sisters, Fanny, Candice, and Sabrina, for their unwavering support and genuine interest in my work. Their presence throughout my thesis has been invaluable.

Lastly, I wish to extend a heartfelt thank you to my girlfriend, Ophelie, for her unwavering support and love. Her decision to stay by my side and relocate to Paris demonstrates her immense dedication. Her continuous presence has been vital in maintaining my enthusiasm and perseverance until the very end of my thesis. I am incredibly grateful for her unwavering support.

To all those mentioned above and to anyone else who has played a role, regardless of its size, in shaping my thesis journey, I offer my sincerest thanks. Your support, encouragement, and contributions have been indispensable, and I am truly grateful for the opportunity to collaborate with such exceptional individuals.

Table of contents

Résumé de la thèse

Le contenu de cette thèse s'appuie sur trois articles de recherche issus des travaux menés à l'Institut de Physique Théorique (IPhT), affilié à l'Université de Paris-Saclay. Les travaux de recherche se sont déroulés d'octobre 2020 à juillet 2023 :

- A. Boudon, P. Brax and P. Valageas, **Subsonic accretion and dynamical friction for a black hole moving through a self-interacting scalar dark matter cloud**, Phys. Rev. D 106.4 (2022). [1]
- A. Boudon, P. Brax et P. Valageas, **Supersonic accretion and dynamical friction for a black hole moving through a self-interacting scalar dark matter cloud**, arXiv:2307.15391 [2]
- A. Boudon et al., **Gravitational waves from binary black holes in a self-interacting scalar dark matter cloud**, arXiv:2305.18540 [3]

En ce qui concerne le statut de publication des articles de recherche, l'un d'entre eux, [1], a été officiellement publié. Les deux autres articles, [2, 3], sont actuellement en cours de processus de publication.

L'objectif principal de cette thèse est de fournir une analyse de l'accrétion de masse et de la friction dynamique subies par un trou noir se déplaçant au sein de matière noire scalaire auto-interagissante. Cela nous permettra d'explorer les applications pratiques de ces calculs dans des systèmes contraints, offrant ainsi un moyen d'étudier la matière noire à travers des phénomènes tels que la décroissance orbitale des objets célestes dans les galaxies et les environnements gazeux contenant de la matière noire. De plus, la thèse examine l'utilisation potentielle des ondes gravitationnelles émises par des binaires de trous noirs entourés de matière noire, explorant spécifiquement le décalage de phase induit par la force de freinage, composée de la force de freinage d'accrétion et de friction dynamique. Ce décalage de phase peut servir de signature caractéristique de la matière noire et permet de faire la distinction entre différents modèles de matière noire.

La motivation de cette recherche découle des défis rencontrés dans la détection des particules massives faiblement interactives (WIMPs), qui ont été et sont encore considérées comme des candidates solides pour la matière noire. Malgré des recherches approfondies, aucune preuve concluante de l'existence de WIMPs n'a été trouvée jusqu'à présent, rendant la détection directe de plus en plus contrainte [4–7]. De plus, les tentatives de simuler l'évolution de la matière noire froide ont révélé des problèmes cosmologiques, notamment le problème de concentration des halos, le problème des satellites manquants et le problème "too-big-to-fail", entre autres [8–12]. Bien que l'incorporation d'effets baryoniques plus détaillés dans les simulations puisse résoudre partiellement ces problèmes, cela reste insuffisant à l'heure actuelle [13–20]. En tant qu'approche alternative, la thèse explore la matière noire sous forme de champ scalaire, considérant la matière noire comme des particules bosoniques.

La matière noire scalaire présente des caractéristiques propres qui la distinguent de la matière noire froide. Une caractéristique notable est l'émergence de solitons [21–48], également appelés étoiles de bosons, qui sont des configurations auto-gravitantes stables du champ scalaire résultant de l'équilibre entre la pression quantique, ou les auto-interactions, et les forces gravitationnelles. Cette propriété de la matière noire scalaire a des implications significatives sur le profil de densité de la matière noire à différentes échelles. À petite échelle, la présence de solitons conduit à un profil de densité différent du profil typique associé à la matière noire froide. Au lieu du profil en forme de pic observé dans les simulations de matière noire froide, le profil de densité de la matière noire scalaire présente une structure centrale en raison des configurations de solitons. Cependant, à grande échelle, son profil de densité rejoint le profil de Navarro-Frenk-White (NFW) attendu généralement pour la matière noire froide. Cette récupération assure la cohérence avec les observations et les attentes théoriques à plus grande échelle tout en fournissant les modifications nécessaires pour résoudre les problèmes à petite échelle mentionnés précédemment. Ainsi, le modèle de matière noire scalaire introduit des changements principalement à petite échelle tout en conservant les caractéristiques familières de la matière noire froide à l'échelle cosmologique.

En raison de leur solution solitonique, les théories de champ scalaire, y compris la théorie de la matière noire "fuzzy", ont initialement montré des promesses pour résoudre les problèmes cosmologiques susmentionnés [8, 11, 49, 50]. Cependant, des contraintes observationnelles récentes, telles que les courbes de rotation des galaxies et la forêt de Lyman-α [51–53], ont imposé des limitations significatives sur la masse de la matière noire "fuzzy", nécessitant généralement des masses supérieures à 10^{-21} eV. Ces contraintes remettent en question la capacité du modèle à résoudre les problèmes cosmologiques qu'il visait à résoudre, diminuant ainsi son attrait en tant que candidat alternatif. Par conséquent, les physiciens ont commencé à explorer d'autres moyens de différencier la matière noire scalaire de la matière noire froide, en se concentrant sur des échelles plus petites. Cette nouvelle génération d'articles se réfère souvent à ce modèle en tant que matière noire ultra-légère. Il englobe le même cadre théorique que la matière noire "fuzzy", mais est généralement considéré à des masses plus élevées. Les physiciens étudiant la matière noire ultra-légère ont exploré les effets ondulatoires et cherché à révéler des phénomènes exotiques, tels que la superradiance, les forces de marée et la résonance avec les ondes gravitationnelles [54–58]. Ce domaine est en expansion rapide et offre des perspectives pour une meilleure compréhension de la dynamique de la matière noire et de ses impacts. À cette fin, certains physiciens ont introduit des auto-interactions parmi les particules de matière noire. En considérant ces interactions comme répulsives, un modèle émerge qui a le potentiel d'expliquer les problèmes cosmologiques tout en étant en accord avec les données observationnelles actuelles.

Bien que l'étude de ces effets soit une voie de recherche fascinante, cette thèse, basée sur les articles [1], [2] et [3], adopte une approche différente. L'accent principal est mis sur l'étude des effets de la matière noire scalaire auto-interagissante sur les trous noirs et sur son utilité pour sonder la matière noire tout en la différenciant des autres modèles. Cette thèse s'efforce de fournir des calculs précis de l'accrétion de masse et de la friction dynamique sur un trou noir en mouvement au sein d'un nuage de matière noire. À travers ces calculs, cette thèse vise à éclaircir les caractéristiques et le comportement de la matière noire autour des trous noirs et à faciliter son identification dans divers scénarios astrophysiques.

Le chapitre 1 offre un aperçu concis de la cosmologie, de la matière noire et de la physique des ondes gravitationnelles. Il couvre le développement historique de l'univers, introduit le modèle ΛCDM et explore les défis de la matière noire. Les modèles alternatifs, y compris les théories de la matière noire scalaire, sont examinés en détail. Le chapitre met également en évidence l'importance des ondes gravitationnelles en astrophysique et expose les objectifs de recherche de la thèse.

Le chapitre 2 présente sur le modèle de matière noire scalaire soumise à une auto-interaction quartique. Il introduit les concepts fondamentaux et les équations qui régissent ce modèle, en considérant à la fois les régimes non relativiste et relativiste. Dans le régime non relativiste, les solitons, qui sont des configurations d'équilibre statiques résultant des auto-interactions, sont explorés. Le comportement des solitons est déterminé par l'équation d'équilibre hydrostatique, ce qui permet d'identifier le potentiel d'auto-interaction. Le chapitre discute de l'espace des paramètres du modèle, en tenant compte des contraintes sur les paramètres scalaires et en précisant les conditions pour les calculs. L'accent est mis sur le régime de Thomas-Fermi, dans lequelle les auto-interactions dominent la pression quantique. Enfin, nous examinons le régime d'accrétion radiale, comme discuté en détail dans [59].

Le chapitre 3 se concentre sur le comportement d'un trou noir interagissant avec un nuage de matière noire scalaire auto-interagissante dans le régime subsonique. Nous commençons par une brève exploration de la solution d'un soliton en mouvement. Ensuite, nous intégrons un trou noir dans le cadre établi pour déduire les équations du mouvement régissant le système. Nous analysons à la fois l'écoulement non linéaire à grandes distances et le régime de petites distances, en incorporant des corrections à l'approximation d'écoulement linéaire. Les expressions dérivées pour le taux d'accrétion et la force de freinage fournissent des informations quantitatives sur l'interaction du trou noir avec le nuage de matière noire. En comparant nos résultats avec d'autres modèles de matière noire, tels que la matière noire froide et la matière noire "fuzzy", nous mettons en évidence les caractéristiques distinctes du modèle de matière noire scalaire auto-interagissante. Nos résultats révèlent notamment une réduction du taux d'accrétion et de la force de freinage par rapport à un gaz parfait, attribuable aux effets d'auto-interaction. La friction dynamique se révèle négligeable dans ce régime, contrairement aux particules sans collision [60–62] ou à la matière noire "fuzzy" [63–65]. Ces résultats ont des implications pour des phénomènes tels que le déphasage de la fréquence d'émission des ondes gravitationnelles et pourraient contribuer à résoudre le problème de synchronisation des amas globulaires de Fornax.

Dans le chapitre 4, nous explorons le régime supersonique pour comprendre l'interaction entre un trou noir et une matière noire scalaire auto-interagissante. En nous appuyant sur notre analyse du régime subsonique, nous découvrons un écoulement de vitesse plus complexe caractérisé par un front de choc. Ce front de choc sépare les régions en amont et en aval, chacune ayant des conditions aux limites distinctes. L'écoulement en amont est uniquement déterminé par la condition initiale, et l'écoulement en aval contient deux constantes d'intégration que nous déterminons en les faisant correspondre à l'écoulement en amont. Cependant, il n'est pas possible de relier les développements perturbatifs des écoulements en amont et en aval près du front de choc en raison de leur divergence, ce qui conduit à une couche limite où les effets non linéaires deviennent significatifs. Pour de faibles vitesses supersoniques, nous retrouvons le même taux d'accrétion que dans le régime subsonique. Cependant, dans le régime hautement supersonique, le débit d'accrétion devient similaire au résultat de Hoyle-Lyttleton pour un gaz isentropique. De plus, notre analyse révèle un nouveau terme similaire au résultat de Chandrasekhar pour le frottement dynamique [60], ce qui indique l'efficacité de notre cadre dans la capture de la dynamique du système.

Enfin, dans le chapitre 5, nous explorons les effets de la force de freinage d'accrétion et de la friction dynamique sur les trous noirs binaires et leur influence sur l'émission des ondes gravitationnelles. En considérant des solitons de taille finie autour de trous noirs binaires, nous étudions leur impact. Les perturbations dans les formes d'ondes gravitationnelles peuvent provenir de différents environnements, et les différencier peut fournir des informations précieuses sur l'environnement des systèmes binaires. Les nuages scalaires affectent les orbites binaires par décélération due à l'accrétion de matière noire et par un ralentissement supplémentaire dû à la friction dynamique dans le régime supersonique. Ces effets introduisent des déviations dans les orbites binaires et perturbent les signaux des ondes gravitationnelles. En analysant l'excentricité, le demi-grand axe et le décalage de phase dans les signaux des ondes gravitationnelles, nous quantifions les impacts de ces forces. À l'aide d'une analyse de Fisher, nous évaluons la détectabilité de deux paramètres clés, ρ_0 et ρ_a, avec des interféromètres futurs tels que LISA et DECIGO [66, 67]. Des perspectives prometteuses pour la détection de ces paramètres émergent, offrant des possibilités de recherche passionnantes. De plus, nous étudions les tailles détectables des solitons dans ce contexte.

Notre étude de l'accrétion de masse et de la friction dynamique au sein des solitons de matière noire scalaire auto-interagissante a révélé plusieurs pistes de recherche pour l'avenir. Celles-ci incluent l'incorporation des effets relativistes pour acquérir une compréhension plus complète des systèmes de matière noire, en explorant notamment les effets de la force de freinage à des fréquences plus élevées près des fusions de trous noirs. De plus, considérer des trous noirs de Kerr (avec spin) améliorerait la réalisme de notre analyse, en accord avec les observations des systèmes de trous noirs binaires. Élargir notre champ d'investigation pour inclure d'autres objets astrophysiques, tels que les étoiles et les étoiles à neutrons, est également crucial. Ces objets offrent des caractéristiques uniques qui peuvent fournir des informations précieuses pour tester les modèles de matière noire. Cependant, il devient important de prendre en compte les réactions réciproques de la matière noire, car l'accrétion de masse n'est généralement pas le facteur dominant dans le régime subsonique. De plus, il est essentiel de considérer des scénarios où les trous noirs se trouvent à proximité des limites des solitons ou lorsque le soliton lui-même est relativement petit. Élargir notre exploration pour englober une plus large gamme de tailles de solitons améliorerait notre capacité à détecter et caractériser les solitons, permettant l'identification de signatures distinctes associées aux modèles de matière noire scalaire.

Summary of the thesis

The content provided in this thesis builds upon three research papers derived from the research conducted at the Institute of Theoretical Physics (IPhT), which is affiliated with the University of Paris-Saclay. The research work took place from October 2020 to July 2023:

- A. Boudon, P. Brax and P. Valageas, **Subsonic accretion and dynamical friction for a black hole moving through a self-interacting scalar dark matter cloud**, Phys. Rev. D 106.4 (2022). [1]
- A. Boudon, P. Brax et P. Valageas, **Supersonic accretion and dynamical friction for a black hole moving through a self-interacting scalar dark matter cloud**, arXiv:2307.15391 [2]
- A. Boudon et al., **Gravitational waves from binary black holes in a self-interacting scalar dark matter cloud**, arXiv:2305.18540 [3]

Regarding the publication status of the research papers, one of them, [1], has been officially published. The two other papers, [2, 3], are currently undergoing the publication process.

The main aim is to provide a comprehensive analysis of the mass accretion and dynamical friction experienced by a black hole moving within a self-interacting scalar field dark matter. This will allow us to explore the practical applications of these calculations in bounded systems, offering a means to probe dark matter through phenomena such as orbital decay of celestial objects in galaxies and gas environments containing dark matter. Furthermore, the thesis investigates the potential use of gravitational waves emitted by binary black holes surrounded by dark matter, specifically exploring the phase shift induced by the drag force, made of accretion drag force and dynamical friction. This phase shift can serve as a characteristic signature of dark matter and may differentiate between various dark matter models.

The motivation behind this research stems from the challenges encountered in detecting weakly interacting massive particles (WIMPs), which were initially and are still considered strong candidates for dark matter. Despite extensive searches, no conclusive evidence of WIMPs has been found yet, rendering direct detection increasingly constraint and unlikely to happen [4–7]. Additionally, attempts to simulate the evolution of cold dark matter have revealed cosmological problems, including the core-cusp problem, the missing satellite problem, and the too-big-to-fail problem among others [8–12]. Although incorporating more detailed baryonic effects in simulations may partially resolve these issues, it remains insufficient at present [13–20]. As an alternative approach, the thesis explores scalar field dark matter, considering dark matter as bosonic particles.

Scalar field dark matter exhibits distinct characteristics that set it apart from cold dark matter. One notable feature is the emergence of solitons [21–48], also called boson stars, which are stable, self-gravitating configurations of the scalar field that form due to the balance between quantum pressure, or self-interactions, and gravitational forces. This property of scalar field dark matter has significant implications for the density profile of dark matter at different scales. At small scales, the presence of solitons leads to a departure from the typical density profile associated with cold dark matter. Instead of the cusp-like profile observed in cold dark matter simulations, the scalar field dark matter density profile exhibits a core-like structure due to the soliton configurations. However, at large scales, the scalar field dark matter density profile recovers the expected Navarro-Frenk-White profile commonly associated with cold dark matter. This recovery ensures consistency with observations and theoretical expectations at larger scales while providing the necessary modifications to address the aforementioned small-scale issues. Thus, the scalar field dark matter model introduces changes primarily at small scales while maintaining the familiar characteristics of cold dark matter on cosmological scales.

Due to their solitonic solution, scalar field dark matter theories, including the fuzzy dark matter theory, initially showed promise in resolving the aforementioned cosmological problems [8, 11, 49, 50]. However, recent observational constraints, such as galaxy rotation curves and the Lyman-α forest [51–53], have placed significant limitations on the mass of fuzzy dark matter, typically requiring masses higher than 10^{-21} eV. These constraints have challenged the ability of the model to address the cosmological problems it aimed to solve, diminishing its appeal as a alternative candidate. Consequently, physicists started to explore other means to differentiate between scalar field dark matter and cold dark matter, focusing on smaller scales. This new generation of papers often refer this model to as ultralight dark matter. It encompasses the same theoretical framework as fuzzy dark matter but is typically considered at higher masses. Physicists investigating ultralight dark matter have explored wave-like effects and sought to unveil exotic phenomena, such as superradiance, tidal forces, and resonance with gravitational waves [54–58]. This field is rapidly expanding and holds promise for further understanding dark matter dynamics and its impacts. To this end, some physicists have introduced self-interactions among scalar field dark matter particles. By considering these interactions as repulsive, a model emerges that has the potential to explain cosmological problems while being in agreement with current observational data.

While the study of such effects is a fascinating avenue of research, this thesis, based on papers [1], [2], and [3], takes a different approach. The primary focus is to investigate the effects of self-interacting scalar field dark matter on black holes and explore its utility in probing dark matter while differentiating it from other models. The thesis endeavors to provide precise calculations of mass accretion and dynamical friction on a moving black hole within a dark matter cloud. Through these calculations, the thesis aims to shed light on the characteristics and behavior of dark matter around black holes and facilitate its identification in various astrophysical scenarios.

Chapter 1 provides a concise overview of cosmology, dark matter, and gravitational wave physics. It covers the historical development of the universe, introduces the ΛCDM model, and explores the challenges of dark matter. Alternative models, including scalar field dark matter theories, are discussed in detail. The chapter also highlights the significance of gravitational waves in astrophysics and outlines the research objectives of the thesis.

Chapter 2 offers a comprehensive investigation of the scalar field dark matter model with a quartic self-interaction. It introduces the fundamental concepts and equations governing this model, considering both nonrelativistic and relativistic regimes. In the nonrelativistic regime, solitons, which are static equilibrium configurations arising from self-interactions, are explored. The behavior of solitons is determined by the hydrostatic equilibrium equation, leading to the identification of the self-interaction potential. The chapter discusses the parameter space of the model, considering constraints on the scalar parameters and specifying the conditions for the computations. Emphasis is placed on the Thomas-Fermi regime, where self-interactions dominate over quantum pressure. Lastly, we examine the radial accretion regime, as extensively discussed in [59].

Chapter 3 focuses on the behavior of a black hole interacting with a cloud of self-interacting dark matter in the subsonic regime. We begin by a concise exploration of the solution of a moving soliton. Following this, we proceed to integrate a black hole into the established framework to deduce the equations of motion governing the system. We analyze both the nonlinear flow at large radii and the regime of small radii, incorporating corrections to the linear flow approximation. The derived expressions for the accretion rate and drag force provide quantitative insights into the interaction of the black hole with the dark matter cloud. By comparing our results with other dark matter models, such as cold and fuzzy dark matter, we highlight the distinct characteristics of the self-interacting scalar field dark matter model. Notably, our findings reveal a reduction in the accretion rate and drag force compared to a perfect gas, attributable to the self-interaction effects. The dynamical friction is founded negligible in this regime, contrary to colissionless particles [60–62] or fuzzy dark matter [63–65]. These results have implications for phenomena like the emission frequency dephasing of gravitational waves and could contribute to resolving the Fornax globular cluster timing problem.

In chapter 4, we explore the supersonic regime to understand the interaction between a black hole and self-interacting dark matter. Building upon our analysis of the subsonic regime, we discover a more intricate velocity flow characterized by a shock front. This shock front separates the upstream and downstream regions, each with distinct boundary conditions. The upstream flow is solely determined by the initial condition, and the downstream flow contains two undetermined integration constants that we determine through matching with the upstream flow. However, connecting the naive perturbative expansions of the upstream and downstream flows near the shock front is not feasible due to their divergence, resulting in a boundary layer where nonlinear effects become significant. For small supersonic velocities, we recover the same accretion rate as in subsonic regime. However, in the highly supersonic regime, the accretion rate becomes similar to the Hoyle-Lyttleton result for isentropic gas. Moreover, our analysis reveals a new term similar to the Chandrasekhar's result for dynamical friction [60], indicating the effectiveness of our framework in capturing the dynamics of the system.

Finally, in chapter 5, we explore the effects of the accretion drag force and dynamical friction on binary black holes and their influence on gravitational wave emission. By considering finite-sized solitons around binary black holes, we explore their impact. Perturbations in gravitational waveforms can arise from various environments, and differentiating between them can provide valuable information about the environment of binary systems. Scalar clouds affect binary orbits through deceleration from dark matter accretion and further slowing due to dynamical friction in the supersonic regime. These effects introduce deviations in binary orbits and perturb gravitational wave signals. Through analyses of eccentricity, semi-major axis, and phase shift in gravitational wave signals, we quantify the impacts of these forces. Using a Fisher analysis, we assess the detectability of two key parameters, ρ_0 and ρ_a, with future interferometers like LISA and DECIGO [66, 67]. Promising prospects for detecting these parameters emerge, offering exciting possibilities for research. Additionally, we investigate the detectable sizes of solitons in this context.

Our investigation into mass accretion and dynamical friction within self-interacting scalar field dark matter solitons has uncovered several avenues for future research. These include incorporating relativistic effects to gain a more comprehensive understanding of dark matter systems, particularly exploring the effects of the drag force at higher frequencies near black hole mergers. Additionally, considering Kerr black holes with spin would enhance the realism of our analysis, aligning with observations of binary black hole systems. Expanding our scope to include other astrophysical objects, such as stars and neutron stars, is also crucial. These objects offer unique characteristics that can provide valuable insights into testing dark matter models. However, it becomes important to account for the back reactions of dark matter, as mass accretion is typically not the dominant factor in the subsonic regime. Furthermore, it is essential to consider scenarios where black holes reside closer to soliton boundaries or when the soliton itself is relatively small. Broadening our exploration to encompass a wider range of soliton sizes would improve our ability to detect and characterize solitons, enabling the identification of distinct signatures associated with scalar field dark matter models.

Conventions and definitions

- In this thesis, we adopt natural units by setting $c = \hbar = 1$ throughout, unless explicitly stated otherwise. Additionally, we define the reduced Planck mass as $M_{\rm pl} = 1/\sqrt{8\pi\mathcal{G}}$, where $\mathcal{G}$ is the Newton gravitational constant.

- To facilitate summation over repeated indices, we employ Einstein's notation. Greek indices $\mu, \nu, \ldots$ range from 0 to 3, while Latin indices $i, j, \ldots$ range from 1 to 3.

- The generic metric tensor $g_{\mu\nu}$, conventioned as $(-, +, +, +)$, determines the determinant of the metric as $g = \det(g_{\mu\nu})$.

- Vectors are represented using bold symbols, such as $\mathbf{x}, \mathbf{y}, \ldots$, while non-bold Latin indices denote vector components, e.g., $x^i, y^j, \ldots$. We often employ a dot notation to denote temporal total derivatives and the number of dots corresponds to the order of the derivative, for instance $\dot{x}$ denotes the first derivative with respect to time, $\ddot{x} = d^2x/dt^2$ denotes the second derivative, and so on.

- The Legendre polynomials P_n are defined by the property that $\int_{-1}^{1} dx P_n(x) P_m(x) = 0$ if $n \neq m$. and $P_\ell^m(x) = (-1)^m (1-x^2)^{m/2} \frac{d^m}{dx^m}(P_\ell(x))$. On the other hand, the Spherical harmonics are given by $Y_\ell^m(\theta, \phi) = \sqrt{\frac{2l+1}{4\pi}\frac{(l-m)!}{(l+m)!}} \mathrm{e}^{im\phi} P_\ell^m(\cos(\theta))$. The Kronecker delta is $\delta_{ij} = 0$ for $i \neq j$ and $\delta_{ij} = 1$ if $i = j$.

- Various functions play a significant role in this thesis, including:
  - The Jacobi elliptic cosinus function

    $$\mathrm{cn(u, k)} = \cos\left(A(u,k)\right) ,$$

    where $A(u,k)$ is the reciprocal of the incomplete elliptic integral of the first kind defined as $F(a,k) = \int_0^a dx/\sqrt{1-k^2\sin^2(x)}$.
  - The hypergeometric function

    $${}_2F_1(a,b,c;z) = \sum_{n=0}^{\infty} \frac{(a)_n (b)_n}{(c)_n} \frac{z^n}{n!} ,$$

    with $(a)_n = 1$ if $n = 0$ and $(a)_n = a(a+1) \times \cdots \times (a+n-1)$ if $n \geq 1$.
  - The gamma function

    $$\Gamma(z) = \frac{1}{z} \prod_{n=1}^{\infty} \frac{(1+1/n)^z}{1+z/n} .$$

1 - Introduction

The chapter covers important topics in cosmology, dark matter and gravitational wave physics. It starts by exploring the history and properties of the universe, leading up to the introduction of the ΛCDM model. The focus then shifts to the study of dark matter, including its challenges and alternative models to the standard cold dark matter paradigm and weakly interacting massive particles. Among the alternative dark matter models, special attention is given to scalar field dark matter theories. We provide a detailed exploration of these models, discussing their motivations, unique characteristics, and implications. We then talk about gravitational waves, their historical significance, and the impact they have on astrophysics. Then, we discuss the aims of this thesis, highlighting the specific research objectives. Finally, an overview of the thesis structure is provided, offering a roadmap for the upcoming chapters.

1.1 . Cosmology

The study of cosmology delves into understanding the universe on its grandest scales. It seeks to uncover the origin, evolution, and fundamental nature of our cosmos. Examining the interactions between matter, energy, and spacetime, to gain a comprehensive understanding of the workings of the universe throughout its history. The origins of cosmology can be traced back to the earliest civilizations that observed and contemplated celestial phenomena. These ancient astronomers laid the groundwork for the scientific pursuit we recognize today. However, it was during the early 20th century that cosmology witnessed significant advancements, driven by the groundbreaking theories and discoveries of scientists such as Albert Einstein and his formulation of the theory of general relativity in 1915 [68]. His theory revolutionized our understanding of gravity and its implications for the structure and dynamics of the universe.

At the core of cosmology lie the fundamental constituents that govern the behavior and characteristics of the universe. Baryonic matter, comprising mainly protons, neutrons, and electrons, forms the familiar matter that constitutes stars, galaxies, and the structures we observe. However, the observable features and dynamics of the universe cannot be adequately explained by baryonic matter alone. Dark matter emerges as a prominent enigma within cosmological investigations. Although imperceptible and non-responsive to electromagnetic radiation, its gravitational influence manifests through its impact on the observed motions of galaxies and galaxy clusters and the cosmic microwave background (CMB). While its energy fraction is around a fourth of the total energy in the universe [69, 70], which is about 5 times more than baryonic matter, the true nature of dark matter remains elusive, presenting a formidable challenge in cosmology and stimulating ongoing research and theoretical inquiry. Similarly perplexing is dark energy, an enigmatic energy that permeates the fabric of spacetime. Its intrinsic property of space is responsible for the observed accelerated expansion of the universe [71]. This property was first observed from measurements of distant supernovae. Finally, Radiation, encompassing photons and other relativistic particles like neutrinos, assumes a vital role in cosmology. The CMB radiation, a remnant of the infancy of the universe when it was merely $380,000$ years old, provides a unique glimpse into its initial conditions and subsequent evolution [69, 72–74].

The unfolding of the history of the universe is a captivating chronicle. It commences with the Big Bang, an explosive event that initiated the expansion of space and the birth of time. In its earliest moments, the universe experienced a period of rapid expansion known as inflation, accounting for its remarkable uniformity on large scales. As the universe cooled, particles gradually coalesced, leading to transformative processes such as the Big Bang nucleosynthesis, the process in which light atomic nuclei such as hydrogen and helium were formed, and baryogenesis, that established an asymmetry between matter and antimatter. This asymmetry laid the groundwork for the formation of cosmic structures that populate our cosmos today [75]. Over billions of years, the gravitational interplay between dark matter, ordinary matter, and the influence of dark energy facilitated the assembly of galaxies, clusters, and superclusters, sculpting the vast cosmic web we observe. Figure 1.1 illustrates the various stages in the evolution of the universe.

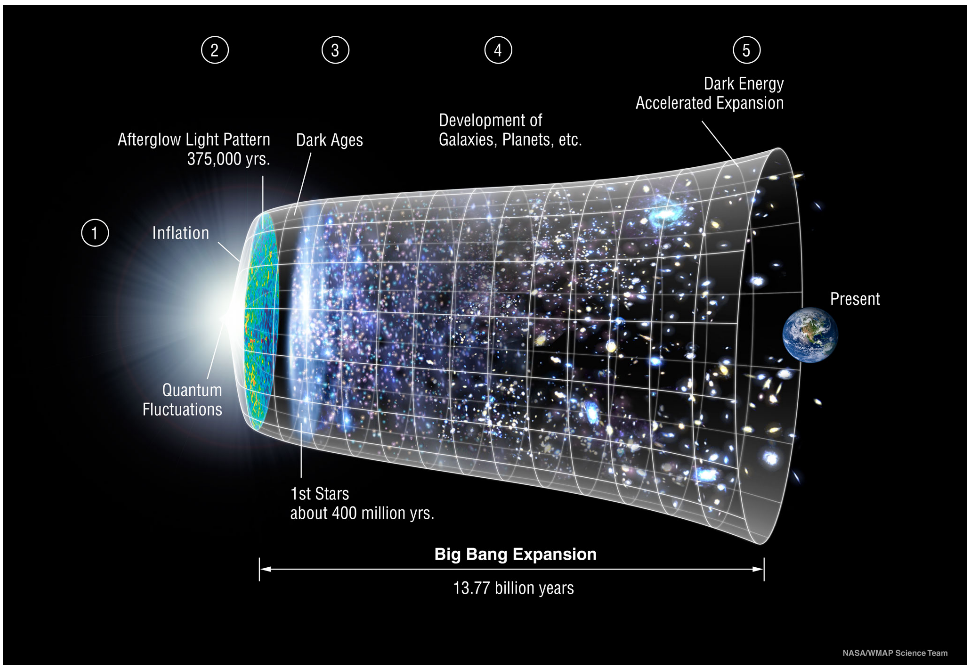

Figure 1.1: Illustration of the theorized stage in the evolution of the universe (Credit: NASA / LAMBDA Archive / WMAP Science team [76]).

The universe possesses important properties that help us understand its nature. One important property is isotropy, which means the universe looks the same in all directions.

This implies a uniform distribution of matter and energy on large scales. In addition to isotropy, the universe also exhibits homogeneity, meaning it has a uniform distribution of matter and energy on large scales. This implies that, on average, the universe appears the same from any given location. The combined properties of isotropy and homogeneity provide a framework for studying the overall structure and behavior of the universe. Observational evidence, such as the CMB radiation and large-scale galaxy surveys, supports these properties [69, 77, 78]. To mathematically describe the isotropic and homogeneous universe, we usually consider the Friedmann-Lemaître-Robertson-Walker metric [79–85]. This metric incorporates the scale factor a, which represents the expansion of the universe with time, the spatial curvature k, and cosmic time t. This metric can be expressed as

$$ds^2 = -dt^2 + a(t)^2 \left[\frac{dr^2}{(1-kr^2)} + r^2(d\theta^2 + \sin^2(\theta) d\phi^2) \right] , \tag{1.1}$$

with a $(-,+,+,+)$ convention for the metric signature. Here, ds^2 represents the spacetime interval, r represents the comoving radial distance, and θ and ϕ represent the angular coordinates. This mathematical framework allows us to investigate the evolution and geometry of the universe. The scale factor a illustrates how the universe expands or contracts over time, influencing the distances between cosmic objects: an increase in $a(t)$ corresponds to an expanding universe, while a decrease indicates contraction. The spatial curvature term k characterizes the overall shape of the universe, distinguishing between a closed, positively curved universe (positive k), an open, negatively curved universe (negative k), or a flat universe (zero curvature). Observations indicate that the universe is remarkably close to being flat. The spatial curvature term,if not zero, is to be very small. One evidence comes from studies of the cosmic microwave background radiation, as detailed measurements of the temperature fluctuations reveal a remarkable uniformity on large scales (with an energy fraction of $-10^{-3} \lesssim \Omega_{\mathrm{k}} \lesssim 10^{-3}$, given by Planck [69]).

1.2 . The ΛCDM model

The standard model of cosmology, known as the ΛCDM model, incorporates the existence of dark matter and dark energy into the framework of general relativity. In this model, dark matter, with its gravitational influence, provides the necessary mass to explain the observed rotation curves of galaxies, the dynamics of galaxy clusters, and the large-scale distribution of matter. Dark energy, often attributed to the cosmological constant Λ, is postulated to explain the accelerated expansion of the universe.

The dark matter is postulated to be composed of non-baryonic particles that interact weakly, if at all, with electromagnetic radiation. These particles are believed to be collisionless, meaning they do not experience significant interactions with each other or with ordinary matter, but massive. Such properties explain why dark matter forms extended, diffuse halos around galaxies, providing the gravitational scaffolding for the observed galactic structures. it is also supposed to be "cold" (CDM), implying that the particles move at relatively low velocities compared to the speed of light. This characteristic is crucial to have a bottom-up formation of cosmic structures [86], meaning that the small structures such as dark matter haloes form first and subsequently merge to build larger structures like galaxies and galaxy clusters, as observations of the large-scale distribution of matter as well as computer simulations based on the ΛCDM model provide compelling evidence for this bottom-up scenario [87–89]. The initial density fluctuations in the early universe, imprinted in CMB radiation, served as the seeds for the formation of dark matter halos. These halos, composed primarily of cold dark matter particles, gradually grew through gravitational attraction and the accretion of surrounding matter. As dark matter halos grew, their gravitational pull attracted ordinary matter, enabling the formation of galaxies and clusters within them. The cold dark matter dominated halos provided a gravitational scaffold that helped to gather baryonic matter, allowing gas to condense and form stars. The hierarchical assembly of structures, driven by the gravitational interactions of dark matter, is consistent with the observed large-scale distribution of galaxies and the clustering patterns revealed by galaxy surveys.

The dynamics of the universe, including its expansion and evolution, are governed by fundamental equations derived from general relativity. The Einstein field equations [68], written as

$$R_{\mu\nu} - \frac{1}{2}Rg_{\mu\nu} + \Lambda g_{\mu\nu} = 8\pi\mathcal{G}T_{\mu\nu}\,, \tag{1.2}$$

describe the curvature of spacetime in the presence of matter and energy. Here, $R_{\mu\nu}$ represents the Ricci curvature tensor, R is the scalar curvature, $g_{\mu\nu}$ is the metric tensor, Λ is the cosmological constant, $\mathcal{G}$ is the gravitational constant, and $T_{\mu\nu}$ denotes the stress-energy tensor that characterizes the distribution of matter and energy in the universe. In addition, the Friedmann equations [79, 80] provide fundamental insights into the expansion of the universe and its energy content. The first Friedmann equation, given by

$$H(t)^2 = \left(\frac{\dot{a}}{a}\right)^2 = \frac{8\pi\mathcal{G}}{3}\rho - \frac{k}{a^2} + \frac{\Lambda}{3}\,, \tag{1.3}$$

relates the rate of change of the scale factor $\dot{a}/a$, which represents the expansion rate of the universe and is defined as the Hubble parameter $H(t)^2$, to the energy density ρ of matter and energy, and the cosmological constant Λ. The scale factor is related to the observed redshift (z) of distant objects through the equation $1 + z = a(t_{\mathrm{observed}}/a(t_{\mathrm{emitted}})$, where t_{observed} and t_{emitted} are the times of observation and emission, respectively. The redshift parameter z quantifies the stretching of light wavelengths due to cosmic expansion. By measuring redshifts, we can infer the expansion rate of the universe at different cosmic epochs, providing insights into its age, dynamics, and evolution. The second Friedmann equation, expressed as

$$\dot{H}(t) + H(t)^2 = \frac{\ddot{a}}{a} = -\frac{4\pi\mathcal{G}}{3}(\rho + 3p) + \frac{\Lambda}{3}\,, \tag{1.4}$$

relates the acceleration $\ddot{a}/a$ of the expansion to the combined effects of matter and energy pressure p on the cosmic scale factor, as well as the cosmological constant Λ. These fundamental equations, derived from general relativity, form the cornerstone of cosmological investigations, providing a mathematical framework to study the dynamics of the universe and its constituents.

1.3 . Cold dark matter and alternatives

Dark matter remains one of the most intriguing puzzles in cosmology and particle physics. The first evidence of its existence appeared in the 1930s by Fritz Zwicky [90, 91], who observed that the visible matter in galaxy clusters was insufficient to account for the observed gravitational effects. Since then, numerous lines of evidence have bolstered the case for the existence of dark matter. Observational evidence for dark matter spans a wide range of cosmic scales. Rotation curves of spiral galaxies, such as the famous measurements of Andromeda nebula by Vera Rubin [92], reveal that the velocity of stars and gas remains constant at large distances from the galactic center, defying expectations based on visible matter alone. This discrepancy suggests the presence of additional unseen matter, which we now attribute to dark matter. In galaxy clusters, gravitational lensing studies, such as the observations of the Bullet Cluster [93–96], provide further evidence. The gravitational lensing effect occurs when the path of light from distant sources is bent by the gravitational field of intervening matter. By mapping the distribution of visible matter through its gravitational lensing effect, it was found that the majority of the mass in the cluster was concentrated away from the visible galaxies, indicating the presence of a significant amount of dark matter. The concordance or ΛCDM model incorporates the existence of cold dark matter. In this model, dark matter is postulated to be made up of non-baryonic particles that interact weakly with electromagnetic radiation. These particles are collectively referred to as Weakly Interacting Massive Particles (WIMPs) and are a leading candidate in the search for dark matter.

From a particle physics perspective, the WIMP paradigm provides a compelling explanation for the observed abundance of dark matter. WIMPs are hypothesized to have been produced in the early universe through processes such as thermal freeze-in or freeze-out [97–102]. Under certain theoretical assumptions, the relic density of WIMPs matches the observed abundance of dark matter inferred from cosmological measurements, lending support to the idea that WIMPs could be the primary constituents of dark matter. However, despite extensive experimental efforts, the direct detection of dark matter particles, particularly WIMPs, has remained unsuccessful to date [4–7]. Experiments such as the Large Underground Xenon (LUX) [103–105] and XENON1T [106–109] have placed stringent constraints on the interaction of WIMPs with ordinary matter, yet no conclusive detection has been made. This absence of direct evidence poses challenges to the WIMP paradigm and has led to a broader exploration of alternative dark matter candidates. New experiments, such as the upcoming Large Hadron Collider (LHC) upgrades and the next generation of direct detection experiments [5, 6, 110–114], aim to explore new regions of parameter space and shed light on the nature of dark matter.

From a cosmological perspective, there are several challenges that arise when comparing the predictions of CDM simulations with observational data. These challenges, often referred to as cosmological problems [8–12], shed light on the complexities of galaxy formation and the properties of dark matter halos. One notable cosmological problem is the "missing satellites problem" [115–118]. According to cold dark matter simulations, there should be a plethora of small dark matter halos hosting dwarf galaxies around larger galaxies like the Milky Way. However, the observed number of dwarf galaxies is significantly lower than predicted. The "too big to fail problem" is another challenge related to the previous one [119–122]. In this case, the observed number of luminous satellites associated with galaxies is considerably lower than expected. This suggests that the most massive subhalos predicted by simulations may not host visible galaxies. The "core-cusp problem" pertains to the density profiles of dark matter halos [49, 50, 123–125]. Cold dark matter simulations predict a central density profile with a steep cusp, while observations of dwarf galaxies suggest a more constant, cored profile. Finally, the distribution of angular momentum in galaxies presents an additional challenge. Simulations tend to predict galaxies with excessive angular momentum, resulting in extended and flattened disks that do not align with observed galactic morphology.

In relation to the topic of Active Galactic Nuclei (AGN), it is worth noting that AGN are powered by the accretion of matter onto supermassive black holes at the centers of galaxies. AGN can have a significant influence on the surrounding baryonic matter and can act as a form of feedback. The energy released by AGN can affect the surrounding gas and regulate the growth of galaxies, influencing their formation and structure. Exploring the connection between AGN activity, baryons, and baryonic feedback is an active area of research in understanding the complex processes shaping galaxies and their environments.

One possible explanation for this discrepancies is the inclusion of baryonic physics in simulations [13–20]. Processes such as gas cooling and feedback mechanisms such as supernovae or interactions with the intergalactic medium, which are not fully captured in pure dark matter simulations, can suppress the formation of low-mass galaxies, redistribute the dark matter and lead to a flatter central density profile or even transfer angular momentum. Active Galactic Nuclei (AGN), which are powered by the accretion of matter onto supermassive black holes at the centers of galaxies, can have a significant influence on the surrounding baryonic matter and can act as a form of feedback. Indeed, the energy released by AGN can affect the surrounding gas and regulate the growth of galaxies, influencing their formation and structure. However, further investigation into the role of baryons and baryonic feedback are required to confirm this explanation. As of today, simulations including such effects are not all in agreements and do not explain all of these discrepancies.

Another avenue of exploration involves alternative dark matter models:

- Axions [127–132], initially proposed to resolve the strong CP problem in particle physics, have emerged as compelling dark matter candidates. Their ultralight mass, weak interactions with ordinary matter, and potential abundance matching the observed dark matter density.

Figure 1.2: Visualization of possible solutions to the dark matter problem (from [126]).

- Ultralight dark matter, also called wave or scalar field dark matter [63, 133–136], is a closely related candidate, which includes axion-like particles and scalar fields with extremely low masses. Often called fuzzy dark matter when the mass is low ($< 10^{-21}$ eV). The motivation for studying ultralight dark matter arises from its potential to address the core-cusp problem, the missing satellite problem and the too-big-to fail problem [8, 11, 49, 50]. These candidates, with their wave-like behavior, could influence the formation and dynamics of cosmic structures on small scales, resulting in cored density profiles and suppressing the abundance of small substructures.

- Sterile neutrinos [137–142], hypothetical particles that do not participate in the weak nuclear force, have gained attention as potential warm dark matter candidates. The motivation for studying sterile neutrinos arises from their ability to address small-scale structure problems associated with cold dark matter. If sterile neutrinos possess the right properties, they could explain the observed properties of dark matter while leaving distinct signatures in astrophysical observations and laboratory experiments.

- Primordial black holes [143–147], hypothetical black holes that could have formed in the early universe, also offer an alternative explanation for dark matter. Depending on their mass spectrum, primordial black holes could account for the observed gravitational effects of dark matter without invoking new particle physics. Their study is motivated by their potential role in explaining various cosmological phenomena, such as the origin of supermassive black holes, the formation of galactic structures, and the gravitational waves detected by LIGO/Virgo. Observational searches for them, including microlensing events and other astrophysical signatures, provide valuable avenues for testing their existence and properties. However, the range of masses in which primordial black holes can potentially explain the entirety of dark matter is limited. In most scenarios studied today, primordial black holes can only contribute a fraction of the total dark matter content.

In addition to alternative particle candidates, modified gravity theories have emerged as serious contenders to explain the observed effects attributed to dark matter. These theories propose modifications to the laws of gravity on cosmological scales as an alternative to the presence of non-baryonic dark matter particles. One prominent modified gravity theory is Modified Newtonian Dynamics (MOND) [148–151], which suggests a modification to the law of gravity at low accelerations. Another modified gravity framework is represented by modified gravity theories like $f(R)$ gravity [152–154], where modifications are introduced to the gravitational action by modifying the curvature scalar R in the field equations. These theories propose changes to the gravitational dynamics on cosmological scales and aim to reproduce the observed accelerated expansion. Modified gravity theories as dark matter candidates offer appealing features, including the potential to explain phenomena at galactic and cosmological scales while circumventing the need for unknown dark matter particles. However, it is worth noting that modified gravity theories face their own set of challenges. These include the need to explain a wide range of observations, including large-scale structure formation, CMB anisotropies, and gravitational lensing, while remaining consistent with other well-established cosmological measurements in the Solar System. Figure 1.2 provides a summary of numerous alternative scenarios regarding dark matter models.

1.4 . Scalar field dark matter

Scalar field dark matter represents a diverse class of theoretical models that propose the existence of a scalar field as the primary constituent of dark matter. These models introduce a scalar field, a fundamental quantity that varies smoothly in space and time, to explain the observed gravitational effects attributed to dark matter. The mass range for scalar field dark matter typically spans from about 10^{-23} eV to 10 eV, covering an impressive range of scales [63, 133, 135, 155, 156]. The lower limit is motivated by quantum mechanics and the uncertainty principle. Quantum mechanics dictates that particles with smaller masses have larger de Broglie wavelengths. Therefore, for scalar field dark matter, a lower mass limit on the order of 10^{-23} eV is set to ensure that the de Broglie wavelength remains sufficiently small to allow the formation of structures on galactic scales.

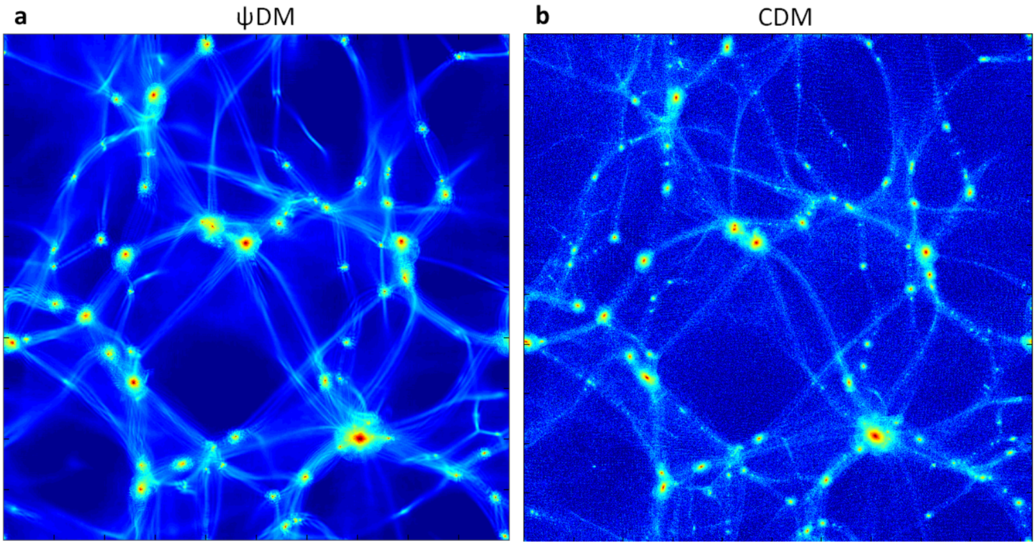

Figure 1.3: Comparison of cosmological large-scale structures formed by standard cold dark matter (CDM) and by wavelike dark matter (ψDM) (from [22]).

If the mass were any smaller, the wave-like behavior of the scalar field would become significant on larger scales, washing out the observed structures. On the other hand, the upper limit is determined by several factors. Firstly, it is related to the requirement that the Compton wavelength of the scalar field should be smaller than the size of the universe. If the mass of the scalar field were too large, its de Broglie wavelength would be too small to produce structures on the scales we observe today. Furthermore, there is another crucial factor that determines these upper limit - the maximum number occupancy of the bosonic particles. Bosonic particles, like those proposed in scalar field dark matter models, obey Bose-Einstein statistics, which allow multiple particles to occupy the same quantum state. However, the quantum statistical limit, arising from the principles of quantum mechanics and the Pauli exclusion principle, imposes a constraint on the maximum number of particles that can occupy a single state. This limit depends on the mass of the bosonic particles. The energy density of dark matter in these scenarios is determined by the misalignment mechanism [157–160]. This mechanism involves the initial freezing of the field, followed by rapid oscillations once its mass surpasses the Hubble rate. When considering scalar-field potentials primarily influenced by their mass term, the energy density declines with the cosmic scale factor, denoted as $a(t)$, following a power law of $a(t)^{-3}$. This behavior is analogous to that of cold dark matter. Consequently, the primary predictions of the standard cold dark matter paradigm on cosmological scales are restored [133, 161–167], as shown in Figure 1.3.

Scalar field dark matter theories are motivated by various cosmological and particle physics considerations. From a cosmological perspective, these models offer potential solutions to long-standing challenges within the standard cold dark matter framework. For instance, the ultralight nature of fuzzy dark matter can address the core-cusp problem, where observed galactic density profiles differ from the predictions of CDM simulations [63, 133–136]. From a particle physics viewpoint, scalar field dark matter models have connections to fundamental theories beyond the Standard Model. For example, ultra-light dark matter candidates often arise in the context of string theory or extensions of the Standard Model [168–172], such as axion-like particles.

These models offer the possibility of the formation of solitonic structures, also called soliton or boson stars, at the center of dark matter haloes [21–48]. They are localized, stationary, and stable equilibrium configurations. This solitonic objects sustained by the gravitational self-attraction of the scalar field and its internal pressure, this last one being most of the time dominated by quantum pressure. The quantum pressure can be understood as a consequence of the wave-like nature of the scalar field particles. The de Broglie wavelength associated with the particles determines the extent to which they can be localized, in agreement with Heisenberg's uncertainty principle. As the scalar field particles become more localized, their momentum becomes less well-defined, resulting in a larger uncertainty in their velocity. This uncertainty in velocity gives rise to a pressure that opposes gravitational collapse. This objects can be considered as the scalar field analogs of compact astrophysical objects, such as neutron stars. They can have sizes ranging from stellar scales (< 1 pc) to galactic scales (usually < 10 kpc) [23, 63, 173, 174]. The size of a soliton is closely related to the Jeans scale, which represents the length scale at which gravitational and pressure forces balance each other, and thus determines the minimum size required for collapse to occur. When the size of a soliton is smaller than the Jeans scale, quantum pressure dominates, resulting in stable structures. If the size exceeds the Jeans scale, gravitational collapse prevails. Figure 1.4 showcases simulations depicting the profile of wave-like dark matter at galactic scales, with solitonic profile at the core. The formation mechanisms of solitonic structures in scalar field dark matter are the subject of ongoing research. The precise conditions and mechanisms that give rise to solitons are complex and depend on the detailed interplay between self-interactions, gravity, and other factors, such as the initial conditions of the scalar field.

One prominent example of scalar field dark matter is the concept of fuzzy dark matter [133]. Fuzzy dark matter suggests that dark matter particles are ultralight bosons with masses on the order of 10^{-23} eV to 10^{-21} eV [64, 175, 176]. These particles possess de Broglie wavelengths on galactic scales, leading to a quantum wave-like behavior that suppresses small-scale structure formation and potentially resolves the core-cusp problem. A subcategory of fuzzy dark matter is Bose-Einstein condensate dark matter [177–180], which proposes that dark matter particles form a Bose-Einstein condensate at low temperatures and densities. In this scenario, the scalar field associated with dark matter undergoes a phase transition, leading to a macroscopic occupation of the lowest energy state. This condensate behavior offers unique features, such as wave interference effects and coherence on large scales, which could impact the formation of cosmic structures. Superfluid dark matter [156, 181, 182] is another concept within scalar field dark matter

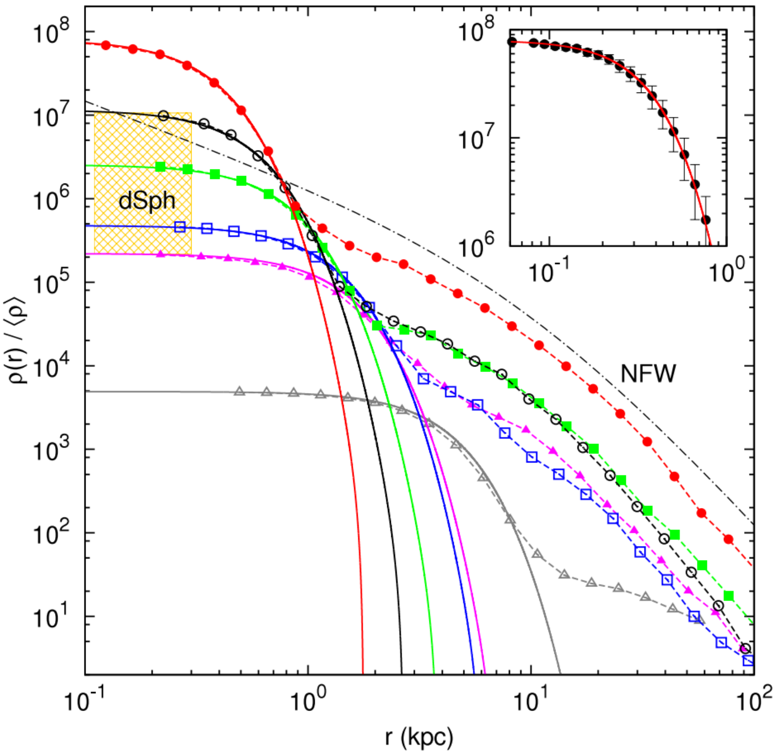

Figure 1.4: Radial density profiles of haloes formed in the ψDM model, with various halo profiles normalizations compared to Navarro-Frenk-White (NFW) profile of cold dark matter (from [22]).

theories. It draws inspiration from the physics of superfluids, where a scalar field develops long-range coherence and exhibits quantum mechanical properties. Superfluid dark matter models suggest that dark matter particles can form a superfluid state, characterized by zero viscosity and irrotational flow.

Unlike other models where the scalar field interacts weakly or non-gravitationally with other matter, self-interacting scalar field dark matter involves interactions among the scalar field particles themselves. The most known models with self-interactions are axion and axion-like particles [127–132], and repulsive scalar field dark matter particles [21, 183–190]. Axions were originally proposed to solve the strong CP problem in particle physics, but they have also emerged as potential dark matter candidates. Axions are characterized by their low mass and their coupling to electromagnetism and hadronic interactions. The mass of axions typically falls within the range of 10^{-6} eV to 10^{-3} eV, making them significantly heavier than other scalar field dark matter candidates. Additionally, axions exhibit attractive self-interactions. Axion-like particles, on the other hand, encompass a broader class of scalar fields that exhibit similar properties to axions but may differ in their mass, coupling strengths, and other characteristics. Some axion-like particles, such as those in string theory compactifications, can have masses at the TeV scale or even higher. Axions and axion-like particles stand out from other scalar field dark matter models due to their unique coupling to electromagnetism and hadronic interactions. These couplings allow them to interact with photons and nucleons, which can lead to distinct observational signatures. Like axions, repulsive scalar field dark matter involves interactions among the scalar field particles themselves. These repulsive interactions can arise through self-interaction potentials, allowing for collective behavior and interactions on different scales, introducing an additional pressure effects among the dark matter particles. The mass of repulsive scalar field dark matter typically encompass the totality of the scalar field dark matter mass range. In this thesis, we will refer to this repulsive dark matter as self-interacting scalar field dark matter.

Scalar field dark matter models undergo meticulous examination through a diverse array of observational and experimental data. These constraints offer valuable insights into the properties and nature of scalar field dark matter. Experiments designed for direct detection seek to measure the interactions between dark matter particles and ordinary matter. In the context of scalar field dark matter, weak or feeble interactions are typically predicted for axions and axion-like particles. Consequently, experiments such as XENON1T [106–108], LUX [103–105], and PandaX [191–193] have established stringent limits on the dark matter-nucleon scattering cross section, ruling out significant portions of the parameter space for specific masses and interaction strengths. The Lyman-α forest [51–53], observed in the spectra of distant quasars, provides valuable insights into the distribution of matter on cosmological scales. Detailed analyses, involving comparisons between theoretical predictions and observational data from surveys like the Sloan Digital Sky Survey (SDSS) [52], have placed constraints on the mass of scalar field dark matter. Solitonic structures, have implications for the rotation curves of galaxies. The observed flatness of galactic velocity curves [38, 194] contradicts the expectations solely based on the distribution of luminous matter. Scalar field dark matter, including self-interacting scenarios, can modify these curves. By comparing theoretical predictions with rotation curve data, constraints on the parameters of scalar field dark matter models can be established. Some constraints can also be obtained using large-scale observables, such as CMB and the baryonic acoustic oscillations [195] The recent detection of gravitational waves resulting from the merger of black holes and neutron stars presents another avenue for constraining scalar field dark matter [196–200]. Dark matter can influence the formation and evolution of black holes, potentially affecting the gravitational wave signals. Comparing the gravitational wave observations from experiments with predictions derived from scalar field dark matter models allows for the imposition of constraints on the relevant parameters within the theory. Large-scale properties of the universe, including CMB radiation and the distribution of large-scale structures like galaxies, offer significant insights into scalar field dark matter. Surveys such as the Dark Energy Survey (DES) [201, 202] provide additional data for investigating the composition and distribution of dark matter.

The specific constraints on scalar field dark matter parameters, such as mass, self-interactions, and other characteristics, depend on the combination of observational and experimental techniques employed. Each constraint and observation targets different aspects of the models, contributing to a comprehensive understanding of their viability.

1.5 . Gravitational waves

The history of gravitational waves dates back to Einstein's theory of general relativity. However, it took several decades for the theoretical understanding of gravitational waves to mature and experimental detection to become feasible. In the 1960s, physicists like Weber [203–206] embarked on experimental endeavors to detect gravitational waves. Weber conducted pioneering experiments using resonant bar detectors [207], although his results faced skepticism and remained unconfirmed. A major breakthrough occurred in 2015 when the Laser Interferometer Gravitational-Wave Observatory (LIGO) and Virgo collaborations achieved the first direct detection of gravitational waves [208]. Figure 1.6 displays the frequency and strain variations over the time of detection of this historical event. This monumental discovery confirmed a key prediction of Einstein's theory and opened a new window for observing the universe.

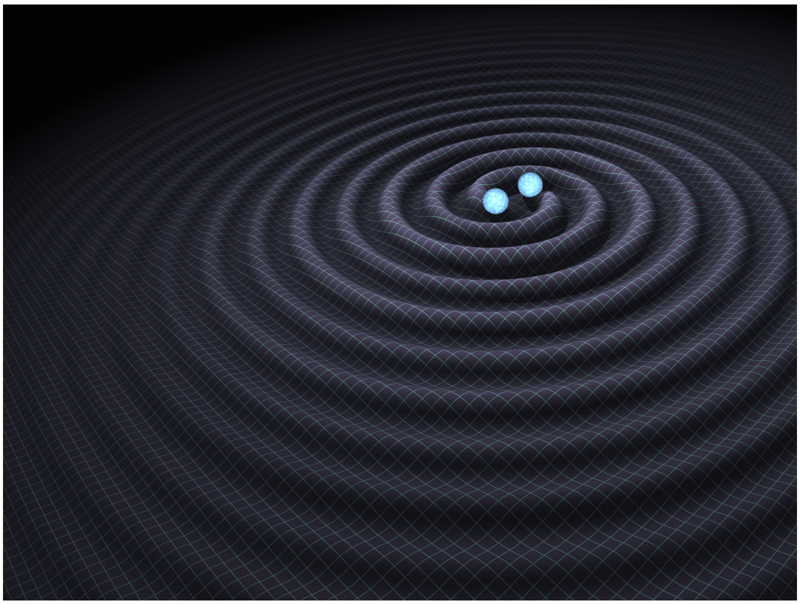

Figure 1.5: This illustration shows the merger of two black holes and the gravitational waves that ripple outward as the black holes spiral toward each other (Credit: R. Hurt (Caltech-IPAC) [209]).

Gravitational waves are ripples in the fabric of spacetime caused by the acceleration of massive objects. According to general relativity, these waves propagate at the speed of light, carrying energy away from their source. Mathematically, gravitational waves are described by the linearized Einstein field equations, involving perturbations of the metric tensor. The resulting wave equation highlights the wave-like nature of gravitational

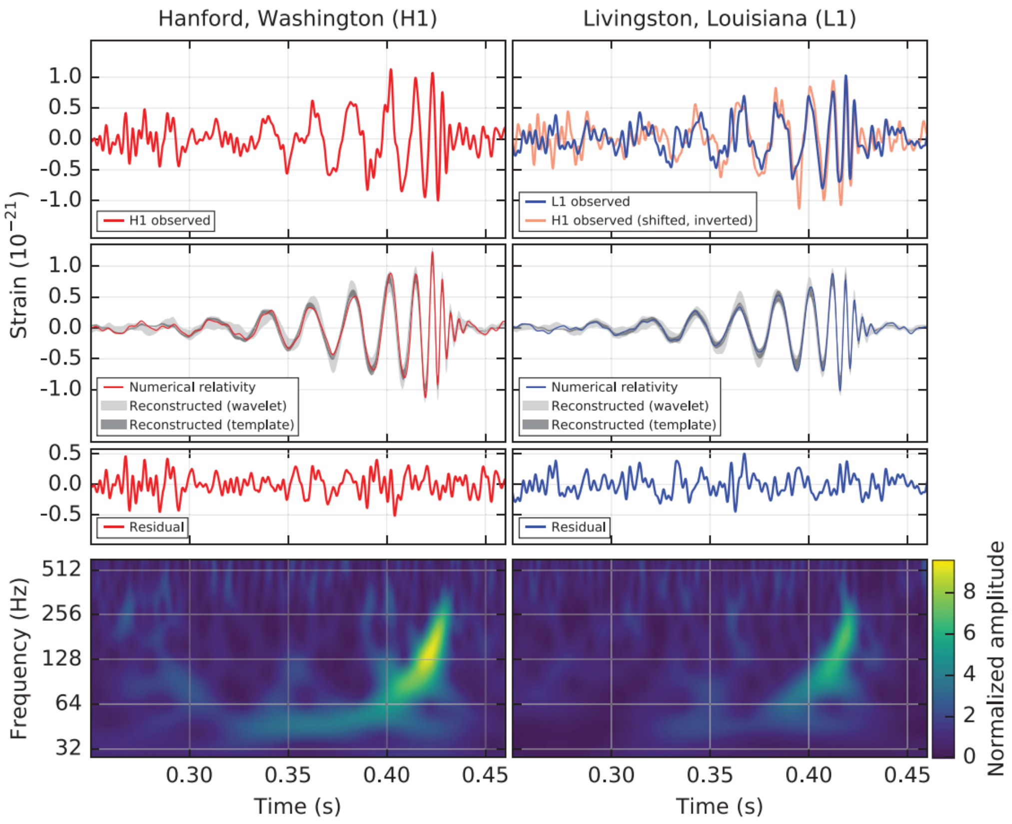

Figure 1.6: The gravitational-wave event GW150914 observed by the LIGO Hanford (H1, left column panels) and Livingston (L1, right column panels) detectors (From [208]).

disturbances, characterized by amplitude, frequency, polarization, and propagation direction. Gravitational wave sources can be classified into astrophysical and cosmological categories (see [210, 211] for reviews). Astrophysical sources include binary systems like merging black holes, neutron stars, or white dwarfs. This case is illustrated in Figure 1.5. Cosmological sources originate from the early universe during cosmic inflation, for instance.

The current generation of gravitational wave detectors primarily consists of ground-based interferometers, prominently represented by the LIGO [212, 213] and Virgo [214, 215] collaborations. These interferometers employ laser interferometry to measure minuscule changes in spacetime induced by passing gravitational waves. LIGO features two widely separated detectors located in Livingston, Louisiana, and Hanford, Washington. Each LIGO detector comprises an L-shaped vacuum chamber with 4-kilometer-long arms. A laser beam is split and sent down each arm, reflecting off mirrors and recombining to form an interference pattern. When a gravitational wave passes through the detectors, it causes minute differences in arm lengths, altering the interference pattern and enabling gravitational wave detection. Virgo, situated near Pisa, Italy, follows a similar design as LIGO, with 3-kilometer-long arms. It operates in coordination with LIGO, enhancing the global network's sensitivity to gravitational wave signals. Future prospects in gravitational wave astronomy involve the development of next-generation detectors. Prominent among these are the Laser Interferometer Space Antenna (LISA) [66] and the DECi-hertz Interferometer Gravitational wave Observatory (DECIGO) [216, 217]. LISA, a collaboration between the European Space Agency (ESA) and the National Aeoronautics and Space Administration (NASA), aims to detect lower-frequency gravitational waves. It comprises three spacecraft forming an equilateral triangle in space, separated by millions of kilometers. LISA will be sensitive to gravitational waves emitted by massive black hole mergers and other astrophysical sources. DECIGO, designed to operate between LISA and ground-based detectors, targets the sub-hertz to kilohertz frequency range. It is expected to detect gravitational waves from sources like inflationary processes in the early universe, providing insights into fundamental cosmic physics.

The current limitations on gravitational wave detection frequencies range from approximately 10 Hz to a few kHz for ground-based detectors like LIGO and Virgo. Within this frequency range, the most significant gravitational wave sources that have been observed are binary systems consisting of compact objects such as black holes and neutron stars [208, 218–221]. For binary black hole mergers, the observed frequencies were typically in the tens to hundreds of hertz range. Binary neutron star mergers, on the other hand, produced gravitational waves with characteristic frequencies in the range of several tens of hertz. While LIGO and Virgo have made groundbreaking discoveries within their frequency band, there is tremendous interest in exploring lower-frequency gravitational waves. This is because lower-frequency gravitational waves can arise from astrophysical phenomena that are not easily detectable within the current range. One crucial target for lower-frequency observations is the inspiral and merger of supermassive black holes in the centers of galaxies. These massive black holes, millions to billions of times more massive than the sun, generate gravitational waves at lower frequencies, typically in the millihertz band. Going to lower frequencies also allows for the study of other astrophysical sources, such as extreme mass-ratio inspirals (EMRIs). EMRIs occur when a stellar-mass compact object, such as a black hole or a neutron star, spirals into a much more massive black hole. These systems produce gravitational waves at frequencies in the sub-hertz range. Observing these waves will enable us to probe the strong gravity regime near the massive black hole and test the predictions of general relativity. The detection and characterization of these waves require space-based observatories, such as the upcoming LISA or DECIGO [197, 222, 223].

As it is a subject of current interest, the European Pulsar Timing Array (EPTA), Parkes Pulsar Timing Array (PPTA), the Chinese Pulsar Timing Array (CPTA) and North American Nanohertz Observatory for Gravitational Waves (NANOGrav) collaborations have made significant contributions in the search for stochastic gravitational wave background and provided the first evidence of its existence [224–227]. Stochastic gravitational waves refer to a random background of gravitational waves that originate from various astrophysical and cosmological sources. They cover a wide range of frequencies, with the low-frequency regime (around 10^{-9} to 10^{-6} Hz) being particularly intriguing. In this range, stochastic gravitational waves can arise from events such as inspiralling supermassive black holes or cosmic strings formed during the early stages of the universe. To detect these stochastic gravitational waves, we employ pulsar timing arrays, including EPTA, PPTA, CPTA and NANOGrav, that utilize precise timing measurements of signals from an array of pulsars distributed across the sky. By monitoring the arrival times of these pulsar signals, we can search for correlated deviations that could be caused by the passage of gravitational waves. Physicists have begun the process of constraining various sources in their search for the initial evidence of a stochastic gravitational wave background [228–233].

Figure 1.7 illustrates the complete frequency range investigated for gravitational waves, showcasing the associated events and different detectors along with their respective frequency range of detection.

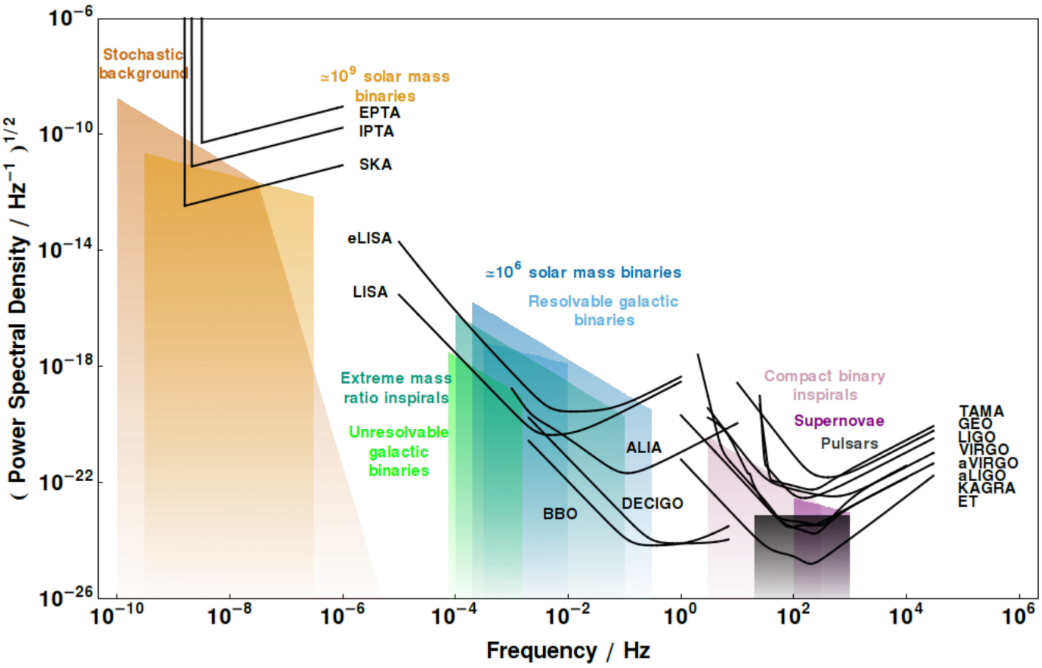

Figure 1.7: A plot of the square root of power spectral density against frequency for a variety of detectors and sources (From [234]).

Testing modified gravity using gravitational waves provides a unique opportunity to investigate the fundamental properties of gravity, as they offer a window into extreme gravitational environments that were previously inaccessible for empirical study. To test modified gravity with gravitational waves, the precise measurements obtained from gravitational wave detectors play a crucial role. By carefully analyzing the gravitational wave data, we can search for potential deviations from the predictions of general relativity [235–238]. Such deviations could manifest as alterations in the waveforms or discrepancies in the overall magnitude of the gravitational wave signals. The detection of such deviations would suggest the presence of modified gravity effects. Furthermore, the statistical analysis of gravitational wave observations from diverse astrophysical sources allows for comparisons between theoretical predictions and empirical data [239, 240]. This approach enables physicists to place constraints on the parameters of modified gravity theories, either ruling out certain ranges or favoring specific modifications. Additionally, the polarization patterns and dispersion properties of gravitational waves offer valuable insights for probing modified gravity theories[241–246]. These theories often predict changes in the polarization content or the propagation speed of gravitational waves. Precise measurements of these properties can, therefore, serve as tests to verify the consistency of modified gravity theories with observational data.

The detection of gravitational waves also provides a unique opportunity to not only study astrophysical phenomena but also to search for potential imprints of dark matter [247]. While dark matter does not directly interact with light or ordinary matter, it could leave subtle signatures in the gravitational wave signals originating from various astrophysical sources. One possibility is the existence of dark matter halos and subhalos. These are small-scale structures made up of dark matter particles, which could form around galaxies or within galaxy clusters. As gravitational waves pass through these structures, they may experience slight distortions or delays, lensing them, leading to detectable modifications in the gravitational wave signal [248–255]. Such effects would depend on the abundance, mass distribution, and interactions of dark matter substructures. Another potential imprint arises from interactions between dark matter and compact astrophysical objects, such as black holes or neutron stars. If dark matter possesses self-interactions or couplings with standard model particles, it could affect the dynamics and gravitational wave emission of these objects [256–258]. Primordial black holes are another avenue where dark matter imprints in gravitational waves is explored [146, 259–261]. They are hypothetical black holes that may have formed in the early universe. If primordial black holes exist and comprise a fraction of dark matter, their mergers with other astrophysical objects would generate gravitational waves with specific characteristics and statistical appearance.

Finally, scalar field dark matter can introduce various processes that may influence the gravitational wave emission from astrophysical sources. These processes include orbital decay resulting from mass accretion or dynamical friction [222, 262–265], superradiance [54–56], and tidal forces [57, 58] are some examples. When scalar field dark matter accretes onto compact astrophysical objects, such as black holes or neutron stars, it can lead to orbital decay. The gravitational interaction between the dark matter particles and the object causes a gradual reduction in the orbital separation of the objects. This effect alters the inspiral dynamics and modifies the emitted gravitational wave signal. The specific properties of the scalar field dark matter, including its density distribution and self-interactions, play crucial roles in determining the magnitude and timescale of the orbital decay. Superradiance, a quantum mechanical phenomenon, can occur when a rotating black hole interacts with a scalar field. Under certain conditions, the scalar field can extract energy and angular momentum from the black hole, resulting in an amplification of the intensity of the gravitational wave signal. Understanding these processes requires detailed theoretical modeling and simulations to fully comprehend their implications on gravitational wave emission.

While these imprints of dark matter in gravitational waves hold great interest, detecting and disentangling them from astrophysical noise pose significant challenges. To search for dark matter imprints, future gravitational wave observatories like LISA and DECIGO, with their extended frequency ranges and enhanced sensitivities, will play crucial roles. These observatories will enable investigations into the interactions between dark matter and astrophysical systems, the presence of dark matter substructures, and the characteristics of dark matter particles themselves.

1.6 . Aims

1.6.1 . Mass accretion and dynamical friction

Mass accretion and dynamical friction play crucial roles in the dynamics and interactions of astrophysical objects within a dense collection of compact bodies, such as dark matter environment or fluid media. The concept of mass accretion refers to the process by which a compact object gains mass through the accumulation of surrounding material. In the context of astrophysics, mass accretion often occurs when an object, such as a black hole, moves through a medium containing a cloud of lighter bodies. As the object traverses the environment, it interacts with and captures nearby matter, leading to an increase in its mass. Dynamical friction, initially studied by Chandrasekhar in 1943 for the collisionless case [60] and later extended to gaseous media [266–269], describes the deceleration of the motion of an object due to its interaction with surrounding particles. When an astrophysical object moves through dark matter or a fluid it experiences a gravitational drag force known as dynamical friction. This force arises from the gravitational interactions between the object and the individual particles in the environment. As a result, the kinetic energy of the object decreases, leading to a reduction in its velocity and orbital separation.

The specific scenario of a black hole moving inside a dark matter soliton or fluid medium presents interesting characteristics. While the collisionless and fuzzy dark matter [63, 64, 176, 270–276] cases have been extensively studied in nonrelativistic and relativistic regimes, the case of a scalar field dark matter model with self-interactions introduces distinct features. In this model, equilibrium configurations of solitons result from a balance between gravity and scalar pressure associated with self-interactions. This differs from fuzzy dark matter models, where equilibrium is achieved through the balance between gravity and the quantum pressure determined by the de Broglie wavelength. Moreover, the nature of drag force experienced by a black hole in this scalar field dark matter model differs significantly from the case of cold dark matter. The behavior of the scalar field in the nonlinear and relativistic regime close to the black hole horizon alters the dynamics and the effects of drag force. These modifications arise from the interplay between the gravitational attraction of the black hole and the specific properties of the scalar field, including its self-interactions.

One of the aims of this thesis is to calculate the mass accretion and dynamical friction experienced by a Schwarzschild black hole moving inside a self-interacting scalar field dark matter soliton, particularly with relevance to current research on gravitational waves. Specifically, we consider both subsonic and supersonic regimes. Previous studies have extensively investigated the calculation of dynamical friction in fuzzy dark matter systems. In the low-velocity regime, the mass accretion is found to be greater than that for collisionless particles [60] or a perfect gas [269, 277]. Furthermore, we demonstrate in this thesis that for self-interacting scalar field dark matter, the dynamical friction null and that the drag force is composed solely of the accretion drag force, contrary to the collisionless and fuzzy dark matter cases. The effect of drag force leads to a dephasing in the emission frequency of gravitational waves, which has implications for the study of binary black holes. Future gravitational wave detectors such as LISA and DECIGO have the potential to detect the differences in dephasing between fuzzy dark matter and this scenario. This distinction could serve as a distinguishing feature that may be experimentally detectable. In another context, the timing problem observed in the orbital decay of clusters of stars, as seen in the Fornax Dwarf Spheroidal galaxy, could be addressed by this models. The discrepancy between the faster orbital decay predicted by cold dark matter numerical simulations and the slower decay observed in these clusters, known as the Fornax globular clusters timing problem, can potentially be resolved by the lower dynamical friction expected in scalar field dark matter compared to cold dark matter. This work was done for BEC dark matter in [176]. For fuzzy dark matter, this tension diminishes for low dark matter masses ($m < 10^{-21}$ eV), although this range of scalar masses may introduce potential tensions with other observables. The lower dynamical friction anticipated in self-interacting models offers a potential avenue for alleviating the tension observed in the Fornax globular clusters timing problem.

1.6.2 . Gravitational wave predictions

The study of mass accretion and dynamical friction in the context of gravitational waves provides valuable insights into probing the environments surrounding binary black holes, especially the properties of their surrounding dark matter [222, 262–265, 278]. One of the key ways to probe the environments of binary black holes is through the analysis of gravitational wave signals. Drag force leaves imprints on the emitted gravitational waves. The gravitational pull exerted on the compact object by the fluid overdensity formed in its wake introduces modifications to the waveforms by adding a phase shift. The accretion of matter onto the compact object affects the gravitational wave emission in a similar fashion. However, to fully exploit these effects as probes of dark matter environments, it is crucial to improve the sensitivity of gravitational wave detectors. Advanced detectors, such as Advanced LIGO [279] or the Einstein Telescope (ET) [280], and future missions like LISA [66] and DECIGO [67], offer promising avenues for enhancing our capabilities to detect and analyze these effects. Moreover, studying the effects of dynamical friction and mass accretion can help distinguish between different dark matter models. By carefully analyzing the gravitational wave signatures, we can discern unique features that arise from specific dark matter scenarios. Comparing the observed waveforms with theoretical models and simulations, we can gain insights into the nature of the dark matter surrounding binary black holes.

We show in this thesis that in the context of binary systems, these effects result in a higher rate of orbital decay compared to binary systems evolving solely due to the emission of gravitational waves. Using standard post-Newtonian (PN) terminology, we find that accretion introduces contributions to the gravitational wave phase at the -4PN level, while dynamical friction becomes a -5.5PN order effect. These additional effects have important implications for the observed gravitational wave signals and the interpretation of the dynamics of binary systems embedded within dark matter environments.

1.7 . Thesis outline

The thesis is organized as follows. In chapter 2.1, we provide an in-depth exploration of the general properties of the self-interacting scalar field dark matter model. We discuss the fundamental characteristics and theoretical framework of this model. This chapter draws upon calculations presented in [59], as well as incorporating additional introductory material from [1, 2]. Moving forward, chapter 3 focuses on the calculation of mass accretion and dynamical friction experienced by a Schwarzschild black hole moving within a self-interacting scalar field dark matter soliton. Specifically, we examine these phenomena in the subsonic regime, considering the detailed dynamics and interaction between the black hole and the scalar field soliton. This chapter builds upon the findings and methodologies presented in [1]. Chapter 4 extends our investigation to the supersonic regime. By considering the unique dynamics and physical properties at supersonic speeds, we gain a comprehensive understanding of the effects on the trajectory of a black hole. This chapter draws upon the research from [2]. In chapter 5, we delve into the impacts of the accretion drag force and dynamical friction on the motion of binary black holes. Here, we investigate the interplay between these effects and the emission of gravitational waves, aiming to uncover distinct signatures that can be used to discern the influence of self-interacting scalar field dark matter. This chapter is primarily based on the comprehensive analysis presented in [3]. Finally, we provide a general conclusion that summarizes the key findings, contributions, and implications of our research.

2 - Self-interacting scalar field dark matter

The aim of this chapter is to provide a comprehensive investigation of scalar field dark matter model with a quartic self-interaction. The primary objectives are to introduce and explore the fundamental concepts and equations that govern the behavior of this model, and to introduce radial accretion as studied in [59]. The analysis encompasses both nonrelativistic and relativistic regimes, with special emphasis on the large-mass limit, in which the self-interaction dominates over quantum pressure [1, 2].

2.1 . Self-interacting scalar field action

We study the scalar-field dark matter model governed by the following action

$$S_\phi = \int d^4x\sqrt{-g}\left[-\frac{1}{2}g^{\mu\nu}\partial_\mu\phi\partial_\nu\phi - V(\phi)\right] . \tag{2.1}$$

The first term represents the kinetic energy of the scalar field, where $g^{\mu\nu}$ denotes the components of the metric tensor and $\partial_\mu\phi$ represents the partial derivatives of the field ϕ with respect to the spacetime coordinates. This term captures the interplay between the scalar field and its derivatives, governing its evolution and behavior throughout spacetime. The second term, $V(\phi)$, characterizes the potential energy associated with the scalar field. The potential is further decomposed into two components

$$V(\phi) = \frac{m_{\rm DM}^2}{2}\phi^2 + V_{\rm I}(\phi) \quad \text{with} \quad V_{\rm I}(\phi) = \frac{\lambda_4}{4}\phi^4, \quad \lambda_4 > 0 . \tag{2.2}$$

The quadratic term introduces a mass parameter $m_{\rm DM}$ which influences the overall dynamics of the scalar field. Meanwhile, the quartic self-interaction term $V_{\rm I}(\phi)$ introduces a coupling constant λ_4 The self-interaction coupling constant can be either attractive and repulsive, leading to different effects on dark matter dynamics. Attractive self-interactions, usually considered for axion-like dark matter, tend to enhance the clustering of dark matter particles, resulting in the formation of dense structures. On the other hand, repulsive self-interactions have the opposite effect, leading to a more diffuse distribution.

By studying the large-scale structure of the universe, such as structure formation [281], the CMB [282], and nucleosynthesis [283], we can derive constraints on the coupling constant of the self-interactions. The impact of self-interactions on the formation and evolution of large-scale structures can be quantified through numerical simulations and compared with observational data. Current constraints indicate that the self-interaction coupling constant should be small, as larger values would lead to deviations from observed structures. On smaller scales, astrophysical observations provide additional constraints on the self-interactions of scalar field dark matter. For example, studies of galactic rotation curves [284], galactic mass [285], the Bullet Cluster [188, 286], and more recently, the speed of gravitational waves [287], the environment of supermassive black holes [288, 289], and superradiance [290] have been employed to investigate the self-interaction coupling constant. Once again, current constraints suggest that the self-interaction coupling constant should be relatively weak to maintain agreement with observed galactic dynamics.

From now on, we will consider a positive coupling constant $\lambda_4 > 0$, ensuring that the self-interaction between scalar field particles is repulsive in nature.

Within the scalar field dark matter model, it becomes crucial to consider the oscillations of the scalar field on both cosmological and galactic scales. These oscillations are primarily driven by the quadratic mass term and are required to dominate, imposing an upper bound on the value of the coupling constant λ_4. This dominance ensures that, at the lowest order, the scalar field behaves like cold dark matter, exhibiting negligible pressure. Consequently, the interaction term acts as a perturbation that subtly modifies the harmonic oscillations of the scalar field, leading to the emergence of an effective pressure. This pressure-induced deviation from the cold dark matter scenario becomes significant on small scales.

A distinctive characteristic scale, denoted as r_a, emerges as a consequence of these considerations. The expression for r_a, as established in previous works [59], is given by

$$r_a = \sqrt{\frac{3\lambda_4}{2}} \frac{M_{\rm Pl}}{m_{\rm DM}^2} \,, \tag{2.3}$$

where $M_{\rm Pl}$ represents the reduced Planck mass. This characteristic scale plays an important role in determining both the Jeans length and the size of hydrostatic equilibria, commonly referred to as solitons. The Jeans length, independent of density and redshift [21, 291], marks the scale below which density perturbations in the cosmological background cease to grow and oscillate. Furthermore, the size of hydrostatic equilibria, which form after the collapse and decoupling from the Hubble expansion, is also dictated by this characteristic scale. In the nonrelativistic regime, which governs large scales in the late universe as well as astrophysical scales far from black hole horizons, a decomposition of solutions becomes feasible. Specifically, solutions to the nonlinear Klein-Gordon equation can be separated into fast oscillations at frequency $m_{\rm DM}$ and a slowly varying envelope that evolves over cosmological or astrophysical timescales. The dynamics of the envelope are then effectively described by the Schrödinger equation. For a more comprehensive analysis of these self-interacting scalar field dark matter scenarios from a cosmological perspective, we refer interested readers to [59]. However, in the subsequent sections, our focus will be directed towards subgalactic scales, where the expansion of the universe is neglected.

2.2 . Nonrelativistic regime

In the regime characterized by Newtonian gravity (nonrelativistic weak gravity), a convenient approach is to express the real scalar field ϕ in terms of a complex field ψ. This can be achieved through the following transformation

$$\phi = \frac{1}{\sqrt{2m_{\rm DM}}}\left(e^{-im_{\rm DM}t}\psi + e^{im_{\rm DM}t}\psi^\star\right) , \tag{2.4}$$

where $\psi^\star$ denotes the complex conjugate of ψ. In this particular regime, where the typical frequencies and momenta of ψ, represented by $\dot{\psi}/\psi$ and $\nabla\psi/\psi$ respectively, are much smaller than the mass parameter $m_{\rm DM}$, the complex scalar field ψ satisfies the Schrödinger equation.

$$i\,\dot{\psi} = -\frac{\nabla^2\psi}{2m_{\rm DM}} + m_{\rm DM}(\Phi_{\rm N}+\Phi_{\rm I})\psi\,, \tag{2.5}$$

where $\Phi_{\rm N}$ corresponds to the Newtonian gravitational potential and $\Phi_{\rm I}$ represents the nonrelativistic self-interaction potential. For the quartic self-interaction, the expression for $\Phi_{\rm I}$ is given by [59]

$$\Phi_{\rm I} = \frac{m_{\rm DM}|\psi|^2}{\rho_a}\,, \quad \text{with} \quad \rho_a = \frac{4m_{\rm DM}^4}{3\lambda_4}\,. \tag{2.6}$$

To facilitate further analysis, it is advantageous to express ψ in terms of its amplitude (and density) ρ and phase s using the Madelung transform [292]. This transform is given by

$$\psi = \sqrt{\frac{\rho}{m_{\rm DM}}}e^{is}\,. \tag{2.7}$$

By applying this transform, the real and imaginary parts of the Schrödinger equation (2.5) yield two new equations

$$\dot{\rho} + \nabla\cdot\left(\rho\frac{\nabla s}{m_{\rm DM}}\right) = 0 \quad \text{and} \quad \frac{\dot{s}}{m_{\rm DM}} + \frac{(\nabla s)^2}{2m_{\rm DM}^2} = -(\Phi_{\rm N}+\Phi_{\rm I})\,. \tag{2.8}$$

Furthermore, the nonrelativistic self-interaction potential can also be expressed in terms of the amplitude ρ from (2.6) and (2.7)

$$\Phi_{\rm I} = \frac{\rho}{\rho_a} = \frac{3\lambda_4\rho}{4m_{\rm DM}^4}\,. \tag{2.9}$$

To simplify the equations further, a curl-free velocity field v is defined as $\mathbf{v} = \nabla s/m_{\rm DM}$. Subsequently, from (2.8) the continuity and Euler equations can be written in the familiar form

$$\dot{\rho} + \nabla\cdot(\rho\mathbf{v}) = 0 \quad \text{and} \quad \dot{\mathbf{v}} + (\mathbf{v}\cdot\nabla)\mathbf{v} = -\nabla(\Phi_{\rm N}+\Phi_{\rm I})\,. \tag{2.10}$$

Thus, in the nonrelativistic regime, we can transition from the Klein-Gordon equation to the Schrödinger equation, and then to a hydrodynamical picture described by the continuity and Euler equations.

It is important to note that in the Hamilton-Jacobi and Euler equations (2.8) and (2.10), the quantum pressure term

$$\Phi_{\rm Q} = -\frac{\nabla^2\sqrt{\rho}}{2m_{\rm DM}^2\sqrt{\rho}}\,, \tag{2.11}$$

has been neglected. The neglect of this term is motivated by the emphasis on a regime where the self-interaction dominates over the quantum pressure. As a result, wavelike effects such as interference patterns are considered negligible. The conditions of validity of this approximation are discussed in section 5.5.2. However, it is crucial to highlight that the dynamics of the system still differ from those of cold dark matter particles due to the presence of self-interaction.

2.3 . Static equilibrium around a black hole

Contrary to cold dark matter, the formation of static equilibrium configurations with zero velocities is possible due to the pressure arising from self-interactions [25, 184, 293]. These configurations are often referred to as Bose-Einstein condensates or boson stars and are distinct from the behavior of cold dark matter. Specifically, in the case of fuzzy dark matter, static solutions where gravity is balanced by the quantum pressure rather than self-interaction are known as solitons [23, 27, 63]. These solitons correspond to bound ground states of the linear Schrödinger equation (2.5) in the presence of the Newtonian gravitational potential. However, in the case of self-interacting scalar field dark matter, there is an additional non-linearity introduced to the Schrödinger equation due to the self-interaction potential $\Phi_{\rm I}$. This potential, along with the Newtonian potential $\Phi_{\rm N}$, contributes to the full potential, reading $\Phi = \Phi_{\rm N} + \Phi_{\rm I}$, in the equation of motion. To determine the properties of these solitons, we consider the equation of hydrostatic equilibrium, from (2.10)

$$\nabla(\Phi_{\rm N} + \Phi_{\rm I}) = 0 \,. \tag{2.12}$$

This equation can be integrated, leading to

$$\Phi_{\rm N} + \Phi_{\rm I} = \alpha \quad \text{with} \quad \alpha = \Phi_{\rm N}(R_{\rm sol}) \,, \tag{2.13}$$

where α is an integration constant determined by the radius $R_{\rm sol}$ of the spherically symmetric soliton, where the density is zero and thus $\Phi_{\rm I} = 0$. The Newtonian gravitational potential $\Phi_{\rm N}$ is composed of contributions from the central black hole and the self-gravity of the scalar cloud, reading $\Phi_{\rm N} = \Phi_{\rm BH} + \Phi_{\rm sg}$. This contributions are given by

$$\Phi_{\rm BH} = -\frac{\mathcal{G} m_{\rm BH}}{r} = -\frac{r_s}{2r} \,, \quad \nabla^2 \Phi_{\rm sg} = 4\pi\mathcal{G}\rho \,, \tag{2.14}$$

where $\mathcal{G}$ is the gravitational constant and $m_{\rm BH}$ is the mass of the black hole, linked to the Schwarzschild radius by $r_s = 2\mathcal{G} m_{\rm BH}$. By taking the divergence of the hydrostatic equilibrium equation (2.10), and using (2.9) and (2.14), we obtain a differential equation for the self-interaction potential

$$\frac{d^2\Phi_{\rm I}}{dr^2} + \frac{2}{r}\frac{d\Phi_{\rm I}}{dr} + \frac{1}{r_a^2}\Phi_{\rm I} = 0 \,, \quad \text{with} \quad r_a = \frac{1}{\sqrt{4\pi\mathcal{G}\rho_a}} \,, \tag{2.15}$$

where r_a was also defined in (2.3).

Introducing the dimensionless radius $x = r/r_a$, we can obtain the differential equation satisfied by spherical Bessel functions of order zero. This leads to the expression for the self-interaction potential $\Phi_\mathrm{I} = a j_0(x) + b y_0(x)$, where a and b are constants. At small radii, the gravitational potential is dominated by the black hole, and using (2.13) we obtain $\Phi_\mathrm{I} \simeq r_s/(2r)$. This determines the constant b. In the nonrelativistic regime, the solution for the density ρ can be expressed as a sum of two terms

$$\rho(r) = \rho_0 \frac{\sin(r/r_a)}{(r/r_a)} + \rho_a \frac{r_s}{2r_a} \frac{\cos(r/r_a)}{(r/r_a)} \,. \tag{2.16}$$

The first term dominates at large radii, where the soliton self-gravity is the main contribution to the gravitational potential. On the other hand, the second term dominates at small radii, where the gravitational potential of the black hole becomes significant. The transition radius r_sg represents the boundary between these two regimes and is typically much smaller than the size of the soliton R_sol and much larger than the Schwarzschild radius r_s

$$R_\mathrm{sol} \simeq \pi r_a \,, \quad r_\mathrm{sg} = r_s \frac{\rho_a}{\rho_0} \,, \quad r_s \ll r_\mathrm{sg} \ll R_\mathrm{sol} \,. \tag{2.17}$$

In the region far inside the soliton, the density is approximately given by

$$r_s \ll r \ll r_\mathrm{sg}^{1/3} r_a^{2/3} : \quad \rho = \rho_0 + \rho_a \frac{r_s}{2r} . \tag{2.18}$$

Expressed in terms of the fields ψ and ϕ, the static soliton can be written as

$$\psi = \sqrt{\frac{\rho}{m_\mathrm{DM}}} e^{-i\alpha\, m_\mathrm{DM} t} \,, \quad \phi = \frac{\sqrt{2\rho}}{m_\mathrm{DM}} \cos[(1+\alpha) m_\mathrm{DM} t] \,, \tag{2.19}$$

where the phase is given by $s = -\alpha m_\mathrm{DM} t$.

In the case of fuzzy dark matter, where the soliton can reach kpc sizes, numerical simulations [23, 27, 63] have shown that outside the soliton core, the scalar field is out of equilibrium and exhibits large density fluctuations. The mean falloff of the scalar field follows the Navarro-Frenk-White (NFW) profile observed in cold dark matter simulations [88]. It is expected that self-interacting scalar field dark matter behaves similarly, assuming there is a unique soliton of kpc size within galaxies. However, we also considers scenarios with smaller values of r_a, where multiple scalar clouds of smaller sizes may exist within a galaxy. The behavior of the dark matter profile beyond the soliton radius is not specified in this context, as our focus is on the interaction between the black hole and the scalar cloud within the relevant radius range. Therefore, the derivation of the scalar flow and its impact on black hole dynamics considers the hydrostatic profile within the bulk of the soliton, specifically at $r_\mathrm{sg} \ll r \ll R_\mathrm{sol}$, as the boundary condition at "large radius". The behavior at $r \gtrsim R_\mathrm{sol}$ is not addressed, as it is not relevant to the investigation of black hole dynamics in this study. Additionally, the dynamics near the border or beyond the scalar cloud do not significantly contribute to the accretion and dynamical friction of the black hole, and the results presented in chapters 3 and 4 are not dependent on those regions.

2.4 . Parameter space

Before going further, we will review the constraints on the scalar parameters $m_{\rm DM}$ and λ_4 and specify the regime in which our computation applies. Additionally, we introduce the third parameter, the density ρ_0, which characterizes the bulk of the soliton and determines various quantities within the soliton.

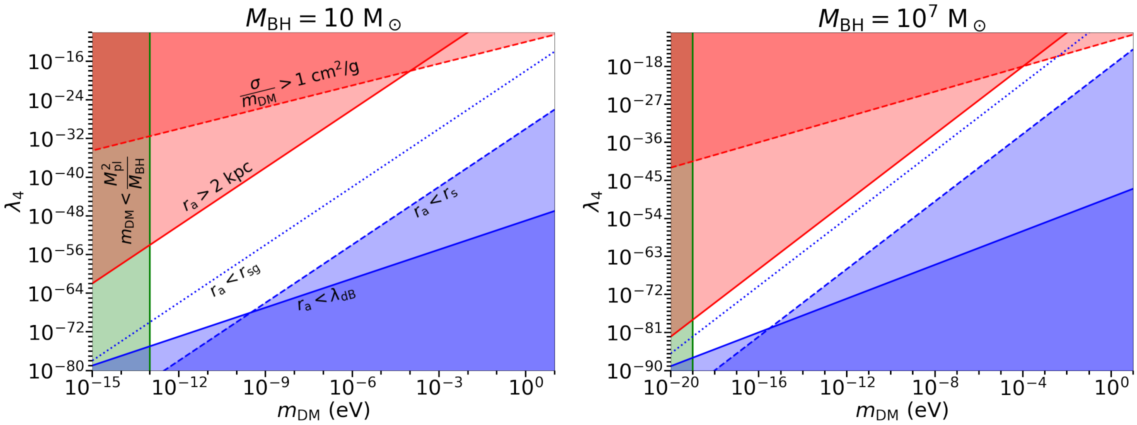

Figure 2.1: Domain in the parameter space $(m_{\rm DM}, \lambda_4)$ where our derivations apply, for a black hole of mass $10\,{\rm M}_\odot$ (left panel) and $10^7\,{\rm M}_\odot$ (right panel). The region in white is the allowed part of the parameter space.

The density ρ_0 in the bulk of the soliton is related to the transition radius $r_{\rm sg}$ (defined in (2.17)), the values in the bulk of the soliton of the self-interaction potential $\Phi_{\rm I0}$ (from (2.9)) and of the scalar-field gravitational potential $\Phi_{\rm sg0}$. It also determines the sound speed $c_{s,0}^2$ (as seen in (3.10) and (3.42))

$$\frac{\rho_0}{\rho_a} \sim \frac{r_s}{r_{\rm sg}} \sim \Phi_{\rm I0} \sim c_{\rm s}^2 \,. \tag{2.20}$$

When in a virialized system, the sound speed is also the typical velocity scale in the soliton, giving $c_{\rm s}^2 \sim v^2 \lesssim 1$.

Throughout the following sections, we focus on the regime where $r_a \gg \lambda_{\rm dB}$, with the de Broglie wavelength $\lambda_{\rm dB} = \frac{2\pi}{m_{\rm DM} v}$ setting the scale at which quantum pressure becomes significant. This regime is also called the Thomas-Fermi regime [294, 295], historically developed in the early 20th century, and is a simplified approach to understand the behavior of quantum systems with many interacting particles. Initially applied to electrons in metals, offering a simpler description of their collective properties, and later extended to atomic nuclei and self-interacting dark matter, this approximation offers a practical way to describe collective behavior without complex quantum calculations. However, it is important to acknowledge that the Thomas-Fermi approximation has limitations. It overlooks quantum effects and assumes certain characteristics of the dark matter distribution.

In terms of the parameters, this condition can be expressed as

$$\lambda_4 \gg \frac{m_{\rm DM}^2}{M_{\rm Pl}^2 v^2} \,, \quad \text{hence} \quad \lambda_4 \gg 10^{-55}\, v^{-2} \left(\frac{m_{\rm DM}}{1\,{\rm eV}}\right)^2 . \tag{2.21}$$

More generally, considering the self-interaction $\Phi_{\rm I}$ dominating over the quantum pressure $\Phi_{\rm Q}$, we find the condition $\lambda_4 \gg \frac{m_{\rm DM}^2}{\rho r^2}$. Within the equilibrium scalar cloud, where $v^2 \sim \Phi_{\rm N} \sim \frac{\rho r^2}{M_{\rm Pl}^2}$, we recover (2.21). Near the Schwarzschild radius r_s, the scalar field density is of the order of $\rho_a \sim \frac{m_{\rm DM}^4}{\lambda_4}$ [190], leading to the condition

$$m_{\rm DM} \gg \frac{M_{\rm Pl}^2}{m_{\rm BH}}, \quad \text{hence} \quad m_{\rm DM} \gg 10^{-12} \left(\frac{m_{\rm BH}}{1\,M_\odot}\right)^{-1} {\rm eV}\,. \tag{2.22}$$

Therefore, our computation applies to stellar-mass black holes for $m_{\rm DM} \gg 10^{-12}\,{\rm eV}$ and to supermassive black holes for $m_{\rm DM} \gg 10^{-18}\,{\rm eV}$.

The regime $\lambda_4 = 0$, where self-interactions are negligible, corresponds to the fuzzy dark matter scenario [63]. In this case, gravity can be balanced by quantum pressure at the scale $\lambda_{\rm dB}$. For galactic halos with $v \simeq 10^{-3}$, in order to observe departures from cold dark matter on galactic scales and address the core-cusp problem, we would require $m_{\rm DM} \sim 10^{-22}$ eV. However, this conflicts with Lyman-α forest constraints [51, 296] and the analysis of galactic rotation curves [194], which indicate $m_{\rm DM} \gtrsim 10^{-20}$ eV.

In the regime (2.21), where self-interactions dominate over the quantum pressure, departures from cold dark matter on galactic scales and potential implications for the core-cusp problem can be achieved for a wide range of masses thanks to the additional parameter λ_4. This parameter is related to the characteristic scale r_a (defined in (2.3) and (2.15)), and we have the following relation [59]

$$\lambda_4 \simeq \left(\frac{r_a}{20\,{\rm kpc}}\right)^2 \left(\frac{m_{\rm DM}}{1\,{\rm eV}}\right)^4 . \tag{2.23}$$

Here, we do not focus solely on the formation of solitons of galactic size that would directly address the core-cusp problem. Instead, we consider the more general case of Thomas-Fermi scalar field dark matter, regardless of its potential impact on ΛCDM galactic-scale tensions. In this scenario, the cloud size r_a can vary from sub-galactic to galactic scales. Assuming the formation of scalar clouds similar to molecular clouds that include stellar or black hole systems, in chapters 3 and 4, we investigate the accretion rate and dynamical friction of a black hole inside such a cloud.

To simplify the computation and the boundary condition at large distances, we assume that $r_a \gg r_{\rm sg}$, meaning the cloud extends beyond the transition radius. This assumption leads to the constraint

$$r_a \gg r_{\rm sg}: \quad \lambda_4 \gg \left(\frac{m_{\rm BH} m_{\rm DM}^2}{M_{\rm Pl}^3 v^2}\right)^2 , \tag{2.24}$$

and consequently

$$\lambda_4 \gg 10^{-20} \left(\frac{v}{10^{-3}}\right)^{-4} \left(\frac{m_{\rm BH}}{1\,M_\odot}\right)^2 \left(\frac{m_{\rm DM}}{1\,{\rm eV}}\right)^4 , \tag{2.25}$$

where $v^2 \sim \Phi_{\rm I} \sim \Phi_{\rm N}$ represents the typical orbital velocity in the gravitational potential well of the scalar cloud, as in (2.20). However, this constraint is not critical, and it would be sufficient to require that the cloud extends well beyond the black hole horizon. In this case, $r_s \ll r_a \ll r_{\rm sg}$, the self-gravity regime is never reached, and the density profile remains dominated by the second term in (2.16). Thus, the scalar cloud radius is approximately $R_{\rm sol} \simeq \pi r_a/2$, which is of the same order as r_a. This condition leads to the constraint

$$r_a \gg r_s : \quad \lambda_4 \gg \left(\frac{m_{\rm BH} m_{\rm DM}^2}{M_{\rm Pl}^3}\right)^2 , \tag{2.26}$$

and therefore

$$\lambda_4 \gg 10^{-32} \left(\frac{m_{\rm BH}}{1\, M_\odot}\right)^2 \left(\frac{m_{\rm DM}}{1\,{\rm eV}}\right)^4 . \tag{2.27}$$

These constraints slightly modify the boundary conditions, but the main steps of the derivation, especially the form (3.4) of the solution, remain valid. However, the dynamical friction F_z will be reduced due to the smaller size of the scalar cloud, which is smaller than the radius $r_{\rm sg}$ where the contribution to F_z typically peaks, as discussed in chapters 3 and 4 below.

Observations of cluster mergers impose an upper bound on the cross-section σ as $\sigma/m_{\rm DM} \lesssim 1\,{\rm cm}^2/{\rm g}$, resulting in the constraint [59]

$$\lambda_4 \lesssim 10^{-12} \left(\frac{m_{\rm DM}}{1\,{\rm eV}}\right)^{3/2} . \tag{2.28}$$

To ensure that the scalar field behaves like dark matter since matter-radiation equality, it is required that $V_{\rm I} \ll V$. This condition leads to the constraint $\lambda_4 \lesssim (m_{\rm DM}/1\,{\rm eV})^4$, which is automatically satisfied for $r_a < 20\,{\rm kpc}$, as given by Equation (2.23). For the classical description of the scalar field to be valid, the occupation number $N \simeq (\rho/m_{\rm DM})\lambda_{\rm dB}^3 \sim \rho/(m_{\rm DM}^4 v^3)$ must be much greater than unity. Equilibrium in the scalar cloud between gravity and self-interaction pressure yields $\Phi_{\rm N} \sim \Phi_{\rm I} \sim \rho\lambda_4/m_{\rm DM}^4$, along with $v^2 \sim \Phi_{\rm N}$ for the typical orbital velocity. This leads to the relation

$$N \sim \frac{1}{\lambda_4 v} \gg 1 , \quad \text{hence} \quad \lambda_4 \ll v^{-1} . \tag{2.29}$$

As long as $v \lesssim 1$, the classical approximation remains valid as long as $\lambda_4 \ll 1$.

To solve the Klein-Gordon equation in curved spacetime in the limit of a large scalar mass (3.4), where $m_{\rm DM}$ is much greater than typical spatial gradients and frequencies, it is required that $m_{\rm DM} \gg 1/r_s$. Thus, the condition becomes

$$m_{\rm DM} \gg \frac{1}{r_s} , \quad \text{hence} \quad m_{\rm DM} \gg \frac{M_{\rm Pl}^2}{M_{\rm BH}} . \tag{2.30}$$

This condition ensures that wave effects are negligible, and we are far from the regime of fuzzy dark matter (as (2.22)).

The validity of our derivations in the parameter space $(m_{\rm DM}, \lambda_4)$ is represented by the central white area in Figure 2.1. The left panel corresponds to a black hole mass of $10\,{\rm M}_\odot$, while the right panel corresponds to $10^7\,{\rm M}_\odot$. The lower bound on the scalar mass $m_{\rm DM}$ is given by (2.22), represented by the vertical green solid line. At low $m_{\rm DM}$, the upper bound on λ_4 is determined by (2.23), considering $r_a \leq 2\,\text{kpc}$, shown as the upper red solid line. For high $m_{\rm DM}$, the upper bound on λ_4 is given by (2.28), shown as the upper red dashed line. The lower bound on λ_4 at low $m_{\rm DM}$ is obtained from (2.21) for $v = 10^{-3}$, represented by the lower blue solid line. At high $m_{\rm DM}$, the lower bound on λ_4 is determined by (2.27), shown as the lower blue dashed line. The condition (2.25) is depicted by the blue dotted line for $v = 10^{-3}$. It is worth noting that we assume to be above this threshold to apply the boundary condition at large distance, although the form (3.4) of the solution remains valid as long as we are above the blue dashed line (2.27). Overall, the allowed region in the parameter space corresponds to a diagonal band $\lambda_4 \sim m_{\rm DM}^4$. For $M_{\rm BH} = 10, \mathrm{M}_\odot$, the valid range is approximately

$$10^{-12}\ \text{eV} \lesssim m_{\rm DM} \lesssim 10^7\ \text{eV}\,, \quad 10^{-75} \lesssim \lambda_4 \lesssim 10^{-3}\,. \tag{2.31}$$

For $M_{\rm BH} = 10^7\,, M_\odot$, the valid range is approximately

$$10^{-19}\ \text{eV} \lesssim m_{\rm DM} \lesssim 10\ \text{eV}\,, \quad 10^{-85} \lesssim \lambda_4 \lesssim 10^{-10}\,. \tag{2.32}$$

2.5 . Isotropic metric

As we neglect the gravitational back-reaction of the scalar cloud, we consider a spherically symmetric metric associated with a black hole at the center of a large soliton. The matching condition at large radii is given by (3.2). To simplify the matching with the usual Newtonian gauge on large scales, a non-rotating black hole is considered, and the isotropic radial coordinate r and time t are used. Thus, the static spherically symmetric metric takes the isotropic form

$$ds^2 = -f(r)\,dt^2 + h(r)\,(dr^2 + r^2\,d\Omega^2)\,. \tag{2.33}$$

In the weak-gravity regime at large radii, far beyond the Schwarzschild radius, the metric functions are given by

$$f = 1 + 2\Phi_{\rm N}\,, \quad h = 1 - 2\Phi_{\rm N}\,, \tag{2.34}$$

where

$$\Phi_{\rm N} = \alpha - \Phi_{\rm I} = \alpha - \frac{\rho_0}{\rho_a} - \frac{r_s}{2r}\,, \tag{2.35}$$

which agrees with (3.2). The first two terms in the last expression correspond to the self-gravity of the scalar cloud, while the last term represents the gravitational potential of the black hole in the Newtonian limit. At smaller scales, where the gravity of the black hole dominates, and far inside the transition radius $r_{\rm sg}$, the isotropic metric functions $f(r)$ and $h(r)$ are given by

$$\frac{r_s}{4} < r \ll r_{\rm sg}: \quad f(r) = \left(\frac{1 - r_s/(4r)}{1 + r_s/(4r)}\right)^4\,, \quad h(r) = \left(1 + \frac{r_s}{4r}\right)^2\,. \tag{2.36}$$

In these coordinates, the black hole horizon is located at a radius $r = r_s/4$.

2.6 . Radial accretion

2.6.1 . Equations of motion

Using the metric (2.33), the Klein-Gordon equation for the scalar field ϕ is given by

$$\frac{\partial^2\phi}{\partial t^2} - \sqrt{\frac{f}{h^3}}\nabla\cdot(\sqrt{fh}\nabla\phi) + f\frac{\partial V}{\partial\phi} = 0\,, \tag{2.37}$$

and the system is spherically symmetric. Consequently as the velocity $v = 0$, the Klein-Gordon equation (2.37) can be expressed as

$$\frac{\partial^2\phi}{\partial t^2} - \sqrt{\frac{f}{h^3}}\frac{1}{r^2}\frac{\partial}{\partial r}\left[r^2\sqrt{fh}\frac{\partial\phi}{\partial r}\right] + fm_{\rm DM}^2\phi + f\lambda_4\phi^3 = 0\,. \tag{2.38}$$

The cubic non-linearity in (2.38) is of the same type as the Duffing equation [297]. This allows for a solution of the form [59]

$$\phi = \phi_0(r)\,{\rm cn}[\omega(r)t - \boldsymbol{K}(r)\beta(r), k(r,\theta)]\,. \tag{2.39}$$

Here, ${\rm cn}(u,k)$ represents the Jacobi elliptic function [298, 299] with argument u, modulus k, and period $4\boldsymbol{K}$, where $\boldsymbol{K}(k) = \int_0^{\pi/2} d\theta/\sqrt{1-k^2\sin^2\theta}$ for $0 \le k < 1$ is the complete elliptic integral of the first kind [298, 299]. The quantity $\boldsymbol{K}(r,\theta)$ is defined as $\boldsymbol{K}[k(r,\theta)]$. Equation (2.39) is a leading-order approximation in the limit $m_{\rm DM} \to \infty$, where spatial gradients of the amplitude ϕ_0 and the modulus k are much smaller than $m_{\rm DM}$, while both ω and β are of the order of $m_{\rm DM}$. The amplitude ϕ_0, angular frequency ω, phase β, and modulus k are considered slow functions of space. This representation is a generalization of nonrelativistic expressions such as (3.1), where the usual trigonometric functions are replaced by the Jacobi elliptic function due to the strong cubic non-linearity. The nonrelativistic regime is recovered for small modulus k, as ${\rm cn}(u,0) = \cos(u)$. Therefore, the modulus k measures the deviation from harmonic oscillations and the nonrelativistic limit.

The oscillations at different radii must be synchronized to avoid a secular growth with time of spatial gradients. This implies that the function $\omega(r)$ is determined by the modulus $k(r)$ as follows

$$\omega(r) = \frac{2\boldsymbol{K}(r)}{\pi}\,\omega_0\,, \tag{2.40}$$

where ω_0 is a constant fundamental frequency set by the boundary conditions. At leading order in the large-$m_{\rm DM}$ limit, the radial derivative is given by

$$\frac{\partial\phi}{\partial r} = -\phi_0\boldsymbol{K}\frac{d\beta}{dr}cn'\ldots\,, \tag{2.41}$$

where the dots represent subleading terms, and ${\rm cn}' = \frac{\partial{\rm cn}}{\partial u}$. Substituting these expression into the Klein-Gordon equation (3.3) and using the differential equations satisfied by the Jacobi elliptic functions, ${\rm cn}'' = (2k^2-1){\rm cn} - 2k^2{\rm cn}^3$, leads to two conditions

$$\left(\frac{d\beta}{dr}\right)^2 = \frac{h}{f}\left(\frac{2\omega_0}{\pi}\right)^2 - \frac{hm_{\rm DM}^2}{(1-2k^2)\boldsymbol{K}^2} \quad \text{and} \quad \frac{\lambda_4\phi_0^2}{m_{\rm DM}^2} = \frac{2k^2}{1-2k^2}\,, \tag{2.42}$$

which will be further interpreted below.

At each radius, (3.6) provide expressions for $d\beta/dr$ and ϕ_0 in terms of the modulus k, which remains to be determined. To determine the profile of $k(r)$, a constant flux F is imposed to ensure a steady-state solution. By enforcing a constant flux, the system achieves a balance between the accretion and the outflow. At leading order, the conservation equation $\nabla_\mu T^\mu_0 = 0$, where T^μ_ν is the energy-momentum tensor of the scalar field, is automatically satisfied because the solution given by (3.4) satisfies the Klein-Gordon equation. Each contribution to $\nabla_\mu T^\mu_0$ at this order oscillates rapidly with time and has a zero mean.

At leading order, the solution satisfies the Klein-Gordon equation, ensuring that the conservation equation is automatically satisfied. However, when considering higher-order terms, there is a possibility that new terms emerge that introduce slow time-dependent behavior, as in the case of celestial mechanics or oscillatory systems with damping. If these secular terms are present and not properly accounted for, they can grow or change slowly over time, leading to violations of the steady-state condition. To avoid such violations when going beyond the leading order, it is necessary to require $\langle \nabla_\mu T^\mu_0 \rangle = 0$, where $\langle \dots \rangle$ represents the average over the oscillations of the solution given by (2.39). This leads to the constraint

$$\frac{d}{dr} \cdot (\rho_{\text{eff}} \nabla \frac{d\beta}{dr}) = 0 \,, \tag{2.43}$$

with the effective density

$$\rho_{\text{eff}} = \sqrt{fh}\phi_0^2 \omega \boldsymbol{K} \langle \text{cn}'^2 \rangle \,. \tag{2.44}$$

Here, (2.43) and the first equation in (2.42) generalize the continuity and Hamilton-Jacobi equations (2.8), respectively, to the strong-field and strong-gravity regimes. The term $\pi\beta/2$ plays the role of the phase s in the hydrodynamical equations. Similarly, they also generalize the hydrodynamical continuity and Euler equations (2.10), respectively. In this case, the term $\pi\nabla\beta/(2m_{\text{DM}})$ plays the role of the curl-free velocity field $\mathbf{v}$.

In addition to these continuity and Euler equations, the second equation of (2.42) is introduced. This equation arises because there are now three fields to determine: the amplitude ϕ_0 (playing the role of the density), the phase β (playing the role of the velocity potential), and the modulus k. The modulus k is coupled to the amplitude through this last equation. In the nonrelativistic low-amplitude regime, the degree of freedom represented by k disappears as $k \to 0$, and the scalar field ϕ follows harmonic oscillations, as described in (3.1). On the other hand, in the large-field regime, the quantity $k(r)$ determines the degree of deviation of the nonlinear oscillator from the harmonic oscillator. This deviation is described by the Jacobi elliptic function $\text{cn}(u, k)$.

2.6.2 . Hydrodynamical infall

The results for radial accretion, as obtained by [59], are depicted in Figure 2.2. In the case of radial accretion, the effective continuity equation (2.43) can be integrated immediately as it only depends on radial derivatives, resulting in $F = \rho_{\text{eff}} \frac{d\beta}{dr}$, where F is the

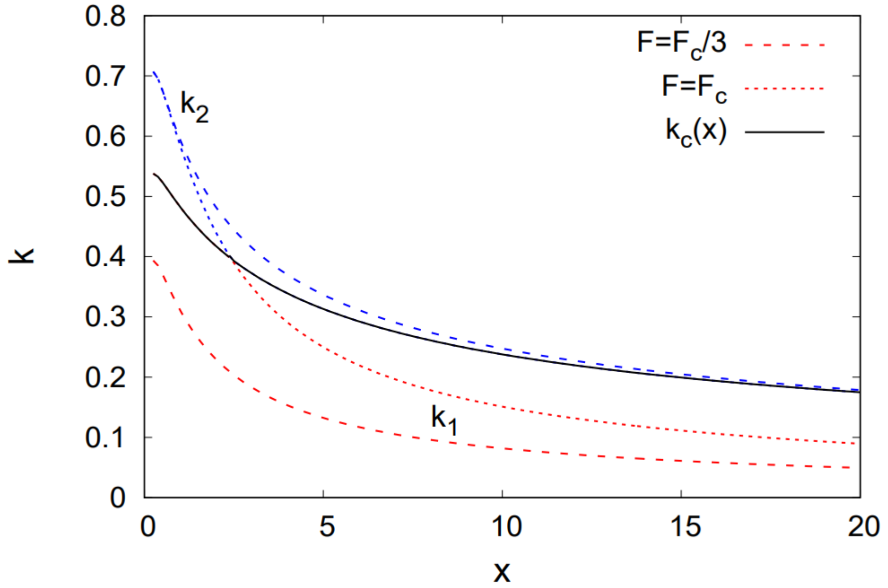

Figure 2.2: The moduli $k_1(x)$ and $k_2(x)$, where $x = r/r_s$ for a constant flux $F_{\rm c}/3$ (dashed lines) and $F_{\rm c}$ (dotted lines). The critical modulus, $k_{\rm c}(x)$ (solid line), equals k_1 for $x <_\star$ and k_2 for $x > x\star$, where $F = F_c$ (from [59]).

constant flux of the scalar field. By using (2.42), it is possible to express $\rho_{\rm eff}\frac{d\beta}{dr}$ in terms of k and r. This leads to a condition of the form $F(r, k)$. As discussed in [190], in this case the range of k is constrained to be between 0 and $k_+(r) < 1/\sqrt{2}$. At the boundaries, $k = 0$ and $k = k_+$, the flux vanishes, while it exhibits a single maximum $|F_{\rm max}(r)|$ at $k_{\rm max}(r)$, slightly below $k_+(r)$. As r increases, both the upper bound $k_+(r)$ and the peak at $k_{\rm max}(r)$ shift to lower values. The maximum $|F_{\rm max}|$ displays growth at both small and large r, reaching a minimum at $\hat{r}_\star \simeq 2.43$, where $F_{\rm c} \equiv F_{\rm max}(r) = F_\star \times F_{\rm s}$ with the minimum peak value $F_\star \simeq 0.66$ and the characteristic flux $F_{\rm s} \sim -r_s m^4/\lambda_4$. At the transition radius $r_{\rm sg}$, the gravitational potential receives equal contributions from the central black hole and the scalar cloud. Inside the soliton core, the potential remains nearly constant, matching the soliton core value. Consequently, beyond $r_{\rm sg}$, the metric functions $h(r)$ and $f(r)$ become almost constant, causing the flux function $F(r, k)$ to maintain a constant shape in k, multiplied by a simple factor $\hat{r}^2$. Hence, the peak value $|F_{\rm max}|$ continues to increase. This specific behavior of $F(k, r)$ results in a unique value for the flux. When $|F| < |F_{\rm c}|$, two distinct solutions, $k_1(r)$ and $k_2(r)$, exist at each radius on opposite sides of the peak $k_{\rm max}(r)$. The function $k(r)$ must remain on the same side of the peak throughout and cannot cross it. Only when $F = F_{\rm c}$, the function $k(r)$ can switch from one branch, $k_1(r)$, to the other, $k_2(r)$, at the radius $\hat{r}_\star$ where both solutions coincide with the peak. The boundary conditions at the horizon favors the high-velocity solution $k_1(r)$, resembling free fall, because self-interactions cannot prevent the free fall of dark matter into the black hole. Conversely, the boundary condition at large radius selects the low-velocity branch $k_2(r)$, supported by the pressure generated by self-interactions, to match the static equilibrium soliton. Consequently, the function $k(r)$ must transition from one branch to another at some intermediate radius. This selection process determines the only physically meaningful flux value, $F = F_{\rm c}$, and the corresponding solution $k_{\rm c}(r)$, which smoothly connects the low-velocity branch $k_2(r)$ for radii greater than $r_{\rm c}$ and the high-velocity branch $k_1(r)$ for radii less than $r_{\rm c}$. The two branches meet at the critical radius $r_{\rm c}$. This selection process is reminiscent of the hydrodynamical case discussed in [300, 301], where the only flux value providing a transonic solution that connects the subsonic (i.e., low-velocity) branch at large radii to the supersonic (i.e., high-velocity) branch at small radii is chosen.

For radii where the black hole gravity dominates, the radial profile according to [190] is given by (2.45) as $\rho \sim \rho_a \frac{r_s}{r}$ and $v_r \sim -\frac{r_s}{r}$. Here, r_s represents the Schwarzschild radius. At larger radii, the boundary conditions give the profile [190]

$$r_s \lesssim r \lesssim r_{\rm sg}: \quad \rho \sim \rho_a \frac{r_s}{r}, \quad v_r \sim -\frac{r_s}{r}\,, \tag{2.45}$$

whereas at larger radii we have

$$r \gtrsim r_{\rm sg}: \quad \rho \simeq \rho_0, \quad v_r \sim -\frac{\rho_a r_s^2}{\rho_0 r^2}\,. \tag{2.46}$$

2.7 . Summary of the chapter

In this chapter, we introduced the self-interacting scalar field dark matter model via its action (2.1). The potential energy is decomposed into quadratic and quartic self-interaction terms, which introduce a mass parameter and a coupling constant, respectively. We consider repulsive interactions, leading to a more diffuse distribution. The constraints on the self-interaction coupling constant are derived from studying the large-scale structure of the universe and astrophysical observations [188, 281–290]. These constraints indicate that the self-interaction coupling constant should be small to maintain agreement with observed structures and galactic dynamics.

We then focus on the nonrelativistic regime, where the Schrödinger equation describes the behavior of the scalar field. The hydrodynamical picture is introduced using continuity and Euler equations (2.10), neglecting the quantum pressure term. Static equilibrium configurations known as solitons can be formed due to the pressure arising from self-interactions. The behavior of solitons is determined by the hydrostatic equilibrium equation, which leads to the determination of the self-interaction potential (2.15). The scalar field exhibits large density fluctuations outside the soliton core, following the Navarro-Frenk-White profile observed in cold dark matter simulations [88].

The parameter space of the model is discussed, considering the constraints on the scalar parameters and the regime in which the computations apply. The Thomas-Fermi regime, where the self-interaction dominates over the quantum pressure, is emphasized. The conditions for the parameters and the relevant black hole masses for the computations are specified.

In the context of radial accretion, the scalar field flux is determined by $F = \rho_{\text{eff}}\frac{d\beta}{dr}$. As we approach the critical radius, a transition occurs from a high-velocity branch, near the black hole, to a low-velocity branch, at larger radii, in the solutions for $k(r)$. The two branches smoothly connect at the critical radius, ensuring a continuous solution. The radial profiles of density and velocity exhibit distinct behaviors depending on whether the dominance lies with the black hole gravity or the scalar cloud pressure. At larger radii, the density decreases inversely proportional to the radius, while the velocity follows an inverse square root relationship. Moving to even larger radii, both the density and velocity remain approximately constant.

Overall, this chapter provides a comprehensive overview of the self-interacting scalar field action, including its implications for large-scale structures, solitons, and interactions with black holes.

3 - Subsonic accretion and dynamical friction for a moving black hole

In this chapter, we study the accretion rate and dynamical friction experienced by a black hole as it moves through a cloud of self-interacting dark matter in the subsonic regime. Our study encompasses both the behavior of the nonlinear flow at large radii, characterized by low velocities, and the regime of small radii with high velocities, as analyzed in [190]. To begin, we provide a brief discussion regarding the field solution of a moving soliton. Subsequently, we incorporate a black hole into the framework in order to derive the equations of motion. Then, we introduce the linear flow approximation as a baseline model. However, we go beyond this approximation by incorporating corrections that account for the transition from the subsonic regime (at large radii) to the supersonic regime (close to the black hole). We then incorporate these corrections into the continuity and Euler equations and develop an iterative scheme to numerically determine the velocity and density profiles. Subsequently, we derive exact expressions for the accretion rate of a black hole and the dynamical friction exerted on it within the subsonic regime. These calculations provide quantitative insights into the interaction between the black hole and the surrounding dark matter cloud. To validate our findings and provide a broader context, we compare our results with previous studies conducted on other models, such as the cold and fuzzy dark matter scenarios. By doing so, we assess the consistency and implications of our subsonic analysis in relation to other theoretical frameworks. This chapter is based on the paper "*Subsonic accretion and dynamical friction for a black hole moving through a self-interacting scalar dark matter cloud*" [1].

3.1 . Moving soliton

If there is no black hole present, the equilibrium solution $\rho_{\rm eq}(r)$ under Galilean invariance can be mapped to a solution that moves at a uniform velocity $\mathbf{v}_0$. This is given by $\rho_{v_0}(\mathbf{r},t) = \rho_{\rm eq}(\mathbf{r}-\mathbf{v}_0 t)$. The phase s now becomes $s = -(\alpha + v_0^2/2)m_{\rm DM}t + m_{\rm DM}v_0 z$ for a velocity along the z-axis, and the scalar field ϕ takes the form

$$\phi = \frac{\sqrt{2\rho}}{m_{\rm DM}} \cos\left[(1+\alpha+v_0^2/2)m_{\rm DM}t - m_{\rm DM}v_0 z\right] . \tag{3.1}$$

From now on, we will consider the scenario where a black hole is moving with velocity $-\mathbf{v}_0$ through the soliton, or equivalently, a soliton is moving with velocity $\mathbf{v}_0$ with respect to a motionless black hole. Neglecting the gravitational back-reaction of the scalar cloud and focusing on scales deep inside the soliton, we can approximate the density ρ, the self-interaction potential $\Phi_{\rm I}$, and the total gravitational potential $\Phi_{\rm N}$ using the expression from (2.18)

$$r \gg r_s : \quad \rho = \rho_0 + \rho_a \frac{r_s}{2r} , \quad \Phi_{\rm I} = \frac{\rho}{\rho_a} , \quad \Phi_{\rm N} = \alpha - \Phi_{\rm I} . \tag{3.2}$$

Together with $\mathbf{v} = \mathbf{v}_0$, these expressions establish the boundary conditions at large-radii in this scenario.

3.2 . Equations of motion

This section employs the same methodology as section 2.6.1.

Upon the inclusion of a black hole in the system, it becomes necessary to account for the isotropic metric given by (2.33). Due to the spherically symmetric metric and the uniform velocity $\mathbf{v} = \mathbf{v}_0 = v_0, \mathbf{e}z$ at large distances, the system exhibits axi-symmetry around the z-axis. As a result, the Klein-Gordon equation (2.37) is modified as followed

$$\frac{\partial^2\phi}{\partial t^2} - \sqrt{\frac{f}{h^3}}\frac{1}{r^2}\frac{\partial}{\partial r}\left[r^2\sqrt{fh}\frac{\partial\phi}{\partial r}\right] - \frac{f}{hr^2\sin\theta}\frac{\partial}{\partial\theta}\left[\sin\theta\frac{\partial\phi}{\partial\theta}\right] + fm_{\rm DM}^2\phi + f\lambda_4\phi^3 = 0\,, \quad (3.3)$$

where the cubic non-linearity in (3.3) still shares the same form as the Duffing equation [297]. This allows for a solution in the form of

$$\phi = \phi_0(r,\theta)\,{\rm cn}[\omega(r,\theta)t - \boldsymbol{K}(r,\theta)\beta(r,\theta), k(r,\theta)]\,. \quad (3.4)$$

Unlike the study of radial accretion presented in [190], where the scalar field configuration is spherically symmetric, the presence of the incoming velocity $\mathbf{v}_0 = v_0\,\mathbf{e}_z$ at large distances makes the configuration only axi-symmetric. Consequently, ϕ_0, ω, β, and k depend on both the radial distance r and the angle θ with respect to the z-axis.

The function ω now takes the form of $\omega(r,\theta) = \frac{2\boldsymbol{K}(r,\theta)}{\pi}\omega_0$. In the limit of large $m_{\rm DM}$, the spatial derivatives yield

$$\frac{\partial^2\phi}{\partial r^2} = \phi_0\left(\boldsymbol{K}\frac{\partial\beta}{\partial r}\right)^2{\rm cn}'' + \dots\,, \qquad \frac{\partial^2\phi}{\partial\theta^2} = \phi_0\left(\boldsymbol{K}\frac{\partial\beta}{\partial\theta}\right)^2{\rm cn}'' + \dots\,, \quad (3.5)$$

where the dots represent higher-order terms. Substituting these expressions into the Klein-Gordon equation (3.3) and utilizing the differential equations satisfied by the Jacobi elliptic functions lead to two conditions

$$(\nabla\beta)^2 = \frac{h}{f}\left(\frac{2\omega_0}{\pi}\right)^2 - \frac{hm_{\rm DM}^2}{(1-2k^2)\boldsymbol{K}^2} \quad \text{and} \quad \frac{\lambda_4\phi_0^2}{m_{\rm DM}^2} = \frac{2k^2}{1-2k^2}\,. \quad (3.6)$$

Similar to (2.43), the conservation equation can be written as

$$\nabla\cdot(\rho_{\rm eff}\nabla\beta) = 0\,, \quad (3.7)$$

where $\rho_{\rm eff}$ is the same as defined in (2.44), but with angular dependencies.

3.3 . Velocity branches and hydrodynamical infall

3.3.1 . Low and high velocity branches

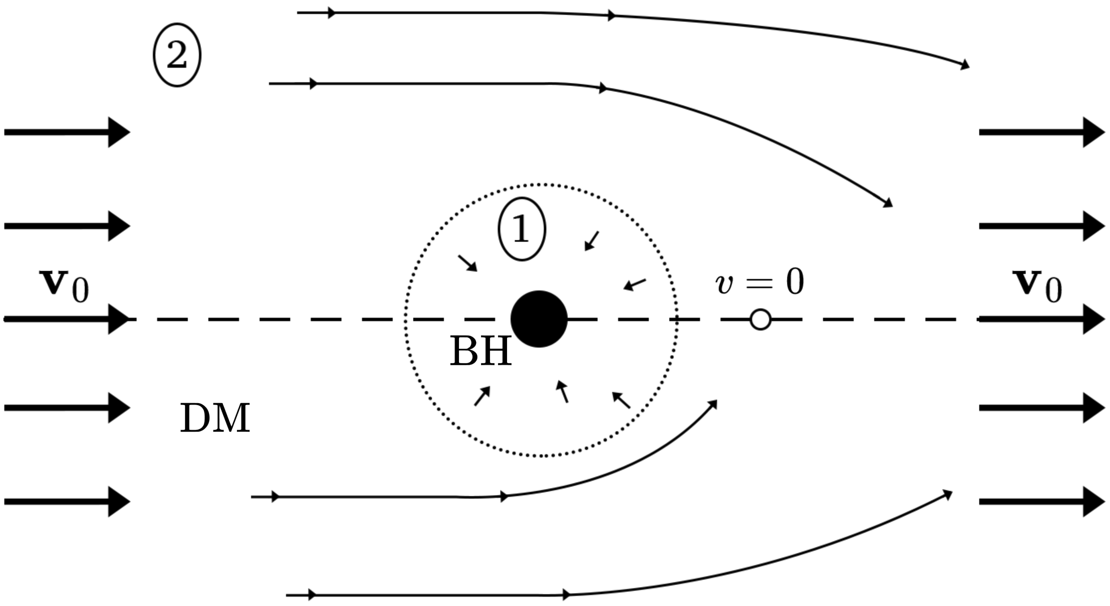

Figure 3.1: Schematic representation of the examined system, where dark matter travel towards a black hole with an initial velocity $\boldsymbol{v}_0$ (at $z \to -\infty$). The gravitational pull of the black hole alters the dark matter streamlines. Region (1) denotes the radial accretion zone of the black hole, while region (2) corresponds to a distant area from the black hole where the flow characteristics are determined in this study. The empty circle positioned behind the black hole indicates a point of zero velocity, marking the boundary between particles falling into the black hole and those that escape.

In the axi-symmetric case considered here, the conservation equation (3.7) becomes a two-dimensional partial differential equation, which cannot be integrated immediately contrary to the radial accretion case (2.43). However, if the homogeneous velocity v_0 at large radii is significantly smaller than the speed of light, it can be assumed that the flow becomes nearly radial well before the critical radius r_c, typically of the order of the Schwarzschild radius. In this case, the flow can be matched to the radial case at a radius $r_\mathrm{m} > r_\mathrm{c}$, providing the inner boundary condition for the system. Consequently, the critical flux F_c selection and the transition from the low-velocity branch to the high-velocity branch can be identified by computing the radial case as done in [190]. Then, the system (3.6) and (3.7) can be solved at large radii along the low-velocity branch to complete the analysis. This approach is valid for the subsonic regime, where the relative velocity v_0 is smaller than the effective speed of sound $c_{s,0}$ of the scalar-field soliton at large radii. Figure 3.1 provides an illustration of the problem. For higher velocities, discontinuities are expected, and their study will be discussed in chapter4.

3.3.2 . Boundary condition at large radii

At very large radii, when $k \ll 1$ (meaning that the deviations from harmonic oscillator are small), the solution (3.4) can be approximated as $\phi = \phi_0 \cos(\omega_0 t - \pi\beta/2)$, where $\boldsymbol{K} \simeq \pi/2$. By comparing this with the nonrelativistic solution (3.1), we obtain the following boundary conditions

$$r \to \infty : \quad \phi_0 = \frac{\sqrt{2\rho}}{m_{\rm DM}} , \quad \beta = \frac{2}{\pi} m_{\rm DM} v_0 z . \tag{3.8}$$

Furthermore, the value of the fundamental frequency ω_0 is given by

$$\omega_0 = (1 + \alpha + v_0^2/2) m_{\rm DM} . \tag{3.9}$$

From the second equation of (3.6), the asymptotic behavior of k can be obtained as follows

$$r \to \infty : \quad k^2 = \frac{\lambda_4 \phi_0^2}{2 m_{\rm DM}^2} = \frac{4\rho}{3\rho_a} = \frac{4}{3}\Phi_{\rm I} . \tag{3.10}$$

The density ρ can be determined using (3.2).

3.3.3 . Comparison with fuzzy dark matter derivations

The behavior of scalar clouds around black holes has been extensively studied, particularly in the case without self-interactions. Previous works, such as [302], focused on a free scalar field in the unperturbed Schwarzschild metric around a black hole. This scenario leads to a linear Klein-Gordon equation in curved spacetime, which can be expanded using spherical harmonics. The radial part of the equation follows a linear second-order differential equation with coefficients that depend on the radius. In the regime $1/m_{\rm DM} \gg r_s$, the problem can be solved by dividing the domain into three regions: close to the black hole, intermediate radii, and large radii. Each region corresponds to a standard differential equation that can be solved using known special functions. By matching the solutions at the inner boundaries, a global solution is obtained.

Recently, [303] revisited this problem by considering spherically symmetric solutions in the Schwarzschild metric. They expressed the general solution for the scalar field in terms of confluent Heun functions and derived various approximate solutions based on the hierarchy between the Compton wavelength $1/m_{\rm DM}$, the Schwarzschild radius r_s, and the self-gravity radius $r_{\rm sg}$. In our case, which corresponds to the large-mass regime (2.30), where $m_{\rm DM} \gg 1/r_s$, we enter regime IV (particle limit) as defined by [303]. In this regime, there is no potential barrier for incoming waves, and the fluid falls into the black hole. At intermediate radii within regime IV, the authors found for fuzzy dark matter (FDM) that

$$\text{FDM}, \quad r_s \lesssim r \lesssim r_{\rm sg} : \quad \phi \sim r^{-3/4} e^{-i m_{\rm DM} t - i 2 m_{\rm DM} \sqrt{r r_s}} . \tag{3.11}$$

This power-law behavior with an exponent of $-3/4$ leads to a corresponding density profile of

$$\text{FDM}, \quad r_s \lesssim r \lesssim r_{\rm sg} : \quad \rho \sim r^{-3/2} . \tag{3.12}$$

The authors of [303] explained that the free-fall velocity onto the black hole scales as $v_r \sim r^{-1/2}$. For a steady-state solution, the matter flux through a shell of radius r, given by $4\pi r^2 \rho v_r$, must be independent of r. This condition implies $\rho \sim r^{-2} v_r^{-1} \sim r^{-3/2}$, which agrees with the derived density profile (3.12). However, these derivations do not apply to our case due to the presence of self-interactions, which introduce a cubic non-linearity to the Klein-Gordon equation (3.3). In contrast to [302], our scenario considers the limit $1/m_{\rm DM} \ll r_s$, where the scalar field probes sub-horizon distances (2.30). Additionally, we account for the self-gravity of the scalar field at large radii, where it dominates over the black hole gravity and converges to the static soliton solution.

To handle the cubic non-linearity, we take advantage of the large scalar mass limit and express the solution in the form (3.4), utilizing the separation of scales from the black hole horizon to the soliton radius. This allows us to treat the scalar field as a locally cubic oscillator at each radius, which is solved exactly using the Jacobi elliptic function. The radial dependence is incorporated through the amplitude ϕ_0, the angular frequency ω, the phase β, the modulus k, and the conservation equation (3.7). In the radial case, the set of coupled one-dimensional equations can be integrated as explained in section 3.3.1 and [190]. For the non-radial case, described in sections 3.4 and 3.5 below, we employ the mapping to familiar hydrodynamical equations to track the behavior of the flow at large nonrelativistic radii, where the transition from uniform incoming flow at velocity $\mathbf{v}_0$ to radial infall occurs.

At large radii far from the black hole horizon, where the modulus k is small, the Jacobi elliptic function (3.4) can be approximated by a cosine term: $\phi \sim \phi_0(r) e^{i\omega(r)t - \boldsymbol{K}\beta(r)}$. Although harmonic oscillations with time are recovered, similar to the fuzzy dark matter case (3.11), the self-interaction non-linearity remains significant. In the bulk of the soliton at large radii, the scalar self-gravity is balanced by the self-interaction pressure. At intermediate radii, this additional pressure support slows down the infall, causing the radial velocity v_r to follow the low-velocity branch discussed in section 3.3.1 instead of the high-velocity branch associated with free-fall velocity $v_r \sim r^{-1/2}$ in the fuzzy dark matter case. Consequently, the density slope is different, with $\rho \propto r^{-1}$ in (2.45) compared to $\rho \propto r^{-3/2}$ in the fuzzy dark matter case (3.12).

In the fuzzy dark matter case, linear theory treatments [64, 65] can be considered using the Keplerian gravitational potential $\Phi_{\rm N} = -r_s/(2r)$ as the background, looking for linear perturbations to both the gravitational potential and the scalar field. However, this approach is not applicable to our case. Due to the pressure induced by self-interactions, the infall is slowed down near the Schwarzschild radius, creating a bottleneck. This bottleneck selects the transonic solution, leading to a density near the horizon of the order of ρ_a and a radial velocity close to the speed of light ($v_r \sim -1$) as shown in (2.45). Consequently, the accretion rate onto the black hole and the infalling flux at all radii are determined by conservation of matter. Therefore, the amplitude in the large-radius Newtonian regime is primarily set by the boundary condition at the black hole horizon. Thus, a fully nonlinear and relativistic treatment is required, and the global solution cannot be obtained through a perturbative weak-gravity approximation alone.

3.4 . Description of the non-linear velocity flow

3.4.1 . Low-k regime

At radii above $r_{\rm c}$, both the modulus k and the gravitational potential $\Phi_{\rm N}$ are small. Indeed $k \simeq 0.4$ at $r_{\rm c}$ and continue to decrease at larger radii, while $\Phi_{\rm N}$ is becoming small at radii much beyond the Schwarzschild radius. In this regime, the first equation of (3.6) and (3.7) can be simplified. The second equation of (3.6) and (2.44) provide expressions for ϕ_0^2 and $\rho_{\rm eff}$ in terms of $m_{\rm DM}$, k, and λ_4 as

$$\phi_0^2 = \frac{2m_{\rm DM}^2 k^2}{\lambda_4} \quad \text{and} \quad \rho_{\rm eff} = \frac{\pi m_{\rm DM}^2 k^2}{2\lambda_4}\omega_0 \propto k^2 \, . \tag{3.13}$$

Meanwhile, the first equation of (3.6) can be rewritten using (3.2)

$$\frac{\pi^2 (\nabla\beta)^2}{4m_{\rm DM}^2} = 2\alpha + v_0^2 - 2\Phi_{\rm N} - \frac{3}{2}k^2 = 2\frac{\rho_0}{\rho_a} + \frac{r_s}{r} + v_0^2 - \frac{3}{2}k^2 \, , \tag{3.14}$$

and is consistent with the boundary conditions (3.8) and (3.10). To further simplify the equations, the dimensionless radius $\hat{r}$ and the rescaled phase $\hat{\beta}$ are introduced

$$\hat{r} = \frac{r}{r_s} \, , \quad \hat{\beta} = \frac{\pi}{2m_{\rm DM} r_s}\beta \, . \tag{3.15}$$

This rescaling allows for a simpler form of (3.14)

$$(\hat{\nabla}\hat{\beta})^2 = \frac{3}{2}k_0^2 + v_0^2 + \frac{1}{\hat{r}} - \frac{3}{2}k^2 = \frac{3}{2}\left[k_+(\hat{r})^2 - k^2\right] \, , \tag{3.16}$$

involving the limiting value $k_+(\hat{r})$, introduced as

$$k_+(\hat{r})^2 = k_0^2 + \frac{2}{3}v_0^2 + \frac{2}{3\hat{r}} \, . \tag{3.17}$$

In this last expression, $k_+(\hat{r})$ represents an upper bound on the modulus k at a given radius r, as the left-hand side of (3.16) is always positive. The low-velocity branch characterized by

$$\text{low-velocity branch:} \quad k \simeq k_+ \, , \quad v^2 \ll k_+^2 \, , \tag{3.18}$$

corresponds to a region where k is close to the upper bound k_+ and the velocity, defined as $\mathbf{v} = \hat{\nabla}\hat{\beta}$, is much smaller than the free-fall value of order $1/\sqrt{\hat{r}}$, in the weak-gravity regime dominated by the black hole gravity. This is because the effective pressure due to the self-interactions slows down the fall towards the black hole. The conservation equation (3.7) then yields the continuity equation

$$\hat{\nabla} \cdot (k^2 \hat{\nabla}\hat{\beta}) = 0 \, . \tag{3.19}$$

Using (3.16), this equation can be further simplified to

$$\hat{\nabla} \cdot \left[\left(k_+(\hat{r})^2 - \frac{2}{3}(\hat{\nabla}\hat{\beta})^2 \right) \hat{\nabla}\hat{\beta} \right] = 0 \, , \tag{3.20}$$

which provides a closed partial differential equation for the phase $\hat{\beta}$ of the field.

At large radii, the modulus $k_+^2 \simeq k_0^2 + 2v_0^2/3$ and the uniform velocity $\hat{\nabla}\hat{\beta} = \mathbf{v}_0$ are solutions of (3.20). The equation (3.20) has solutions equivalent to the radial solution at matching radius r_m, as explained in section 3.3.1.

In summary, the simplified equations describe the behavior of the scalar field at radii above the critical radius r_c, where the modulus k is small. The continuity equation provides a closed partial differential equation for the phase $\hat{\beta}$, which then determines the density ρ and the modulus k of the scalar field, accounting for the departure from harmonic oscillations.

3.4.2 . Isentropic potential flow

The expressions (3.19) and (3.16) can be interpreted as the steady-state continuity equation and Bernoulli equation for an isentropic potential flow

$$\hat{\nabla} \cdot (\hat{\rho}\mathbf{v}) = 0 \quad \text{and} \quad \frac{v^2}{2} + V + H = 0\,, \tag{3.21}$$

with the curl-free velocity $\mathbf{v} = \hat{\nabla}\hat{\beta}$, the external-force potential $V(\hat{r})$ and the enthalpy $H(\hat{\rho})$. In this potential flow interpretation, we have the mapping

$$\hat{\rho} = \frac{3}{2}k^2\,, \quad V(\hat{r}) = -\frac{3}{4}k_+^2(\hat{r})\,, \quad H(\hat{\rho}) = \frac{\hat{\rho}}{2}\,. \tag{3.22}$$

The effective pressure $\hat{P}(\hat{\rho})$, defined by $dH = d\hat{P}/\hat{\rho}$, read

$$\hat{P}(\hat{\rho}) = \hat{\rho}^2/4\,, \tag{3.23}$$

with a polytropic exponent of $\gamma_\mathrm{ad} = 2$. By rearranging the Bernoulli equation (3.21), the density $\hat{\rho}$ can be expressed in terms of the velocity v

$$\hat{\rho} = \gamma + \frac{1}{\hat{r}} - v^2\,. \tag{3.24}$$

Here, γ is a parameter given by

$$\gamma = \frac{3}{2}k_0^2 + v_0^2\,, \quad \text{hence} \quad \frac{3}{2}k_+^2 = \gamma + \frac{1}{\hat{r}}\,. \tag{3.25}$$

Thus, the density, velocity, and external-force potential in the scalar field system correspond to the density, velocity, and external potential of the potential flow. The effective pressure follows a polytropic relation, and the density can be expressed in terms of the velocity and a parameter γ related to the initial conditions.

3.5 . Scalar-field flow around the black hole

3.5.1 . Linear flow

Equations (3.18) and (3.20) describe the behavior of dark matter in the low-velocity radial accretion regime at small radii but far above the Schwarzschild radius. In this regime, the term $(\hat{\nabla}\hat{\beta})^2$ is small compared to k_+^2 in (3.20). However, at large radii where $\mathbf{v} \simeq \mathbf{v}_0$, this is only true if $v_0 \lesssim k_0$, meaning that the black hole moves with a speed smaller than the speed of sound of the soliton cloud. Here, we focus on this regime, and the high-velocity supersonic case will be studied in chapter 4. To analyze the flow in the low-velocity regime, it is helpful to consider the "linear flow" associated with the linearized version of (3.20), given by

$$\hat{\nabla} \cdot \left[k_+(\hat{r})^2 \hat{\nabla}\hat{\beta} \right] = 0\,, \tag{3.26}$$

as this is a good approximation at all radii. This linear equation can be explicitly solved due to the simple form of the kernel k_+^2. The spherical symmetry of k_+^2 allows us to expand the angular part of the linear modes in terms of spherical harmonics, specifically the Legendre polynomials $P_\ell(\cos\theta)$. Since the solutions sought are axially symmetric, only the modes $Y_\ell^0(\theta,\varphi)$ are needed. Thus, the independent axially symmetric modes $G_\ell(x,\theta)$ can be written as $G_\ell(\hat{r},\theta) = G_\ell(\hat{r})\, P_\ell(\cos\theta)$, where we separated the radial and angular dependencies. The radial part of the equation for $\ell \neq 0$ is given by

$$\frac{d}{d\hat{r}} \left(\hat{r}^2 k_+^2 \frac{dG_\ell}{d\hat{r}} \right) - \ell(\ell+1) k_+^2 G_\ell = 0\,. \tag{3.27}$$

By introducing the characteristic radius $\hat{r}_\gamma = 1/\gamma$, the growing and decaying modes for $\ell = 0$ are given by

$$G_0^+(\hat{r}) = 1 \quad \text{and} \quad G_0^-(\hat{r}) = \ln\left(1 + \frac{1}{\gamma\hat{r}}\right)\,. \tag{3.28}$$

For $\ell \neq 0$, the modes are given by hypergeometric functions ${}_2F_1(x_0, x_1; x_2; x_3)$ as

$$G_\ell^+(\hat{r}) = (\gamma\hat{r})^{a-\nu}\; {}_2F_1(a, 1-b; 1-b+a; -\gamma\hat{r})\,, \tag{3.29}$$

$$G_\ell^-(\hat{r}) = (\gamma\hat{r})^{-\nu}\; {}_2F_1(a, b; c; -1/(\gamma\hat{r}))\,, \tag{3.30}$$

where $\nu = \left(1 + \sqrt{1 + 4\ell(\ell+1)}\right)/2$, $a = \nu + \sqrt{\nu(\nu-1)}$, $b = \nu - \sqrt{\nu(\nu-1)}$, and $c = 2\nu$. These mode functions exhibit specific behaviors at small and large radii. At small radii ($\hat{r} \ll \hat{r}_\gamma$), the solutions behave as

$$\begin{aligned} \ell = 0: &\quad G_0^+(\hat{r}) = 1\,, \quad G_0^-(\hat{r}) \sim \ln(1/\hat{r})\,, \\ \ell \neq 0: &\quad G_\ell^+(\hat{r}) \sim \hat{r}^{\sqrt{\ell(\ell+1)}}\,, \quad G_\ell^-(\hat{r}) \sim \hat{r}^{-\sqrt{\ell(\ell+1)}}\,, \end{aligned} \tag{3.31}$$

while at large radii ($\hat{r} \gg \hat{r}_\gamma$), they behave as

$$\begin{aligned} \ell = 0: &\quad G_0^+(\hat{r}) = 1\,, \quad G_0^-(\hat{r}) \sim \hat{r}^{-1}\,, \\ \ell \neq 0: &\quad G_\ell^+(\hat{r}) \sim \hat{r}^{\ell}\,, \quad G_\ell^-(\hat{r}) \sim \hat{r}^{-\ell-1}\,. \end{aligned} \tag{3.32}$$

In the large-radius limit, the usual Laplacian modes are recovered at leading order, as the k_+^2 goes to a constant.

The boundary conditions for the linear flow are specified at large and inner radii. At large radii, the condition $\mathbf{v} \to v_0\,\mathbf{e}_z$ is imposed, leading to $\hat{\beta} = v_0 \hat{r} \cos\theta$. At the inner radius $\hat{r}_{\rm m}$, the boundary condition sets the radial component, $v_r \simeq v_r(\hat{r}_{\rm m})$, which can be expressed as

$$\hat{r} = \hat{r}_{\rm m} : \quad \frac{\partial \hat{\beta}}{\partial \hat{r}} \simeq v_r^{\rm m} \,, \quad \frac{\partial \hat{\beta}}{\partial \theta} \simeq 0 \,. \tag{3.33}$$

At the linear level, denoted by the superscript L, these boundary conditions only generate the monopole and the dipole components of $\hat{\beta}$, given by

$$\hat{\beta}^L = \hat{\beta}_0^L(\hat{r}) + \hat{\beta}_1^L(\hat{r}) \, \cos(\theta), \tag{3.34}$$

with the monopole

$$\hat{\beta}_0^L(\hat{r}) = \frac{v_r^{\rm m}}{G_0^{-\prime}(\hat{r}_{\rm m})} G_0^-(\hat{r}) \,, \tag{3.35}$$

and the dipole, defined using gamma functions $\Gamma(x)$,

$$\hat{\beta}_1^L(\hat{r}) = \frac{v_0}{\gamma} \, (\gamma\hat{r})^{\sqrt{2}} \, \frac{\Gamma(-1+\sqrt{2})\,\Gamma(2+\sqrt{2})}{\sqrt{2}\,\Gamma(1+2\sqrt{2})} \, {}_2F_1(2+\sqrt{2}, -1+\sqrt{2}; 1+2\sqrt{2}; -\gamma\hat{r}) \,. \tag{3.36}$$

In the range where the flow is approximately radial, it is found that the velocity decreases as $v_r \sim 1/r$, which is consistent with the results obtained in [190] for purely radial accretion. The modulus k also decreases, approximately given by $k^2 \simeq k_+^2 \simeq 2/(3\hat{r})$, while the density ρ follows a similar trend, proportional to k^2 and thus also proportional to $1/r$. This behavior leads to a constant radial flux $F \propto r^2 \rho v_r$, which is a requirement for a steady state.

The selection of the matching radius $r_{\rm m}$ between the radial accretion regime and the large radii resolution is a crucial decision. It is important to choose $r_{\rm m}$ when we are still in proximity to the black hole, within the range of the radial accretion regime. Although this regime can extend up to tens of Schwarzschild radii, it is prudent to select a small matching radius while making sure that the value of k remains sufficiently small to be on the low-velocity branch. As a numerical example, let us consider $\hat{r}_{\rm m} \sim 10$ and $v_r(\hat{r}_{\rm m}) \sim 0.1$ (obtained from the radial accretion calculation), slightly beyond the critical radius $\hat{r}_{\rm c}$ associated with the transition between the low and high-velocity branches. At small radii ($\hat{r} \ll \hat{r}_\gamma$), we have the following approximations

$$\hat{\beta}_0^L \sim \ln(1/\hat{r}) \,, \quad \hat{\beta}_1^L \sim \frac{v_0}{\gamma} (\gamma\hat{r})^{\sqrt{2}} \,, \quad \frac{\partial \hat{\beta}_0^L}{\partial \hat{r}} \sim -1/\hat{r} \,, \quad \frac{\partial \hat{\beta}_1^L}{\partial \hat{r}} \sim v_0 (\gamma\hat{r})^{\sqrt{2}-1} \,, \tag{3.37}$$

while at large radii ($\hat{r} \gg \hat{r}_\gamma$), the behaviors are given by

$$\hat{\beta}_0^L \sim (\gamma\hat{r})^{-1} \,, \quad \hat{\beta}_1^L \sim v_0 \hat{r} \,, \quad \frac{\partial \hat{\beta}_0^L}{\partial \hat{r}} \sim -1/(\gamma\hat{r}^2) \,, \quad \frac{\partial \hat{\beta}_1^L}{\partial \hat{r}} \sim v_0 \,. \tag{3.38}$$

Therefore, we find that the linear flow becomes radial at a transition radius $\hat{r}_{\rm t}$ greater than $\hat{r}_\gamma$ if $v_0 \ll \gamma$. This condition can be expressed as

$$v_0 \ll k_0^2 : \quad \hat{r}_{\rm t} = \frac{1}{\sqrt{\gamma v_0}} \gg \hat{r}_\gamma \,. \tag{3.39}$$

In the case of larger velocities, the transition occurs below $\hat{r}_\gamma$,

$$k_0^2 \ll v_0 \ll 1 : \quad \hat{r}_{\rm t} = \gamma^{-1}(v_0/\gamma)^{-1/\sqrt{2}} \ll \hat{r}_\gamma \, . \tag{3.40}$$

In relaxed systems, it is expected that $v_0^2 \sim k_0^2$, meaning that the squared velocity is of the order of the gravitational potential of the scalar soliton, with $k_0^2 \ll 1$. This leads to $v_0 \sim k_0 \gg k_0^2$. Consequently, the linear flow typically becomes radial far inside the radius $\hat{r}_\gamma$. At that point, the amplitude of the dipole $\hat{\beta}_1^L$ has already somewhat decreased compared to the large-distance uniform flow $\mathbf{v}_0$, as indicated by the exponents in (3.37). Thus, the pressure associated with the self-interactions slows down the linear flow before it becomes fully radial and accelerates towards the black hole

3.5.2 . Large-radius expansions

To go beyond the linear-flow approximation and examine the behavior at large radii, we can expand the flow in terms of a large-radius expansion. This expansion allows us to explicitly observe the transition from a subsonic to a supersonic regime as the relative velocity $\mathbf{v}_0$ exceeds the sound speed. Additionally, we can determine the analytical expressions for the subleading odd corrections (of order $\hat{r}^0$) and even corrections (of order $1/\hat{r}$) to the uniform-flow potential $\hat{\beta}_0 = v_0 \hat{r} \cos\theta$.

It is known that the hydrodynamical Euler equation can lead to discontinuous solutions with shocks or contact discontinuities, which also applies to our case. A low velocity v_0 corresponds to a subsonic and continuous flow at large radii, while a high velocity v_0 leads to a supersonic flow with a bow shock. However, at small radii near the Schwarzschild radius, there is always a supersonic high-velocity region, as explained in section 3.3.1.

At large radii, where the velocity is close to $\mathbf{v}_0$, we can write $\hat{\beta} = v_0 \hat{r} \cos\theta + \delta\hat{\beta}$ and linearize the equation of motion (3.20) with respect to $\delta\hat{\beta}$. This results in the following equation

$$\frac{\partial^2 \delta\hat{\beta}}{\partial \hat{x}^2} + \frac{\partial^2 \delta\hat{\beta}}{\partial \hat{y}^2} + \left(1 - \frac{4 v_0^2}{3 k_0^2}\right) \frac{\partial^2 \delta\hat{\beta}}{\partial \hat{z}^2} = \frac{2 v_0 \cos\theta}{3 k_0^2 \hat{r}^2} \, , \tag{3.41}$$

where we use Cartesian coordinates $\{\hat{x}, \hat{y}, \hat{z}\}$ and assume $\mathbf{v}_0 = v_0 \, \mathbf{e}_z$. The source term on the right-hand side is due to the gravitational effect of the black hole, which causes the flow to deviate from the homogeneous flow $\mathbf{v}_0$. By introducing the sound speed $c_{s,0}$ as

$$c_{s,0} = \frac{\sqrt{3}}{2} k_0 \quad \text{and} \quad c_{s,0}^2 = \frac{d\hat{P}_0}{d\hat{\rho}_0} \, , \tag{3.42}$$

the equation of motion (3.41) changes its character from elliptic to hyperbolic when v_0 equals the sound speed. This leads to the following classification

$v_0 < c_{s,0}$: elliptic subsonic flow ,
$v_0 > c_{s,0}$: hyperbolic supersonic flow .

It is important to note that this linear analysis of the perturbation $\delta\hat{\beta}$ is different from the "linear flow" studied in section 3.5.1. In the linear flow analysis, we linearized the equation of motion (3.20) with respect to $\hat{\beta}$ itself, assuming small velocities everywhere compared to $k_+^2(\hat{r})$, which implies $v_0 \ll c_{s,0}$ at large radii. On the other hand, in this section, we consider linear perturbations with respect to the dominant uniform flow $\mathbf{v}_0$ at large distances, and we do not assume that v_0 is small. Therefore, although the analysis (3.41) is restricted to large radii, it allows us to study all regimes of v_0. In particular, it reveals that even at large distances, the cubic non-linearity in (3.20) introduces a more diverse behavior than the "linear flow" (3.34), as the dynamics can transition from elliptic (as in the low-velocity case) to hyperbolic.

For subsonic flows, the partial differential equation (3.41) becomes elliptic, indicating a smooth flow. By introducing the parameter $\mu > 0$ given by $\mu^2 = 1 - v_0^2/c_{s,0}^2$ for $0 \leq v_0 < c_{s,0}$, and rescaling the coordinates from $\{\hat{x}, \hat{y}, \hat{z}\}$ to $\{\tilde{x}, \tilde{y}, \tilde{z}\}$ with $\tilde{x} = \hat{x}$, $\tilde{y} = \hat{y}$, $\tilde{z} = \hat{z}/\mu$, we recover the Laplace equation in the left-hand side of (3.41). Using the Green function of the 3D Laplacian, the inhomogeneous solution is obtained as

$$\delta\hat{\beta}_{\text{odd}}(\hat{\mathbf{x}}) = -\frac{v_0}{6\pi k_0^2} \int \frac{d\hat{\mathbf{x}}'\ \hat{z}'}{\hat{r}'^{\,3}\ \sqrt{\mu^2|\hat{\mathbf{x}}'-\hat{\mathbf{x}}|^2 + (1-\mu^2)(\hat{z}'-\hat{z})^2}}\,, \tag{3.43}$$

where we moved back to the coordinates $\{\hat{x}, \hat{y}, \hat{z}\}$. Performing the integration, the solution for $\delta\hat{\beta}_{\text{odd}}$ is

$$\delta\hat{\beta}_{\text{odd}}(\hat{\mathbf{x}}) = \frac{1}{2v_0} \ln\left[\frac{\mu(1+\cos\theta)}{\cos\theta + \sqrt{\mu^2 + (1-\mu^2)\cos^2\theta}}\right]. \tag{3.44}$$

This solution is odd in $\cos\theta$ and does not depend on $\hat{r}$. The radial velocity component is vanishing, and the angular velocity component δv_θ is given by

$$\delta v_\theta(\hat{\mathbf{x}}) = \frac{1}{2v_0\hat{r}\sin\theta}\left[\frac{1}{\sqrt{\mu^2 + (1-\mu^2)\cos^2\theta}} - 1\right]. \tag{3.45}$$

This solution is even in $\cos\theta$ and decays as $1/\hat{r}$. The homogeneous solutions of (3.41) are solutions of the Laplace equation in the rescaled coordinates. Expanding in spherical harmonics, we obtain growing and decaying modes. The leading-order decaying solution is the monopole $\delta\hat{\beta} \propto \tilde{r}^{-1}$, which gives the even component

$$\delta\hat{\beta}_{\text{even}} = \frac{B}{\hat{r}}\left[\mu^2 + (1-\mu^2)\cos^2\theta\right]^{-1/2}, \tag{3.46}$$

where we moved back to the coordinates $\{\hat{x}, \hat{y}, \hat{z}\}$. This solution decays as $1/\hat{r}$ and is even in $\cos\theta$. The even components of the velocity potential decay faster than the odd components and correspond to a subsubleading correction. The quadratic terms over $\delta\hat{\beta}^2$ are not necessary to obtain the even component because of the partial decoupling of different parities in the nonlinear equation (3.20). Indeed, the odd term (3.44) only generates an odd term at order $1/\hat{r}^3$. Therefore, at order $1/\hat{r}^3$ the even component is fully determined by the linear operator on the left-hand side of (3.41), which gives (3.46).

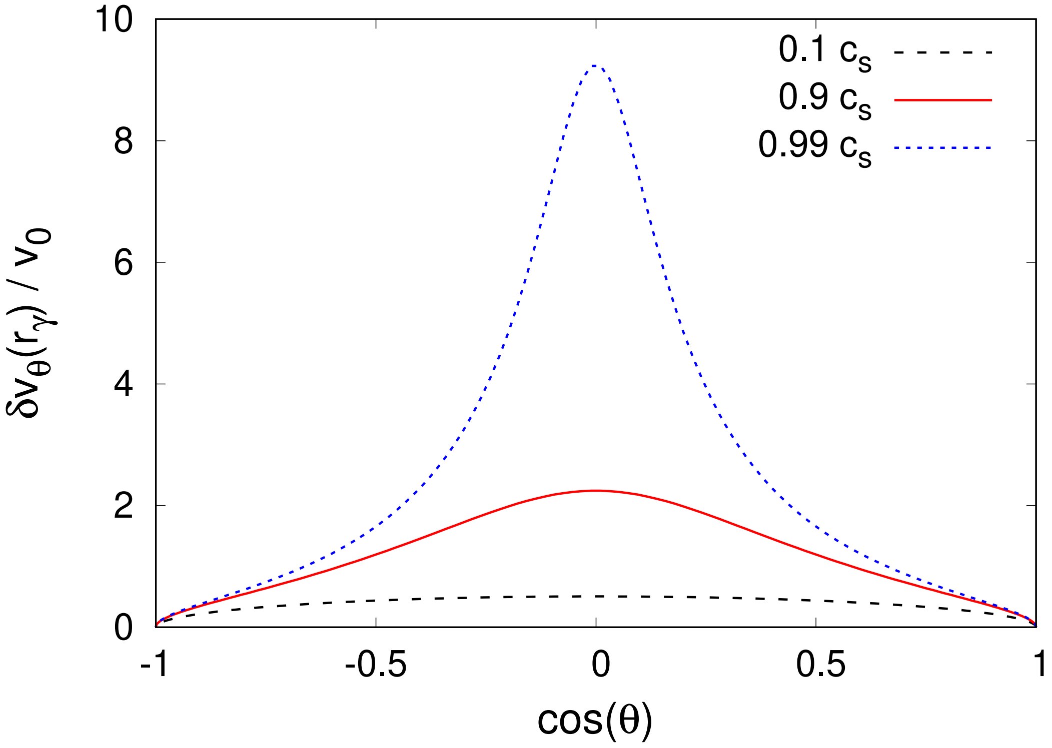

Figure 3.2: Linear perturbation δv_θ to the angular velocity, from (3.45), normalized by v_0. We show the cases $v_0 = 0.1c_{s,0}$, $0.9c_{s,0}$ and $0.99c_{s,0}$, at the radius $\hat{r}_\gamma$.

The behavior of the solutions at large radii is analyzed by expanding $\delta\hat{\beta}$ in Legendre polynomials. The large-radius behaviors are

$$\hat{r} \gg \hat{r}_\gamma : \quad \delta\hat{\beta}_{2\ell+1} \sim \hat{r}^0 \,, \quad \delta\hat{\beta}_{2\ell} \sim \hat{r}^{-1} \,, \tag{3.47}$$

while for $v_0 \to 0$, both odd and even multipoles decay as

$$v_0 \to 0 : \quad \delta\hat{\beta}_n \sim v_0^n \,. \tag{3.48}$$

The angular velocity δv_θ is shown in Figure 3.2. For small v_0 ($v_0 \to 0$), the linear flow (3.34) is recovered as multipoles beyond the dipole become negligible as seen from (3.48), we have $\delta\hat{\beta}_{\rm odd} \propto -\cos\theta$ and the angular velocity behaves as $\delta v_\theta \propto (\sin\theta)/\hat{r}$. By symmetry, the angular velocity vanishes along the z-axis, when $\theta = 0$ and $\theta = \pi$. As v_0 increases, the central peak grows, and it diverges for $v_0 \to c_{s,0}$ as $1/\mu$. The angular velocity is positive, indicating that for $\theta \simeq \pi/2$ the first-order perturbation $\delta\mathbf{v}$ is opposite to the incoming flow $\mathbf{v}_0$, causing a slowdown near the black hole, before turning and falling increasingly fast into the black hole near the Schwarzschild radius. The singularity associated with the transition to the supersonic regime appears very close to $c_{s,0}$, for $v_0 \gtrsim 0.9c_{s,0}$. Comparing this behavior with that of linear flow (3.34), we see that they agree at large radii as

$$r \gg r_\gamma : \quad \beta_0^L \propto 1/r\,, \quad \beta_1^L = v_0 r - \frac{v_0}{2\gamma} + \frac{v_0}{2\gamma^2 r} + \dots\,. \tag{3.49}$$

Here, the subleading term $-\frac{v_0}{2\gamma}$ in the dipole component generates a positive correction to the angular velocity, given by $\frac{v_0\sin(\theta)}{2\gamma r}$. The key difference between this behavior and the linear flow (3.34) lies in the cubic non-linearity described by equation (3.20), which generates non-zero contributions to all higher-order multipoles.

At large radii, the phase $\hat\beta$ can be expanded as $\hat\beta = v_0 r\cos\theta + \delta\hat\beta_{\rm odd} + \delta\hat\beta_{\rm even}$ where the expansion is done over odd and even components with respect to $u = \cos\theta$. For $\hat r \gg \hat r_\gamma$, the odd and even components are

$$\delta\hat\beta_{\rm odd} = \delta\hat\beta^{(0)}_{\rm odd}(\theta) + \frac{1}{\hat r}\delta\hat\beta^{(1)}_{\rm odd}(\theta) + \mathcal{O}\left(\frac{1}{\hat r^2}\right) \quad \text{and} \quad \delta\hat\beta_{\rm even} = \frac{1}{\hat r}\delta\hat\beta^{(1)}_{\rm even}(\theta) + \mathcal{O}\left(\frac{1}{\hat r^2}\right)\,, \tag{3.50}$$

where $\delta\hat\beta^{(0)}_{\rm odd}$ is given by (3.44) and $\delta\hat\beta^{(1)}_{\rm even}/\hat r$ is given by (3.46). These large-distance tails, generated by nonlinear mode couplings, can be expanded in Legendre multipoles

$$\delta\hat\beta^{(0)}_{\rm odd}(\theta) = \sum_{\ell=0}^{\infty} a_{2\ell+1} P_{2\ell+1}(\cos\theta) \quad \text{and} \quad \delta\hat\beta^{(1)}_{\rm even}(\theta) = \sum_{\ell=0}^{\infty} b_{2\ell} P_{2\ell}(\cos\theta)\,. \tag{3.51}$$

The coefficients a_n and b_n satisfy recursion relations. The order of magnitude of the coefficients a_n and b_n depends on the velocity v_0 relative to the speed of sound $c_{s,0}$. If $v_0 \sim c_{s,0}$, the coefficients remain of the same order as a_1 and b_0. However, if $v_0 \ll c_{s,0}$, the coefficients decay at higher orders as $(v_0/c_{s,0})^n$. Thus, for small velocities $v_0 \ll c_{s,0}$, the linear flow is recovered as higher orders become negligible and the coefficients a_1 and b_0 take their linear flow values.

The velocity field $\mathbf{v} = \hat\nabla\hat\beta$ yields

$$\begin{aligned} v_r &= v_0\cos\theta - \frac{1}{\hat r^2}\left(\delta\hat\beta^{(1)}_{\rm odd} + \delta\hat\beta^{(1)}_{\rm even}\right) + \dots\,, \\ v_\theta &= -v_0\sin\theta + \frac{1}{\hat r}\frac{d\delta\hat\beta^{(0)}_{\rm odd}}{d\theta} + \frac{1}{\hat r^2}\left(\frac{d\delta\hat\beta^{(1)}_{\rm odd}}{d\theta} + \frac{d\delta\hat\beta^{(1)}_{\rm even}}{d\theta}\right) + \dots\,. \end{aligned} \tag{3.52}$$

The deviations from the uniform flow $\mathbf{v}_0$ decay as $1/\hat r^2$ for the radial velocity and as $1/\hat r$ for the angular velocity. Furthermore, the angular velocity and the velocity squared are even up to order $1/\hat r$. For the density, from (3.24) we have

$$\hat\rho_{\rm even} = \hat\rho_0 + \frac{1}{\hat r} + \frac{2v_0\sin\theta}{\hat r}\frac{d\delta\hat\beta^{(0)}_{\rm odd}}{d\theta} + \dots \quad \text{and} \quad \hat\rho_{\rm odd} = \frac{2v_0}{\hat r^2}\left[\cos\theta\,\delta\hat\beta^{(1)}_{\rm even} + \sin\theta\frac{d\delta\hat\beta^{(1)}_{\rm even}}{d\theta}\right] + \dots\,, \tag{3.53}$$

where $\hat\rho_0 = \frac{3k_0^2}{2} = \gamma - v_0^2$. Thus, the density field is even up to order $1/\hat r$.

When going back to physical coordinates, the explicit expressions for $\rho_{\rm even}$ and $\rho_{\rm odd}$ are given using (3.44)

$$\rho_{\rm even} = \rho_0 + \frac{\mathcal{G} m_{\rm BH}\rho_0}{c_{s,0}\sqrt{(c_{s,0}^2 - v_0^2)r^2 + v_0^2 z^2}} + \dots \quad \text{and} \quad \rho_{\rm odd} = \frac{4B\rho_0\mathcal{G}^2 m_{\rm BH}^2 v_0 c_{s,0} z}{[(c_{s,0}^2 - v_0^2)r^2 + v_0^2 z^2]^{3/2}} + \dots\,. \tag{3.54}$$

The even component agrees with the results for the linear density perturbation in an isothermal gas caused by the motion of a star, as found in [266, 277]. The new odd component, proportional to the coefficient B, is related to the accretion by the black hole and is the source of accretion drag force.

Expanding $\hat{\rho}_{\rm even}$ in powers of v_0, we have

$$\hat{\rho}_{\rm even} = \hat{\rho}_0 + \frac{1}{\hat{r}} + \frac{v_0^2}{2c_{s,0}^2\hat{r}} \sin^2\theta + \dots \, . \tag{3.55}$$

Thus, at large radii ($\hat{r} \gg \hat{r}_\gamma$) and for $v_0 \ll c_{s,0}$, the density correction due to the motion of the black hole is much smaller than the static contribution associated with the black hole, $\hat{\rho}_0 \gg 1/\hat{r} \gg v_0^2/(c_{s,0}^2\hat{r})$. Therefore, it is reasonable to neglect this correction to the self-gravity of the dark matter perturbation. At smaller radii, the gravity of the black hole dominates over the scalar-field background self-gravity and, consequently, over the scalar perturbation as well.

3.5.3 . Numerical scheme

In the subsonic regime considered in this chapter, the flow remains close to the linear solution given by (3.34). Importantly, there is no shock at large radii. Therefore, an iterative approach starting from this linear approximation can be used to efficiently solve the problem numerically. Practically, (3.20) is written as

$$\hat{\nabla} \cdot (k_+^2 \hat{\nabla}\hat{\beta}) = S \, , \quad \text{with} \quad S = \frac{2}{3}\hat{\nabla} \cdot [(\hat{\nabla}\hat{\beta})^2 \hat{\nabla}\hat{\beta}] \, . \tag{3.56}$$

To solve this system (3.56), an iterative scheme is employed. First, starting from the linear flow $\hat{\beta}^L$, the source term S is computed using the second equation. Then, an improved flow $\hat{\beta}$ is obtained by solving the first equation. The fields are expanded using Legendre multipoles, and the Green's function of the linear operator $\hat{\nabla} \cdot [k_+^2 \hat{\nabla}(\cdot)]$ is utilized, as explained in Appendix A.1. These two steps (computing S and solving the equation) are repeated iteratively until the flow converges.

3.5.4 . Numerical results

In our numerical computations, we choose the value $k_0 = 10^{-3}$, which corresponds to the order of magnitude associated with the equilibrium between self-interactions of the scalar field and gravity. This choice is motivated by the fact that in the bulk of the soliton, far from the black hole horizon, we have $k^2 \sim \Phi_{\rm I} \sim \Phi_{\rm N}$ from (2.13) and (3.10), where $\Phi_{\rm N} \sim 10^{-6}$ represents the typical amplitude of the gravitational potential in astrophysical and galactic systems. In these systems, which are dominated by gravity, the typical velocities are also of the order of $v^2 \sim \Phi_{\rm N}$, which is equivalent to the magnitude of the speed of sound, given that $c_{s,0}^2 \sim k_0^2$. Since we focus on the subsonic regime, we choose $v_0 = c_{s,0}/2$ in the following numerical computations. This choice is consistent with the expected order of magnitude and ensures that v_0 remains below the sound speed. As for the matching radius, we select $\hat{r}_{\rm m} = 80$ to satisfy the constraints discussed in section 3.3.1. It is important to note that the precise values of these parameters do not affect the behavior of the scalar field flow; rather, they only depend on the properties $k_0 \ll 1$ and $v_0 < c_{s,0}$.

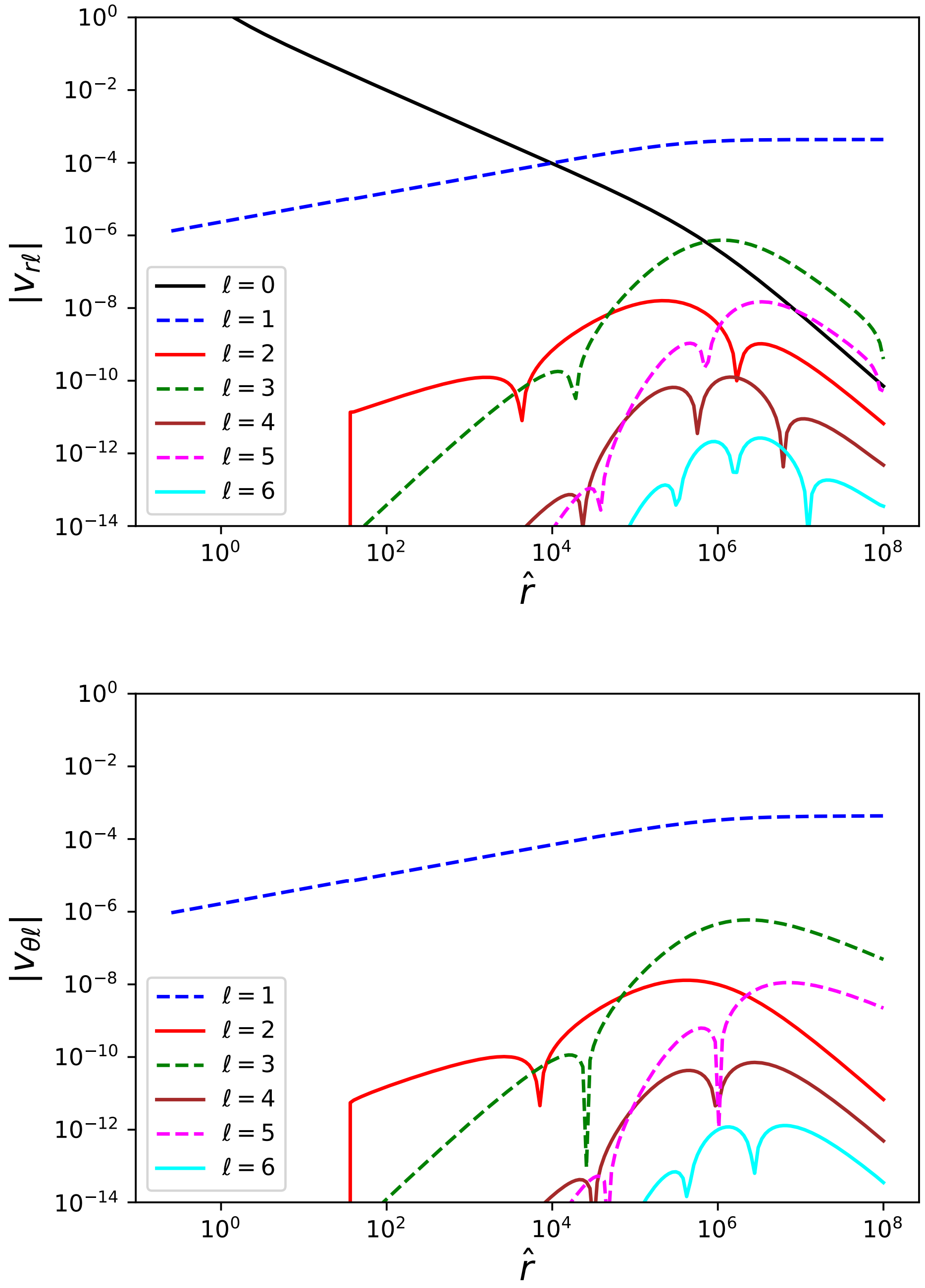

Figure 3.3: First Legendre multipoles of the radial velocity $v_{r\ell}$ (upper panel) and of the angular velocity $v_{\theta\ell}$ (lower panel), as defined in (3.58). The solid lines show even indices ℓ whereas the dashed lines show odd ℓ.

The Legendre multipoles of the phase β are obtained through the iterative scheme described in the previous section, as explained below (3.56). Further details can be found in Appendix. After a few iterations, the scheme converges, and the results shown in Figure 3.3 correspond to the values obtained after the 9th iteration. This convergence is facilitated by the fact that the nonlinear flow remains close to the linear approximation (3.34) in the subsonic regime $v_0 < c_{s,0}$.

Figure 3.3 illustrates the Legendre multipoles of the radial and angular velocities, denoted as v_r and v_θ, respectively. These quantities are defined as

$$v_r = \sum_\ell v_{r\ell} P_\ell(\cos\theta), \quad v_\theta = -\sin\theta \sum_\ell v_{\theta\ell} P'_\ell(\cos\theta)\,, \tag{3.57}$$

with the velocity components

$$v_{r\ell} = \frac{d\hat{\beta}_\ell}{d\hat{r}} \quad \text{and} \quad v_{\theta\ell} = \frac{\hat{\beta}_\ell}{\hat{r}}\,. \tag{3.58}$$

At small radii ($r < r_{\rm m}$), we utilize the radial monopole obtained from radial accretion in [190] and the linear dipole obtained for the linear flow (3.34). This choice sets the inner boundary condition, and we solve the nonlinear system (3.56) only for $r > r_{\rm m}$. Consequently, the higher-order multipoles are truncated at $\hat{r}_{\rm m}$. This truncation is justified since these higher-order multipoles are negligible compared to the monopole at radius $\hat{r}_{\rm m}$. It is important to note that the radial velocity v_r diverges at the Schwarzschild radius [190]; however, this is an artifact resulting from the choice of coordinates and the interpretation of $d\hat{\beta}/d\hat{r}$ as a velocity is valid only in the nonrelativistic regime.

Figure 3.3 demonstrates the partial decoupling of odd and even components, which is discussed in Appendix and section 3.5.2. The odd multipoles of the phase $\hat{\beta}$ exhibit a constant tail at large distances, in addition to the linear dipole associated with the uniform flow $\mathbf{v}_0$. In contrast, the even multipoles decrease as $1/\hat{r}$, as described in (3.50) and (3.51). Consequently, for the angular velocity $v_\theta = (1/\hat{r})\partial\hat{\beta}/\partial\theta$, the even multipoles decay as $1/\hat{r}$, while the odd multipoles decay as $1/\hat{r}^2$, as indicated in (3.52). It is worth noting that in the notation (3.57), even components of v_θ correspond to odd ℓ. These distinct decay rates can be observed in the lower panel of the figure, where solid lines represent odd components and dashed lines represent even components. Additionally, it should be noted that the constant odd tail of the phase $\hat{\beta}$ does not contribute to the radial velocity $v_r = \partial\hat{\beta}/\partial\hat{r}$. As a result, only the leading even tail and the subleading odd tail of order $1/\hat{r}$ in $\hat{\beta}$ contribute to the radial velocity, and all multipoles of the radial velocity decay at the same rate $1/\hat{r}^2$, as shown in the upper panel and expressed in (3.52).

The asymptotic regime at large distances is only reached beyond $\hat{r}_\gamma \sim 10^6$, and for higher-order multipoles, it is attained at even larger radii. This radius $r_\gamma \sim r_{\rm sg}$ corresponds to the point where the self-gravity and pressure of the scalar field become comparable to the gravity of the black hole. At larger radii, the influence of black hole gravity is screened by the collective response of the scalar field (its pressure), resulting in a rapid decay of velocity corrections to the uniform flow $\mathbf{v}_0$. Furthermore, it should be noted that even for the relatively large velocity $v_0 = c_{s,0}/2$, the corrections to the linear flow (3.34) remain small, as indicated by the magnitude of higher-order multipoles with $\ell \geq 2$. Thus, as will be evident in Figure 3.5 below, the flow can be seen as a combination of a monopole radial accretion, which closely resembles the purely radial result, and a dipole term associated with the uniform velocity $\mathbf{v}_0$ at infinity. These findings are consistent with the numerical results obtained by [304, 305] for the motion of a black hole in a perfect gas, utilizing either Newtonian or relativistic treatments.

In Figure 3.4, we present our results for the Legendre multipoles $\hat{\rho}_\ell$ of the density field, multiplied by a factor $\hat{r}$. We can see that the monopole component dominates at all radii. This dominance arises because the density approaches a constant value $\hat{\rho}_0$ associated with the soliton at large radii, while at small radii, the flow becomes radial, as shown in Figure 3.3. This radial flow implies a spherically symmetric configuration. In agreement with (3.53), the product $\hat{r}\hat{\rho}_{r\ell}$ approaches a constant value for the even multipoles beyond $\ell = 0$ as the radius increases, while it decreases as $1/\hat{r}$ for the odd multipoles. At small values of $\hat{r}$, the monopole component grows as $1/\hat{r}$, while the higher-order multipoles either grow more slowly or decrease. Specifically, for the linear flow (3.34), using (3.37), we obtain that the dipole component behaves as $\hat{r}^{\sqrt{2}-2}$ at small radii. Consequently, $\hat{r}\hat{\rho}_{\ell=1} \propto \hat{r}^{\sqrt{2}-1} \to 0$.

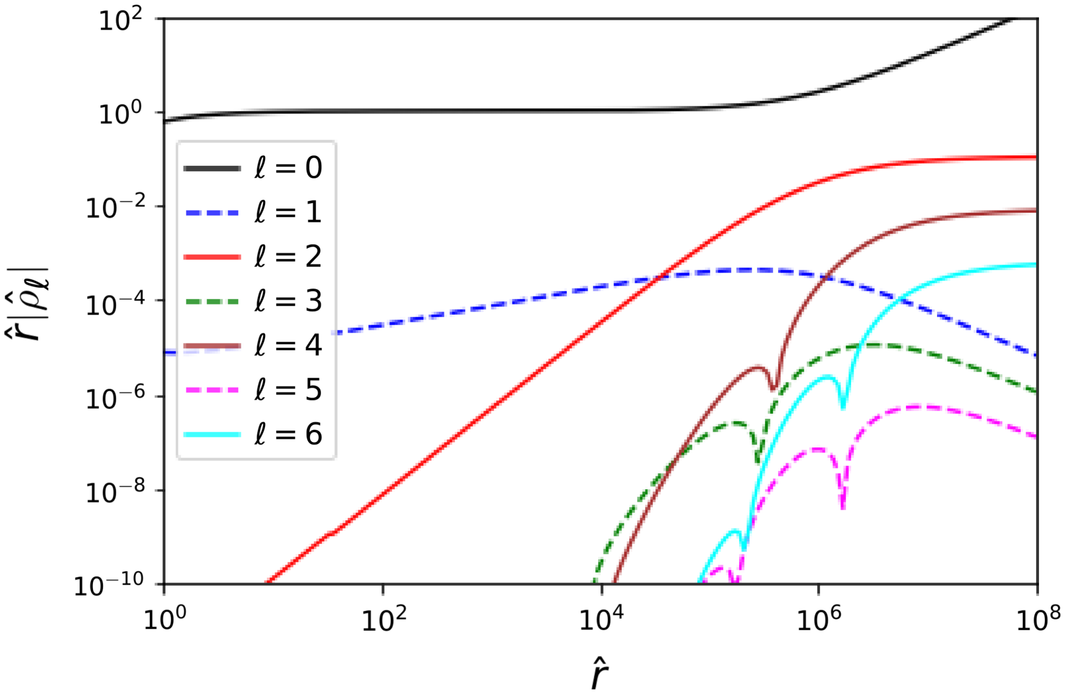

Figure 3.4: First Legendre multipoles of the density multiplied by a factor $\hat{r}$, $\hat{r}\hat{\rho}_{r\ell}$.

In Figure 3.5, we present maps of the scalar velocity and density fields. The black hole is located at the center of the plots, and the scalar-field dark matter approaches from the left with a uniform velocity $\mathbf{v}_0$ and density ρ_0. The upper row of panels displays maps of the velocity field, represented by arrows with unit length, at different scales. We zoom in on the black hole from left to right. The middle row shows the corresponding maps of the magnitude $|\mathbf{v}|$ of the velocity.

In the left panels, which represent the largest scale, the flow is mostly unaffected by the gravitational pull from the black hole and maintains its incoming velocity $\mathbf{v}_0$, moving from left to right. As shown in the panel below in the middle row, the flow exhibits approximate symmetry under $\hat{z} \leftrightarrow -\hat{z}$, indicating that v^2 is an almost even function of $\cos\theta$. This is consistent with the large-radius expansions discussed in section 3.5.2 and Appendix, as well as shown in Figure 3.3. According to (3.52), at large distances, the first correction $\delta\mathbf{v}$ to the velocity, relative to the incoming velocity $\mathbf{v}_0$, is an even angular velocity $\delta v_{\theta\text{even}} \propto 1/\hat{r}$. Consequently, this leads to an even correction to the velocity magnitude, $\delta v^2_{\text{even}} \propto 1/\hat{r}$. This behavior is in agreement with the pattern observed in the left panels, where the streamlines slightly converge towards the black hole symmetrically with respect to $\hat{z} \leftrightarrow -\hat{z}$. This behavior is distinct from that of free point particles and resembles the flow in a gas. It arises due to the pressure generated by self-interactions, which increases near the black hole as the density grows. At large distances, the primary effect is that dark matter particles are initially decelerated as they approach $\hat{z} = 0$ and subsequently accelerated to regain the velocity $\mathbf{v}_0$ downstream.

In the middle-column panels, which represent intermediate scales, the deflection of the streamlines towards the black hole becomes more evident. A turning point on the $\hat{z}$-axis is visible somewhat behind the black hole. This demarcates the region, far from the black hole, where the streamlines escape towards infinity to the right of the figure, and the inner region where the streamlines fall into the black hole. Notably, there is no corresponding turning point to the left of the black hole, as the dark matter approaching from the left along the $\hat{z}$-axis continues moving straight towards the black hole until it plunges into it. This asymmetry in the flow is a clear signature distinguishing it from the case of potential flow around a compact object without accretion, such as the flow of water around a hard ball. Mathematically, this disparity arises from the different boundary conditions around the object: the radial infall at the black hole horizon in our case or the vanishing normal velocity at the surface of the ball in the typical hydrodynamical scenario. As demonstrated in previous sections, the boundary condition at infinity corresponds to the dipole in (3.34), while the boundary condition near the center corresponds to the monopole of this same equation. Consequently, the two boundary conditions possess different parity, indicating that the flow is neither purely odd nor even. The phase is odd at large distances and transitions to even near the black hole, exhibiting a complex pattern in the intermediate region. This asymmetry in the flow is also connected to the accretion onto the black hole, which determines the inner boundary condition. Therefore, the drag force experienced by the black hole, resulting from this asymmetry, is directly related to the accretion rate. We will derive the explicit expression for drag force in section 3.7.

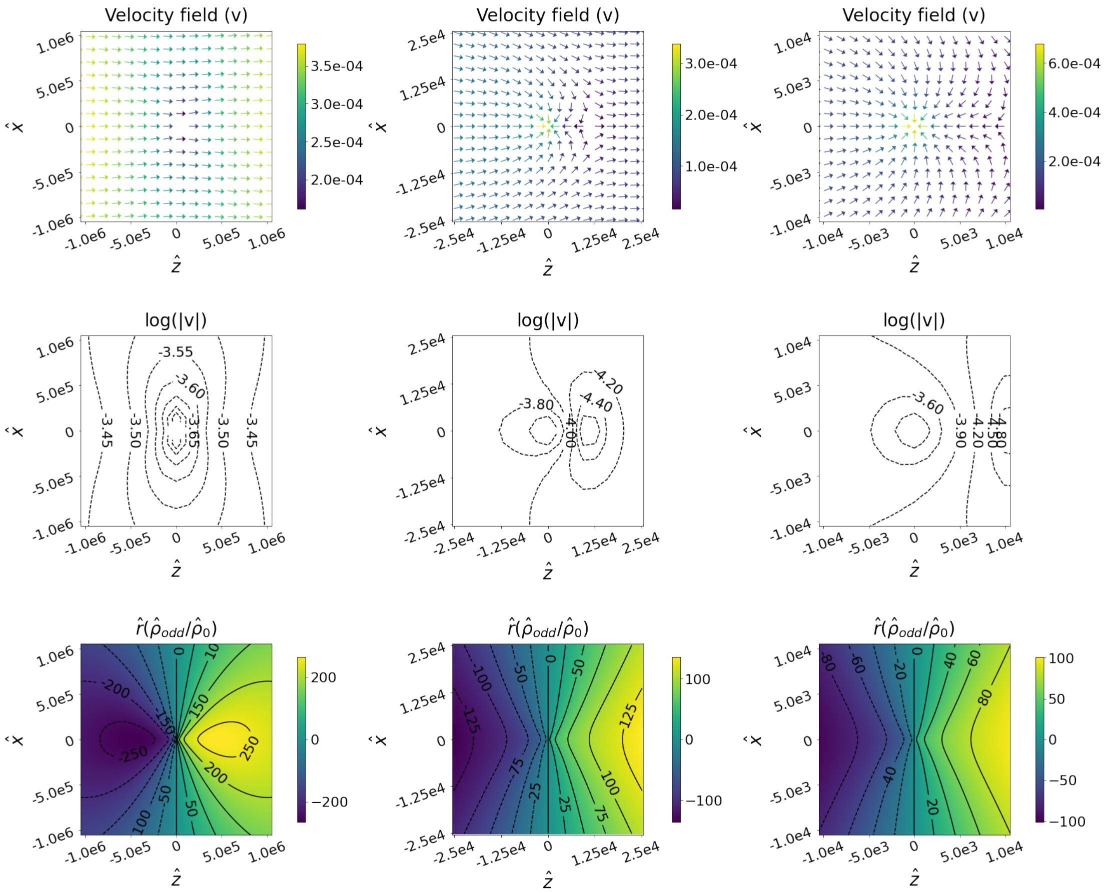

Figure 3.5: Flow (top panels), iso-velocities contours (middle panels) and odd-component of the density field $\hat{r}\hat{\rho}_{\mathrm{odd}}/\hat{\rho}_0$ (bottom panels) for the scalar-field at different scales (10^6, 2.5×10^4 and 10^4 r_s). The velocity and the density are computed from the multipoles of $\hat{\beta}$. The black hole is located at the center of the figures, at $\hat{z} = \hat{x} = 0$, where $\hat{z} = z/r_s$ and $\hat{x} = x/r_s$.

In the right-column panels, the flow becomes predominantly radial as we zoom in closer to the black hole. This corresponds to the dominance of the monopole component at small radii, as observed in Figure 3.3. The velocity magnitude increases as the flow is accelerated by the gravitational pull of the black hole during its infall. As explained in section 3.3.1, below a critical radius r_c, the flow transitions to the high-velocity branch, where the pressure from self-interactions can no longer counteract gravity, and the dark matter reaches the black hole horizon in a free fall, similar to free particles.

The lower row in Figure 3.5 displays maps of the odd component of the density field, specifically the ratio $\hat{r}\hat{\rho}_{\mathrm{odd}}/\hat{\rho}_0$. We highlight the odd component to emphasize the asymmetry in the flow and the formation of a wake behind the black hole. The drag experienced by the black hole arises from the asymmetry of the flow since a symmetric flow would not generate any drag force. However, it would be challenging to discern this effect in a map of the total density, as the even component dominates on all scales, as observed in Figure 3.4. In the subsonic regime considered in this paper, the total density appears nearly spherically symmetric at all scales, similar to the case of a perfect gas in both Newtonian and relativistic numerical simulations [304, 305].

We introduce the factor $\hat{r}$ to highlight the radii that primarily contribute to the gravitational pull on the black hole through the overdense wake of dark matter, as the gravitational force is proportional to $\int d\mathbf{r}\rho\mathbf{r}/r^3 \sim \int d\ln r(r\rho)$. According to (3.21), a decrease in velocity corresponds to an increase in density, given by $\hat{\rho} = 3k_+^2(\hat{r})/2 - v^2$. Thus, the turning point in the velocity field, situated behind the black hole, corresponds to an enhanced density compared to the radial reference. This clearly illustrates the asymmetry and the presence of a wake behind the black hole. As seen in the figure, in agreement with Figure 3.4, the product $\hat{r}\hat{\rho}_{\rm odd}$ reaches a peak at a large radius $\hat{r}_\gamma \sim 10^6$. This radius $\hat{r}_{\rm sg}$ also marks the point at which the self-gravity of the soliton becomes comparable to the black hole gravity. Consequently, beyond $\hat{r}_\gamma$, the self-interaction pressure dominates over the black hole gravity and screens its influence on the dark matter distribution. This leads to a large-scale cutoff, which also eliminates the Coulomb logarithm from the dynamical friction encountered by collisionless particles in Chandrasekhar's classical study (see Appendix B.1).

3.6 . Mass accretion by the black hole

3.6.1 . Relationship with large-radius expansions

In a steady state, the accretion of matter by the black hole can be described by the flux of matter through any closed surface surrounding it. Mathematically, this can be written as

$$\dot{\hat{M}}_{\rm BH} = -\int_{\hat{S}} \mathbf{d}\hat{\mathbf{S}} \cdot \hat{\rho}\mathbf{v}\,, \tag{3.59}$$

where $\dot{\hat{M}}_{\rm BH}$ is the accretion rate and $\mathbf{d}\hat{\mathbf{S}}$ represents the surface element. This equation holds as long as the radius of the surface $\hat{S}$ is large enough for the low-k nonrelativistic regime (3.21) to be valid. Interestingly, it can be shown that the accretion rate $\dot{\hat{M}}_{\rm BH}$ does not depend on the specific choice of surface $\hat{S}$. The difference between fluxes through $\hat{S}$ and any smaller or larger surface $\hat{S}'$ can be expressed as the integral of $\hat{\nabla}\cdot(\hat{\rho}\mathbf{v})$ over the volume $\hat{V}_{\hat{S},\hat{S}'}$ between the two surfaces. However, from (3.21), this integral evaluates to zero. Therefore, the accretion rate can be obtained using the large-distance expansion (3.50) by selecting a surface that is much larger than the radius $\hat{r}_\gamma$. Assuming the surface $\hat{S}$ to be a sphere with radius $\hat{r}$, the mass flux can be expressed as

$$\dot{\hat{M}}_{\rm BH} = -2\pi\hat{r}^2 \int_{-1}^{1} du\, \hat{\rho} v_r\,, \tag{3.60}$$

where $u = \cos\theta$. This equation indicates that only the monopole component of the radial momentum $\hat{\rho}v_r$ contributes to the mass flux. At leading order $1/\hat{r}^2$, this component is

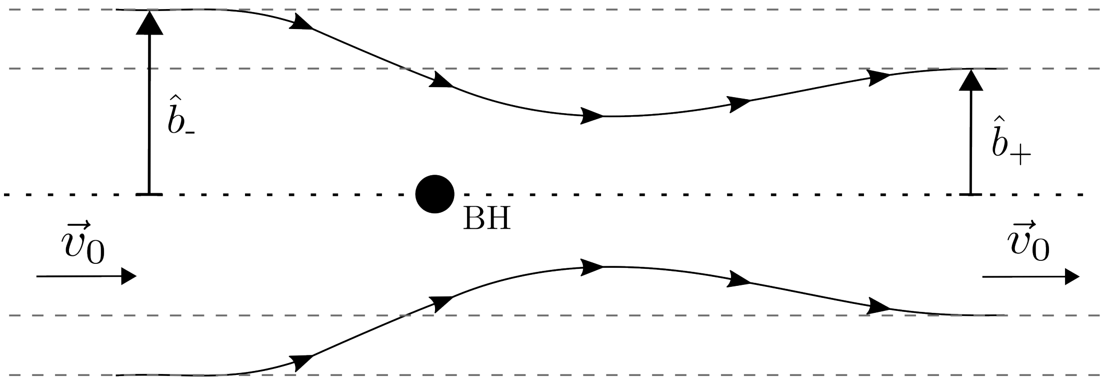

Figure 3.6: The axi-symmetric cylinder following the streamlines used for the computation of (3.62).

determined by the even series $b_{2\ell}$ in (3.51). Substituting these terms, the expression for the accretion rate becomes

$$\dot{M}_{\rm BH} = 4\pi \left[b_0 \left(\gamma - \frac{5}{3} v_0^2 \right) + b_2 \frac{8 v_0^2}{15} \right] , \tag{3.61}$$

which does not depend on the radius $\hat{r}$, as expected.

Alternatively, the accretion of mass by the black hole can be computed by following the scalar-field streamlines, similar to how the trajectories of free particles are tracked. However, unlike the free case, the streamlines in this scenario do not escape to $\hat{z} \to \infty$ with a non-zero deflection angle θ_∞. Due to the effective pressure generated by self-interactions, the flow remains smooth without shocks or caustics, as long as the subsonic regime is maintained. At large distances downstream, the velocity again becomes $\mathbf{v}_0$, and the streamlines align parallel to the z-axis. This behavior is depicted in the upper row of the velocity field shown in Figure 3.5. To calculate the mass loss, a closed surface $\hat{S}$ is chosen to be a cylinder with a varying transverse radius $\hat{b}(\hat{z})$ that follows the streamlines, as shown in Figure 3.6. The incoming impact parameter at $\hat{z}_- \to -\infty$ is denoted as $\hat{b}_-$, and the outgoing transverse radius at $\hat{z}_+ \to +\infty$ is denoted as $\hat{b}_+$. Due to the asymmetry caused by the mass loss into the black hole, the streamlines are not perfectly symmetric, and therefore, $\hat{b}_+ \neq \hat{b}_-$. The mass loss can then be expressed as

$$\dot{M}_{\rm BH} = 2\pi \int_0^{\hat{b}_-} d\hat{b}\, \hat{b}\, \hat{\rho} v_z |_{\hat{z}_-} - 2\pi \int_0^{\hat{b}_+} d\hat{b}\, \hat{b}\, \hat{\rho} v_z |_{\hat{z}_+} . \tag{3.62}$$

This is the difference between the upstream and downstream mass fluxes, as there is no mass flux through the transverse surface of the cylinder.

The streamlines $\hat{r}(\theta)$ can be obtained by integrating

$$\text{streamlines}: \quad \frac{d\hat{r}}{d\theta} = \frac{\hat{r} v_r}{v_\theta} , \tag{3.63}$$

or from the stream function Ψ defined by

$$\frac{\partial \Psi}{\partial \theta} = \rho r^2 \sin\theta\, v_r \quad \text{and} \quad \frac{\partial \Psi}{\partial r} = -\rho r \sin\theta\, v_\theta\,, \tag{3.64}$$

which ensures the continuity equation (3.21) is satisfied, as the streamlines correspond to curves of constant Ψ. Using the expansions (3.51), the large-distance expansions of the velocity and density fields, streamlines, and the stream function can be obtained. The expression for $\hat{r}(\theta)$ is

$$\hat{r}(\theta) = \frac{\hat{b}}{\sin\theta} - \frac{1}{\hat{b} v_0 \sin\theta} \sum_\ell b_{2\ell}(1+\cos\theta P_{2\ell}) + \dots\,, \tag{3.65}$$

where only the leading orders in the impact parameter $\hat{b}$ of the even and odd components of the streamlines are considered. The first term gives the leading order $\hat{r}\sin\theta = \hat{b}$, which corresponds to an even straight line of constant transverse radius $\hat{b}$ parallel to the z-axis when neglecting black hole gravity. The second term gives the first asymmetric contribution, which is a subleading correction. It is worth noting that the asymmetry only appears at the next subleading order, as the leading correction to the flow is even in $\hat{z} \leftrightarrow -\hat{z}$, as mentioned in section 3.5.2 and (3.52). The impact parameter upstream is $(\hat{r}\sin\theta)_{\hat{z}\to-\infty} = \hat{b}$, while the transverse radius downstream is given by

$$(\hat{r}\sin\theta)_{\hat{z}\to+\infty} = \hat{b} - \frac{2}{\hat{b} v_0} \sum_\ell b_{2\ell} + \mathcal{O}\left(\frac{1}{\hat{b}^2}\right)\,, \tag{3.66}$$

where the series in $b_{2\ell}$ can be expressed in terms of b_0 and b_2 using the explicit expression (3.46) and noticing that $\delta\hat{\beta}^{(1)}_{\text{even}}(\theta=0) = B = \sum_\ell b_{2\ell}$. This leads to the expression

$$B = \sum_\ell b_{2\ell} = \frac{b_0}{3}\frac{3\gamma - 5v_0^2}{\gamma - v_0^2} + \frac{4b_2}{15}\frac{2v_0^2}{\gamma - v_0^2}\,, \tag{3.67}$$

where the multiplying factors for b_0 and b_2 where calculated using (A.15). Additionally, using the explicit expression (3.46), b_0 and b_2 can be expressed in terms of B. For instance, b_0 can be written as

$$b_0 = B\frac{c_{s,0}}{2v_0}\ln\left(\frac{c_{s,0}+v_0}{c_{s,0}-v_0}\right) = B\left[1 + \frac{v_0^2}{3c_{s,0}^2} + \dots\right]\,. \tag{3.68}$$

Going back to the expression (3.62) for the accretion rate, we can choose the large-distance limit of the cylinder such that $|\hat{z}_\pm| \gg \hat{b}_\pm \gg \hat{r}_\gamma$. Then, the angles θ_- and θ_+ go to π and 0, the density and velocity go to $\hat{\rho}_0 = \gamma - v_0^2$ and $\mathbf{v}_0$, respectively. With these considerations, the expression for the accretion rate can be simplified

$$\dot{\hat{M}}_{\text{BH}} = \pi\hat{\rho}_0 v_0(\hat{b}_-^2 - \hat{b}_+^2) = 4\pi\hat{\rho}_0 \sum_\ell b_{2\ell} = 4\pi\hat{\rho}_0 B\,. \tag{3.69}$$

We used (3.66), to obtain the relationship between the upstream and downstream transverse radii $\hat{b}_{\pm}$, and the first equality in (3.67). As expected, using the second equality in (3.67) makes us recover (3.61).

The expression (3.69) gives the even component of the phase $\hat{\beta}_{\rm even}$ in terms of the black hole accretion rate, and B can be expressed as $B = \dot{\hat{M}}_{\rm BH}/(4\pi\hat{\rho}_0)$. The value of B is determined by the boundary conditions close to the black hole, specifically at the matching radius $r_{\rm m}$. This implies that the calculation performed to derive (3.69) remains valid when considering radial accretion at least up to the distance $r_{\rm m}$. In the subsonic regime, this condition is always satisfied. However, at supersonic velocities, it may not hold true in certain scenarios. Specifically, if a shock front, which typically arises in supersonic flows, is located sufficiently close to the black hole the accretion pattern can deviate from the radial case due to distinct behavior exhibited by particles in the upstream region. As described in section 3.3.1, at small radii, the flow is in the relativistic regime with a radial pattern, where the monopole radial velocity grows like $1/r$, while higher multipoles decrease. At the critical radius $r_{\rm c}$, the flow smoothly transitions from the low-velocity branch $v \ll k_+$ to the high-velocity branch $v \simeq k_+$. This transition also sets the critical value $F_{\rm c}$ of the scalar-field flux, which is regulated by the pressure associated with scalar self-interactions. This connection between the large-distance behavior (3.50) and the small-scale relativistic physics near the black hole horizon is established. By returning to physical coordinates, the flux obtained for the radial case is [190]

$$\dot{m}_{\rm BH} = 4\pi F_\star \frac{r_s^2 m^4}{\lambda_4} = 3\pi F_\star \rho_a r_s^2 \,, \tag{3.70}$$

where $F_\star \simeq 0.66$ is a numerical value obtained from the computation of the unique profile extending from the Schwarzschild radius to the outer static soliton.

Comparing (3.69) and (3.70), we find

$$\dot{m}_{\rm BH} = 4\pi\rho_0 r_s^2 B \quad \text{with} \quad B = F_\star \frac{3\rho_a}{4\rho_0} = \frac{F_\star}{k_0^2} \,, \tag{3.71}$$

where B is now expressed in terms of ρ_a and ρ_0. From (3.51), the monopole of the radial velocity at large distances is given by $v_{r_0} = -b_0 r_s^2/r^2$. Using (3.71) and (3.68), this expression agrees, in the limit $v_0 \to 0$, with the result $v_r = -F_\star m^4 r_s^2/(\lambda_4 \rho_0 r^2)$ obtained in [190] for the radial case.

As we focus on the subsonic case, $v_0 < c_{s,0} \ll 1$, ensuring that $v_0 \ll 1$, the flow becomes radial well before reaching the critical radius $r_{\rm c}$, and the self-regulated critical flux $F_{\rm c}$ is identical to the one obtained in the purely radial case. Thus, the accretion rate by the black hole is given by (3.70), which does not depend on v_0. However, the scalar-field flow at large radii does depend on v_0, including its monopole component, as seen from (3.68), which exhibits a singularity as $v_0 \to c_{s,0}$. As demonstrated in Figures 3.2 and 3.3, even at $v_0 = c_{s,0}/2$, the flow remains close to the linear flow (3.34), with only small nonlinear corrections. Numerical analysis confirms that the coefficient b_0 for the monopole of $\hat{\beta}$ in the large-distance regime agrees with the prediction (3.68)-(3.71).

3.6.2 . Comparison with previous works and other systems

The expression (3.70) implies

$$\dot{m}_{\rm BH} \sim \rho_0 r_s^2 / c_{s,0}^2 \sim \rho_0 \mathcal{G}^2 M_{\rm BH}^2 / c_{s,0}^2 \,. \tag{3.72}$$

This is different from the radial accretion of collisionless particles with an isotropic and mono-energetic distribution at the characteristic velocity $c_{s,0}$ [306]

$$\text{collisionless:} \quad \dot{m}_{\rm free} = \frac{16\pi\rho_0 \mathcal{G}^2 M_{\rm BH}^2}{c_{s,0}} \,. \tag{3.73}$$

It is also different from the classical radial Bondi accretion rate [300] for an isothermal gas, $\dot{m}_{\rm Bondi} \sim \rho_0 r_s^2 / c_{s,0}^3$, which also corresponds to the subsonic limit of the so-called "Bondi-Hoyle-Lyttleton accretion rate" [307, 308]

$$\text{Bondi-Hoyle:} \;\; \dot{m}_{\rm Bondi-Hoyle} = \frac{2\pi\rho_0 \mathcal{G}^2 M_{\rm BH}^2}{(c_{s,0}^2 + v_0^2)^{3/2}} . \tag{3.74}$$

The hydrodynamical accretion rate (3.74) is much greater than the collisionless accretion rate (3.73), by a factor $(1/c_{s,0})^2 \sim 10^6$. This is because collisions restrict tangential motion and funnel particles in the radial direction [306]. The scalar-field accretion rate is in-between these two cases. As expected, for the same hydrodynamical reason, it is higher than the free rate, as the flow is more efficiently converted into a radial pattern at small radii, but now by a factor $1/c_{s,0} \gg 1$. However, it is much smaller than the accretion rate of the perfect gas rate, by a factor $c_{s,0} \ll 1$. Thus, the scalar-field self-interactions are much more efficient in resisting the black hole gravity and slowing down the infall. This is because the scalar field has a different equation of state and deviates from a perfect gas in the relativistic regime, which sets the critical flux $F_{\rm c}$ and the normalization of the global profile [190]. This agrees with the fact that for a perfect gas with an adiabatic index $\gamma_{\rm ad} > 5/3$, there is no Newtonian steady transonic solution, but one exists in General Relativity [305, 306]. This again shows the critical role of relativistic effects at small radii for steep equations of state.

The expression (3.70) can be understood in simple terms. It means that close to the black hole horizon r_s, where the infall velocity is close to the speed of light, the scalar density is of the order of ρ_a, as can be checked by an explicit computation of the scalar profile (see [190] and (2.45)). From (2.6), this is the density where the self-interaction potential $\Phi_{\rm I}$ is of order unity, and the self-interaction term $V_{\rm I} = \lambda_4 \phi^4 / 4$ is of the order of the mass term $m^2 \phi^2 / 2$. This characteristic density provides an upper bound on ρ, and hence on the accretion rate, as the infall velocity cannot be greater than the speed of light.

3.7 . Drag force

3.7.1 . Relationship with large-radius expansions

As the black hole moves through the scalar-field cloud, it is slowed down by a drag force. By symmetry, this force $\mathbf{F} = F_z \mathbf{e}_z$ is directed along the z-axis. As sketched in Figure 3.7, let us consider an open subsystem formed by the black hole and the scalar field inside a surface S_{in} that encloses the black hole, far enough from the horizon for Newtonian dynamics to hold but close enough for its mass M to be dominated by the black hole mass M_{BH}. The surface $S_{\text{in}} = \partial V_{\text{in}}$ bounds a volume V_{in}. Outside this volume, the scalar cloud extends up to the soliton radius R_{sol} at a much greater distance. This defines the outer volume V_{out}. Going back to physical coordinates, the change of momentum of this subsystem, of volume V_{in}, reads

$$\frac{dp_z}{dt} = \mathcal{G} M_{\text{BH}} \int_{V_{\text{out}}} d\mathbf{r} \rho(\mathbf{r}) \frac{\mathbf{r} \cdot \mathbf{e}_z}{r^3} - \int_{\partial V_{\text{in}}} \mathbf{dS} \cdot P \mathbf{e}_z - \int_{\partial V_{\text{in}}} \mathbf{dS} \cdot \rho \mathbf{v} v_z \, . \tag{3.75}$$

The first term, integrated over the volume V_{out} of the scalar cloud, is the usual dynamical friction term due to the gravitational wake [309]. It represents the gravitational pull from the scalar-field overdensity generated behind the black hole through the deflection of the streamlines under the black hole gravity. The second term, which is absent in collisionless media such as the stellar cloud considered by Chandrasekhar's classical study [60], is the pressure exerted by the outer cloud on the subsystem. The third term is the contribution of the momentum flux through the surface S_{in}. This term is clearly related to the local influx of matter and therefore the infall of mass into the black hole, i.e., accretion. However, it vanishes if the flow is radial close to the black hole.

In the limit of an infinite constant-density scalar cloud, the first gravitational term suffers from the same divergence as the Newtonian gravitational force in an infinite homogeneous universe, associated with the so-called "Jeans swindle". To address this, it is common to integrate first over angles or regularize Newtonian gravity with a damping factor $e^{-\kappa|\mathbf{r}-\mathbf{r}'|}$ and then take the limit $\kappa \to 0$ at the end of the computations [310]. This implies that a constant-density background does not contribute, and only the asymmetry of the perturbed scalar density field contributes, associated with the wake behind the black hole.

By considering the surface S_{in} as the inner boundary of the outer volume V_{out} (which changes the sign of $\mathbf{dS}$) and introducing the external surface S_{out} of the scalar cloud itself, we can express the pressure term as

$$-\int_{\partial V_{\text{in}}} \mathbf{dS} \cdot P \mathbf{e}_z = \int_{\partial V_{\text{out}}} \mathbf{dS} \cdot P \mathbf{e}_z - \int_{S_{\text{out}}} \mathbf{dS} \cdot P \mathbf{e}_z = \int_{V_{\text{out}}} d\mathbf{r} \frac{\partial P}{\partial z} - \int_{S_{\text{out}}} \mathbf{dS} \cdot P \mathbf{e}_z \, , \tag{3.76}$$

where we used the divergence theorem in the right-hand terms. If the scalar cloud is isolated in vacuum, the pressure term vanishes at the cloud boundary. However, this is not the case if we choose a surface S_{out} that is inside the scalar cloud but large enough for the drag force to have converged. Noticing that the first term in (3.75) is also the opposite of the gravitational attraction by the black hole of the outer scalar cloud, we obtain

$$\frac{dp_z}{dt} = \int_{V_{\text{out}}} d\mathbf{r} \left[\rho \frac{\partial \Phi_{\text{BH}}}{\partial z} + \frac{\partial P}{\partial z} \right] - \int_{S_{\text{out}}} \mathbf{dS} \cdot P \mathbf{e}_z - \int_{\partial V_{\text{in}}} \mathbf{dS} \cdot \rho \mathbf{v} v_z . \tag{3.77}$$

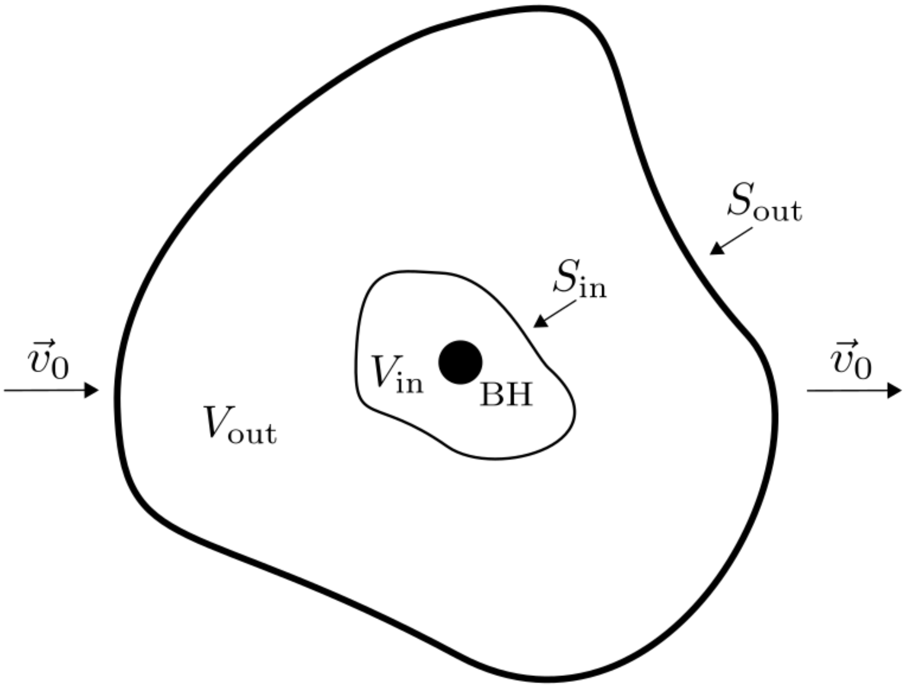

Figure 3.7: Inner and outer surfaces used in (3.75).

Far inside the soliton boundary, the steady-state Euler equation associated with the continuity and Bernoulli equations (3.21) reads

$$\nabla \cdot (\rho \mathbf{v} v_z) = \rho \mathbf{v} \cdot \nabla v_z = -\rho \frac{\partial \Phi_{\rm BH}}{\partial z} - \frac{\partial P}{\partial z} \, . \tag{3.78}$$

Substituting this into (3.77), we obtain the drag force on the black hole as

$$F_z = \frac{dp_z}{dt} = -\int_{S_{\rm out}} \mathbf{dS} \cdot \rho \mathbf{v} v_z - \int_{S_{\rm out}} \mathbf{dS} \cdot P \mathbf{e}_z \, . \tag{3.79}$$

This expression no longer depends on the inner surface $S_{\rm in}$ or the bulk of the volume $V_{\rm out}$. Therefore, we can shrink the inner surface $S_{\rm in}$ towards the black hole. The first term in (3.79) expresses the conservation of momentum as for collisionless systems: in the steady state, the momentum that enters the external boundary $S_{\rm out}$ is equal to the gain of momentum of the black hole (similar to (3.59), where the accretion of mass by the black hole is equal to the mass inflow through any enclosing surface S). The second term takes into account the impact of the pressure when the surface $S_{\rm out}$ is taken within the soliton cloud. The clear interpretation of (3.79) means that it could have been used at once as the definition of the net drag force in a steady state, as in [277] for the case of the isothermal gas. The interest of the derivation above is to clarify its link with the expression (3.75), which contains the more familiar gravitational wake term associated with the usual meaning of dynamical friction in the case of free particles.

3.7.2 . Relationship with the accretion rate

Regarding the black hole accretion rate, we can observe that the drag force converges to a finite value that does not depend on the shape of the surface $S_{\rm out}$ in the large-distance limit. By choosing a distant sphere centered on the black hole as the surface $S_{\rm out}$, as shown in the upper panel of Figure. 3.6, in dimensionless variables, we obtain the monopole contribution $\hat{F}_z = -4\pi\hat{r}^2(\hat{\rho}v_r v_z + \cos\theta\hat{P})_{\ell=0}$. At large radius r, using the large-distance expansions derived from (3.51), the factors $\hat{r}$ cancel out as expected, and we obtain $\hat{F}_z = v_0\hat{\dot{M}}_{\rm BH}$, where $\hat{\dot{M}}_{\rm BH}$ is the black hole accretion rate obtained in (3.61). Alternatively, choosing the elongated cylinder that follows the streamlines as the surface $S_{\rm out}$, as done in the computation (3.62) and shown in the lower panel of Figure 3.6, we find that the first term in (3.79) gives $\hat{F}_z = \pi\hat{\rho}_0 v_0^2(\hat{b}_-^2 - \hat{b}_+^2) = v_0\hat{\dot{M}}_{\rm BH}$. An explicit computation using the expansions derived from (3.51) shows that the pressure integral of the second term vanishes as $1/b$. Thus, both computations yield the same result

$$F_z = \dot{M}_{\rm BH} v_0 \, . \tag{3.80}$$

Hence, the drag force can be expressed as the product of the accretion rate and the relative velocity, while the conventional dynamical friction vanishes. This is because, similar to a gas in the subsonic regime, the medium has sufficient time to adjust and accommodate the presence of the black hole. This holds true only when the relative velocity between the black hole and the medium is lower than the speed of sound as will be discussed in chapter 4. However, the situation differs for collisionless particles or fuzzy dark matter, as they do not interact through collisions or direct interactions (in the case of fuzzy dark matter, quantum pressure does not exert an effective pressure that would lead to collisions and consequently dark matter remains relatively "free" in this scenario). Instead, their gravitational interactions dominate. Consequently, dynamical friction can be significant even in the subsonic regime for these particles, as the absence of collisions allows them to maintain their gravitational influence, resulting in the persistence of dynamical friction. Using (3.72), we can approximate the drag force as

$$F_z \sim \rho_0 r_s^2 v_0 / c_{\rm s}^2 \sim \mathcal{G}^2 M_{\rm BH}^2 \rho_0 v_0 / c_{s,0}^2 \, . \tag{3.81}$$

The numerical computation of the scalar-field profile is consistent with the prediction (3.80). As explained in section 3.3.1, the scalar-field cloud is matched to the radial flow at the matching radius $r_{\rm m}$, slightly beyond the critical radius $r_{\rm c}$ associated with the transition from the low-velocity to the high-velocity branch. By choosing the sphere of radius $r_{\rm m}$ as the inner surface $S_{\rm in}$, the second and third terms of (3.75) vanish due to symmetry. The first gravitational term is given by $(4\pi/3)\mathcal{G}M_{\rm BH}\int_{r_{\rm m}}^{\infty} dr\rho_{\ell=1}$, representing the dipole of the scalar-cloud density field. The unperturbed background does not contribute, and the density decays as $1/r^2$ at large distances, as seen in (3.54) and Figure 3.4. The numerical computation agrees with (3.80).

3.7.3 . Comparison with previous works and other systems

In the literature, there can be some confusion regarding the net drag force and the dynamical friction. In the collisionless case, as described in Chandrasekhar's classical work [60], the dynamical friction arises from the long-range gravitational interaction between the perturber (in this case, the black hole) and the distant stars of the stellar cloud. The summation of the velocity changes experienced during these distant encounters leads to the well-known result (3.83), which is recalled below. This corresponds to the first term in (3.75). An alternative approach is to compute the perturbation to the steady-state distribution of the stars caused by the perturber [309]. By bending the trajectories of the distant stars, the perturber generates a gravitational wake behind it. The overdensity in this wake is responsible for the deceleration of the perturber [62]. Computing the gravitational pull from this overdense wake reproduces Chandrasekhar's result. This corresponds to the first term in (3.75). Another source of momentum exchange arises when there is accretion onto the perturber, whether it is a black hole or a massive star. This additional source is associated with the momentum deposited by the accreted material and is sometimes referred to as "capture drag" or "accretion drag" force. In some studies, these two sources of momentum exchange are estimated separately and found to be of the same order, typically given by the Chandrasekhar's expression (3.83), and both contributions are either added or the latter formula is used alone. However, naive estimates can lead to confusion and result in double counting.

In our explicit computation (3.80), we find that the net drag force is actually equal to a naive estimate of the momentum exchange associated with accretion. This raises the question of where the contribution associated with the long-range gravitational interaction has gone. Furthermore, we observe that the contribution from the long-range gravitational interaction, given by the first term in (3.75), is nearly equal to (3.80). The explanation becomes clear when examining (3.75), where the first term represents the dynamical friction associated with the long-range gravitational interaction, and the third term represents the deposited momentum. However, the magnitude of the deposited momentum is much smaller than the naive estimate $\dot{M}_{\mathrm{BH}} v_0$ because matter falls nearly radially onto the black hole near the horizon due to the gravitational interaction that bends the flow (combined with fluid pressure). Therefore, it is not possible to separate both effects. Fortunately, (3.79) provides a simple expression for the net drag force that does not require the separation of gravitational friction and accretion drag. Hence, we prefer to use the term "net drag force" to describe the total force experienced by the black hole, which is the relevant quantity for practical purposes. One advantage of the expression (3.79) is that it allows us to obtain the analytical result (3.80) by leveraging the relationship with the large-distance expansions. This is particularly useful as accretion rates and drag forces can be challenging to compute accurately through numerical simulations, which may vary by factors of a few or more depending on the numerical scheme [305]. Another crucial point is that this expression enables us to understand the drag force from the perspective of an effective theory. By performing the integral at large distances while accounting for all the nonlinear and relativistic effects near the Schwarzschild radius, we can determine the values of the accretion rate and drag force, as explained in section 3.3.1 and (3.54) and

(3.71).

As mentioned in previous sections, the relationship (3.80) explicitly shows that the drag force diminishes as the accretion rate approaches zero. The dynamical friction being null, the drag force is only due to the accretion drag. In this scenario, the potential flow exhibits symmetry with respect to the $\hat{z} = 0$ plane, resulting in no net force along the $\hat{z}$ axis. This observation aligns with the hydrodynamical analogy derived in section 3.4.2 for nonrelativistic subsonic motion of a star in an isothermal gas without accretion, as demonstrated by linear steady-state analysis [266, 268, 269]. However, our result (3.80) does not rely on a linear treatment. Instead, it utilizes Gauss's theorem to express the total drag force in terms of the asymptotic behavior of the fields at large distances (3.79). This formulation simply reflects the conservation of mass and momentum in a steady state. Moreover, the accretion rate itself (3.70) involves a fully nonlinear and relativistic treatment that spans from large radii down to the Schwarzschild radius [190].

When the accretion rate is non-zero, the drag force no longer vanishes. This is because the accretion onto the black hole, accompanied by a radial inward velocity flow near the black hole horizon, breaks the symmetry with respect to the $\hat{z} = 0$ plane. This asymmetry is evident from the presence of a turning point $r_{\rm turn}$ slightly behind the black hole, associated with a local maximum of the dark matter density field in the wake. A similar relationship between accretion and the drag force, as given in (3.80), was found in [277] for a black hole moving in an isothermal gas. The proportionality to $\dot{m}_{\rm BH}$ is not surprising since the dynamical friction in a perfect fluid without accretion vanishes, and the relationship's form could be anticipated through dimensional analysis. However, the coefficient being unity is not evident a priori (in the extreme case of free particles, as mentioned in (3.84) below, the drag force is non-zero even in the absence of accretion). Despite this formal similarity to the perfect gas case, as indicated in (3.72), the accretion rate for the scalar field is much smaller compared to the isothermal gas case. Consequently, the drag force is also significantly reduced. In the case of the isothermal gas, [277] obtains

$$\text{Subsonic perfect gas:} \quad F_{\rm perfect\ gas} = \dot{m}_{\rm BH} v_0 \sim \mathcal{G}^2 m_{\rm BH}^2 \rho_0 v_0 / c_{s,0}^3 \,, \tag{3.82}$$

and we find that both the accretion rate and the accretion drag are smaller for the scalar field dark matter by a factor $c_{s,0} \ll 1$, as shown in our result (3.81). The result (3.82) was also obtained by [269] using linear theory, without accretion but considering finite-time effects. It is consistent with hydrodynamic simulations [311]. The accretion drag force exhibits a similar behavior in the case of collisionless particles and fuzzy dark matter. It is proportional to the accretion rate multiplied by the velocity in both scenarios.

Now, we will compare the null dynamical friction we found in the subsonic regime with other established research findings. Our dynamical friction significantly differs from the one obtained by Chandrasekhar [60] for free particles, which has been confirmed by numerical simulations [61, 62]

$$\text{Collisionless:} \quad F_{\rm free} \simeq 16\pi^2 C \mathcal{G}^2 m_{\rm BH}^2 \rho_0 / v_0^2 \int_0^{v_0} dv\, v^2 f(v) \,, \tag{3.83}$$

where the particle velocity distribution $f(\mathbf{v})$ is normalized to unity and assumed to be isotropic. Here, C represents the Coulomb logarithm $C \approx \ln(b_{\rm max}/b_{\rm min})$, with $b_{\rm min} \sim \mathcal{G} m_{\rm BH}/v_0^2$ and $b_{\rm max}$ is an infrared cutoff on the impact parameter $b_{\rm max}$, typically taken as the size of the cloud. For a relative velocity v_0 smaller than the stellar cloud velocity dispersion $c_{s,0}$, the expression becomes

$$v_0 < c_{s,0}: \quad F_{\rm free} \sim C\mathcal{G}^2 m_{\rm BH}^2 \rho_0 v_0 / c_{s,0}^3 \,. \tag{3.84}$$

Another notable scalar-field scenario is the fuzzy dark matter model [133], where the self-interactions are negligible, but the de Broglie wavelength is significantly large. This choice corresponds to a scalar mass of approximately 10^{-22} eV, allowing for wavelike effects to extend up to galactic scales and potentially mitigate small-scale tensions present in the cold dark matter framework. In the model, the dynamical friction in the presence of an $1/r$ potential [312], corresponding to Coulomb scattering of a plane wave by the external Newtonian gravity of the black hole black hole, has been studied by [63]. As in our case, the calculations are performed in a reference frame where the test object, here a black hole $m_{\rm BH}$, is stationary at the origin while the dark matter fluid flows past with velocity v and uniform density ρ before perturbation by the test object. The gravitational interaction between the dark matter and the test object is considered, while self-gravity of the dark matter is neglected for simplicity. The time-independent Schrödinger equation for the wavefunction ψ has a solution in terms of a confluent hypergeometric function $M[a, b, z]$. The wavefunction depends on the coordinate z parallel to the velocity, the associated momentum $k = m_{\rm DM} v$, and the radial distance r from the point mass as $\psi = \mathcal{R} e^{ikz} M[i\beta, 1, ik(r - z)]$. The dimensionless parameter β, defined as $\beta = \mathcal{G} m_{\rm BH} m_{\rm dm}^2/k$, is introduced. It represents the ratio of the characteristic length scale to the de Broglie wavelength. The regime of interest is $\beta \gg 1$. The dynamical friction force is then obtained by integrating the momentum flux density tensor of the fluid over a surface, resulting in a surface integral of the form $F_{\rm FDM} = \oint \rho\, \partial\Phi_{\rm N}/\partial z\, dr$ when considering a steady-state system, where $\Phi_{\rm N}$ is the gravitational potential and $\rho = |\psi|^2$. Finally, the dynamical friction can be expressed as

$$\text{FDM:} \quad F_{\rm FDM} \sim \frac{\mathcal{G}^2 m_{\rm BH}^2 \rho_0}{v_0^2} C(\beta, kR)\,, \tag{3.85}$$

where R denotes the size of the scalar cloud, and $C(\beta, kR)$ is a function involving confluent hypergeometric functions. Assuming the size of the soliton is much larger than the self-gravity radius $r_{\rm sg}$, typically, we have $\beta \ll 1$ and $kR \lesssim 1$ in the subsonic regime considered in this paper. In this limit, [63] finds that $C \sim (kR)^2$, leading to the following expression for the dynamical friction

$$\frac{r_{\rm sg}}{R} c_{s,0} \ll v_0 < c_{s,0}: \quad F_{\rm FDM} \sim \frac{\mathcal{G}^2 m_{\rm BH}^2 \rho_0}{c_{s,0}^2}\,, \tag{3.86}$$

where $c_{s,0}$ is a velocity scale defined as $c_{s,0}^2 = |\Phi_{\rm N}|$ (analogous to the virial velocity in a classical system). This result is also supported by related studies [64, 65]. Comparing this expression (3.86) with the classical result (3.84) obtained from Chandrasekhar's formula, we observe that the dynamical friction for fuzzy dark matter is larger by a factor of

$c_{s,0}/v_0 > 1$. Unlike the classical result, the fuzzy dark matter case does not involve an integration over a distribution function $f(v)$ with a cutoff at v_0, representing the exclusion of higher-velocity stars contributing to the dynamical friction. Within the soliton, which acts as a coherent state with a vanishing phase, all scalar-cloud velocities are zero (similar to a Bose-Einstein condensate) and below the black hole velocity v_0. However, there is still a milder cutoff proportional to $(kR)^2 \propto (v_0/c_{s,0})^2$, resulting in the aforementioned expression (3.86), which is related to the number of available modes in the vibration spectrum of the scalar field. The expression (3.86) aligns with the findings of [270] (based on a different approach, their equation (4.12), considering the scalar cloud radius comparable to the Jeans length) and [176] employing a hydrodynamical approach that also incorporates weak quartic self-interactions). It also roughly agrees with numerical simulations [272]. Thus, we conclude that scalar field dark matter with self-interactions results in a smaller dynamical friction compared to fuzzy dark matter, by a factor of $v_0 \ll 1$. If the size of the fuzzy dark matter cloud is significantly greater than the de Broglie wavelength ($kR \gg 1$), the classical scaling (3.84) is recovered [40]. In this case, the scalar field behaves like a collection of particles with a size of λ_{dB}.

It is important to note that the result (3.85) was derived using linear perturbation theory and Newtonian gravity [63, 64], but it is expected to be a reasonable approximation for fuzzy dark matter as long as the Compton wavelength of the scalar cloud is much greater than the black hole horizon, see also [275]. Additionally, the large-mass limit examined in this paper assumes $1/m_{\mathrm{DM}} \ll r_s$. In contrast, our result (3.81), obtained for the motion of a black hole within the scalar cloud, incorporates fully nonlinear and relativistic effects near the Schwarzschild radius, which determine the accretion rate and drag force. Hence, we are exploring different systems and regimes in our study. In our case, the self-interactions dominate over quantum pressure, and the Compton wavelength $1/m_{\mathrm{DM}}$ is much smaller than all astrophysical scales, including the size of the scalar cloud and the black hole horizon.

3.8 . Summary of the chapter

In the chapter, the focus was on the subsonic regime, where the relative velocity between the compact object (Schwarzschild black hole) and the scalar-field dark matter soliton is smaller than the speed of sound. We examined the flow of dark matter in this regime for a system with a quartic self-interacting potential. In the nonrelativistic regime, it is found that the dark matter behaves as an isentropic potential flow with a polytropic index of $\gamma_{\mathrm{ad}} = 2$. This behavior indicates the collective effects associated with the self-interactions, and the system in the subsonic regime resembles a perfect gas more than a collection of individual particles. The flow in the low-velocity regime remains close to a simple linear approximation, described by a monopole (determined by radial accretion at the Schwarzschild radius) and a dipole (resulting from uniform flow at large distances). The nonlinear equations of motion are solved beyond this linear approximation using an iterative numerical scheme. Large-distance expansions up to subleading order are derived, providing explicit results for the accretion by the black hole and its dynamical friction. The nonlinear and relativistic effects near the black hole horizon are taken into account, as they play a crucial role in the analysis.

In comparison to a perfect gas, the accretion rate in the self-interacting scalar field dark matter scenario is much smaller, by a factor of $c_{s,0} \ll 1$. This is because the scalar field departs from a perfect gas in the relativistic regime, and the accretion rate is determined by the large-field regime close to the Schwarzschild radius, where the self-interactions significantly slow down the infall. The relationship between the accretion rate and the drag force ($F_z = \dot{m}_{\rm BH} v_0$) is recovered. However, unlike collisionless particles and fuzzy dark matter, but similar to a perfect gas, the dynamical friction in our case is nonexistent in the subsonic regime.

The presence of self-interacting scalar field dark matter with reduced drag force can have significant implications for various astrophysical phenomena. One such implication is the potential decrease in the dephasing of the emission frequency of gravitational waves compared to fuzzy dark matter and cold dark matter. This effect could be relevant to addressing the Fornax globular cluster timing problem if the system is influenced by the reduced drag force [313]. However, it is important to note that the analysis presented in this study specifically applies to the case of a black hole with its boundary condition at the Schwarzschild radius. In the case of globular clusters and stellar objects with negligible accretion, the leading-order result predicts zero drag force, as observed in the subsonic regime for perfect fluids [269]. Nonetheless, a more accurate treatment that considers the perturbation to the fluid self-gravity is expected to reveal a small but nonzero dynamical friction, as demonstrated by [270].

4 - Supersonic accretion and dynamical friction for a moving black hole

In this Chapter, we investigate the influence of a cloud of self-interacting dark matter on the accretion rate and dynamical friction experienced by a black hole. Building upon the exploration of the subsonic regime of the chapter 3 , we now delve into the supersonic regime. We reveal that the velocity flow exhibits a more intricate behavior than in the subsonic case. The presence of a shock front, induced by the transonic solution, necessitates a differentiated treatment of the upstream and downstream regions. We examine this phenomenon and elucidate the associated boundary conditions at the shock front. With the foundations laid, we proceed to quantify the mass accretion and dynamical friction of the black hole within the self-interacting system. Our analysis reveals similarities to the Chandrasekhar's result [60], suggesting that our framework effectively captures the essential dynamics of the system. This chapter is based on the paper "*Supersonic accretion and dynamical friction for a black hole moving through a self-interacting scalar field dark matter cloud*" [2].

4.1 . Description of the non-linear velocity flow

4.1.1 . Supersonic regime

In the context of hydrodynamical flows around moving bodies, such as airplanes, the behavior of acoustic waves depends on the velocity of the body. In the subsonic regime studied in chapter 3, where the velocity of the body is lower than the speed of sound, acoustic waves can propagate to all points in space after a long time, reaching a steady state. This means that the fluid at any point adapts to the presence of the moving body, and the flow is smooth, determined by the boundary conditions at infinity and at the surface of the body (in this case, the Schwarzschild radius).

At supersonic velocities, however, acoustic waves cannot catch up with the speed of the body. Instead, they are pushed downstream, confined within the Mach cone. As a result, the flow upstream remains unperturbed or at rest, and the matching to the boundary conditions on the surface of the body is facilitated by the formation of a shock wave originating at the front tip of the body or slightly before it. The shock discontinuity enables the flow to transition to a new pattern downstream, which can then satisfy the boundary conditions on the body's surface. In the case of a black hole moving at supersonic speeds within a dark matter cloud, a similar behavior arises. However, an additional complication appears due to the presence of nonlinear effects and boundary layers on both sides of the shock. Consequently, it is not possible to apply perturbative treatments as in chapter 3 on both sides of the shock and impose junction conditions on the shock itself. In the supersonic regime, a more intricate analysis is required, involving the division of the large-distance expansions into four distinct domains:

- The upstream region located far before the shock.
- The boundary layer situated just before the shock.
- The boundary layer positioned just after the shock.
- The downstream region far behind the shock.

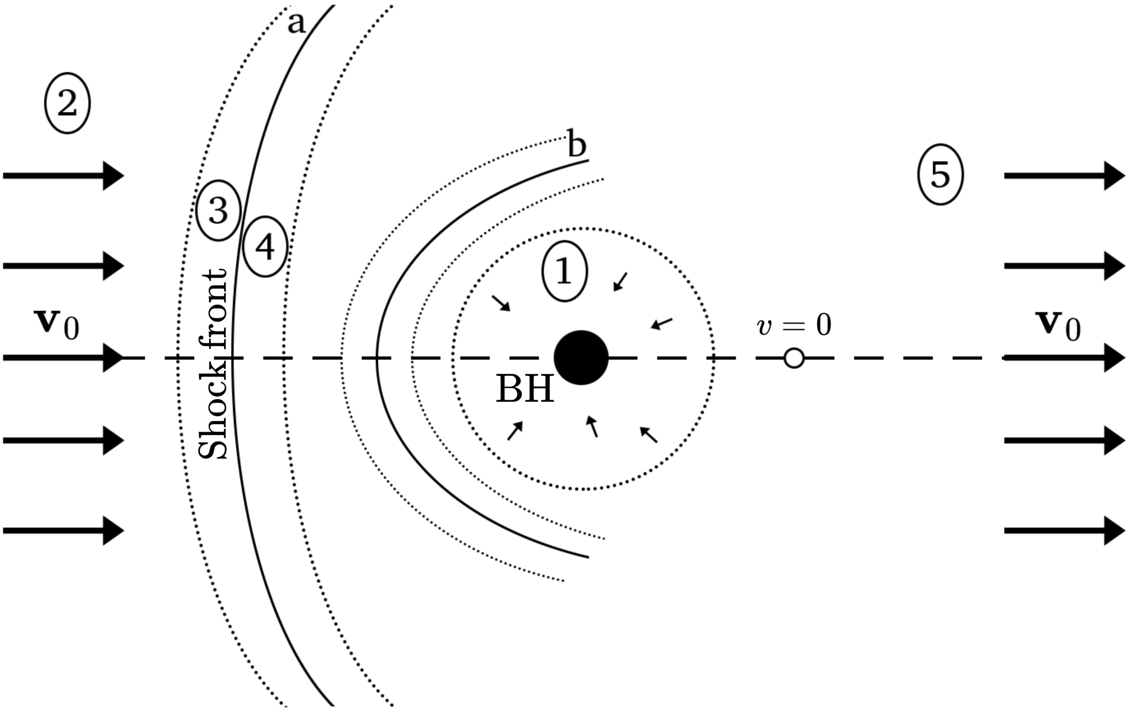

Figure 4.1: Schematic illustration of the investigated system, showcasing the motion of dark matter with an initial velocity $\boldsymbol{v}_0$ (at $z \to -\infty$) towards a black hole. Two shock fronts are depicted as solid lines: (a) represents a small initial supersonic velocity $v_0 \simeq c_{s,0}$, while (b) corresponds to a somewhat larger initial supersonic velocity $v_0 \gg c_{s,0}$ but for which we can still consider radial accretion close to the black hole ($v_0 < c_{s,0}^{2/3}/(3F_\star)^{1/3}$). The nomenclature used is valid for both (a) and (b). Region (1) indicates the radial accretion zone of the black hole. Then, for the case (a): Region (2) indicates the upstream region located far ahead of the shock. Region (3) corresponds to the upstream region in close proximity to the shock (upstream boundary layer). Region (4) represents the downstream region near the shock (downstream boundary layer). Region (5) denotes the downstream region situated far beyond the shock. The empty circle positioned behind the black hole represents a point of zero velocity.

The far upstream and downstream regimes can still be studied using large-distance expansions similar to the one in chapter 3. This approach allows for a standard perturbative treatment, where each order $\hat{\beta}_n$ satisfies a linear differential equation with a right-hand side that depends on the lower-order terms $\hat{\beta}_m$ with $m < n$. However, the functions $\hat{\beta}_n$ take different forms in the upstream and downstream regions and may include logarithmic contributions involving $\ln(\hat{r})$. The presence of boundary layers necessitates new expansions that account for nonlinear effects. The complete solution requires the matching of these four regions. This matching process involves two asymptotic matchings: one between each boundary layer and either the upstream or downstream bulk flow, and another junction condition along the shock between the two boundary layers. Additionally, the solution must be matched with the uniform velocity v_0 at infinity, and the location of the shock must be determined. The matching to the radial inflow at the Schwarzschild radius naturally emerges as a constant of integration. The problem is depicted in Figure 4.1 for visual representation.

4.1.2 . Upstream region

Unlike the subsonic case, where we deal with a boundary-value problem, in the supersonic regime, we encounter a Cauchy problem. This means that instead of specifying boundary conditions, we have an initial condition upstream at $\hat{z} \to -\infty$. Expanding (3.20) over $1/\hat{r}$ and collecting the leading-order terms of order $1/\hat{r}^2$ as in (3.41) for the subsonic regime, the equation of motion now takes the form of a wave equation

$$\frac{\partial^2 \hat{\beta}_0}{\partial x^2} + \frac{\partial^2 \hat{\beta}_0}{\partial y^2} - \frac{1}{c_z^2} \frac{\partial^2 \hat{\beta}_0}{\partial z^2} = \frac{v_0 u}{\rho_0} \frac{1}{\hat{r}^2} \,, \tag{4.1}$$

where we use the notation c_z to represent the propagation speed and introduced $u = \cos(\theta)$. The parameter v_0 is chosen such that $v_0 > c_{s,0}$, with

$$\frac{1}{c_z^2} = \frac{v_0^2}{c_{s,0}^2} - 1 \,, \quad c_z > 0 \,. \tag{4.2}$$

In the far region away from the boundary layer, the flow remains smooth, allowing us to employ a large-distance expansion as in chapter 3. However, we will observe that the terms $\hat{\beta}_n$ may include logarithmic factors $\ln(\hat{r})$.

Let us consider the case of large velocities v_0, where the effective pressure in the soliton becomes negligible, and we expect to recover the collisionless case. To find a solution at first order, we assume the form

$$\hat{\beta}_0 = a \ln(\hat{r}) + f_0(u) \,, \tag{4.3}$$

where a is a parameter to be determined. Substituting this into (3.20) and collecting the terms of order $1/\hat{r}^2$, we obtain the differential equation

$$(1-u^2)\left[(1+c_z^2)u^2 - 1\right] f_0'' + u\left[3 + c_z^2 - 3(1+c_z^2)u^2\right] f_0' = 1 + \frac{c_z^2}{2v_0 u} + a\left[1 - 2(1+c_z^2)u^2\right] \,, \tag{4.4}$$

which is a first-order equation over f_0'. The general solution is given by

$$f_0' = \frac{1 - 2v_0 a u^2}{2v_0(1-u^2)} + \frac{b}{(1-u^2)\sqrt{(1+c_z^2)u^2 - 1}} \,, \tag{4.5}$$

where b is an integration constant.

To avoid an unphysical singularity at the upstream Mach cone $\theta = \pi - \theta_c$, the constant b must be zero. Defining the Mach angle θ_c by $0 < \theta_c < \pi/2$ as $\sin(\theta_c) = c_z/\sqrt{1 + c_z^2} = c_{s,0}(t)/v_0 = 1/\mathcal{M}$, where $\mathcal{M}$ is the Mach number and $c_s = \rho/\rho_a$ is the local speed of sound (not to confuse it with the constant speed of sound at bulk density $c_{s,0} = \rho_0/\rho_a$), we have $u_c = \cos(\theta_c) = 1/\sqrt{1 + c_z^2}$, and $\tan(\theta_c) = c_z$. The singular behavior of the second term in (4.5) occurs on the upstream and downstream Mach cones $\theta = \pi - \theta_c$ and $\theta = \theta_c$. To avoid an upstream singularity at $\pi - \theta_c$, we must have $a = -1/(2v_0)$. This nonzero value for a indicates that the logarithmic term a $\ln(\hat{r})$ cannot be ignored. Therefore, we find

$$f_0'(u) = \frac{1}{2v_0(1-u)}, \quad f_0(u) = -\frac{\ln(1-u)}{2v_0}. \tag{4.6}$$

Here, we disregard the integration constant in f_0, as it only affects the constant of integration in the velocity potential $\hat{\beta}$, which plays no role in the equations of motion. This yields the upstream solution

$$\hat{\beta}_0 = -\frac{\ln(\hat{r}(1-u))}{2v_0}, \tag{4.7}$$

and the velocity components at first order are

$$v_{r,1} = -\frac{1}{2v_0\hat{r}}, \quad v_{\theta,1} = -\frac{1+u}{2v_0\hat{r}\sqrt{1-u^2}}, \quad v_1^2 = \frac{1}{\hat{r}^2}, \quad \rho_1 = 0. \tag{4.8}$$

Therefore, at this first order, we recover the long-distance solution of the collisionless case. This is because, at this order, the density is not modified by the deflection of the particle trajectories by the black hole, resulting in $\rho_1 = 0$. In this case, there are no pressure effects due to the absence of density gradients.

Unlike the subsonic case, the solution (4.7) is neither odd nor even. This is due to the logarithmic term introducing the factor au in (4.5). Physically, this loss of parity is manifested by the bow shock, which breaks parity. This behavior is also related to the hyperbolic nature of the equation of motion (4.7), which distinguishes between the limits $\hat{z} \to \pm\infty$, with the far upstream region $\hat{z} \to -\infty$ associated with the initial condition of the Cauchy problem. Two other differences from the subsonic case, where $v_{r,1} = 0$ and $v_{\theta,1} > 0$, are that we now have $v_{r,1} < 0$ and $v_{\theta,1} < 0$. In the supersonic case, the dominant gravitational effect of the black hole accelerates the dark matter fluid, with $v^2 > v_0^2$.

Let us now examine the second-order correction $\hat{\beta}_1$, which is of order $1/\hat{r}$, obtained by collecting the terms of order $1/\hat{r}^3$ in (3.20) and using the expression (4.7) for the first-order term $\hat{\beta}_0$. This gives the linear differential equation

$$\frac{\partial^2 \hat{\beta}_1}{\partial x^2} + \frac{\partial^2 \hat{\beta}_1}{\partial y^2} - \frac{1}{c_z^2}\frac{\partial^2 \hat{\beta}_1}{\partial z^2} = \frac{1}{2\hat{\rho}_0 v_0 \hat{r}^3}. \tag{4.9}$$

In the upstream supersonic regime, the fields at a point r only depend on the properties of the flow in the upwind Mach cone. To solve (4.9), we must use the retarded propagator of the linear wave equation. We have

$$\hat{\beta}_1 = \frac{c_z^2}{2\hat{\rho}_0 v_0} \int \frac{d\hat{x}' d\hat{y}' d\hat{z}'}{(\hat{r}'^2 + a^2)^{3/2}} \int \frac{dp_x dp_y d\omega}{(2\pi)^3} \frac{\mathrm{e}^{ip_x(\hat{x}-\hat{x}') + ip_y(\hat{y}-\hat{y}') - i\omega(\hat{z}-\hat{z}')}}{(\omega + i\epsilon)^2 - c_z^2(p_x^2 - p_y^2)}. \tag{4.10}$$

Here, we have used the Fourier-space expression of the retarded propagator and introduced a smoothing cutoff $a > 0$ to regularize the small-scale divergence of the source $1/\hat{r}^3$, replacing $1/\hat{r}^3$ with $1/(\hat{r}^2+a^2)^{3/2}$. After performing the integrals and taking the limit $a \to 0^+$, we obtain

$$\hat{\beta}_1 = -\frac{c_z^2}{2\hat{\rho}_0 v_0 \hat{r}} \int_1^\infty \frac{dy}{(c_z^2+y^2)\sqrt{\sin^2\theta + y^2\cos^2\theta}} \,, \tag{4.11}$$

which behaves as $1/\hat{r}$. It is important to note that this expression only applies to the half-plane $\hat{z} < 0$. This integral is even over $\hat{z}$ (i.e., over u), but its first derivative is discontinuous at $u = 0$. Therefore, we need to use the analytic continuation of (4.11) to extend this result to $u > 0$. Alternatively, we can return to the differential equation (4.9) and assume the ansatz

$$\hat{\beta}_1 = \frac{f_1(u)}{\hat{r}} \,, \tag{4.12}$$

ensuring that there are no logarithmic corrections. This leads to a second-order differential equation over f_1

$$(1-u^2)\left[(1+c_z^2)u^2-1\right] f_1'' + u\left[5+3c_z^2-5(1+c_z^2)u^2\right] f_1' + (1+c_z^2)(1-3u^2) f_1 = \frac{1+c_z^2}{4v_0^3} \,. \tag{4.13}$$

The two integration constants are determined by the requirement that both $f_1(-1)$ and $f_1(-u_c)$ are finite. The resulting expressions are

$$-1 \le u \le -u_c : \quad f_1(u) = \frac{1+c_z^2}{8v_0^3\sqrt{(1+c_z^2)u^2+1}} \ln\left(\frac{1-(1+c_z^2)u - c_z\sqrt{(1+c_z^2)u^2-1}}{1-(1+c_z^2)u + c_z\sqrt{(1+c_z^2)u^2-1}}\right) , \tag{4.14}$$

$$-u_c \le u \le u_c : \quad f_1(u) = \frac{1+c_z^2}{4v_0^3\sqrt{1-(1+c_z^2)u^2}} \left(\pi/2 - \arctan\frac{1-(1+c_z^2)u}{\sqrt{1-(1+c_z^2)u^2}}\right) , \tag{4.15}$$

which agree with (4.11). The analytic continuation from $u < -u_c$ to $u > -u_c$ is obtained by using the property $\arctan(x) = i \ln\left[(1-ix)/(1+ix)\right]/2$. To derive (4.15) from (4.14), we utilize the property $\arctan(1/x) = \pi/2 - \arctan(x)$ for $x > 0$, ensuring an expression that is regular at $u = \pm 1/(1+c_z^2)$. The appropriate form of arctan must be used to achieve a regular expression over the desired range of u. Close to the shock at $u \to u_c$, we obtain the Taylor expansion

$$u \to u_c^- : \quad f_1(u) = -\frac{\pi(1+c_z^2)^{3/4}}{4v_0^3\sqrt{2(u_c-u)}} + \dots \,. \tag{4.16}$$

The singularity at u_c, where the second-order velocities $v_{r,2}$ and $v_{\theta,2}$ diverge, indicates the breakdown of this perturbative approach near the shock, close to the downwind Mach cone.

In the supersonic regime, the equations of motion exhibit a hyperbolic nature. In this region, the solution is solely determined by the local properties of the fluid, including the sound speed c_s, the relative velocity v_0, and the gravitational influence of the long-range gravity of the black hole. Remarkably, the solution in the upstream domain is independent of the boundary conditions at the Schwarzschild radius and does not involve any free integration constants.

4.1.3 . Downstream region

In the far downstream region, we can once again employ a large-distance expansion, which may include logarithmic factors such as $\ln(\hat{r})$. However, we need to be cautious as the first-order upstream solution (4.7) is singular on the $\hat{z}$-axis downstream, specifically at $\theta = 0$ and $u = 1$. This singularity indicates that the upstream solution does not hold true in the downstream region for $\theta < \theta_s$, where $\theta_s(\hat{r})$ represents the polar angle of the axi-symmetric shock front at radius $\hat{r}$. To find the downstream solution, we still use the general form (4.3) for the velocity potential $\hat{\beta}$, and we ensure continuity across the shock. This means that the term a $\ln(\hat{r})$ must be the same in both the upstream and downstream functions, resulting in $a = -1/(2v_0)$ once again. However, the solution must now be regular at $u = 1$, which determines the value of b. The second integration constant for f_0 is set by continuity at $u = u_{\rm c}$. The resulting downstream solution is given by

$$f_0(u) = -\frac{\ln(1+u)}{2v_0} + \frac{1}{2v_0} \ln\left(\frac{1 + (1+c_z^2)u - c_z\sqrt{(1+c_z^2)u^2 - 1}}{-1 + (1+c_z^2)u + c_z\sqrt{(1+c_z^2)u^2 - 1}} \right) , \tag{4.17}$$

which in return gives

$$\begin{aligned} v_{r,1} &= -\frac{1}{2v_0\hat{r}} , \quad v_{\theta,1} = -\frac{1}{2v_0\hat{r}\sqrt{1-u^2}} \left(1 + u - \frac{2c_z}{\sqrt{\frac{u^2}{u_{\rm c}^2} - 1}} \right) , \\ v_1^2 &= \frac{1}{\hat{r}} - \frac{2c_z}{\hat{r}\sqrt{\frac{u^2}{u_{\rm c}^2} - 1}} , \quad \hat{\rho}_1 = \frac{2c_z}{\hat{r}\sqrt{\frac{u^2}{u_{\rm c}^2} - 1}} . \end{aligned} \tag{4.18}$$

We can observe that the scalar-field density $\hat{\rho}$ is increased behind the shock, with the increment decreasing as $1/\hat{r}$ at larger distances. In contrast, the upstream density (4.8) remains unmodified at this order. The radial velocity v_r is continuous across the shock, which is consistent with the continuity of $\hat{\beta}$ for a shock that maintains a fixed direction θ_s at leading order in the far distance.

The jump conditions for an isentropic potential flow across a shock differ from the Rankine-Hugoniot jump conditions applicable to the Navier-Stokes equations. Indeed, the Navier-Stokes equations incorporate viscous effects and thermal conduction. The Rankine-Hugoniot jump conditions derived from these equations encompass conservation of mass, momentum, and energy, capturing the alterations in density, velocity, and thermodynamic quantities across the shock front. On the other hand, for an isentropic potential flow the fluid flows without dissipative effects, such as viscosity and thermal conduction. This simplified model enables a streamlined analysis of fluid dynamics, particularly for compressible flows. However, when a shock is encountered, the jump conditions for an isentropic potential flow deviate from the Rankine-Hugoniot jump conditions. In isentropic potential flow, the jump conditions only consider conservation of mass and momentum. There is no energy equation or entropy. The jump conditions entail the continuity of the velocity potential $\hat{\beta}$, which also implies the continuity of the tangential velocity v_{t}, and the continuity of the transverse mass flow $\hat{\rho} v_{\mathrm{n}}$, where v_{n} is the normal velocity. At a large distance, $v_{\mathrm{t}} = v_r$ and $v_{\mathrm{n}} = v_\theta$ at leading order, thus preserving the continuity of v_r. Furthermore, the condition of continuity of $\hat{\rho} v_\theta$ at order $1/\hat{r}$ yields the angle of the shock, confirming that the shock follows the Mach cone at large distances ($\theta_s \to \theta_c$).

It is worth noting that the first-order angular velocity $v_{\theta,1}$ and density $\hat{\rho}_1$ of diverge at u_{c}, precisely on the downwind Mach cone. This divergence arises from the expansion of the function $f_0(u)$ as u approaches u_{c}

$$u \to u_{\mathrm{c}}^{+} : \quad f_0(u) = -\frac{\ln(1-u_{\mathrm{c}})}{2v_0} - \frac{(1+c_z^2)^{3/4}}{c_z v_0}\sqrt{2(u-u_{\mathrm{c}})} + \dots\,, \tag{4.19}$$

indicating the breakdown of the perturbative analysis near the shock. To properly account for the effects, nonlinear considerations in a boundary layer just behind the shock become necessary. Notably, this singularity manifests at the first-order f_0, in contrast to the upstream case where it emerged at the second order f_1 in (4.16).

In the forthcoming section below, we will explore the matching conditions that arise along the boundary layers and the shock, which give rise to logarithmic contributions that affect the downstream bulk flow. Consequently, the second-order expression of the velocity potential undergoes modification from (4.12) through the inclusion of an additional logarithmic term. Thus, we can write it as

$$\hat{\beta}_1 = \frac{f_1(u) + g_1(u)\ln(\hat{r})}{\hat{r}}\,. \tag{4.20}$$

To obtain these modified expressions, we substitute the above equation into the equation of motion and consider the first-order result (4.17). By collecting terms of order $1/\hat{r}^3$ and $\ln(\hat{r})/\hat{r}^3$, we arrive at two coupled linear second-order differential equations involving f_1 and g_1. In order to ensure regularity at $u = 1$, we determine an integration constant for each of these two functions. This leads to the following solutions

$$g_1 = \frac{C_2}{\sqrt{(1+c_z^2)u^2-1}}\,, \tag{4.21}$$

and

$$\begin{aligned} f_1 = &-\frac{3(1+c_z^2)^2 u}{2v_0^3[(1+c_z^2)u^2-1]} + \frac{1}{\sqrt{(1+c_z^2)u^2-1}}\left\{\frac{(1+c_z^2)^{3/2}}{2c_z v_0^3}\ln\left[\frac{\sqrt{1+c_z^2}u+1}{\sqrt{1+c_z^2}u-1}\right]\right. \\ &+C_1 + \frac{C_2}{2}\ln\left[\frac{[(1+c_z^2)u^2-1]^2[1+(1+c_z^2)u-c_z\sqrt{(1+c_z^2)u^2-1}]}{(1+u)^2[-1+(1+c_z^2)u+c_z\sqrt{(1+c_z^2)u^2-1}]}\right] \\ &\left.+\frac{1+c_z^2}{4c_z v_0^3}\ln\left[\frac{(1+u)^3[-1+(1+c_z^2)u+c_z\sqrt{(1+c_z^2)u^2-1}]^4}{[(1+c_z^2)u^2-1]^2[1+(1+c_z^2)u-c_z\sqrt{(1+c_z^2)u^2-1}]^3}\right]\right\}\,, \end{aligned} \tag{4.22}$$

where C_1 and C_2 are two integration constants to determine.

4.1.4 . Shock front and boundary layers

In our previous analysis, we observed that the large-distance expansions of the upstream and downstream bulk flows diverge as u approaches u_c. This divergence indicates that the zeroth-order approximation becomes insufficient in describing the dynamics close to u_c. Consequently, boundary layers emerge on both sides of the shock, where nonlinear effects become significant, necessitating a departure from the polynomial expansion of chapter 3.

A thorough examination reveals that these boundary layers possess a width of approximately $\Delta u \sim \hat{r}^{-2/3}$. This suggests that the variations in flow properties are better described by powers of $\hat{r}^{-1/3}$ instead of solely relying on a $1/\hat{r}$ dependence. Moreover, logarithmic contributions reappear. To begin, we must determine the location $\theta_s(\hat{r})$ of the shock front, which can be expressed through the large-distance expansion

$$\theta_s(\hat{r}) = \theta_c + \frac{\theta_1}{\hat{r}^{2/3}} + \frac{\theta_2 + \psi_2 \ln(\hat{r})}{\hat{r}} + \frac{\theta_3 + \psi_3 \ln(\hat{r})}{\hat{r}^{4/3}} + \dots . \tag{4.23}$$

This expansion, in turn, determines the expansion of $u_\mathrm{s}(\hat{r}) = \cos(\theta_s(\hat{r}))$.

Considering that the boundary layer has a width of order $\hat{r}^{-2/3}$, we introduce the boundary-layer coordinate

$$U = \hat{r}^{2/3}[u - u_\mathrm{s}(\hat{r})] . \tag{4.24}$$

We observe from (4.16) that the upstream bulk flow diverges as $v_\theta \sim \hat{r}^{-2}(u_\mathrm{c} - u)^{-3/2}$, while (4.19) demonstrates that the downstream bulk flow diverges as $v_\theta \sim \hat{r}^{-1}(u - u_\mathrm{c})^{-1/2}$. Consequently, the singularity close to the shock occurs at a lower order in $1/\hat{r}$ on the downstream side. This asymmetry gives rise to two distinct expansions. For the upstream boundary layer just before the shock, we have

$$U < 0: \quad \hat{\beta} = v_0 \hat{r} u - \frac{1}{2v_0} \ln(\hat{r}(1-u)) + \frac{F_2(U)}{\hat{r}^{2/3}} + \frac{F_3(U)}{\hat{r}} + \dots . \tag{4.25}$$

For the downstream boundary layer just after the shock, we have

$$U > 0: \quad \hat{\beta} = v_0 \hat{r} u - \frac{1}{2v_0} \ln(\hat{r}(1-u_\mathrm{c})) + \frac{F_1(U)}{\hat{r}^{1/3}} + \frac{F_2(U)}{\hat{r}^{2/3}} + \frac{F_3(U) + \mathcal{F}_3(U)\ln(\hat{r})}{\hat{r}} + \dots . \tag{4.26}$$

In both cases, the regular part of the bulk flow over u is retained. In the upstream case (4.25), this includes the first two terms of order $\hat{r}$ and $\hat{r}^0$, while in the more singular downstream case (4.26), it includes only the first term of order $\hat{r}$ (along with the constant associated with the second term). Consequently, the boundary-layer expansion over U commences at order $\hat{r}^{-2/3}$ in the upstream case, while it starts at an earlier order of $\hat{r}^{-1/3}$ in the downstream case. Notably, the upstream boundary layer does not exhibit logarithmic terms ($\ln(\hat{r})$), just like the upstream second-order bulk flow (4.12). However, logarithmic terms arise due to nonlinear effects in both the shock curve (4.23) and the downstream boundary layer (4.26). In comparison to standard one-dimensional boundary-layer theory, $\hat{r}^{-1/3}$ assumes the role of the small parameter, and U serves as the boundary-layer coordinate stretched to account for the infinitesimal width $\Delta u \sim \hat{r}^{-2/3}$.

In the upcoming sections 4.2 and 4.3, we will calculate the accretion rate onto the black hole and its dynamical friction. This computation involves surface integrals over a sphere with radius R, where we take the limit $R \to \infty$ to utilize the large-distance expansions described earlier. These integrals incorporate a geometric area prefactor of $\hat{r}^2$. Consequently, we must compute velocity and density fields up to order $1/\hat{r}^2$ to determine the constant term governing the accretion rate and dynamical friction. This necessitates reaching order $1/\hat{r}$ in both the bulk flows and the boundary layers (4.25) and (4.26).

We proceed by simultaneously computing the boundary-layer expansions and the shock front order by order over $\hat{r}^{-1/3}$. At zeroth order, no boundary layers are present, and we extend the upstream and downstream bulk flows $\hat{\beta}_0$ up to the shock front. As determined by the Mach cone at large distances, the matching condition at the shock front also determines the zeroth-order term θ_c in the shock expansion (4.23).

The next order is associated with the term $\theta_1/\hat{r}^{2/3}$ in the shock expansion (4.23) and the terms $F_1/\hat{r}^{1/3}$ in the boundary-layer expansions (4.25) and (4.26). Notably, the term F_1 is absent in the upstream boundary layer. As previously noted, this is because the singularity of the upstream bulk flow appears at a higher order in $1/\hat{r}$ compared to the downstream bulk flow. Therefore, at this order, we truncate the shock expansion (4.23) at the term $\theta_1/\hat{r}^{2/3}$, the upstream bulk flow obtained in section 4.1.2 extends down to the shock θ_s, and there is only one boundary layer behind the shock, given by the expansion (4.26) truncated at the term $F_1/\hat{r}^{1/3}$.

The upstream bulk flow, given by (4.6) and (4.15), provides the boundary conditions at the angular location θ_s, i.e., at $U = 0$. Using the downstream boundary-layer expression (4.26), the continuity of the velocity potential $\hat{\hat{\beta}}$ and the normal momentum $\hat{\rho} v_{\mathrm{n}}$ gives

$$F_1(0) = 0\,, \quad F_1'(0) = -\frac{4 v_0 \theta_1}{9 c_z}\,. \tag{4.27}$$

By substituting the expansion (4.26) into the equation of motion and collecting terms of order $\hat{r}^{-5/3}$, we obtain the nonlinear differential equation

$$\left(U - \frac{c_z \theta_1}{\sqrt{1+c_z^2}}\right) F_1'' + \frac{1}{2}\left(1 - \frac{9 c_z^2}{v_0 \sqrt{1+c_z^2}} F_1''\right) F_1' = 0\,. \tag{4.28}$$

This nonlinear differential equation highlights the significance of nonlinear effects in the boundary layer, which were not captured in the perturbative treatment of section 4.1.3. The solution can be expressed parametrically in terms of the auxiliary variable Y

$$U = \frac{c_z \theta_1}{\sqrt{1+c_z^2}} + \frac{16 v_0^3 \theta_1^3 - 729 c_z^3 Y^3}{243 v_0 c_z \sqrt{1+c_z^2}\, Y^2}\,, \quad F_1 = \frac{-64 v_0^3 \theta_1^3 + 729 c_z^3 Y^3}{486 v_0 c_z \sqrt{1+c_z^2}\, Y}\,, \tag{4.29}$$

where $0 < Y < 4 v_0 \theta_1/(9 c_z)$, and we used the boundary conditions (4.27) to determine two integration constants. Then, we expand this result at large U, in terms of $1/U$, in the rear of the boundary layer. Expressed in terms of u, we obtain the expansion

$$\hat{\beta} \simeq \hat{r} v_0 u + \left[-\frac{\ln(\hat{r}(1-u_{\mathrm{c}}))}{2v_0} - \frac{8 v_0 \theta_1^{3/2} \sqrt{u-u_{\mathrm{c}}}}{3^{5/2} c_z^{1/2} (1+c_z^2)^{1/4}} + \dots \right] + \frac{1}{\hat{r}} \left[-\frac{8 c_z v_0 \theta_1^3}{81 (1+c_z^2)(u-u_{\mathrm{c}})} + \dots \right] . \tag{4.30}$$

The dots in the brackets correspond to higher orders over $u - u_{\mathrm{c}}$ generated by higher orders in the boundary-layer expansion (4.26) (the functions $F_2, F_3, \dots$), while the dots at the end correspond to higher orders over $1/\hat{r}$. This expansion must be matched with the expansion of the downstream bulk flow (4.17) and (4.22) as $u \to u_{\mathrm{c}}^+$

$$\hat{\beta} \simeq \hat{r} v_0 u + \left[-\frac{\ln(\hat{r}(1-u_{\mathrm{c}}))}{2v_0} - \frac{(1+c_z^2)^{3/4} \sqrt{2(u-u_{\mathrm{c}})}}{v_0 c_z} + \dots \right] + \frac{1}{\hat{r}} \left[-\frac{3(1+c_z^2)}{4 v_0^3 (u-u_{\mathrm{c}})} + \dots \right] . \tag{4.31}$$

The matching of both terms in θ_1 between (4.30) and (4.31) gives

$$\theta_1 = \left(\frac{3}{2} \right)^{5/3} \left(\frac{1+c_z^2}{v_0 c_z^{1/2}} \right)^{2/3} . \tag{4.32}$$

This determination of the coefficient θ_1 also fixes the location of the shock (4.23) at this order. The successful matching of both θ_1 terms in (4.30) serves as validation for our computation. This asymptotic matching procedure, which involves aligning the large-U behavior of the boundary layer with the small $u - u_{\mathrm{c}}$ behavior of the downstream bulk flow, allows us to obtain a global solution that spans across all regions of space.

The width of the boundary layer, characterized by $\hat{r}^{-2/3}$, is determined through (4.28). This scaling ensures a balance between the linear and nonlinear terms in (4.28) as the powers of $\hat{r}$ cancel each other out. It is this non-linearity that permits the regularization of the divergences at the shock, as observed in the perturbative treatment of the bulk flow in section 4.1.3.

Moving on to higher orders, specifically F_2 and F_3, we employ the same method to compute the shock and the boundary layers at these orders: $\{\theta_2, \psi_2; F_2\}$ and $\{\theta_3, \psi_3; F_3, \mathcal{F}_3\}$. However, we now encounter the presence of two boundary layers. The functional form of $F_2, F_3, \mathcal{F}_3$ is obtained by substituting into the equation of motion, while the integration constants are determined through the junction conditions. At this stage, we perform two separate asymptotic matchings: one between the rear of each boundary layer and the bulk flow, and another involving simple junction conditions between the two boundary layers at the shock. A detailed computation reveals that introducing logarithmic terms in the expansions (4.23) and (4.26) is necessary to satisfy these junction conditions. Consequently, this complete procedure fully determines the coefficient ψ_2 in the shock expansion (4.23) and the integration constant C_2 in the bulk downstream solution (4.21) and (4.22). However, the integration constant C_1 in (4.22) remains undetermined and is expressed in terms of θ_2. Due to their lengthiness and limited illustrative value, the expressions for these higher-order results are not provided here.

4.2 . Mass accretion by the black hole

We now have the global solution for the flow at large distances, except for the unknown parameter θ_2. This parameter will be determined by the accretion rate onto the black hole, which corresponds to the boundary condition at the Schwarzschild radius, a factor we have not yet considered. In a steady state, the accretion rate onto the black hole is given by the matter flux through any closed surface surrounding the black hole. Choosing a sphere of radius $\hat{r}$, the accretion rate can be expressed as in (3.60)

$$\dot{m}_{\rm BH} = -2\pi\hat{r}^2 \int_1^{-1} du\, \rho\, v_r \,. \tag{4.33}$$

Hence, we can determine $\dot{m}_{\rm BH}$ from the large-distance expansion by calculating the radial momentum $\hat{\rho} v_r$ up to the order of $1/\hat{r}$. Since we obtained separate expressions for the scalar field profile in four different regions (the upstream and downstream bulk flows and the boundary layers), with two asymptotic matchings in between, we define the angular function

$$\dot{m}_{\rm BH}(u) = -2\pi\hat{r}^2 \int_u^{-1} du\, \hat{\rho}\, v_r \,, \tag{4.34}$$

which gives us the accretion rate in each domain based on the appropriate expression for the scalar field flow. We determine the integration constants by considering the asymptotic matchings at the rear of the two boundary layers and the continuity at the shock location. This allows us to determine the global function $\dot{m}_{\rm BH}(u)$ and the total accretion rate $\dot{m}_{\rm BH}(1)$. The result is

$$\begin{aligned} \dot{m}_{\rm BH} = &-\frac{4\pi c_z v_0 \theta_2}{\sqrt{1+c_z^2}} - \frac{\pi(20+12c_z^2+\sqrt{3}\pi)}{3v_0} - \frac{4\pi\sqrt{1+c_z^2}}{3v_0} \\ &\times \ln\left[\frac{16(\sqrt{1-c_z^2}-1)^3 v_0^2}{3c_z^4(1+c_z^2)}\right] - \frac{2\pi}{9v_0} \ln\left[\frac{(\sqrt{1-c_z^2}-1)^{18} v_0^{16}}{2^{16}3^{18}c_z^{20}(1+c_z^2)^{11}}\right] , \end{aligned} \tag{4.35}$$

which determines θ_2 as a function of $\dot{m}_{\rm BH}$. It is worth noting that the result (4.35) does not depend on the radius $\hat{r}$. Any terms involving higher powers of $\hat{r}$ eventually cancel out, resulting in a finite value as $\hat{r}$ approaches infinity. This agrees with the fact that the matter flux is independent of the choice of surface enclosing the black hole in the stationary regime.

As previously mentioned, equation (4.35) establishes a connection between the unidentified parameter θ_2 at significant distances and the rate of accretion. It is important to note that the large-distance expansion, by design, does not possess knowledge pertaining to the inner boundary conditions, as these fall outside its realm of applicability. Consequently, it cannot ascertain the value of the accretion rate. Nevertheless, the flow at significant distances continues to be influenced by the accretion rate due to the constant-flux condition in the steady state. This influence is explicitly demonstrated in equation (4.35). In this study, we abstain from engaging in a numerical computation of axisymmetric relativistic flow down to the event horizon. Instead, we opt to present a simplified approximation that is expected to encapsulate the primary behavioral aspects.

In the case of radial accretion, the expression for the accretion rate is provided by equation (3.70). In Chapter 3, we demonstrated the validity of this accretion rate in the subsonic regime $v_0 \lesssim c_{s,0}$. This validity holds true until we approach the transition radius, where $r_{\rm sg} \gg r_s$, and the flow rapidly adopts an approximately radial configuration, effectively reverting to the radial solution. It is important to note that this accretion rate is significantly lower than the spherical Bondi accretion rate [300], denoted as $\dot{M}_{\rm Bondi} \sim \rho_0 r_s^2 / c_{s,0}^3$, primarily due to the steep effective adiabatic index $\gamma = 2$.

In the supersonic regime, one would typically anticipate the Hoyle-Lyttleton accretion rate [308, 314] to manifest as follows

$$\dot{M}_{\rm HL} = \frac{4\pi \rho_0 \mathcal{G}^2 m_{\rm BH}^2}{v_0^3} = \frac{\pi \rho_0 r_s^2}{v_0^3} . \tag{4.36}$$

However, for situations characterized by moderate Mach numbers, this accretion rate closely aligns with the Bondi prediction and remains significantly higher than the radial accretion rate (3.70). The latter represents the maximum achievable flux for radial symmetry, constrained by the effective pressure linked to the self-interactions [190]. Lower accretion rates are associated with solutions that are either entirely subsonic (an infeasible outcome due to the boundary condition at the black hole horizon) or completely supersonic. Hence, in the regime where $\dot{M}_{\rm HL} > \dot{M}_{\rm BH,radial}$, a bow shock materializes. This shock serves to decelerate and deflect the dark matter, facilitating the alignment with the boundary conditions at the black hole horizon, where the accretion rate is substantially lower. This gives rise to a subsonic region surrounding the black hole, wherein the flow transitions to an approximately radial configuration in close proximity to the black hole horizon, subsequently matching the accretion rate. In a somewhat analogous manner, due to the vast difference between the maximum possible accretion rate (3.70) and the incoming flow (4.36), the black hole, adorned with the surrounding scalar cloud featuring substantial self-interactions, behaves akin to an obstacle. This analogy draws parallels to a solid sphere moving through a fluid or a space shuttle navigating through the atmosphere.

At high velocities, characterized by $v_0^3 > c_{s,0}^2/(3F_\star)$, the Hoyle-Lyttleton accretion rate as expressed in equation (4.36) becomes smaller in magnitude when compared to the value defined by equation (3.70), which corresponds to the upper limit of achievable flux. This implies that matter can directly plunge into the black hole along a trajectory described by a fully supersonic solution. Consequently, the black hole ceases to function as an obstacle and instead acts as a gravitational sink, freely capturing infalling matter. However, on the z-axis situated behind the black hole, a wake and a conical shock still persist. This phenomenon arises because streamlines originating from all directions converge toward the symmetry axis but are unable to traverse it. Additionally, a stagnation point materializes on the z-axis behind the black hole, where the velocity becomes zero. This is due to the fact that the radial velocity must exhibit a negative value close to the horizon and be on the order of the speed of light, while it tends toward a positive value close to v_0 at greater radial distances. This turning point effectively separates the streamlines that eventually fall into the black hole from those that escape to infinity. Clearly, this region behind the black hole is characterized by subsonic conditions. Therefore, a subsonic region always persists behind the black hole, regardless of the velocity conditions. Consequently, for high velocities, it is reasonable to expect that the shock becomes attached to the black hole. This configuration comprises an upstream supersonic region that extends all the way down to the horizon on the front side of the black hole, while on the back side, a narrow shock cone emerges, encompassing a subsonic region. This observation aligns with the characteristics of the accretion column as described in the Hoyle-Lyttleton analysis [308, 314]. For a more comprehensive examination of this regime, we delve into further details in the Appendix C. Upon closer investigation, we find that pressure forces do not significantly alter the core properties of Hoyle-Lyttleton accretion. Consequently, for velocities surpassing $c_{s,0}^{2/3}$, a narrow accretion column forms on the rear side of the black hole.

In summary, we can categorize the behaviors into two regimes

$$v_0 < \frac{c_{s,0}^{2/3}}{(3F_\star)^{1/3}} \;:\; \dot{m}_{\rm BH} = \frac{12\pi F_\star \rho_0 \mathcal{G}^2 m_{\rm BH}^2}{c_{s,0}^2}\,, \tag{4.37}$$

$$v_0 > \frac{c_{s,0}^{2/3}}{(3F_\star)^{1/3}} \;:\; \dot{m}_{\rm BH} = \frac{4\pi \rho_0 \mathcal{G}^2 m_{\rm BH}^2}{v_0^3}\,. \tag{4.38}$$

4.3 . Drag force

In chapter 3, using the Euler equation of motion associated with the Bernoulli equation (3.21), we derived the expression for the drag force on the black hole

$$\hat{F}_z = -2\pi \hat{r}^2 \int_1^{-1} du\, (\hat{\rho}\hat{v}_r\hat{v}_z + \hat{P}u)\,, \tag{4.39}$$

where we chose the integration surface to be a sphere of radius $\hat{r}$. Similar to the accretion rate in (4.34), we define a function $\hat{F}_z(u)$ to compute the drag force in each angular domain, up to integration constants. By applying junction conditions and asymptotic matching, we obtain the global function, and the full drag force can be obtained from $\hat{F}_z(u=1)$. Using (4.35) to express θ_2 in terms of $\dot{m}_{\rm BH}$, we find

$$\hat{F}_z = \dot{\hat{M}}_{\rm BH} v_0 + \frac{2\pi c_z^2}{3(1+c_z^2)} \ln\left(\mathrm{e}\frac{4v_0^4 c_z \hat{r}^2}{18(1+c_z^2)^2}\right)\,. \tag{4.40}$$

In dimensional units, this can be expressed as follows

$$F_z = \dot{m}_{\rm BH} v_0 + \frac{\pi}{3}\rho_a r_s^2 \frac{c_{s,0}^2}{v_0^2} \ln\left[\frac{e v_0^4 c_z r^2}{18(1+c_z^2)^2 r_s^2}\right]\,. \tag{4.41}$$

In this manner, our computation encompasses and combines two distinct components contributing to the overall drag force, which can be written as

$$F_z = F_{\rm acc} + F_{\rm df}\,. \tag{4.42}$$

The first term in this expression is directly linked to the accretion of matter by the black hole, and as a result, it pertains to the momentum transfer associated with this accretion process. Conversely, the second term represents the classical dynamical friction, which is associated with the long-range gravitational attraction emanating from the wake formed behind the black hole. This phenomenon becomes particularly relevant when pressure forces exert their influence.

4.4 . Numerical computation

To confirm the behaviour of the system for moderate Mach numbers, we conducted a numerical calculation to analyze the flow of dark matter around a black hole using the publicly available AMRVAC code [315, 316]. This code is designed for solving partial differential equations in computational hydrodynamics and astrophysics, employing a parallel adaptive mesh refinement framework. Previous studies on the Bondi-Hoyle accretion of a polytropic gas [317, 318] have also utilized the AMRVAC code. These studies focused on a polytropic gas with a polytropic index $\gamma = 5/3$. In contrast to our case, they needed to include the energy equation in addition to the continuity and Euler equations since entropy is not conserved at the shock. However, since our fluid represents a scalar field rather than a perfect gas, we do not require the energy equation.

To solve the problem, we employed the continuity and Euler equations for an isentropic polytropic gas with a polytropic index $\gamma = 2$, as described in chapter 3 in the non-relativistic regime. The boundary condition at large radii was determined by the uniform flow with density ρ_0 and velocity v_0. The matching radius $r_{\rm m}$ was defined by the radial solution (3.71), recovered in (4.37). As for the initial conditions, we approximated the density ρ by $\rho = \rho_0 \max(1, r_{\rm sg}/(2r))$, which is an approximation of the radial solution. For the initial velocity, we considered $v_r = \dot{m}_{\rm BH}/(4\pi\rho r^2) + v_0$ and $v_\theta = -v_0 \sin(\theta)$ representing a combination of the uniform flow $\mathbf{v_0}$ and radial infall. We then solved the dynamics over time until the results reached a steady state.

To facilitate our calculations, we employed a two-dimensional spherical mesh (with no dependence on the azimuthal angle ϕ) that exhibited uniform stretching in the radial direction. The upper radius was set to 50 times the self-gravity radius ($50 r_{\rm sg}$), while the lower radius was set to 0.005 times this radius ($0.005 r_{\rm sg}$). We used a temporally first-order scheme since we were solely interested in obtaining a steady state. The hllc flux scheme was employed. To work with quantities of order unity in the transition region, we used dimensionless coordinates and fields, namely $r/r_{\rm sg}$, ρ/ρ_0, and $v/c_{s,0}$. Throughout the computational domain, we verified that the Bernoulli invariant (3.21) remained constant.

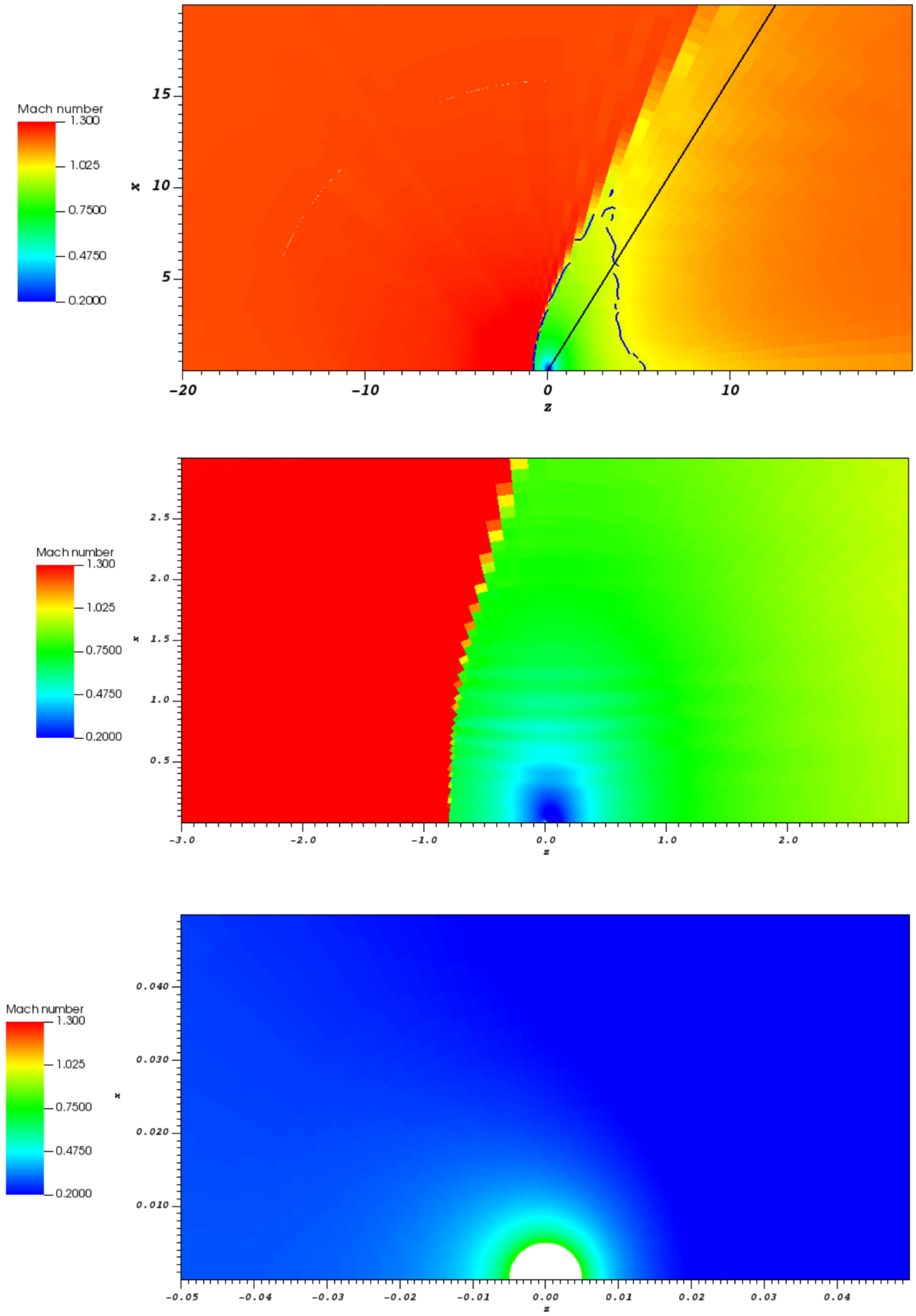

Figure 4.2: Numerical computation of the scalar dark matter flow around a black hole, as viewed in the black hole frame with the dark matter coming from the left at the uniform velocity $\mathbf{v_0}$ parallel to the horizontal axis. We take $\mathcal{M}_0 = v_0/c_{s,0} = 1.2$ and $c_{s,0} = 0.05$. The coordinates are in units of the transition radius $r_{\rm sg}$. The panels show maps of the Mach number $\mathcal{M} = v/c_s$ as we zoom closer to the black hole going from the upper to the lower panel.

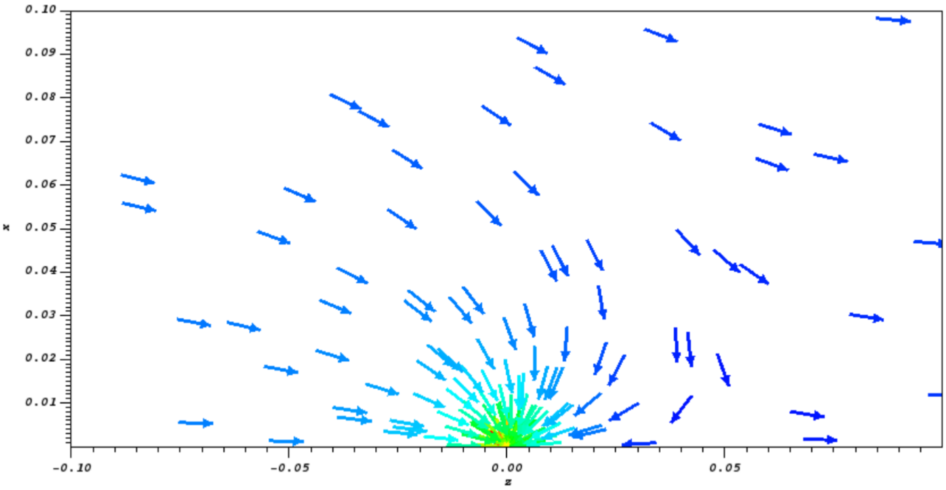

Figure 4.3: Same as Figure 4.2, but shows a map of the velocity field

Figure 4.2 and 4.3 illustrates our results for the case where $v_0/c_{s,0} = 1.2$ and $c_{s,0} = 0.05$, with the aid of the visualization tool VisIt [319]. In the two upper panels, the formation of a bow shock upstream of the black is clearly observed, occurring at a distance of approximately $0.8r_{\rm sg}$ along the z-axis. Following the shock, the velocity decreases while the density and local sound speed increase, resulting in a distinct drop in the Mach number $\mathcal{M} = v/c_s$. This drop is more evident in the velocity maps than in the density maps, which are primarily influenced by the radial increase in the vicinity of the black hole. Initially, the Mach number continues to decrease closer to the black hole until reaching a radius of $0.2r_{\rm sg}$, after which it increases as we approach the supersonic regime beyond the computational domain. The lower-left panel reveals that the Mach number has not yet reached unity at the inner radius of the grid due to the imposition of boundary conditions at a matching radius that is still in the nonrelativistic regime. However, it is noticeable that the system becomes spherically symmetric near the black hole, as evidenced by the spherical color contours representing the Mach number.

Previous studies [317, 318] focusing on a perfect gas with a polytropic index $\gamma = 5/3$ found that the shock is attached to the black hole (in their case, a point mass considering Newtonian gravity). In our study, it is evident that the bow shock is detached from the black hole horizon and located at a radius approximately equal to $r_{\rm sg}$ for $v_0 \sim c_{s,0}$. This discrepancy arises due to the stiffer equation of state ($\gamma = 2$) we adopted, which significantly reduces the radial accretion rate (4.37) compared to the conventional Bondi result. Consequently, the flow becomes more radial near the black hole, justifying our approximation. However, this approximation would not be valid for a perfect gas with $\gamma = 5/3$. In that case, since the shock is attached to the point mass, the flow remains strongly asymmetric near the central object, rendering the radial approximation unreliable. The flow pattern is clearly visible in the velocity field depicted in the lower-right panel, exhibiting a radial infall near the back hole and a stagnation point behind the black hole along the

z-axis. The flow remains close to the uniform velocity $\mathbf{v_0}$ at large distances.

In the upper panel, the black solid straight line originating from the origin represents the Mach angle, as given by $\theta_c = \arcsin(c_{s,0}/v_0)$. It is evident that this line aligns with the slope of the shock front at large distances. The blue solid line indicates the sonic line, where the Mach number crosses unity ($\mathcal{M} = 1$). The left segment of this line, which follows the shock, corresponds to the shock discontinuity where $\mathcal{M}$ drops from $\mathcal{M}_{\text{upstream}} > 1$ to $\mathcal{M}_{\text{downstream}} < 1$. Therefore, although the contour plot displays this line, the Mach number does not reach unity continuously along the line but undergoes a discontinuous transition. The right segment of the sonic line extends from the shock to the z-axis in the downstream region and represents a genuine sonic line, where $\mathcal{M} = 1$. While the shock effectively decelerates the incoming flow in proximity to the black hole, the velocity remains close to $\mathbf{v_0}$ at large distances in the transverse plane. Consequently, the flow becomes subsonic after the shock near the z-axis while remaining supersonic at larger distances. Furthermore, far downstream behind the black hole, the flow converges to the bulk velocity $\mathbf{v_0}$ and becomes supersonic again. As a result, there exists a finite-size region behind the shock, encompassing the black hole, where the flow is subsonic. This region is demarcated by the sonic line represented by the blue solid line in the upper-left panel. Within this subsonic region, the flow decelerates and becomes approximately radial as it approaches the black hole. The plots do not depict the region below the matching radius r_{m} and slightly above the black hole horizon, but in that region, the flow becomes supersonic once again and relativistic. Consequently, there are effectively two sonic lines.

As explained in Section 4.2, we anticipate a pronounced asymmetry as velocity increases, extending all the way down to the black hole horizon. This results in a shock that is no longer detached, along with a fully supersonic flow on the front side of the black hole. However, it is important to note that this high-Mach regime surpasses the capabilities of our numerical code. Consequently, we defer a comprehensive investigation of the accretion flow near the black hole at these elevated Mach numbers to future research endeavors. For an in-depth examination of this regime, please refer to Appendix C, where we adapt the standard Bondi-Hoyle-Lyttleton analysis [308, 314, 320] to our specific case.

4.5 . Comparison of accretion drag and dynamical friction

Referring to (4.41) and (4.37)-(4.38), we observe that the accretion drag on the black hole displays distinct behaviors for low and high velocities

$$v_0 < \frac{c_{s,0}^{2/3}}{(3F_\star)^{1/3}} \ : \ F_{\text{acc}} = \frac{12\pi F_\star \rho_0 \mathcal{G}^2 m_{\text{BH}}^2 v_0}{c_{s,0}^2}\,, \tag{4.43}$$

$$v_0 > \frac{c_{s,0}^{2/3}}{(3F_\star)^{1/3}} \ : \ F_{\text{acc}} = \frac{4\pi \rho_0 \mathcal{G}^2 m_{\text{BH}}^2}{v_0^2}\,. \tag{4.44}$$

For velocities in the range $v_0 \gtrsim c_{s,0}$, the dynamical friction term in (4.41) assumes the form

$$F_{\mathrm{df}} = \frac{8\pi \rho_0 \mathcal{G}^2 m_{\mathrm{BH}}^2}{3 v_0^2} \ln \left(\frac{r_a}{r_{\mathrm{UV}}} \right) . \tag{4.45}$$

Here, r_{UV} is determined by

$$r_{\mathrm{UV}} \simeq \sqrt{\frac{18}{e}} r_{\mathrm{sg}} \mathcal{M}_0^{-3/2} = \sqrt{\frac{18}{e}} r_s v_0^{-3/2} c_{s,0}^{-1/2} . \tag{4.46}$$

This effective small-scale cutoff is explicitly derived from the analytical computation in (4.41). Notably, the pressure stemming from the self-interactions moderates the contributions from small scales to the dynamical friction. Unlike the collisionless scenario, the Coulomb logarithm does not exhibit a divergence at small scales. However, a logarithmic divergence at large scales persists, reminiscent of Chandrasekhar's seminal calculation for a stellar cloud [60]. In our case, the large-scale cutoff is not a free parameter but corresponds to the soliton radius $R_{\mathrm{sol}} = \pi r_a$ as defined in (2.17). It is worth noting that the radius r_{UV} consistently exceeds the Schwarzschild radius, as both v_0 and $c_{s,0}$ are smaller than the speed of light.

Consequently, we can conclude that at low velocities, the accretion drag is substantially smaller than the dynamical friction

$$v_0 \ll \frac{c_{s,0}^{2/3}}{(3F_\star)^{1/3}} \;:\quad F_{\mathrm{acc}} \ll F_{\mathrm{df}} . \tag{4.47}$$

On the other hand, at high velocities, the accretion drag becomes comparable to the dynamical friction

$$v_0 > \frac{c_{s,0}^{2/3}}{(3F_\star)^{1/3}} \;:\quad F_{\mathrm{acc}} \sim F_{\mathrm{df}} . \tag{4.48}$$

These observations are based on the behaviors described in (4.37)-(4.38), as elaborated further in the Appendix C.

4.6 . Comparison to other models

We often compute Bondi and Hoyle-Lyttleton accretion rates for a perfect gas using the formula [300, 308, 314]

$$\dot{m}_{\mathrm{BHL}} = \frac{4\pi \rho_0 \mathcal{G}^2 m_{\mathrm{BH}}^2}{(c_{s,0}^2 + v_0^2)^{3/2}} . \tag{4.49}$$

This formula balances between subsonic and supersonic regimes. At low velocities, the accretion rate drops because of efficient self-interactions. But at higher velocities, it aligns with the Hoyle-Littleton prediction

$$v_0 \ll c_{s,0}^{2/3} \;:\quad \dot{m}_{\mathrm{BH}} \ll \dot{m}_{\mathrm{BHL}} , \qquad v_0 \gg c_{s,0}^{2/3} \;:\quad \dot{m}_{\mathrm{BH}} \simeq \dot{m}_{\mathrm{BHL}} . \tag{4.50}$$

For systems without collisions, when a black hole moves significantly faster than the average speed of the surrounding cloud particles, Chandrasekhar's dynamical friction expression becomes relevant [60–62]

$$\text{collisionless:} \quad F_{\text{free}} \simeq \frac{4\pi\rho_0 \mathcal{G}^2 m_{\text{BH}}^2}{v_0^2} \ln\left(\frac{b_{\max}}{b_{\min}}\right) . \tag{4.51}$$

Here, $b_{\max}$ and $b_{\min}$ are respectively large-scale and small-scale cutoffs. One usually takes $b_{\max} = R$ given by the size of the cloud, while $b_{\min} = 2\mathcal{G}m_{\text{BH}}/v_0^2$ refers to the critical impact parameter associated with bound orbits if their angular velocity is assumed to vanish when they meet the $z-$axis behind the black hole [308]. More generally, $b_{\min}$ corresponds to orbits with a deflection angle of order unity.

In the context of a perfect gas, within the supersonic domain, dynamical friction is described as [269, 316, 321–323]

$$\text{Perfect gas:} \quad F_{\text{gas}} = \frac{4\pi\rho_0 \mathcal{G}^2 m_{\text{BH}}^2 \mathcal{I}}{v_0^2} , \tag{4.52}$$

with $\mathcal{I} = \ln(1 - 1/\mathcal{M}^2)/2 + \ln(b_{\max}/b_{\min})$. At very high Mach numbers $\mathcal{M} \gg 1$, this expression further refines. The first term of $\mathcal{I}$ vanishes while only the second term remains. In this regime, this result is the same as (4.51).

For Fuzzy Dark Matter (FDM), characterized by scalar masses about 10^{-22} eV and where dark matter self-interactions are neglected, the dynamical friction is [63]

$$\text{FDM:} \quad F_{\text{FDM}} = \frac{4\pi\rho_0 \mathcal{G}^2 m_{\text{BH}}^2 C(\beta, kr)}{v_0^2}, \tag{4.53}$$

where $C(\beta, kr)$ is the confluent hypergeometric functions. The parameters β and k are defined as $\beta = \mathcal{G}m_{\text{BH}}m_{\text{DM}}/v_0$ and $k = m_{\text{DM}}v_0$, respectively. Under the conditions $\beta \ll 1$ and $kr \gg 1$, this also aligns closely with Chandrasekhar's outcome as $C \sim \ln(kr)$.

In the domain of supersonic interactions, these systems predominantly exhibit dynamical friction reminiscent of the Chandrasekhar model, as indicated by (4.51). However, variations in the Coulomb logarithm are noteworthy. The prefactor, complex in its nature, frequently leans on intuitive assumptions rather than rigorous derivations for its determination. Uniquely, our analysis deduces the ultraviolet cutoff directly from (4.46), anchored on the analytical result from (4.41). The principle of momentum conservation in a steady state, linking drag force to momentum flux over extended distances, underpins this derivation. Consequently, the radius r_{UV} materializes as a region experiencing notable deviations in the incoming velocity of dark matter, essentially mirroring the role of the critical impact parameter $b_{\min} \sim \mathcal{G}m_{\text{BH}}/v_0^2$ in a collisionless environment. Yet, the system's intrinsic physics and self-interactions significantly influence r_{UV}, as its dependence on $c_{s,0}$ from (4.46) exemplifies. Certainly! Here's a rephrased version: Adopting the size of the cloud as the infrared cutoff is common across various systems. A distinctive feature of scalar dark matter is its independence from the mass of the cloud. The comparison between the radius $r_{\rm UV}$ from (4.46) and the collisionless critical impact parameter $b_{\rm min} \sim \mathcal{G} m_{\rm BH}/v_0^2$ is best expressed as

$$r_{\rm UV} \sim b_{\rm min} \sqrt{\frac{v_0}{c_{s,0}}} \, . \tag{4.54}$$

Such a relationship emerges from the collective pressure effects significantly altering velocity fields at minuscule scales, diverging from collisionless models as explored in Section. 4.5. Consequently, the resulting Coulomb logarithm in (4.45) is diminished compared to its counterpart in (4.51). Beyond its logarithmic component, the prefactor in (4.45) is diminished by a $2/3$ factor compared to (4.51).

4.7 . Summary of the chapter

In hyperbolic systems like supersonic flows, conflicting boundary conditions upstream and downstream (or at the surface of the perturber) give rise to discontinuities known as shock fronts. In section 4.1.2, we showed that the upstream bulk flow is fully determined by the initial condition at $\hat{z} \to -\infty$, and there are no free parameters remaining in (4.6), (4.14) and (4.14) to satisfy the inner boundary conditions at the Schwarzschild radius. This is because, in the supersonic regime, information from the perturber cannot propagate beyond the Mach cone. In our case, unlike traditional hydrodynamic systems such as airplanes, the black hole's long-range gravity has an impact at all distances upstream. It causes the streamlines to bend towards the black hole through the $1/\hat{r}$ term in the equation of motion (3.20), which corresponds to the gravitational effect. However, there is no advanced information about the geometry and properties at the Schwarzschild radius. Similarly, the upstream flow is unaware of the need to ensure a smooth flow downstream along the $\theta = 0$ axis. This leads to a singularity at $u = 1$ in the upstream solution (4.6). In the case of collisionless particles, downstream crossing and the development of a multistreaming flow are possible. However, in our self-interacting scalar field model, such behavior cannot occur.

The matching of the boundary conditions at the Schwarzschild radius and downstream along the $\theta = 0$ axis is permitted by a shock front, which separates the upstream bulk flow of section 4.1.2 from the downstream bulk flow of section 4.1.3. While the upstream bulk flow obtained earlier is completely determined by the initial conditions at $\hat{z} \to -\infty$, the downstream bulk flow, which depends partially on the boundary conditions at $\hat{z} \to \infty$ along $\theta = 0$, still has two undetermined integration constants C_1 and C_2 at the second order (4.21) and (4.22). These constants will be determined through matching with the upstream flow. However, it is not possible to connect the upstream and downstream bulk flows up to the shock front because both solutions diverge as $u \to u_{\rm c}$. This implies that near $u_{\rm c}$, the first or second-order velocity terms become larger than the zeroth-order velocity v_0, causing the breakdown of the large-distance expansion. As a result, a boundary layer emerges on both sides of the shock, where nonlinear effects play a crucial role.

A dynamical friction term that closely aligns with the Chandrasekhar result emerges due to the shock front restricting the ability of dark matter to adapt to the black hole at large scales. Owing to the pressure induced by the self-interactions of the dark matter, we observe a factor of $2/3$ to this force. This results in a reduced dynamical friction in our study, in comparison to the scenarios involving collisionless particles, fuzzy dark matter, and the perfect gas. Additionally, the self-interactions dictate the small-scale cutoff and we still observe a divergence at large scales, analogous to Chandrasekhar result. In our analysis, the large-scale cutoff corresponds to the size of the soliton.

For moderate Mach numbers ($c_{s,0} < v_0 < c_{s,0}^{2/3}$), our findings indicate that the accretion rate continues to adhere to the radial prediction, which is notably lower than the Bondi-Hoyle-Lyttleton projection. This discrepancy can be attributed to the presence of a stiff effective equation of state characterized by an adiabatic index $\gamma = 2$. This stiff equation of state regulates the infall of matter onto the black hole in the vicinity of the Schwarzschild radius. In this scenario, the bow shock remains detached from the black hole and is situated upstream of it. On the far side of the shock, a subsonic region encapsulates the black hole, culminating in a stagnation point downstream. Within this region, the flow tends to adopt an approximately radial configuration in proximity to the black hole. As we approach the Schwarzschild radius, the flow reverts to a supersonic state, mirroring the behavior observed in the radial case. Numerical simulations, for instance, those with $\mathcal{M}_0 = 1.2$, affirm these dynamics. For high Mach numbers ($v_0 > c_{s,0}^{2/3}$), the accretion rate is closer to the Hoyle-Lyttleton accretion rate, which is then smaller than what is obtained in the radial case. As in the classical Hoyle-Lyttleton analysis, the majority of the accretion takes place in the accretion column positioned behind the black hole. This configuration results in a persistent strong asymmetry in the accretion flow all the way down to the Schwarzschild radius. The shock is now attached to the rear of the black hole, forming the boundary of this narrow accretion column.

5 - Gravitational waves from binary black holes in a soliton

In this chapter, we explore the impacts of the accretion drag force and dynamical friction on the motion of binary black holes. Specifically, we investigate how these forces affect the emission of gravitational waves. We begin by deriving the precise effects of the accretion drag force, the dynamical friction and the dark matter halo gravity on the dynamics of binary black holes. By analyzing the resulting changes in eccentricity and semi-major axis. Building upon these findings, we then examine the phase shift induced by the forces in the emitted gravitational waves from binary black holes. Through detailed calculations, we quantify the contributions of these forces to the phase shift, shedding light on their influence on the observed gravitational wave signals. Then, we employ a Fisher analysis to extract information from the model. We focus on two key parameters, ρ_0 and ρ_a, and investigate their detectability using different future interferometers such as LISA, B-DECIGO, ET, and Adv-LIGO, and by considering various events. The results obtained from the Fisher analysis reveal promising prospects for detecting these parameters. Particularly, LISA and B-DECIGO show strong potential for uncovering the dynamics of binary black holes, offering exciting possibilities for future research in the field. Finally, we explore the detectable soliton sizes. This chapter is based on the paper "*Gravitational waves from binary black holes in a self-interacting scalar field dark matter cloud*" [3].

5.1 . Reminder of the forces considered

5.1.1 . Accretion drag force

For the model described by the equations (2.1) and (2.2), it was demonstrated in [190], and recovered in chapters 3 and 4, that the accretion rate of scalar field dark matter onto a black hole can be categorized into two distinct regimes

$$v_{\rm BH} < v_{\rm acc} \dot{m}_{\rm BH} = \dot{m}_{\rm max} \,, \tag{5.1}$$

$$v_{\rm BH} > v_{\rm acc} \dot{m}_{\rm BH} = \dot{m}_{\rm BHL} \,. \tag{5.2}$$

These regimes are further characterized as

$$v_{\rm acc} = \frac{c_{s,0}^{2/3}}{(3F_\star)^{1/3}} \,, \quad \dot{m}_{\rm max} = 3\pi F_\star \rho_a r_s^2 = \frac{12\pi F_\star \rho_0 \mathcal{G}^2 m_{\rm BH}^2}{c_{s,0}^2} \,, \quad \dot{m}_{\rm BHL} = \frac{4\pi \rho_0 \mathcal{G}^2 m_{\rm BH}^2}{v_{\rm BH}^3} \,, \tag{5.3}$$

where a dot above a variable represents its time derivative. The value $F_\star \approx 0.66$ arises from a numerical analysis of the critical flux [190]. This flux is linked to the sole radial transonic solution that bridges the supersonic infall at the Schwarzschild radius with the static equilibrium soliton at extensive ranges. Such a critical behavior echoes findings from traditional hydrodynamic flow studies, as presented in Refs. [300, 301]. It closely aligns with a polytropic gas scenario having an index $\gamma = 2$ [1, 190]. Nevertheless, as one approaches the black hole, the behavior deviates from standard polytropic gas dynamics, transitioning into the relativistic domain. Close to the Schwarzschild radius, the scalar field is better represented by the nonlinear Klein-Gordon equation rather than traditional hydrodynamics [190]. This deviation indicates a disparity between the critical flux, $\dot{m}_{\max}$, and the conventional Bondi result $\dot{m}_{\text{Bondi}} \sim \rho_0 \mathcal{G}^2 m_{\text{BH}}^2 / c_{s,0}^3$. This difference becomes evident when considering the reliance of $\dot{m}_{\max}$ on the speed of light, a feature absent in the typical Bondi outcome.

For higher velocities, the scenario aligns with the conventional accretion column depiction [314, 320], and the Bondi-Hoyle-Lyttleton accretion rate, $\dot{m}_{\text{BHL}}$, is realized. Here, the majority of accretion originates from the slim wake trailing the BH, defined by a conical shock within the Mach angle $\sin\theta_c = 1/\mathcal{M} \ll 1$, where $\mathcal{M} = v_{\text{BH}}/c_{s,0}$ denotes the black hole Mach number. Conversely, in the low-velocity regime, the Bondi-Hoyle-Lyttleton accretion rate surpasses the maximum allowable accretion rate, $\dot{m}_{\max}$, restricted by the effective pressure resulting from self-interactions. Here, the accretion column expands beyond a slender cone to encompass the black hole from all directions. A prominent bow shock forms ahead of the black hole, leading to a subsonic area that encircles the black hole and diverts the bulk of the dark matter flux. Proximate to the horizon, the flow turns nearly radial, reverting to the accretion rate $\dot{m}_{\max}$.

Let us now consider a scenario where a black hole, with velocity $\mathbf{v}_{\text{BH}}$, traverses this scalar cloud. Under the nonrelativistic condition $v_{\text{BH}} \equiv |\mathbf{v}_{\text{BH}}| \ll 1$, and from the cloud's reference frame, the accretion of zero-momentum dark matter does not alter the momentum of the black hole. Instead, it decelerates its velocity following

$$m_{\text{BH}} \dot{\mathbf{v}}_{\text{BH}}|_{\text{acc}} = -\dot{m}_{\text{BH}} \mathbf{v}_{\text{BH}} \,. \tag{5.4}$$

5.1.2 . Dynamical friction

Dynamical friction also plays a role in decreasing the velocity of the black hole. Similar to what is described in hydrodynamics [266, 268, 269], the dynamical friction force becomes null for subsonic speeds ($v_{\text{BH}} < c_{s,0}$). However, it is important to note that this threshold is only an approximation. A perturbative treatment to higher orders, which takes the back-reaction of the scalar field onto the black hole into account, should smooth out the transition at $c_{s,0}$ and give a small but non-zero force in the subsonic regime [270]. Nevertheless, using a sharp transition at v_c provides a conservative estimate for the impact of dynamical friction on the motion of a black hole. In this supersonic context, studied in Chapter 4, the added force acting on the black hole is depicted as

$$m_{\text{BH}} \dot{\mathbf{v}}_{\text{BH}}|_{\text{df}} = -\frac{8\pi \mathcal{G}^2 m_{\text{BH}}^2 \rho_0}{3 v_{\text{BH}}^3} \ln\left(\frac{r_{\text{IR}}}{r_{\text{UV}}}\right) \mathbf{v}_{\text{BH}} \,. \tag{5.5}$$

Here, r_{IR} represents the conventional large-radius cutoff, while r_{UV} serves as the small-radius cutoff for the logarithmic Coulomb factor and is defined as

$$r_{\text{UV}} = 6\sqrt{\frac{2}{e}} \frac{\mathcal{G} m_{\text{BH}}}{c_{s,0}^2} \left(\frac{c_{s,0}}{v_{\text{BH}}}\right)^{3/2} , \tag{5.6}$$

where e denotes Euler's number (distinct from the orbital eccentricity, $\mathfrak{e}$.

Interestingly, (5.5) mirrors the collisionless model presented by Chandrasekhar [60], but it comes with a multiplied factor of $2/3$. Additionally, in this scenario, $r_{\rm UV}$ is determined by the scalar field's physics and its inherent pressure, as opposed to the minimum impact parameter, $b_{\rm min} \sim \mathcal{G} m_{\rm BH}/v_{\rm BH}^2$. Considering $r_{\rm UV} \sim b_{\rm min}\sqrt{v_{\rm BH}/c_{s,0}} > b_{\rm min}$, the dynamical friction (5.5) appears to be less than the collisionless outcome, exhibiting a damping ratio less than $2/3$.

In the context of a consistent linear trajectory, the infra-red cutoff can be defined by the size of the soliton, which is dependent on $m_{\rm DM}$ and λ_4 as illustrated by (2.3). However, for objects following circular orbits with a radius of $r_{\rm orb}$, both numerical models and analytical evaluations propose that for a gaseous medium, a fitting approximation can be achieved with $r_{\rm IR} = 2r_{\rm orb}$ [324, 325]. A logical deduction can be drawn from this: by estimating dynamical friction through the momentum interchange with distant encounters or impact parameter streamlines b, as highlighted in [60], the duration of the encounter is $\Delta t \sim b/v_{\rm BH}$. This time must be shorter than the orbital period $P_{\rm orb} \sim r_{\rm orb}/v_{\rm BH}$ to ensure that the black hole does not alter its course during the encounter, leading to the conclusion that $b \lesssim r_{\rm orb}$. If we gauge the dynamical friction from the gravitational pull by the black hole's aftermath, at a significant distance in the resting frame of the black hole, matter diverges at a radial velocity $v_{\rm BH}$. Thus, the wake remains consistent behind the black hole up to a distance of $d \sim v_{\rm BH} P_{\rm orb}/2$, which reaffirms the large-radius cutoff $d \lesssim r_{\rm orb}$. Consequently, we adopt

$$r_{\rm IR} = 2r_{\rm orb}\,. \tag{5.7}$$

This is aligned with the norm observed for gaseous mediums [324].

5.1.3 . Dark matter halo gravity

If we simplify the primary part of the soliton to be a spherical halo with density ρ_0 and radius $R_{\rm sol}$, placed at the point $\mathbf{x}_0$, the gravitational potential of this halo can be described as:

$$\Phi_{\rm halo}(\mathbf{x}) = \begin{cases} \frac{2\pi}{3}\mathcal{G}\rho_0|\mathbf{x}-\mathbf{x}_0|^2\,, & \text{if } |\mathbf{x}-\mathbf{x}_0| < R_{\rm sol}\,, \\ \text{undefined otherwise.} \end{cases} \tag{5.8}$$

From this, the gravitational acceleration resulting from the halo is derived as

$$m_{\rm BH}\dot{\mathbf{v}}_{\rm BH}|_{\rm halo} = -\frac{4\pi}{3}\mathcal{G} m_{\rm BH}\rho_0(\mathbf{x}-\mathbf{x}_0)\,. \tag{5.9}$$

This last equation reveals the force exerted by the dark matter halo on the black hole within its domain.

5.2 . Binary motion

We focus on a binary system of two black holes and study their dynamics during the inspiraling phase in the Newtonian regime. In this regime, the Keplerian orbital motion of the black holes is perturbed by the accretion of dark matter, the dynamical friction, the dark matter halo, as well as by the emission of gravitational waves. Both effects contribute to a reduction in the separation between the black holes until they eventually merge. The system under consideration is depicted in Figure 5.1 for visual reference. It is important to note that in a more realistic framework, other effects, such as baryonic feedback, may also come into play. However, for the purpose of this study, we do not consider these effects and solely focus on the drag forces caused by dark matter. Additionally, it should be mentioned that exotic effects, such as superradiance or ionization, which can arise in the case of self-interacting dark matter, have not been studied here. These effects, while intriguing, are beyond the scope of our current analysis.

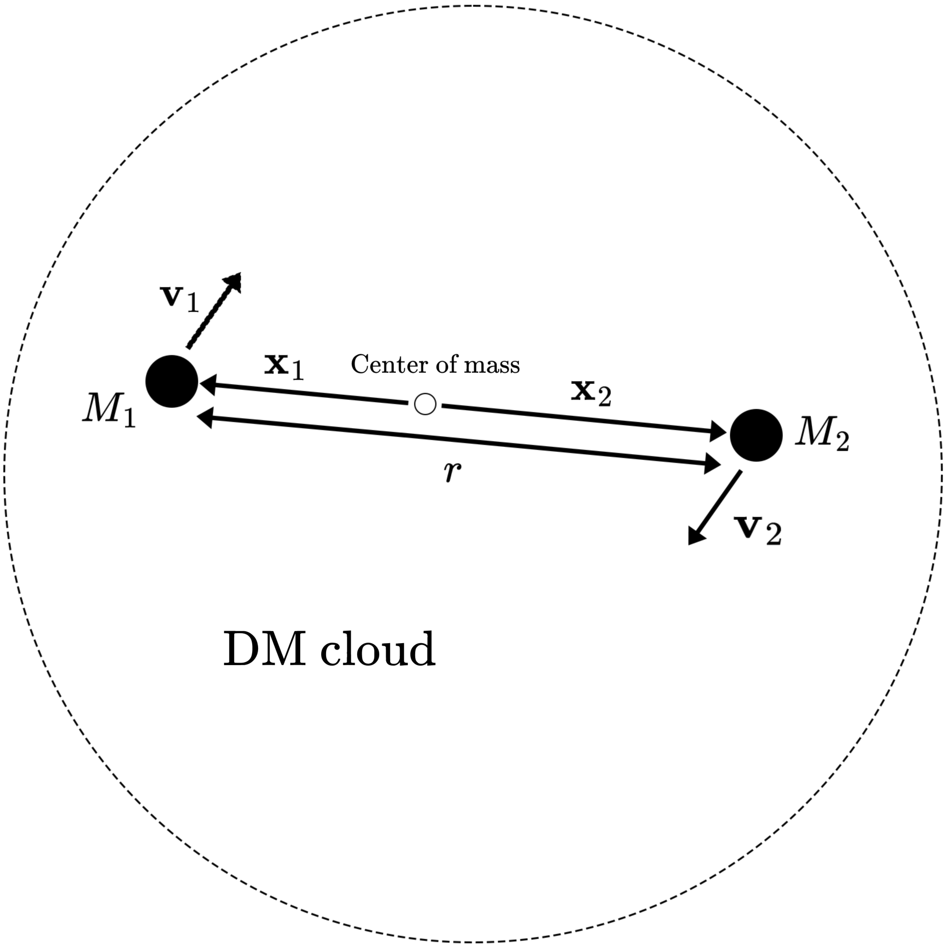

Figure 5.1: Conceptual depiction of the investigated system, not to scale. The illustration showcases the inspiral of two black holes within a dark matter cloud around their center of mass. One black hole is characterized by the following quantities: mass (m_1), position ($\boldsymbol{x}_1$), and velocity ($\boldsymbol{v}_1$), while the other black hole possesses the following quantities: mass (m_2), position ($\boldsymbol{x}_2$), and velocity ($\boldsymbol{v}_2$).

During the inspiraling phase at large distances, we can analyze the perturbations of the Keplerian motion at the first order. This allows us to separately consider the influence of the scalar cloud and the effect of gravitational waves on the dynamics of the binary system. By treating these perturbations, we can examine the impact of the scalar cloud, which arises from the accretion of dark matter, and the influence of GW emission on the orbital motion of the black holes.

5.2.1 . Keplerian motion

To compute the perturbation of the orbits at first order, we employ the standard method of osculating orbital elements [326]. This method allows us to derive the drift of the orbital elements that determine the shape of the orbits. To define our notations, let us first recall the properties of Keplerian orbits. At zeroth order, the binary system consists of two black holes with masses $\{m_1, m_2\}$, positions $\{\boldsymbol{x}_1, \boldsymbol{x}_2\}$, and velocities $\{\boldsymbol{v}_1, \boldsymbol{v}_2\}$. By introducing the relative distance $\boldsymbol{r}$ and the relative velocity $\boldsymbol{v}$, defined as

$$\boldsymbol{r} = \boldsymbol{x}_1 - \boldsymbol{x}_2, \quad \boldsymbol{v} = \boldsymbol{v}_1 - \boldsymbol{v}_2 \,, \tag{5.10}$$

we can reduce the problem to a one-body problem. We also define the total mass $m = m_1 + m_2$ and the reduced mass $\mu = m_1 m_2/m$. The equation of motion for the relative separation is given by

$$\ddot{\boldsymbol{r}} = -\frac{\mathcal{G}m}{r^3}\boldsymbol{r} \,. \tag{5.11}$$

The center of mass remains at rest if its initial velocity vanishes. Furthermore, we have the following expressions for the positions of the black holes

$$\boldsymbol{x}_1 = \frac{m_2}{m}\boldsymbol{r}, \quad \boldsymbol{x}_2 = -\frac{m_1}{m}\boldsymbol{r} \,, \tag{5.12}$$

with the origin of the coordinates chosen as the barycenter of the binary system. The solution for bound orbits in the Keplerian regime is described by an ellipse. The radial distance r is given by

$$r = \frac{p}{1 + \mathfrak{e}\cos(\phi - \omega)}, \tag{5.13}$$

where $p = (1 - \mathfrak{e}^2)a$ is the semi-latus rectum, a is the semi-major axis, $\mathfrak{e}$ is the eccentricity, and ω is the longitude of the pericenter. The orbital motion occurs in the plane defined by the orthogonal unit vectors $(\boldsymbol{e}_x, \boldsymbol{e}_y)$, perpendicular to the axis defined by $\boldsymbol{e}_z$. In spherical coordinates, the polar angle $\theta = \pi/2$ remains constant, while the azimuthal angle ϕ evolves. The total angular momentum $\boldsymbol{L}$ is conserved and given by

$$\boldsymbol{L} = m_1 \boldsymbol{x}_1 \times \boldsymbol{v}_1 + m_2 \boldsymbol{x}_2 \times \boldsymbol{v}_2 = \mu \boldsymbol{h} \,, \tag{5.14}$$

where $\boldsymbol{h} = \boldsymbol{r} \times \boldsymbol{v} = h\, \boldsymbol{e}_z$ represents the specific angular momentum, $h = r^2\dot{\phi}$, and $p = h^2/(\mathcal{G}M)$. The constancy of ω is related to the conservation of the Runge-Lenz vector

$$\boldsymbol{A} = \frac{\boldsymbol{v} \times \boldsymbol{h}}{\mathcal{G}m} - \boldsymbol{e}_r = \mathfrak{e}(\cos\omega\, \boldsymbol{e}_x + \sin\omega\, \boldsymbol{e}_y) \,. \tag{5.15}$$

We can also define the true anomaly φ as the azimuthal angle measured from the direction of the pericenter $\varphi = \phi - \omega$. The rate of change of φ with respect to time is given by

$$\dot{\varphi} = \sqrt{\frac{\mathcal{G}m}{p^3}}(1 + \mathfrak{e}\cos\varphi)^2 \,. \tag{5.16}$$

The period P of the orbital motion is determined by Kepler's third law

$$P = 2\pi\sqrt{\frac{a^3}{\mathcal{G}m}} \,, \quad f_{\rm orb} = \frac{1}{2\pi}\sqrt{\frac{\mathcal{G}m}{a^3}} \,. \tag{5.17}$$

5.2.2 . Drag force from dark matter

As mentioned in section 5.1, the equations of motion for the two black holes are given by

$$\begin{aligned} m_1\ddot{\mathbf{x}}_1 &= \mathcal{G}m_1m_2\frac{\mathbf{x}_2 - \mathbf{x}_1}{|\mathbf{x}_2 - \mathbf{x}_1|^3} - \dot{m}_1\dot{\mathbf{x}}_1 - f_1\dot{\mathbf{x}}_1 - g_1(\mathbf{x}_1 - \mathbf{x}_0) \,, \\ m_2\ddot{\mathbf{x}}_2 &= \mathcal{G}m_1m_2\frac{\mathbf{x}_1 - \mathbf{x}_2}{|\mathbf{x}_1 - \mathbf{x}_2|^3} - \dot{m}_2\dot{\mathbf{x}}_2 - f_2\dot{\mathbf{x}}_2 - g_2(\mathbf{x}_2 - \mathbf{x}_0) \,, \end{aligned} \tag{5.18}$$

where we take into account the Newtonian gravity of the binary, the accretion of dark matter, the dynamical friction and the halo gravity, with

$$f_i(t) = \Theta_{{\rm df},i}\frac{8\pi\mathcal{G}^2m_i^2\rho_0}{3v_i^3}\ln\left(\frac{r_{{\rm IR},i}}{r_{{\rm UV},i}}\right) \,, \quad g_i = \frac{4\pi}{3}\mathcal{G}m_i\rho_0 \,. \tag{5.19}$$

Here, $\Theta_{{\rm df},i}$ is a Heaviside factor associated with the two conditions $v_i > c_{s,0}$ and $r_{{\rm IR},i} > r_{{\rm UV},i}$. We expect our use of a sharp transition to provide a conservative estimate for the impact of the dynamical friction on the motion of a black hole.

This gives for the separation $\mathbf{r}$ the equation of motion

$$\ddot{\mathbf{r}} = -\frac{\mathcal{G}m}{r^3}\mathbf{r} - \left(\frac{\dot{\mu}}{\mu} + \frac{m_2f_1}{m_1m} + \frac{m_1f_2}{m_2m}\right)\dot{\mathbf{r}} - \frac{4\pi\mathcal{G}\rho_0}{3}\mathbf{r} \,. \tag{5.20}$$

Here we used (5.12) to express $\mathbf{x}_i$ in terms of $\mathbf{r}$ in the last two terms, as we work at first order in the perturbations $\dot{m}_i$, f_i and g_i. Thus, we obtain an equation of motion of the form

$$\ddot{\mathbf{r}} = -\frac{\mathcal{G}m(t)}{r^3}\mathbf{r} - F(t)\dot{\mathbf{r}} - G\mathbf{r} \,. \tag{5.21}$$

Here and in the following, we assumed that at zeroth-order the center of mass of the binary is at rest in the scalar cloud, or more generally that its velocity is small as compared with the binary orbital velocity $\mathbf{v}$.

For circular orbits with $v = \sqrt{\mathcal{G}m/a}$, we obtain

$$\frac{r_{{\rm IR},i}}{r_{{\rm UV},i}} = \sqrt{\frac{ec_{s,0}m^2\mu^5}{18vm_i^7}} \,, \quad \frac{v_i}{c_{s,0}} = \frac{\mu v}{m_ic_{s,0}} \,, \tag{5.22}$$

and the Heaviside factor in (5.19) reads

$$\Theta_{\mathrm{df},i} = \Theta\left(\frac{m_i}{\mu} < \frac{v}{c_{s,0}} < \frac{em^2\mu^5}{18m_i^7}\right) , \tag{5.23}$$

which is unity when the conditions are satisfied and zero otherwise. We can see that the conditions $r_{\mathrm{IR},i} > r_{\mathrm{UV},i}$ and $v_i > c_{s,0}$ can only be simultaneously satisfied by the smaller black hole of the binary, when the symmetric mass ratio ν defined by

$$\nu = \mu/m = m_1m_2/m^2 \tag{5.24}$$

is below

$$\nu \lesssim 0.16\,. \tag{5.25}$$

Following the method of the osculating orbital elements [326], we obtain the impact of the accretion and of the dynamical friction by computing the perturbations to the orbital elements. It is clear from (5.21) that the orbital plane remains constant. In particular, the specific angular momentum $\mathbf{h}$ remains parallel to $\mathbf{e}_z$ and evolves as

$$\dot{\mathbf{h}} = -F(t)\mathbf{h}\,, \tag{5.26}$$

whereas the Runge-Lenz vector evolves as

$$\dot{\mathbf{A}} = -\left(\frac{\dot{m}}{m} + 2F(t)\right)(\mathbf{A} + \mathbf{e}_r) + \frac{Ghr}{\mathcal{G}m}\mathbf{e}_\phi\,. \tag{5.27}$$

This gives next the evolution of the eccentricity and of the semi-major axis

$$\dot{\mathfrak{e}} = -\left(\frac{\dot{m}}{m} + 2F(t)\right)(\mathfrak{e} + \cos\varphi) - \frac{Gha(1-\mathfrak{e}^2)\sin\varphi}{\mathcal{G}m(1+\mathfrak{e}\cos\varphi)}, \tag{5.28}$$

$$\dot{a} = -\frac{2a^2}{h}\left[\frac{\dot{m}}{m} + F(t)\right](1 - \mathfrak{e}\cos\varphi), \tag{5.29}$$

where $\mathfrak{e}$ is the eccentricity and a the semi-major axis, and φ is the true anomaly. Using the expression from (5.16), the differentiation in terms of the true anomaly can be written, at first order, as

$$\frac{d\mathfrak{e}}{d\varphi} = -\sqrt{\frac{p^3}{\mathcal{G}m}}\left\{\left(\frac{\dot{m}}{m} + 2F(t)\right)\frac{\mathfrak{e} + \cos\varphi}{(1+\mathfrak{e}\cos\varphi)^2} + \frac{Gha(1-\mathfrak{e}^2)}{\mathcal{G}m}\frac{\sin\varphi}{(1+\mathfrak{e}\cos\varphi)^3}\right\} , \tag{5.30}$$

$$\frac{da}{d\varphi} = -\sqrt{\frac{p^3}{\mathcal{G}m}}\left\{\left(\frac{\dot{m}}{m} + 2F(t)\right)\frac{a}{1-\mathfrak{e}^2}\frac{1+\mathfrak{e}^2+2\mathfrak{e}\cos\varphi}{(1+\mathfrak{e}\cos\varphi)^2} + \frac{2Gh\mathfrak{e}a^2}{\mathcal{G}m}\frac{\sin\varphi}{(1+\mathfrak{e}\cos\varphi)^3}\right\} . \tag{5.31}$$

The perturbations induced by the dark matter cause oscillations and secular changes in the orbital elements. To determine the cumulative drift associated with the secular effects, we average over one orbital period P using the formula

$$\langle\dot{a}\rangle = \frac{1}{P}\int_0^P dt\,\dot{a} = \frac{1}{P}\int_0^{2\pi} d\varphi\,\frac{da}{d\varphi}\,, \tag{5.32}$$

where $\langle\dot{a}\rangle$ represents the average change in the semi-major axis over one period.

5.2.3 . Accretion impact on orbital motion

Initially, we examine the effect of dark matter accretion on orbital behavior. This can be characterized by the term $\dot{m}/m$ and the contribution $F_{\rm acc} = \dot{\mu}/\mu$ to $F(t)$. Our attention is on scenarios where accretion rates have minimal variations relative to orbital movements, thereby approximating them as constant throughout a single period. As indicated in (5.2), the accretion rate remains constant at low velocities and declines proportional to v_i^{-3} at greater velocities. Hence, we deduce

$$\frac{\dot{m}}{m} + 2\frac{\dot{\mu}}{\mu} = A_{\rm acc} + \frac{B_{\rm acc}}{v^3} \,, \tag{5.33}$$

where

$$A_{\rm acc} = \frac{12\pi F_\star \mathcal{G}^2 \rho_0 \mu}{c_{s,\,0}^2 c} \sum_{i=1}^{2} \Theta(v_i < v_{\rm acc}) \left(2 + \frac{m_i^2}{m\mu}\right) \,,$$
$$B_{\rm acc} = 4\pi \mathcal{G}^2 \rho_0 \mu \sum_{i=1}^{2} \Theta(v_i > v_{\rm acc}) \frac{m_i^3}{\mu^3} \left(2 + \frac{m_i^2}{m\mu}\right) \,. \tag{5.34}$$

When we consider lower orders of eccentricity $\mathfrak{e}$, from (5.30) and (5.31) we find

$$\langle \dot{\mathfrak{e}} \rangle_{\rm acc} = \frac{3\mathfrak{e}}{2} \left(\frac{a}{\mathcal{G}m}\right)^{3/2} B_{\rm acc} \,, \quad \langle \dot{a} \rangle_{\rm acc} = -aA_{\rm acc} - a\left(\frac{a}{\mathcal{G}m}\right)^{3/2} B_{\rm acc} \,. \tag{5.35}$$

In scenarios of low velocity, eccentricity remains unchanged, while it rises at high velocities given $\mathfrak{e} > 0$. Orbital size consistently decreases. The result in (5.35) for the semi-major axis is evident for circular orbits when considering the persistence of the total angular momentum.

5.2.4 . Dynamical friction impact on orbital motion

Dynamical friction can be represented as

$$F_{\rm df} = \frac{m_2 f_1}{m_1 m} + \frac{m_1 f_2}{m_2 m} \,, \tag{5.36}$$

leading us to

$$2F_{\rm df}(t) = \frac{B_{\rm df}}{v^3} + \frac{C_{\rm df}}{v^3} \ln\left(\frac{v}{c_{s,\,0}}\right) \,, \tag{5.37}$$

with

$$B_{\rm df} = \frac{8\pi\mathcal{G}^2\rho_0\mu}{3} \sum_{i=1}^{2} \Theta_{{\rm df},i} \frac{m_i^3}{\mu^3} \ln\left(\frac{em^2\mu^5}{18m_i^7}\right) \,, \quad C_{\rm df} = -\frac{8\pi\mathcal{G}^2\rho_0\mu}{3} \sum_{i=1}^{2} \Theta_{{\rm df},i} \frac{m_i^3}{\mu^3} \,. \tag{5.38}$$

At the lower order of eccentricity $\mathfrak{e}$, we derive

$$\langle \dot{\mathfrak{e}} \rangle_{\rm df} = \frac{3\mathfrak{e}}{2} \left(\frac{a}{\mathcal{G}m}\right)^{3/2} \left[B_{\rm df} + C_{\rm df} \ln\left(\sqrt{\frac{\mathcal{G}m}{a}} \frac{1}{c_{s,\,0}}\right) - \frac{C_{\rm df}}{3}\right] \,,$$
$$\langle \dot{a} \rangle_{\rm df} = -a \left(\frac{a}{\mathcal{G}m}\right)^{3/2} \left[B_{\rm df} + C_{\rm df} \ln\left(\sqrt{\frac{\mathcal{G}m}{a}} \frac{1}{c_{s,\,0}}\right)\right] \,. \tag{5.39}$$

Consequently, dynamical friction tends to boost eccentricity when $\mathfrak{e} > 0$, while constricting the size of the orbit. The increase of the eccentricity is directly connected to the expression of the force (5.37), as the dominant term is proportional to $1/v^3$. As explained in [327] in the case of dynamical friction for a gaseous medium, because forces at periapse tend to circularize the orbit while those at apoapse tend to make it more eccentric, the dynamical friction, which is stronger at the periapse have the effect of increasing the eccentricity.

5.2.5 . Effect of gravitational waves emission

The emission of gravitational waves is well known to cause the orbits to become more circular and tighter until the black holes merge. At the lowest order in a post-Newtonian expansion and using the quadrupole formula, the drifts of the eccentricity and semi-major axis are given by the standard results [326]. The drift of eccentricity is

$$\langle \dot{\mathfrak{e}} \rangle_{\mathrm{gw}} = -\frac{304\nu}{15a}\mathfrak{e}\left(\frac{\mathcal{G}m}{a}\right)^3 (1-\mathfrak{e}^2)^{-5/2}\left(1+\frac{121}{304}\mathfrak{e}^2\right), \tag{5.40}$$

and the drift of semi-major axis is

$$\langle \dot{a} \rangle_{\mathrm{gw}} = -\frac{64\nu}{5}\left(\frac{\mathcal{G}m}{a}\right)^3 \frac{1+\frac{73}{24}\mathfrak{e}^2+\frac{37}{96}\mathfrak{e}^4}{(1-\mathfrak{e}^2)^{7/2}}. \tag{5.41}$$

Throughout this chapter, the lowest post-Newtonian order (5.41) is considered. This order is sufficient for the purpose of estimating the dark matter density thresholds associated with a significant impact on the gravitational wave signal. As discussed in Section 5.3, the dark matter corrections are most important in the early inspiral and behave as negative post-Newtonian orders. Consequently, they are not degenerate with higher post-Newtonian orders. See Appendix D for more details on the calculation of the gravitational wave contribution.

In our analysis, we operate under the assumption that the influence of dark matter on the binary system is less pronounced than the effects of gravitational wave emissions, which are known to reduce eccentricity. Consequently, we focus our attention on circular orbits, denoted by $\mathfrak{e} = 0$.

5.2.6 . Influence of halo gravity

Upon examining (5.30) and (5.31), it becomes evident that the G-term, related to halo gravitation, does not affect the eccentricity of the orbit or its size over one complete period, yielding $\langle \dot{\mathfrak{e}} \rangle_{\mathrm{halo}} = 0$ and $\langle \dot{a} \rangle_{\mathrm{halo}} = 0$. In the context of the approximation described in (5.9), where the halo gravitational potential is constant over time, this force is conserved. This alteration of the standard Keplerian potential does lead to a shift in both the orbital frequency and the emanation of gravitational waves. When we consider only the effects of the binary system and halo gravitation, the motion equation defined in (5.20) aligns with the energy equation given by

$$E = \frac{1}{2}\mu v^2 - \frac{\mathcal{G}\mu m}{r} + \frac{2\pi\mathcal{G}\rho_0\mu r^2}{3}. \tag{5.42}$$

Applying the Euler-Lagrange motion equations, the velocity for circular orbits with radius a is

$$v_\phi = \sqrt{\frac{\mathcal{G}m}{a}} \left(1 + \frac{2\pi\rho_0 a^3}{3m}\right) . \tag{5.43}$$

For simplicity, all subsequent discussions will involve calculations to the linear order in ρ_0. This allows us to infer that relative adjustments to standard Keplerian findings are influenced by the proportion of the dark matter within the orbital radius to the aggregate mass of the binary system. This yields the orbital frequency and energy equations

$$f_{\rm orb} = \frac{1}{2\pi}\sqrt{\frac{\mathcal{G}m}{a^3}} \left(1 + \frac{2\pi\rho_0 a^3}{3m}\right) , \tag{5.44}$$

and

$$E = -\frac{\mathcal{G}m\mu}{2a} + \frac{4\pi\mathcal{G}\rho_0\mu a^2}{3} . \tag{5.45}$$

As anticipated, increased system mass, and therefore enhanced gravitation, results in an uptick in orbital frequency. Applying the quadrupole formula, sourced from [326]

$$\mathcal{P} = \frac{\mathcal{G}}{5} \dddot{I}^{(jk)} \dddot{I}^{(jk)}, \quad I^{(jk)} = \nu m \mathbf{r}^j \mathbf{r}^k , \tag{5.46}$$

where $\mathcal{P}$ denotes the gravitational wave energy loss rate and $I^{(jk)}$ is the mass quadrupole moment. For circular orbits

$$\mathcal{P} = \frac{32\nu^2\mathcal{G}^4 m^5}{5a^5} \left(1 + \frac{4\pi\rho_0 a^3}{m}\right) . \tag{5.47}$$

Considering the equilibrium equation, $\frac{dE}{dt} = -\mathcal{P}$, the evolution rate of the orbital radius is

$$\langle \dot{a} \rangle_{\rm gw} = -\frac{64\nu\mathcal{G}^3 m^3}{a^3} \left(1 - \frac{4\pi\rho_0 a^3}{3m}\right) . \tag{5.48}$$

This result is congruent with (5.41) for $\mathfrak{e} = 0$ when dark matter halo effects are deemed insignificant. It's noteworthy that while the augmented halo gravitation intensifies the radiative loss, as per (5.47), this intensification is offset by the greater energy, as demonstrated in (5.45), thereby diminishing the rate of orbital drift.

5.3 . Gravitational wave phase and the impact of dark matter

5.3.1 . Constant mass approximation

By considering first-order perturbations, we can combine the contributions from dark matter accretion, dynamical friction, and gravitational wave emission to obtain the total drift of the orbital radius

$$\langle \dot{a} \rangle = \langle \dot{a} \rangle_{\rm acc} + \langle \dot{a} \rangle_{\rm df} + \langle \dot{a} \rangle_{\rm gw} . \tag{5.49}$$

The drift in position is contingent upon the individual masses of the two black holes as well as their respective rates of accretion. For lower accretion rates, it is permissible to assume that both m_i and $\dot{m}_i$ remain unchanged throughout the duration of observation. If this observation encompasses $\mathcal{N}$ orbital cycles, with an average $\mathcal{N} \approx 100$, then it becomes necessary for $\dot{m}_i \mathcal{N} P \ll m_i$. Given the peak accretion rate as per (5.2), we obtain

$$\rho_a \ll \frac{c^3 f}{24\pi F_\star \mathcal{G}^2 m_> \mathcal{N}}\,, \tag{5.50}$$

Here, $f = 2/P_{\rm orb}$ represents the gravitational wave frequency, which is precisely double the orbital frequency, and $m_> = \max(m_1, m_2)$. From this, we derive

$$\rho_a \ll 6\times 10^{10}\,\mathcal{N}^{-1}\left(\frac{m_>}{1M_\odot}\right)^{-1}\left(\frac{f}{1\,{\rm Hz}}\right)\,{\rm g\cdot cm^{-3}}\,. \tag{5.51}$$

The most stringent constraint is related to the prospective detection of Massive Binary Black Holes (MBBH) using the LISA space interferometer at frequencies $f \gtrsim 10^{-4}{\rm Hz}$. This establishes an upper limit of $\rho_a \ll 0.01\,{\rm g/cm^3}$. This value considerably surpasses anticipated dark matter densities. As a reference, the dark matter density in the Solar system approximates $10^{-24}{\rm g/cm^3}$ [328–336]. Conversely, the baryonic densities of accretion disks around supermassive black holes can reach up to $10^{-9}{\rm g/cm^3}$ for thick accretion disks and $10^{-1}{\rm g/cm^3}$ for thin accretion disks [197]. Therefore, the limit imposed by equation (5.51) remains valid up to the baryonic densities observed in accretion disks. Beyond these densities, it becomes imperative to factor in the temporal variation of black hole masses and their accretion rates. This inclusion will amplify the deviation from the signal typically associated with a binary system in a vacuum, thereby accentuating the influence of dark matter on the waveform. Thus, our calculations offer a modest estimation of the detection threshold. Numerical checks confirm that considering $m_i(t) = m_i(t_0) + \dot{m}_i(t-t_0)$ with a constant accretion rate does not alter the results presented in section 5.5.1.

5.3.2 . Phase and coalescence time

In the limit of small eccentricity $\mathfrak{e} \ll 1$, the drift (5.49) can be expressed as

$$\dot{a} = -\frac{64\nu c}{5}\left(\frac{\mathcal{G}m}{a}\right)^3\left(1-\frac{4\pi\rho_0 a^3}{3m}\right) - aA_{\rm acc} - a\left(\frac{a}{\mathcal{G}m}\right)^{3/2}\left[B_{\rm acc} + B_{\rm df} + C_{\rm df}\ln\left(\sqrt{\frac{\mathcal{G}m}{a}}\frac{1}{c_{s,0}}\right)\right]\,. \tag{5.52}$$

The gravitational wave frequency, denoted as $\mathfrak{f}$, is double the orbital frequency as represented by (5.44). This relationship can be formally expressed as

$$\mathfrak{f} = \frac{1}{\pi}\sqrt{\frac{\mathcal{G}m}{a^3}}\left(1+\frac{2\pi\rho_0 a^3}{3m}\right)\,. \tag{5.53}$$

For clarity in this section, we employ a gothic font for $\mathfrak{f}$. This is to differentiate between $\mathfrak{f}$, which represents the time-varying frequency sweep, and f, a variable designated for the Fourier-transform in the ensuing analysis of time-sequence data in the Fourier space.

Incorporating first-order dark matter perturbations, the rate of change of $\mathfrak{f}$ with respect to time is

$$\dot{\mathfrak{f}} = \frac{1}{\pi}\sqrt{\frac{\mathcal{G}m}{a^3}}\left(\frac{\dot{m}}{2m}-\frac{3\dot{a}}{2a}\right) + \mathcal{G}\rho_0\left(\frac{a^3}{\mathcal{G}m}\right)^{1/2}\frac{\dot{a}}{a}\,. \tag{5.54}$$

When we integrate this with the relationships from (5.52) and (5.53), and factor in the accretion terms as defined by (5.2) and (5.34), it results in

$$\frac{\dot{\mathfrak{f}}}{\mathfrak{f}} = D_{\rm gw} + D_{\rm halo} + D_{\rm acc} + D_{\rm df}\,, \tag{5.55}$$

where the terms on the right side are detailed as

$$\begin{aligned}
D_{\rm gw} &= \mathfrak{f}^{8/3}\frac{96\pi^{8/3}\nu}{5}(\mathcal{G}m)^{5/3}\,,\\
D_{\rm halo} &= -\mathfrak{f}^{2/3}\frac{256\pi^{5/3}\nu\rho_0\mathcal{G}^{8/3}m^{5/3}}{3}\,,\\
D_{\rm acc} &= \frac{12\pi F_\star\mathcal{G}^2\rho_0\mu}{c_{s,0}^2}\sum_{i=1}^{2}\Theta(\mathfrak{f}<f_{{\rm acc},i})\left(3+2\frac{m_i^2}{m\mu}\right)\\
&\quad+\mathfrak{f}^{-1}4\mathcal{G}\rho_0\sum_{i=1}^{2}\Theta(\mathfrak{f}>f_{{\rm acc},i})\frac{m_i^3}{\mu^2 m}\left(3+2\frac{m_i^2}{m\mu}\right)\,,\\
D_{\rm df} &= -\mathfrak{f}^{-1}\frac{4\mathcal{G}\rho_0}{3}\sum_{i=1}^{2}\Theta(f_{{\rm df},i}^{-}<\mathfrak{f}<f_{{\rm df},i}^{+})\frac{m_i^3}{\mu^2 m}\ln\left(\frac{\mathfrak{f}}{f_{{\rm df},i}^{+}}\right)\,.
\end{aligned}$$

Furthermore, the accretion and drag forces are expressed as

$$f_{{\rm acc},i} = \frac{c_{s,0}^2 m_i^3}{3\pi F_\star\mathcal{G}m\mu^3}\,,\quad f_{{\rm df},i}^{-} = \frac{c_{s,0}^3 m_i^3}{\pi\mathcal{G}m\mu^3}\,,\quad f_{{\rm df},i}^{+} = \frac{e^3 c_{s,0}^3 m^5\mu^{15}}{5832\pi\mathcal{G}m_i^{21}}\,. \tag{5.56}$$

In (5.55), we have dissected the contributions from gravitational waves. Specifically, we have divided these into the standard term, $\mathfrak{f}^{8/3}$, related to Keplerian orbits, and a correction term, $\mathfrak{f}^{2/3}$, attributed to the influence of the dark matter halo. Let us consider the phase integration, represented as $\Phi(t) = 2\pi\int d\mathfrak{f}\,(\mathfrak{f}/\dot{\mathfrak{f}})$, and the time integration, symbolized by $t = \int d\mathfrak{f}\,(1/\dot{\mathfrak{f}})$ over the gravitational wave frequency [337]. This gives us

$$\Phi(\mathfrak{f}) = \Phi_c + \Phi_{\rm gw} + \Phi_{\rm halo} + \Phi_{\rm acc} + \Phi_{\rm df}\,, \tag{5.57}$$

$$t(\mathfrak{f}) = t_c + t_{\rm gw} + t_{\rm halo} + t_{\rm acc} + t_{\rm df}\,. \tag{5.58}$$

Here, Φ_c and t_c denote the phase and time at coalescence, respectively. The following introduces some specific contributions

$$\Phi_{\rm gw} = -2\pi\int_{\mathfrak{f}}^{\infty} d\mathfrak{f}\frac{1}{D_{\rm gw}},\ldots \tag{5.59}$$

and so forth.

Equations (5.57) and (5.58) implicitly articulate the function $\Phi(t)$, which delineates the GW phase against time. We have assumed a linear approximation over the dark matter contributions to frequency drift, hypothesizing that they are lesser in magnitude than the Keplerian gravitational wave input. Our findings in Section 5.3.3 corroborate this assumption in practical scenarios. This assumption is also sufficient for gauging the requisite dark matter density thresholds for detection. At exceedingly high densities, our drift frequency calculations may be questionable, but the manifestation of dark matter in the data remains unambiguous. It is worth noting that the influence of dark matter is more pronounced during the early inspiral stages, specifically at lower frequencies. Thus, relativistic adjustments to the orbital motion won't significantly affect our evaluations for dark matter detection thresholds.

For the gravitational wave signal represented as $h(t) = \mathcal{A}(t)\cos[\Phi(t)]$, where $\Phi(t)$ is implicitly described by (5.57) and (5.58), and $\mathcal{A}(t) \propto \mathfrak{f}^{2/3}$ when neglecting dark matter amplitude corrections [326], the Fourier-space data analysis considers the transform

$$\tilde{h}(f) = \int dt\, e^{i2\pi ft} h(t)\,. \tag{5.60}$$

Using the stationary phase approximation [337], the resultant is $\tilde{h}(f) = \mathcal{A}(f)e^{i\Psi(f)}$, detailed as

$$\mathcal{A}(f) \propto f^{-7/6},\, \Psi(f) = 2\pi f t_\star - \Phi(t_\star) - \pi/4\,, \tag{5.61}$$

where the saddle-point $t_\star$ is established by $\mathfrak{f}(t_\star) = f$ as $\dot{\Phi} = 2\pi\mathfrak{f}$. Utilizing the relationships presented in (5.57) and (5.58), the expression for $\Psi(f)$ is formulated as

$$\Psi(f) = 2\pi f t_c - \Phi_c - \frac{\pi}{4} + \Psi_{\text{gw}} + \Psi_{\text{halo}} + \Psi_{\text{acc}} + \Psi_{\text{df}}\,. \tag{5.62}$$

Here, the various components are delineated as follows

$$\begin{aligned} \Psi_{\text{gw}} &= 2\pi\left[\int_f^\infty df\,\frac{1}{D_{\text{gw}}} - f\int_f^\infty \frac{df}{f}\,\frac{1}{D_{\text{gw}}}\right]\,, \\ \Psi_{\text{halo}} &= 2\pi\left[f\int_f^\infty \frac{df}{f}\,\frac{D_{\text{halo}}}{D_{\text{gw}}^2} - \int_f^\infty df\,\frac{D_{\text{halo}}}{D_{\text{gw}}^2}\right]\,, \ldots\,. \end{aligned} \tag{5.63}$$

As referenced by [337]

$$\Psi_{\text{gw}} = \frac{3}{128}\left(\pi\mathcal{G}\mathcal{M}f\right)^{-5/3}\left[1 + \frac{20}{9}\left(\frac{743}{336} + \frac{11}{4}\nu\right) \times \left(\pi\mathcal{G}mf\right)^{2/3}\right]\,, \tag{5.64}$$

where the chirp mass $\mathcal{M}$ is defined as

$$\mathcal{M} = \nu^{3/5} m\,. \tag{5.65}$$

Subsequently, other contributions are defined as

$$\Psi_{\text{halo}} = \frac{25\pi}{924}\rho_0\mathcal{G}^3\mathcal{M}^2\left(\pi\mathcal{G}\mathcal{M}f\right)^{-11/3}\,, \tag{5.66}$$

$$\begin{aligned} \Psi_{\text{acc}} = &-\frac{25\pi\mathcal{G}^3\mathcal{M}^2\rho_0}{38912}\left(\pi\mathcal{G}\mathcal{M}f\right)^{-16/3}\sum_{i=1}^{2}\Theta(f > f_{\text{acc},i}) \times \frac{m_i^3}{\mu^2 m}\left(3 + 2\frac{m_i^2}{m\mu}\right) \\ &- \frac{75\pi F_\star \nu^{2/5}\mathcal{G}^3\mathcal{M}^2\rho_a}{26624}\left(\pi\mathcal{G}\mathcal{M}f\right)^{-13/3} \times \sum_{i=1}^{2}\Theta(f < f_{\text{acc},i}) \\ &\times \left(3 + 2\frac{m_i^2}{m\mu}\right)\left[1 - \left(\frac{f}{f_{\text{acc},i}}\right)^{13/3} + \frac{13}{19}\left(\frac{f}{f_{\text{acc},i}}\right)^{16/3}\right]\,, \end{aligned} \tag{5.67}$$

$$
\begin{aligned}
\Psi_{\rm df} = {} & \frac{875\pi\mathcal{G}^3\mathcal{M}^2\rho_0}{11829248}\,(\pi\mathcal{G}\mathcal{M}f)^{-16/3}\sum_{i=1}^{2}\frac{m_i^3}{\mu^2 m}\Theta(f^-_{{\rm df},i} < f^+_{{\rm df},i}) \\
& \times\Bigg\{\Theta(f^-_{{\rm df},i} < f < f^+_{{\rm df},i})\left[1+\frac{304}{105}\ln\frac{f}{f^+_{{\rm df},i}}-\frac{361}{105}\left(\frac{f}{f^+_{{\rm df},i}}\right)^{16/3}+\frac{256}{105}\left(\frac{f}{f^+_{{\rm df},i}}\right)^{19/3}\right] \\
& +\Theta(f < f^-_{{\rm df},i})\left[-\frac{361}{105}\left(\frac{f}{f^+_{{\rm df},i}}\right)^{16/3}+\frac{361}{105}\left(\frac{f}{f^-_{{\rm df},i}}\right)^{16/3}+\frac{5776}{315}\left(\frac{f}{f^-_{{\rm df},i}}\right)^{16/3}\ln\frac{f^-_{{\rm df},i}}{f^+_{{\rm df},i}}\right. \\
& \left.+\frac{256}{105}\left(\frac{f}{f^+_{{\rm df},i}}\right)^{19/3}-\frac{256}{105}\left(\frac{f}{f^-_{{\rm df},i}}\right)^{19/3}-\frac{4864}{315}\left(\frac{f}{f^-_{{\rm df},i}}\right)^{19/3}\ln\frac{f^-_{{\rm df},i}}{f^+_{{\rm df},i}}\right]\Bigg\}\,, \qquad (5.68)
\end{aligned}
$$

Lastly, the inclusion of the factors Θ denotes that solely the smaller black hole contributes to dynamical friction when a specific range is encountered where both conditions, $v_i > V_\star$ and $v_i < V_{\rm rel}$ are met.

In the gravitational phase (5.64), the inclusion of the first post-Newtonian 1 PN order [337] disrupts the degeneracy between the black hole masses m_1 and m_2. This is indicated by the leading term exclusively depending on the chirp mass $\mathcal{M}$. Thus, the phase in (5.64) is dependent on both m_1 and m_2, allowing the gravitational wave signal to constrain both black hole masses. Although higher-order 1.5 PN and 2 PN terms can constrain the black hole spins as per [337], this paper does not account for spins.

5.3.3 . Comparative significance of the contributions

Referring to (5.64) and (5.66), we derive

$$
\frac{\Psi_{\rm halo}}{\Psi_{\rm gw}} = \frac{800\rho_0\mathcal{G}}{693\pi f^2} \approx 2\times10^{-8}\frac{\rho_0}{1\,{\rm g\cdot cm^{-3}}}\left(\frac{f}{1\,{\rm Hz}}\right)^{-2}, \qquad (5.69)
$$

maintaining only the predominant term in $\Psi_{\rm gw}$. It is noteworthy that this ratio remains unaffected by black hole masses and is rather small. Thus, the gravitational potential of the dark matter cloud can often be overlooked.

Now for the accretion impact, let us define $m_> = \max(m_1, m_2)$ and $m_< = \min(m_1, m_2)$ as the larger and smaller masses of the binary respectively. Drawing from (5.56), we get

$$
\begin{aligned}
f_{{\rm acc},<} &\approx 3\times10^4\frac{\rho_0}{\rho_a}\left(\frac{m_>}{1\,M_\odot}\right)^{-1}{\rm Hz}\,, \\
f_{{\rm acc},>} &\approx 3\times10^4\frac{\rho_0}{\rho_a}\left(\frac{m_>}{m_<}\right)^{3}\left(\frac{m_>}{1\,M_\odot}\right)^{-1}{\rm Hz}\,. \qquad (5.70)
\end{aligned}
$$

Given that $\rho_0 \ll \rho_a$, these frequencies usually lie below 1 Hz. Consequently, the lesser mass black hole may encounter both accretion scenarios within the observable frequency range. The impact of accretion is predominantly noticeable for the more substantial black hole due to the factors in (5.67). Emphasizing on this aspect, we determine

$$f > f_{\mathrm{acc},>} : \frac{\Psi_{\mathrm{acc},>}}{\Psi_{\mathrm{gw}}} \approx 0.1 \left(\frac{m_>}{m_<}\right)^4 \frac{\rho_0}{1\,\mathrm{g}\cdot\mathrm{cm}^{-3}} \left(\frac{m_>}{1\,M_\odot}\right)^{-5/3} \left(\frac{f}{1\,\mathrm{Hz}}\right)^{-11/3}, \tag{5.71}$$

$$f < f_{\mathrm{acc},>} : \frac{\Psi_{\mathrm{acc},>}}{\Psi_{\mathrm{gw}}} \approx 5 \times 10^{-6} \left(\frac{m_>}{m_<}\right) \frac{\rho_a}{1\,\mathrm{g}\cdot\mathrm{cm}^{-3}} \left(\frac{m_>}{1\,M_\odot}\right)^{-2/3} \left(\frac{f}{1\,\mathrm{Hz}}\right)^{-8/3}. \tag{5.72}$$

Clearly, accretion has a more pronounced effect on the phase than the influence from the gravity of the cloud. Yet, when juxtaposed with the regular gravitational waves contribution Ψ_{gw}, it is relatively minor. Interestingly, this effect is more pronounced for small masses and lower frequencies, suggesting its heightened significance during the initial phases of inspiral.

Finally, for the dynamical fiction impact, based on (5.56), we compute

$$\begin{aligned} f^-_{\mathrm{df},<} &\approx 6 \times 10^4 \left(\frac{\rho_0}{\rho_a}\right)^{3/2} \left(\frac{m_>}{1\,M_\odot}\right)^{-1} \mathrm{Hz}\,, \\ f^-_{\mathrm{df},>} &\approx 6 \times 10^4 \left(\frac{\rho_0}{\rho_a}\right)^{3/2} \left(\frac{m_>}{m_<}\right)^3 \left(\frac{m_>}{1\,M_\odot}\right)^{-1} \mathrm{Hz}\,, \end{aligned} \tag{5.73}$$

and

$$\begin{aligned} f^+_{\mathrm{df},<} &\approx 2 \times 10^2 \left(\frac{\rho_0}{\rho_a}\right)^{3/2} \left(\frac{m_>}{m_<}\right)^6 \left(\frac{m_>}{1\,M_\odot}\right)^{-1} \mathrm{Hz}\,, \\ f^+_{\mathrm{df},>} &\approx 2 \times 10^2 \left(\frac{\rho_0}{\rho_a}\right)^{3/2} \left(\frac{m_<}{m_>}\right)^{15} \left(\frac{m_>}{1\,M_\odot}\right)^{-1} \mathrm{Hz}\,. \end{aligned} \tag{5.74}$$

This reveals that predominantly, the smaller black hole experiences a strong dynamical friction, especially when the mass ratio is large. Further calculations show

$$f^-_{\mathrm{df},<} < f < f^+_{\mathrm{df},<} \; : \; \frac{\Psi_{\mathrm{df}}}{\Psi_{\mathrm{gw}}} \approx 7 \times 10^{-3} \frac{\rho_0}{1\,\mathrm{g}\cdot\mathrm{cm}^{-3}} \left(\frac{m_>}{1\,M_\odot}\right)^{-5/3} \left(\frac{f}{1\,\mathrm{Hz}}\right)^{-11/3}. \tag{5.75}$$

In comparison to the accretion effect, this is scaled down by a factor of $(m_</m_>)^4$. This occurs because the larger black hole dominates accretion, whereas, based on our assumptions, only the smaller black hole undergoes significant dynamical friction. Once more, this difference is less prominent when compared to the primary gravitational waves effect, Ψ_{gw}. Similar to the accretion effect, its significance rises during the initial inspiral phase, thanks to the inverse relation with frequency.

5.3.4 . Effective post-Newtonian orders

The phase Ψ elements scaling with f^α can be attributed an effective post-Newtonian order $n = 3\alpha/2 + 5/2$. For instance, the gravitational influence of the cloud is characterized by a -3 PN tier, as in (5.66). The accretion process contributes -4 PN at lower frequencies and -5.5 PN at upper ones when dominant terms are isolated. Within the frequency bounds $f^-_{\mathrm{df}} < f < f^+_{\mathrm{df}}$, dynamical friction also imparts a -5.5 PN tier. These negative tiers underscore the heightened significance of dark matter contributions at lower frequencies during the earlier inspiral stages. Notably, these are non-synonymous with conventional relativistic adjustments, which are linked with positive post-Newtonian orders.

The back-reaction of the scalar field is not considered in this analysis. Studies of the fuzzy dark matter scenario have shown that the scalar field back-reaction gives a -6 PN effect contribution, which is too small to be observed [271, 338]. However, the dynamical friction can heat the gas and lead to a depletion of dark matter in the vicinity of the orbital radius, reducing the actual amount of dynamical friction [264, 339]. The effect of self-interactions on dynamical friction is lessened by the effective pressure in the self-interacting case considered in this analysis. Additionally, the small-scale cutoff given by (4.46) makes the dynamical friction insensitive to the local dark matter density. Worthy of mention at the 5 PN order are deformability influences stemming from non-zero Love numbers for black holes increased by scalar fields, as elaborated in [57, 58]. Focusing on the lower scalar-mass threshold in fuzzy dark matter paradigms, where $\alpha = m_{\rm DM} m_{\rm BH} \mathcal{G} \ll 1$, findings suggest these influences intensify at α^{-8} and gain prominence for $\alpha \lesssim 0.1$. This research, however, narrows down to the higher scalar-mass spectrum, where $\alpha \gg 1$ as depicted in (2.30). Consequently, we anticipate negligible tidal Love numbers. Another important difference is the predominance of the self-interactions in our case.

5.3.5 . Characteristics of dark matter: Parameters ρ_a and ρ_0

From prior discussions, it is evident that the gravitational wave signal is influenced by the surrounding dark matter environment through two distinct parameters: ρ_a and ρ_0. Specifically, ρ_a is associated with the characteristic density as detailed in equation (2.3), which arises from the self-interaction of dark matter. On the other hand, ρ_0 represents the overall density of the dark matter cloud.

Considering the gravitational influence of the cloud, detailed in equation (5.66), as well as the high-frequency accretion (5.67) and the dynamic friction (5.68), these properties scale with ρ_0. Conversely, low-frequency accretion, as indicated in (5.67), scales with ρ_a. Moreover, the thresholds presented in equation (5.56) are contingent on $c_{s,0} \propto \sqrt{\rho_0/\rho_a}$. Given these relationships, it is theoretically possible to deduce both parameters if observational data encompasses the low-frequency accretion phase or at a minimum, captures one of the mentioned frequency thresholds.

5.4 . Fisher information matrix

5.4.1 . Fisher analysis

We employ a Fisher analysis to estimate the detectable dark matter densities, namely ρ_a and ρ_0, through the measurement of gravitational waves emitted by binary black holes during their inspiral phase. The Fisher matrix, denoted by Γ_{ij}, is given by [337, 340]

$$\Gamma_{ij} = 4\,\mathrm{Re} \int_{f_{min}}^{f_{\rm max}} \frac{df}{S_n(f)} \left(\frac{\partial \tilde{h}}{\partial \theta_i} \right)^{\star} \left(\frac{\partial \tilde{h}}{\partial \theta_j} \right) , \tag{5.76}$$

where $\{\theta_i\}$ represents the parameters to be measured and $S_n(f)$ denotes the noise spectral density, which relies on the specific gravitational wave interferometer utilized. The quantities f_{min} and $f_{\max}$ denote the lower and upper boundaries of the frequency spectrum associated with each event. These boundaries are influenced by the characteristics of the interferometer, as outlined in section 5.4.3, as well as by potential constraints such as the nonrelativistic cutoff discussed in section 5.4.5. The signal-to-noise ratio is defined as

$$(\text{SNR})^2 = 4\int_{f_{min}}^{f_{\max}} \frac{df}{S_n(f)}\,|\tilde{h}(f)|^2\,. \tag{5.77}$$

By expressing the gravitational waveform as $\tilde{h}(f) = \mathcal{A}_0 f^{-7/6} e^{i\Psi(f)}$, analogous to (5.61) and (5.62), we derive the expression for Γ_{ij} as

$$\Gamma_{ij} = \frac{(\text{SNR})^2}{\int_{f_{min}}^{f_{\max}} \frac{df}{S_n(f)} f^{-7/3}} \int_{f_{min}}^{f_{\max}} \frac{df}{S_n(f)} f^{-7/3} \frac{\partial\Psi}{\partial\theta_i}\frac{\partial\Psi}{\partial\theta_j}\,, \tag{5.78}$$

where the parameters considered are $\{\theta_i\} = \{t_c, \Phi_c, \ln(m_1), \ln(m_2), \rho_0, \rho_a\}$. It is worth noting that the amplitude $\mathcal{A}_0$ represents an additional parameter, but it is not considered further as the Fisher matrix is block-diagonal and the amplitude is decorrelated from the other parameters $\{\theta_i\}$ [337].

In comparison to the study presented in [222], we disregard the effective spin χ_{eff}, defined as $\chi_{\text{eff}} = (m_1\chi_1 + m_2\chi_2)/M$, which was taken into account solely for calculating the last stable orbit using the analytical PhenomB templates [341]. This omission is due to the fact that our results for the accretion rate and dynamical friction have been derived specifically for Schwarzschild black holes. However, we anticipate that the order of magnitude obtained for the dark matter densities will remain valid even for moderate spins. Another distinction from [222] is that, in addition to the dark matter density ρ_0, which describes the bulk of the cloud, we introduce a second characteristic density ρ_a. This density characterizes the dark matter density near the Schwarzschild radius and is directly linked to the strength of dark matter self-interaction. By utilizing the Fisher matrix, we obtain the covariance $\Sigma_{ij} = \left(\Gamma^{-1}\right)_{ij}$, providing the standard deviation on the various parameters as $\sigma_i = \langle(\Delta\theta_i)^2\rangle^{1/2} = \sqrt{\Sigma_{ii}}$. See Appendix E for more details on Fisher analysis.

5.4.2 . Exploring the (ρ_0, ρ_a) parameter space

In our study, we analyze detection thresholds within a dark matter medium. We approximate that the influence of dark matter is small, enabling us to linearize its effects. Consequently, the phase changes represented by equations (5.66) to (5.68) are directly related to the densities ρ_0 or ρ_a at fixed speed of sound $c_{s,0}$. The gravitational influences due to halo effects (5.66), high-frequency or high-velocity accretion (5.67), and dynamical friction (5.68) scale with the bulk density ρ_0. In contrast, the accretion during low-frequency or low-velocity conditions (5.67) scales with the characteristic density ρ_a, associated with the maximum allowed accretion rate. In the absence or minimal presence of a dark matter halo, the standard waveform parameters given by $\{\theta_i\}_{i=1,4} = \{t_c, \Phi_c, \ln(m_1), \ln(m_2)\}$ are shaped by the primary four components of the phase (5.62). This includes the t_c,

Φ_c elements, and the gravitational wave component $\Psi_{\rm gw}$. This configuration mirrors the routine assessment for binary systems in a vacuum setting. For a small dark matter halo, especially when ρ_0 and ρ_a are zero, this provides the 4×4 elements Γ_{ij} (where $1 \leq i, j \leq 4$) of the Fisher matrix. The existence of a dark matter background becomes relevant in the phase from equations (5.66) to (5.68). These effects possess amplitudes that are functions of ρ_0 or ρ_a and include other factors like the Heaviside function Θ and more gradual variations represented by $1 + (f/f_{\rm acc})^{13/3}$ or $\ln(f/f_{\rm df}^{+})$. The frequency set (5.56) hinges not on ρ_0 and ρ_a separately, but on the sound speed $c_{s,0}$. This is represented by the ratio y given by

$$y = \frac{\rho_a}{\rho_0} = \frac{1}{c_{s,0}^2} \geq 1\,. \tag{5.79}$$

Hence, the various accretion and dynamical friction conditions are bounded by certain values of y, which carve out specific angular regions in the (ρ_0, ρ_a) parameter space. The physical region of the positive quadrant, characterized by $\{\rho_0 \geq 0, \rho_a \geq 0\}$, is confined to the upper diagonal where $\rho_a \geq \rho_0$, owing to the limitation $c_{s,0} \leq 1$. For a specified binary system with an observational frequency range denoted as $[f_{\rm min}, f_{\rm max}]$, we can introduce accretion thresholds based on y as follows

$$f_{\rm min} < f_{{\rm acc},i}: \quad y < y_{{\rm acc},i}^{+}\,, \quad y_{{\rm acc},i}^{+} = \frac{m_i^3}{3\pi F_\star \mathcal{G} m \mu^3 f_{\rm min}}\,, \tag{5.80}$$

$$f_{\rm max} < f_{{\rm acc},i}: \quad y < y_{{\rm acc},i}^{-}\,, \quad y_{{\rm acc},i}^{-} = \frac{m_i^3}{3\pi F_\star \mathcal{G} m \mu^3 f_{\rm max}}\,. \tag{5.81}$$

Additionally, dynamical friction thresholds can be defined as

$$f_{\rm min} < f_{{\rm df},i}^{+}: \quad y < y_{{\rm df},i}^{+}\,, \quad y_{{\rm df},i}^{+} = \left(\frac{e^3 m^5 \mu^{15}}{5832\pi \mathcal{G} m_i^{21} f_{\rm min}}\right)^{2/3}\,, \tag{5.82}$$

$$f_{\rm max} > f_{{\rm df},i}^{-}: \quad y > y_{{\rm df},i}^{-}\,, \quad y_{{\rm df},i}^{-} = \left(\frac{m_i^3}{\pi \mathcal{G} m \mu^3 f_{\rm max}}\right)^{2/3}\,. \tag{5.83}$$

If we arrange the black hole masses such that $m_1 \geq m_2$, the following relations hold

$$m_1 \geq m_2: \quad y_{\rm acc,1}^{+} \geq y_{\rm acc,2}^{+} \quad \text{and} \quad y_{\rm acc,1}^{-} \geq y_{\rm acc,2}^{-}\,. \tag{5.84}$$

It is worth noting that only the smaller black hole, m_2, undergoes significant dynamical friction. The behavior of the accretion term $\Psi_{\rm acc}$ is divided as:

- For $y > y_{\rm acc,1}^{+}$: There is no accretion dependence on ρ_a.
- For $y < y_{\rm acc,2}^{-}$: Accretion is independent of ρ_0.

The dependence on $c_{s,0}$ in the terms inside (5.67) converges quickly to one below the threshold $f_{{\rm acc},i}$. Similarly, the behavior of the dynamical friction term $\Psi_{\rm df}$ can be segmented as:

- For $y > y_{\rm df,2}^{+}$: No dynamical friction is observed.

- For $y^-_{\mathrm{df},2} < y < y^+_{\mathrm{df},2}$: The system experiences dynamical friction.
- When $y < y^-_{\mathrm{df},2}$: Dynamical friction overlaps with t_c and Φ_c.

Furthermore, the terms inside (5.68) disregard the dependence on $c_{s,0}$.

In the domain of high-y

$$y > \max(y^+_{\mathrm{acc},1}, y^+_{\mathrm{df},2}) \,, \tag{5.85}$$

the phase Ψ predominantly responds to ρ_0, mediated by the halo gravity as illustrated in (5.66) and the high-frequency spectrum of the accretion as depicted in (5.67). This indicates an absence of constraints on ρ_a, and that the gravitational wave data solely yield an upper limit for the ambient density ρ_0. Consequently, the Fisher matrix, given by (5.76), materializes as a 5×5 matrix. From this, the covariance matrix can be represented as $\Sigma_{ij} = \left(\Gamma^{-1}\right)_{ij}$, and the standard deviation of ρ_0 is defined as $\sigma_{\rho_0} = \sqrt{\Sigma_{\rho_0\rho_0}}$. This aligns with the detection threshold $\rho_{0\star} = \sigma_{\rho_0}$: halos possessing an large dark matter density can be discerned using gravitational wave data, but halos with lesser density remain indistinguishable from vacuum binaries. As observed in Section 5.3.3, the influence of halo gravity is minor when compared with the impact of accretion. When correlations between binary parameters $\{t_c, \Phi_c, \ln(m_1), \ln(m_2)\}$ and ρ_0 are negligible, the detection threshold, $\rho_{0\star}$, can be approximated using the expression

$$\rho_{0\star} \gtrsim \frac{1}{\mathrm{SNR}} \frac{19456 c^6}{25\pi \mathcal{G}^3 m_1^2} (\pi \mathcal{G} m_1 f_{\min})^{16/3} \left(\frac{m_2}{m_1}\right)^5 \,, \tag{5.86}$$

which can be further refined to

$$\rho_{0\star} \gtrsim \frac{3 \times 10^{-6}}{\mathrm{SNR}} \left(\frac{m_2}{m_1}\right)^5 \left(\frac{m_1}{1\,M_\odot}\right)^{10/3} \left(\frac{f_{\min}}{1\,\mathrm{Hz}}\right)^{16/3} \mathrm{g/cm}^3 \,. \tag{5.87}$$

This suggests that this lower boundary improves for instruments sensitive to lower frequencies and for binaries exhibiting a larger mass ratio. However, when engaging in a comprehensive Fisher analysis, partial overlaps between various parameters combined with the restricted frequency range $[f_{\min}, f_{\max}]$ designate a detection threshold slightly exceeding the one described by (5.87).

In the subsequent discussion on IMRI and EMRI cases in Section 5.5.1, we identify an intermediate range where dynamical friction becomes significant, while accretion remains unaffected by ρ_a

$$y^-_{\mathrm{df},2} < y^+_{\mathrm{acc},1} < y < y^+_{\mathrm{df},2} \,. \tag{5.88}$$

When we simplify our analysis by not considering the $c_{s,0}$ dependence in the terms of (5.68), the function Ψ_{df} is viewed as linearly dependent on ρ_0 for a set density ratio y. Consequently, the Fisher matrix (5.76) remains a 5×5 matrix. Using the standard deviation $\sigma_{\rho_0} = \sqrt{\Sigma_{\rho_0\rho_0}}$, we deduce the point $(\rho_{0\star} = \sigma_{\rho_0}, \rho_{a\star} = y\sigma_{\rho_0})$. This point establishes a boundary in the (ρ_0, ρ_a) plane, indicating the detection threshold.

Finally, for small values of y defined as

$$1 \leq y < y^+_{\mathrm{acc},1} \,, \tag{5.89}$$

the accretion influence is a function of ρ_a, whereas the gravitational impact of the halo consistently depends on ρ_0. Given this, we are working with two dark matter parameters, rendering the Fisher matrix as a 6×6 entity. To further this analysis, for a specific density ratio y, we evaluate the corresponding Fisher ellipse in the (ρ_0, ρ_a) plane. Its intersection with the direction $\rho_a/\rho_0 = y$ is also assessed. Consequently, from the 6×6 Fisher matrix Γ_{ij}, we deduce the equivalent 6×6 covariance matrix Σ_{ij}. Marginalizing over the binary parameters $\{t_c, \Phi_c, \ln(m_1), \ln(m_2)\}$, we then establish a new 2×2 covariance matrix $\hat{\Sigma}_{ij}$, pertinent to the rows and columns of the remaining parameters ρ_0 and ρ_a. This results in the 2×2 Fisher matrix $\hat{\Gamma} = \hat{\Sigma}^{-1}$, determining the Fisher ellipse in the (ρ_0, ρ_a) plane. The boundary point becomes

$$\rho_{0\star} = \left(\hat{\Gamma}_{\rho_0\rho_0} + 2y\hat{\Gamma}_{\rho_0\rho_a} + y^2\hat{\Gamma}_{\rho_a\rho_a}\right)^{-1/2} , \quad \rho_{a\star} = y\rho_{0\star} . \tag{5.90}$$

Notably, most of the dark matter signal emerges from the accretion influence at low frequencies, leading to a near constant threshold for ρ_a. Ignoring parameter correlations, we deduce

$$\rho_{a\star} \gtrsim \frac{1}{\mathrm{SNR}} \left| \frac{\partial \Psi_{\mathrm{acc}}}{\partial \rho_a} \right|^{-1} , \tag{5.91}$$

$$\rho_{a\star} \gtrsim \frac{1}{\mathrm{SNR}} \frac{13312 c^6}{75\pi F_\star \mathcal{G}^3 m_1^2} \left(\pi \mathcal{G} m_1 f_{\mathrm{min}}\right)^{13/3} \left(\frac{m_2}{m_1}\right)^2 , \tag{5.92}$$

that can finally be expressed as

$$\rho_{a\star} \gtrsim \frac{0.08}{\mathrm{SNR}} \left(\frac{m_2}{m_1}\right)^2 \left(\frac{m_1}{1\,M_\odot}\right)^{7/3} \left(\frac{f_{\mathrm{min}}}{1\,\mathrm{Hz}}\right)^{13/3} \mathrm{g/cm}^3 . \tag{5.93}$$

This lower boundary is more pronounced for instruments that probe low frequencies and binaries exhibiting a larger mass ratio. Nevertheless, owing to some overlap and the confined frequency range, the detection limit derived from the Fisher matrix inversion slightly exceeds the given estimate.

5.4.3 . Gravitational-wave detectors

The gravitational-wave detectors considered in our analysis are as follows:

- LISA (Laser Interferometer Space Antenna) [66]: a space-based gravitational-wave observatory designed to detect low-frequency gravitational waves in the millihertz range. It consists of three spacecraft forming an equilateral triangle with laser interferometry to measure the minute changes in distance caused by passing gravitational waves.

- B-DECIGO (Deci-hertz Interferometer Gravitational wave Observatory) [67]: a preliminary test for the technologies planned to be used in DECIGO, a future proposed detector concept aiming to detect gravitational waves in the frequency range from

0.1 hertz to 10 hertz. It utilizes a pair of satellites connected by a long arm to measure the gravitational wave-induced changes in the arm length.

- ET (Einstein Telescope) [280]: a third-generation ground-based gravitational-wave detector. It aims to operate at lower frequencies compared to current detectors like Advanced LIGO. ET would employ an underground triangular configuration of interferometers with arms of several tens of kilometers in length.

- Adv-LIGO (Advanced Laser Interferometer Gravitational wave Observatory) [279]: an upgraded version of the LIGO detector. It operates on Earth and is designed to detect gravitational waves in the frequency range from a few tens of hertz to a few kilohertz. Adv-LIGO consists of multiple kilometers-long interferometer arms with high-precision optical components.

For our analysis, we utilize the noise spectral densities provided in the following references: Adv-LIGO: Barsotti et al. [342], ET: Hild et al. [343], LISA: LISA Consortium [344], B-DECIGO: Isoyama et al. [345].

The frequency ranges relevant to our analysis are detailed in Table 5.1. Additionally, we define the PhenomB inspiral-merger transition value as f_1 following the formulation in [341]. Moreover, we introduce $f_{\rm obs} = 4.149\times 10^{-5}\left(\frac{\mathcal{M}}{10^6 M_\odot}\right)^{-\frac{5}{8}}\left(\frac{T_{\rm obs}}{1\,\rm yr}\right)^{-\frac{3}{8}}$, which represents the frequency at a given observational time before the merger, as defined in [346]. In our computations, we consider $T_{\rm obs} = 4$ years as the observational duration.

Detector \ Frequency	$f_{\rm min}(\rm Hz)$	$f_{\rm max}(\rm Hz)$
LISA	$\max\left(2\times 10^{-5}, f_{\rm obs}\right)$	$min\left(10^2, f_1\right)$
B-DECIGO	10^{-2}	$min\left(1, f_1\right)$
ET	3	f_1
Adv-LIGO	10	f_1

Table 5.1: Gravitational waves frequency band considered for the LISA, B-DECIGO, ET and Adv-LIGO interferometers, where $f_{\rm obs}$ is the frequency of the binary 4 years before the merger [346] and f_1 is the PhenomB inspiral-merger transition value [341].

5.4.4 . Events

We focus on the description of six events, consisting of two ground-based (taking the mean detected values for two famous events, which are the first detected gravitational waves GW150914 [347] and GW170608 [348]) and four space-based events. The latter four events specifically pertain to the LISA detector, given its distinct detection range compared to the others. All the events under consideration involve binary black holes. The space-based events encompass various types of binaries, including Massive Binary Black Holes (MBBH), Intermediate Binary Black Holes (IBBH), Intermediate Mass Ratio Inspiral (IMRI), and Extreme Mass Ratio Inspiral (EMRI). It is important to note that all of these events fall under the same classification as the events considered by [222]. We specifically focus on black hole binaries and do not consider binaries involving neutron stars. The specific details of these events, including relevant parameters, are provided in Table 5.2. Additionally, to provide a comprehensive overview, we include information about the spins and $\chi_{\rm eff}$ (which determines the upper frequency cutoff of the data analysis) for each event.

Properties / Event	m_1 ($\mathrm{M}_\odot$)	m_2 ($\mathrm{M}_\odot$)	χ_1	χ_2	$\chi_{\rm eff}$
MBBH	10^6	5×10^5	0.9	0.8	0.87
IBBH	10^4	5×10^3	0.3	0.4	0.33
IMRI	10^4	10	0.8	0.5	0.80
EMRI	10^5	10	0.8	0.5	0.80
GW150914	35.6	30.6	0.13	0.05	0.09
GW170608	11	7.6	0.13	0.50	0.28

Table 5.2: Details on masses and spins of the considered events. The information on GW150914 and GW170608 are taken from [221].

The Signal-to-Noise Ratio (SNR) values for these events are obtained from [222] and summarized in Table 5.3.

Detector / Event	LISA	B-DECIGO	ET	Adv-LIGO
MBBH	3×10^4	×	×	×
IBBH	708	×	×	×
IMRI	22	×	×	×
EMRI	64	×	×	×
GW150914	×	2815	615	40
GW170608	×	2124	502	35

Table 5.3: Value of the signal-to-noise ratio (SNR) of the considered events for each detector, taken from [222].

5.4.5 . Relativistic corrections

The dynamical friction formulae utilized in this analysis are valid under the nonrelativistic limit $v \ll 1$. In the case of relativistic corrections, a corrective prefactor of $\gamma^2(1+v^2)^2$ is typically introduced to the dynamical friction [273, 349, 350]. This prefactor can be derived in the collisionless scenario by considering the relativistic formula for the deflection angle in scattering and the relativistic Lorentz boost between the fluid and black hole frames [349]. It is important to note that this approximation remains valid in the highly supersonic case, where streamlines at large radii follow collisionless trajectories due to the negligible impact of pressure effects.

For velocities as high as $v^2 \sim 0.137$, the relativistic correction only introduces a multiplicative factor of approximately 1.5. Since dark matter contributions are most significant during the early inspiral phase, it can be observed that relativistic corrections can be neglected without significantly altering the order of magnitude of the results. To ensure that relativistic corrections remain modest, the analysis is typically truncated below the frequency f_γ, where $v^2 = 0.137$. This truncation guarantees that relativistic corrections remain within an acceptable range. By considering these factors, we can affirm that relativistic corrections do not significantly impact the overall magnitude of the results, especially during the early inspiral phase where the dark matter contributions are most relevant.

5.5 . Detection and constraints

5.5.1 . Detection prospects

The results for the detection thresholds in the (ρ_0, ρ_a) plane, following the Fisher matrix analysis outlined in Section 5.4, are presented in Figures 5.2 and 5.3.

In the context of the LISA-MBBH scenario, which is depicted in the upper left quadrant of Figure 5.2, several pertinent observations can be made:

- The black dashed line sloping downwards represents the physical boundary, specified by the condition $y = 1$ (where $c_{s,0} = 1$).
- The blue dotted lines correspond to the thresholds $y^+_{\mathrm{acc},1}$ and $y^-_{\mathrm{acc},1}$, whereas the green dot-dashed lines denote the thresholds $y^+_{\mathrm{acc},2}$ and $y^-_{\mathrm{acc},2}$. For reference, lines of constant-y are parallel to the diagonal $y = 1$ in the logarithmic $(\log(\rho_0), \log(\rho_a))$ plane. Notably, due to $\nu > 0.16$, dynamical friction is absent.

Above the threshold line $y^+_{\mathrm{acc},1}$, we enter the large-y regime, as specified by (5.85). Within this regime, ρ_a remains unconstrained, leading to a defining boundary $\rho_0 > \rho_{0\star}$, with $\rho_{0\star} \approx 8 \times 10^{-13} \mathrm{g/cm}^3$. When juxtaposed with the approximation in (5.87), which predicts $\rho_{0\star} \gtrsim 10^{-14} \mathrm{g/cm}^3$ (given $f_{\min} \approx 6 \times 10^{-5}\,\mathrm{Hz}$), it's evident that the Fisher analysis, being more refined, returns a higher value—yet both remain in the same order of magnitude. Consequently, the area bounded by $\rho_{0\star}$ on the right and above the line $y^+_{\mathrm{acc},1}$ is marked as a potential detection region for dark matter, predominantly due to the accretion influence $\Psi_{\mathrm{acc},1}$ on the larger black hole. In the space between $y^+_{\mathrm{acc},1}$ and $y = 1$, the dynamics operate in the low-y regime (5.89). Here, the phase is influenced by both ρ_0 and ρ_a. The Fisher analysis gives a nearly horizontal boundary of $\rho_a > \rho_{a\star}$, with $\rho_{a\star} \approx 5 \times 10^{-9}\mathrm{g/cm^3}$. This is to be compared with the rudimentary calculation in (5.93) which suggests $\rho_{a\star} \gtrsim 10^{-11}\mathrm{g/cm^3}$. Even though the refined Fisher analysis provides a superior value, both assessments are broadly in agreement in terms of magnitude. This harmonization especially holds for the estimates (5.87) and (5.93), which cohesively signal the significant disparity between the thresholds $\rho_{0\star}$ and $\rho_{a\star}$. The resultant shaded region between $y^+_{\mathrm{acc},1}$ and $y = 1$, and above $\rho_{a\star}$, is hence demarcated as another dark matter detection zone, predominantly due to the accretion effect of $\Psi_{\mathrm{acc},1}$ on the larger black hole, albeit in a low-velocity self-regulated mode. For the LISA-IBBH scenario, portrayed in the lower left quadrant of Figure 5.2, similar behavioral patterns are shown. Notably, for $f_{\mathrm{min}} \approx 6 \times 10^{-4}\,\mathrm{Hz}$, the simple approximations from (5.87) and (5.93) project values of $\rho_{0\star} \gtrsim 10^{-14}\mathrm{g/cm^3}$ and $\rho_{a\star} \gtrsim 10^{-9}\mathrm{g/cm^3}$. These are further fine-tuned by the detailed Fisher analysis to $\rho_{0\star} \approx 5 \times 10^{-13}\mathrm{g/cm^3}$ and $\rho_{a\star} \approx 3 \times 10^{-8}\mathrm{g/cm^3}$.

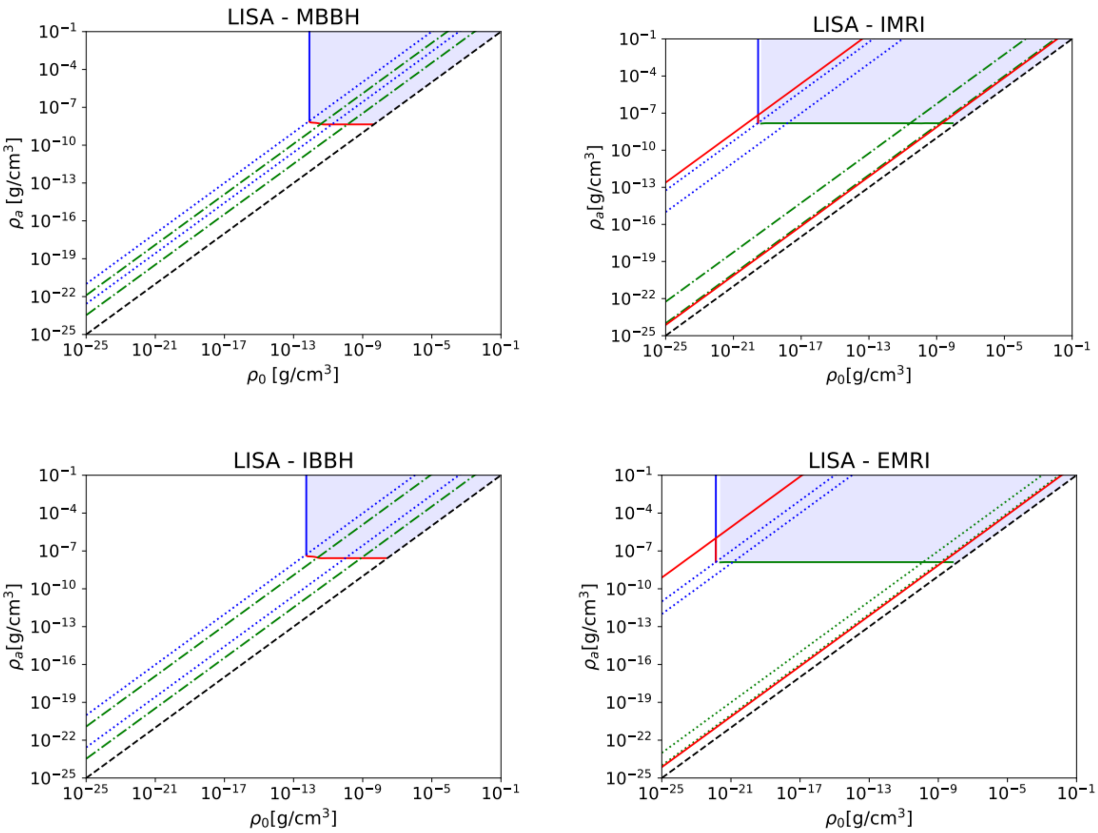

Figure 5.2: Maps of the detection prospects with LISA for different events, in terms of the dark matter parameters ρ_0 and ρ_a. The lower right area below the black dashed line is not physical. The shaded upper right area shows the region of the parameter space where the dark matter environment can be detected.

Consider now the LISA-IMRI scenario as displayed in the upper right section of Figure 5.2. Beyond the thresholds $\{y^+_{\rm acc,1}, y^-_{\rm acc,1}\}$ and $\{y^+_{\rm acc,2}, y^-_{\rm acc,2}\}$, the red solid lines indicate dynamical friction thresholds $\{y^+_{\rm df,2}, y^-_{\rm df,2}\}$. Above the line $y^+_{\rm df,2}$, the system enters the large-y regime, described by (5.85), with a constraint at $\rho_{0\star} = 3\times 10^{-20}{\rm g/cm^3}$. This value is consistent, within a factor of 100, with the approximation given by (5.87), yielding $\rho_{0\star} \gtrsim 10^{-21}{\rm g/cm^3}$ when $f_{\rm min} \approx 6\times 10^{-3}\,{\rm Hz}$. Within the band $y^+_{\rm acc,1} < y < y^+_{\rm df,2}$, the system operates in the intermediate regime (5.88). Here, a minimal dependence on ρ_a via $c_{s,0}$ is observed as per (5.68), rendering the boundary approximately vertical. For values below $y^+_{\rm acc,1}$, the low-y regime (5.89) prevails, with the accretion term now significantly influenced by ρ_a, resulting in an approximate horizontal constraint at $\rho_{a\star} \approx 2\times 10^{-8}{\rm g/cm^3}$. The basic prediction from (5.93) suggests $\rho_{a\star} \gtrsim 10^{-9}{\rm g/cm^3}$, which aligns, within a factor of 100, with the precise Fisher analysis, reflecting the substantial disparity between $\rho_{0\star}$ and $\rho_{a\star}$. The LISA-EMRI scenario, depicted in the lower right section of Figure 5.2, offers analogous patterns. Given $f_{\rm min} \approx 3\times 10^{-3}\,{\rm Hz}$, rudimentary predictions from (5.87) and (5.93) propose $\rho_{0\star} \gtrsim 10^{-24}{\rm g/cm^3}$ and $\rho_{a\star} \gtrsim 10^{-10}{\rm g/cm^3}$. In contrast, the precise Fisher analysis computation yield $\rho_{0\star} \approx 10^{-22}{\rm g/cm^3}$ and $\rho_{a\star} \approx 10^{-8}{\rm g/cm^3}$. Analogous patterns are evident in Figure 5.3 for B-DECIGO, ET, and Adv-LIGO detectors when considering stellar-mass binaries. Notably, the MBBH and IBBH scenarios lack a dynamical friction regime. The B-constraints from B-DECIGO on dark matter environments mirror those from LISA. However, neither ET nor Adv-LIGO can detect dark matter clouds at realistic densities.

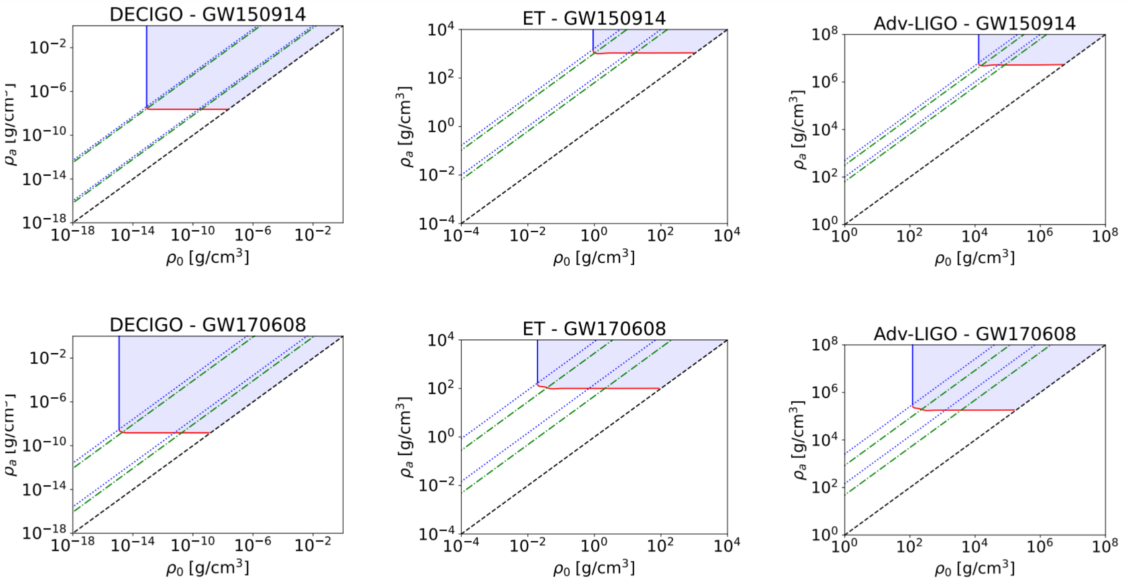

Figure 5.3: Maps of the detection prospects for three different interferometers (from left-to-right: B-DECIGO, ET, and Adv-LIGO), for the two events GW150914 (top line) and GW170608 (bottom line). The color convention is the same scheme as for Figure 5.2.

In every instance, the domain of detection encompasses an upper right region, defined on the left by $\rho_{0\star}$, beneath by $\rho_{a\star}$, and to the right by the diagonal $\rho_a = \rho_0$. The rudimentary estimates from (5.87) and (5.93) generally fall below the exact $\rho_{0\star}$ and $\rho_{a\star}$

thresholds by a factor of roughly 100. Yet, they capture the main patterns and the differential between $\rho_{0\star}$ and $\rho_{a\star}$. Dark matter detection is mainly influenced by the accretion contribution, $\Psi_{\rm acc}$, on the larger black hole. Above the diagonal $y^+_{\rm acc,1}$, which traverses the bottom-left segment of this domain, the accretion rate scales with ρ_0. Conversely, beneath the diagonal $y^+_{\rm acc,1}$, it scales with ρ_a. Thus, above $y^+_{\rm acc,1}$, we evaluate ρ_0, while below it, we assess ρ_a.

Detector Event	LISA	B-DECIGO	ET	Adv-LIGO
MBBH ($\rho_{a\star}$ in g/cm^3)	5×10^{-9}	×	×	×
IBBH	3×10^{-8}	×	×	×
IMRI	2×10^{-8}	×	×	×
EMRI	10^{-8}	×	×	×
GW150914	×	2×10^{-8}	10^3	5×10^6
GW170608	×	2×10^{-9}	101	2×10^5

Table 5.4: Value $\rho_{a\star}$ of the minimum density parameter ρ_a (in g/cm^3) that can be measured and enables a detection of the presence of a dark matter cloud. We show our results for all events presented in Figures 5.2 and 5.3.

Detector Event	LISA	B-DECIGO	ET	Adv-LIGO
MBBH ($\rho_{0\star}$ in g/cm^3)	8×10^{-13}	×	×	×
IBBH	5×10^{-13}	×	×	×
IMRI	3×10^{-20}	×	×	×
EMRI	10^{-22}	×	×	×
GW150914	×	8×10^{-14}	0.9	10^4
GW170608	×	10^{-15}	0.02	120

Table 5.5: Value $\rho_{0\star}$ of the minimum density parameter ρ_0 (in g/cm^3) that can be measured. We show our results for all events presented in Figures 5.2 and 5.3

Tables 5.4 and 5.5 present the minimum detectable densities ρ_a and ρ_0 for each event. Except, for the LISA-EMRI scenario, the measurement of ρ_0 is only possible at much higher densities than the typical dark matter density on galaxy scales, which is about 10^{-26} to 10^{-23} g/cm^3 [88, 89, 351, 352]. For comparison, it is noted that accretion disks have a baryonic matter density below $\sim 0.1\,{\rm g/cm^3}$ for thin disks and below $10^{-9}{\rm g/cm^3}$ for thick disks [197], with a lower bound around $10^{-16}{\rm g/cm^3}$. Gravitational waveforms can therefore only probe ρ_0 for densities that are significantly above the mean dark matter densities but below those of baryonic accretion disks. However, because of the lack of dissipative and radiative processes, the mechanisms enabling dark matter to reach such high densities must be different from those of baryonic disks. It is suggested that such dark matter clouds could instead form in the early universe, as discussed in scenarios like [353, 354], where the dark matter density field would be extremely clumpy, resembling a distribution of small and dense clouds, similar to primordial black holes or macroscopic dark matter scenarios but with larger-size objects. Hence, the studied scenarios suggests that detection is plausible for LISA and B-DECIGO, though not guaranteed. Conversely, it is evident that ET and Adv-LIGO are not conducive to the detection of this specific dark matter, as their detection thresholds exceed the maximum densities expected in thin baryonic disks.

Our results indicate that the minimal value $\rho_{0\star}$ of the bulk density ρ_0, which represents the detection threshold, is in close agreement with the results obtained for σ_0 in [222] using collisionless dynamical friction. The expression (5.5) for the drag force due to dynamical friction is quite general and applies to various media, ranging from collisionless particles to gaseous and scalar-field dark matter scenarios, up to a multiplicative factor. This is not surprising since, in the supersonic regime, pressure forces and self-interactions are negligible. However, the Coulomb logarithm and validity criteria depend on the specific properties of the medium. For instance, in the case of collisionless particles with a monochromatic velocity distribution characterized by a Dirac peak at velocity $v_{\rm c}$ (equivalent to $c_{s,0}$), the classical result for dynamical friction [60] vanishes if the compact object moves at a velocity $v < v_{\rm c}$. In our case, dynamical friction vanishes when $v < c_{s,0}$ [1]. For the B-DECIGO, ET, and Adv-LIGO events, as well as the MBBH and IBBH cases observed by LISA, the threshold $\rho_{0\star}$ obtained from Figures 5.2 and 5.3 lies within the region where dynamical friction is efficient for both black holes, leading to results similar to those in [222] (where the Coulomb logarithm is assumed to be of order unity).

5.5.2 . Detection threshold for ρ_a and parameter space

In this section, the detection threshold $\rho_{a\star}$ obtained in Table 5.4 is compared with the allowed parameter space of the dark matter model in the $(m_{\rm DM}, \lambda_4)$ plane. This comparison aims to determine whether the scenario of black hole binary systems embedded in dark matter clouds can be efficiently probed by the measurement of gravitational waves emitted by such systems. The results are displayed in Figures 5.4 and 5.5, representing the outcomes for LISA and B-DECIGO experiments, respectively. We exclude ET and Adv-LIGO from consideration due to their requisite bulk densities, which are likely higher than realistic densities.

The colored regions in the figures correspond to distinct limits based on observational constraints or the regime considered in the calculations. As observed in Figures 5.2 and 5.3, the detection threshold for ρ_a is mostly independent of ρ_0, although it can vary somewhat between domains where dynamical friction is important or not. To provide a specific threshold for ρ_a, the values $\rho_{0\star}$ presented in Table 5.5 are adopted. From (2.3), a constant

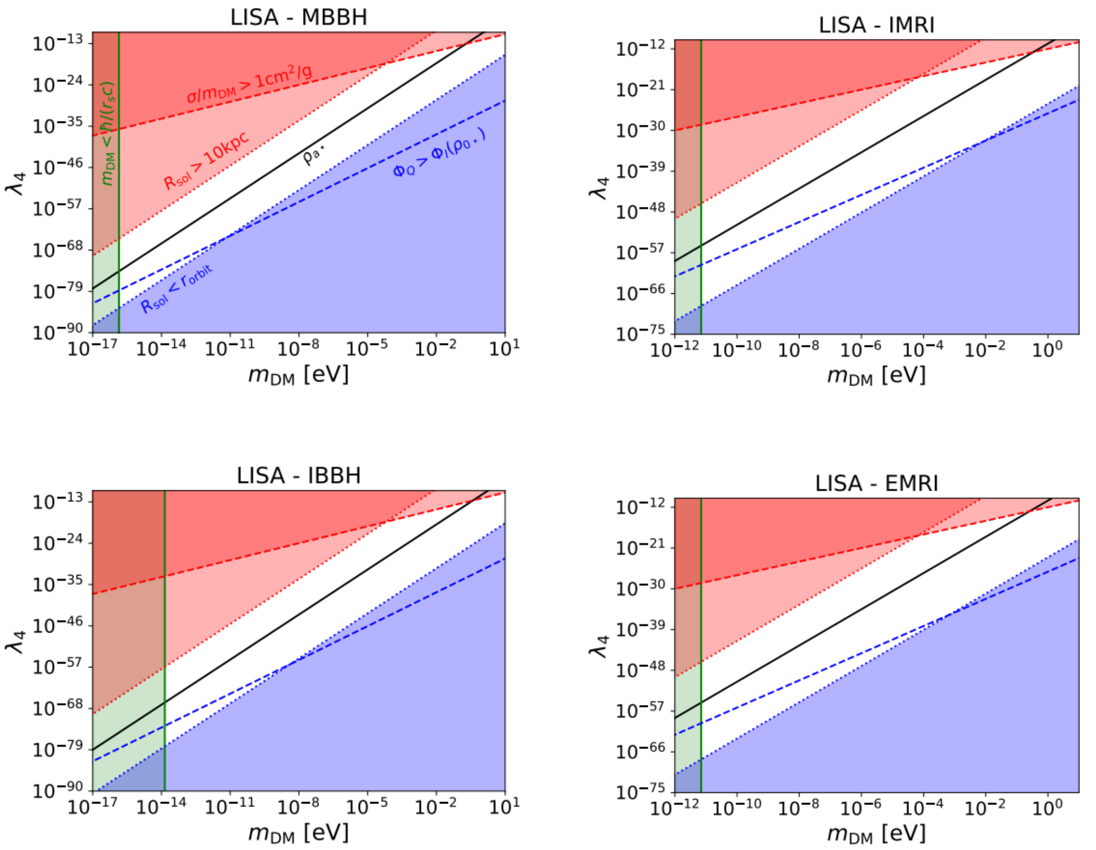

Figure 5.4: Domain over the parameter space ($m_{\rm DM}$, λ_4) where our derivations are applicable, in the case of the LISA interferometer and assuming a bulk dark matter density $\rho_{0\star}$ as in Table 5.5. The white area represents the allowed parameter space. The upper left red region is excluded by observational constraints. In the lower right blue region the scalar field dark matter model is allowed but the assumptions used in our computations must be revised. The black line corresponds to the detection limit obtained in Figure 5.2. Parameter values above this line are beyond the detectability range of the interferometer.

detection threshold $\rho_{a\star}$ for ρ_a corresponds to an upper limit for λ_4 that scales as $m_{\rm DM}^4$

$$\rho_a \text{ is measured if } \lambda_4 < \frac{4 m_{\rm DM}^4}{3 \rho_{a\star}} . \tag{5.94}$$

This can be rewritten as

$$\lambda_4 < 3 \times 10^{-19} \left(\frac{\rho_{a\star}}{1\,{\rm g/cm^3}} \right)^{-1} \left(\frac{m_{\rm DM}}{1\,{\rm eV}} \right)^4 . \tag{5.95}$$

The black solid line labeled $\rho_a = \sigma_{\rm a}$ in Figures 5.4 and 5.5 represents this upper limit, indicating the maximum value of λ_4 for which ρ_a can be measured.

The constraints that determine the parameter space of the model are described, and these constraints are represented by the colored regions in the plots. Firstly, the large

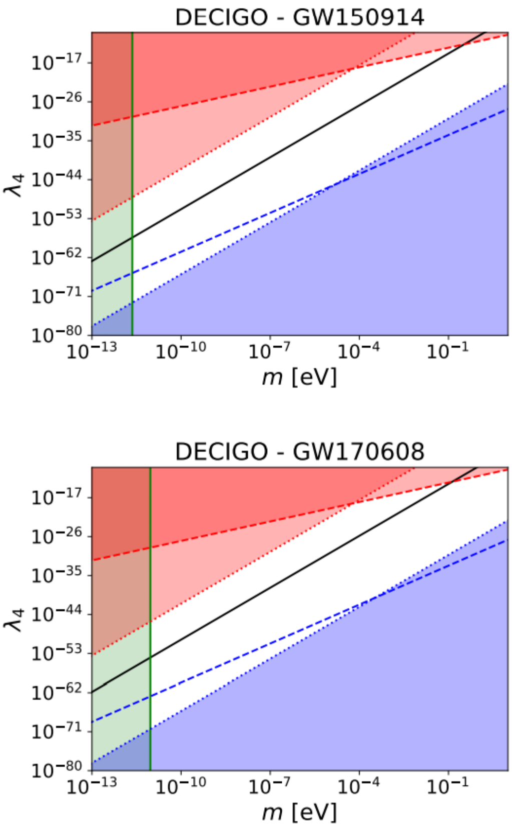

Figure 5.5: Domain over the parameter space ($m_{\rm DM}$, λ_4) where our derivations are applicable and detection threshold, as in Figure 5.4 but for the B-DECIGO interferometer.

scalar mass limit condition(2.30) is required for the larger of the two black holes embedded in the soliton. This is because we assumed that the de Broglie and Compton wavelengths of the scalar field are smaller than the horizon of the black hole. This condition can also be expressed as

$$m_{\rm DM} > \frac{1}{2\mathcal{G}m_<} \,. \tag{5.96}$$

This condition ensures the validity of the accretion rate (5.2) and the dynamical friction (5.5), which were derived in [1, 2, 190] under the assumption of a large-mass limit, where $\partial_r \ll m_{\rm DM}$. The exclusion of the parameter space due to this condition is indicated by the green area marked by a vertical line on the left side of the figures.

Observations of cluster mergers, such as the bullet cluster, provide an upper bound on the dark matter cross-section, $\sigma/m_{\rm DM} \lesssim 1$ cm^2/g [355]. This upper bound translates to the constraint

$$\lambda_4 < 10^{-12} \left(\frac{m}{1\,\rm eV}\right)^{\frac{3}{2}} , \tag{5.97}$$

which is represented by the dashed red line in the upper left corner of the figures.

Another observational limit is shown by the upper left red solid line, which represents the maximum size of dark matter solitons. To ensure that these solitons fit inside galaxies, a condition of $R_{\rm sol} < 10$ kpc is imposed. This condition leads to an upper bound on λ_4 given by

$$\lambda_4 < 0.03 \left(\frac{R_{\rm sol}}{10\,{\rm kpc}}\right)^2 \left(\frac{m_{\rm DM}}{1\,{\rm eV}}\right)^4 . \tag{5.98}$$

This condition is parallel to the detection threshold (5.95) and is somewhat above it in Figures 5.2 and 5.3. Therefore, the largest solitons would not be detected by gravitational waves. This will be further discussed in section 5.5.3.

The derivation of the accretion rate (5.2) and dynamical friction (5.5) assumes that self-interactions dominate over quantum pressure [1, 2, 190], in contrast to scenarios involving fuzzy dark matter where the latter dominates and self-interactions are neglected. The self-interaction potential is given by $\Phi_{\rm I} = \rho/\rho_a$, while the quantum pressure is given by $\Phi_{\rm Q} = -\nabla^2\sqrt{\rho}/(2m_{\rm DM}^2\sqrt{\rho})$. This results in the condition $\rho/\rho_a > /(r^2 m_{\rm DM}^2)$, where ρ and r represent the density and length scale of interest. This condition, which holds near the black hole horizon with $\rho \sim \rho_a$ and $r \sim r_s$, coincides with the condition (5.96) and is already enforced. Requiring that this condition also holds over the bulk of the soliton, at density ρ_0 and radius $r \sim R_{\rm sol}$, gives an additional constraint

$$\lambda_4 > \frac{8 m_{\rm DM}^3 \sqrt{\mathcal{G}}}{3\sqrt{\pi}\sqrt{\rho_0}} . \tag{5.99}$$

This constraint can be rewritten as

$$\lambda_4 > 7 \times 10^{-26} \left(\frac{\rho_0}{7 \times 10^{-25}\,{\rm g/cm^3}}\right)^{-\frac{1}{2}} \left(\frac{m_{\rm DM}}{1\,{\rm eV}}\right)^3 . \tag{5.100}$$

The blue region in the bottom right corner of the figures, below the blue solid line, is excluded by this constraint. It is important to note that this constraint is the only one that depends on the density parameter ρ_0, and it becomes less stringent as ρ_0 increases. Therefore, if ρ_0 is much larger than the mean dark matter density of the Milky Way, this constraint is less restrictive and moves down in the $(m_{\rm DM}, \lambda_4)$ plane. While this constraint excludes the region below it, it does not exclude the entire model. However, it does indicate that our derivation of the dynamical friction needs revision as the bulk of the soliton is now governed by quantum pressure instead of self-interactions. Nevertheless, this revision is not expected to significantly alter our results because the dynamical friction form (5.5) is quite general and applies to most models in the supersonic regime, resembling the classical result by Chandrasekhar for collisionless particles [60]. In the supersonic regime, the details of self-interactions and pressure terms are not crucial, and only the Coulomb logarithm may change, depending on the specifics of the physics involved. Therefore, this line does not exclude the model itself, nor does it change the fact that the region below it in the $(m_{\rm DM}, \lambda_4)$ plane leads to the measurement of ρ_a by the gravitational wave interferometer, through the accretion effects where our assumptions still hold.

The area below the dashed blue line in the figures represents the parameter space where the size of the soliton is smaller than the initial orbit of the binary system during the measurement. To ensure the validity of our calculation across all frequencies, we must consider the constraint

$$\lambda_4 > \frac{16\mathcal{G} m_{\rm DM}^4 r_{\rm orbit}^2}{3\pi} , \tag{5.101}$$

which can be expressed as

$$\lambda_4 > 3 \times 10^{-10} \left(\frac{m_{\rm DM}}{1\,{\rm eV}}\right)^4 \left(\frac{r_{\rm orbit}}{1\,{\rm pc}}\right)^2 . \tag{5.102}$$

For $r_{\rm orbit}$, the maximum orbital radius is considered, computed using Kepler's third law at the earliest measurement time associated with the frequency $f_{\rm obs}(4\,{\rm yr})$. This constraint is parallel to the soliton-size condition (5.98) and the detection threshold $\rho_{a\star}$ in (5.95).

Hence, the white area in the parameter space indicates where the dark matter model is realistic and all our calculations successfully apply. More precisely, the upper bounds associated with the red exclusion regions correspond to unphysical regions of the parameter space, whereas the lower bounds associated with the blue exclusion regions indicate regions where some of our computations need revision. However, even within the detection domain below the black solid line, it should still be possible to measure ρ_a.

Figures 5.4 and 5.5 show that the detection threshold $\rho_{a\star}$ runs through the white area in all cases. Particularly, it is parallel but below the upper bound associated with the soliton size limit and above the lower bound associated with the orbital radius limit. Therefore, while the largest solitons cannot be detected, a significant portion of the available parameter space could lead to detection by interferometers such as LISA and B-DECIGO.

5.5.3 . Constraints on the soliton radius

The parameters $m_{\rm DM}$ and λ_4 also determine the size of the soliton, denoted as $R_{\rm sol}$, as shown in (2.3) and (2.16). Since $R_{\rm sol}$ is more relevant for observational purposes than the coupling parameter λ_4, the application domain of our computations and the detection threshold $\rho_{a\star}$ are shown in Figures 5.6 and 5.7 in the parameter space $(m_{\rm DM}, R_{\rm sol})$ instead of the $(m_{\rm DM}, \lambda_4)$ plane shown in Figures 5.4 and 5.5. It can be observed that no experiment can probe solitons on galactic scales, where $R_{\rm sol} \gtrsim 1$ kpc, which have been proposed as a solution to the small-scale problems encountered by the standard cold dark matter scenario. Typically, LISA can probe models associated with $10^{-10} \lesssim R_{\rm sol} \lesssim 10^{-3}$ kpc, while B-DECIGO can probes soliton as small as $R_{\rm sol} \sim 10^{-11}$ kpc. These astrophysical scales range from hundreds of thousands of kilometers to distances around the typical distance between stars in the Milky Way (~ 5 light years). Once again, LISA and B-DECIGO cover a significant fraction of the parameter space. LISA can probe models with a scalar mass in the range $10^{-16} \lesssim m_{\rm DM} \lesssim 1$ eV. On the other hand, B-DECIGO is restricted to $10^{-12} \lesssim m_{\rm DM} \lesssim 1$ eV.

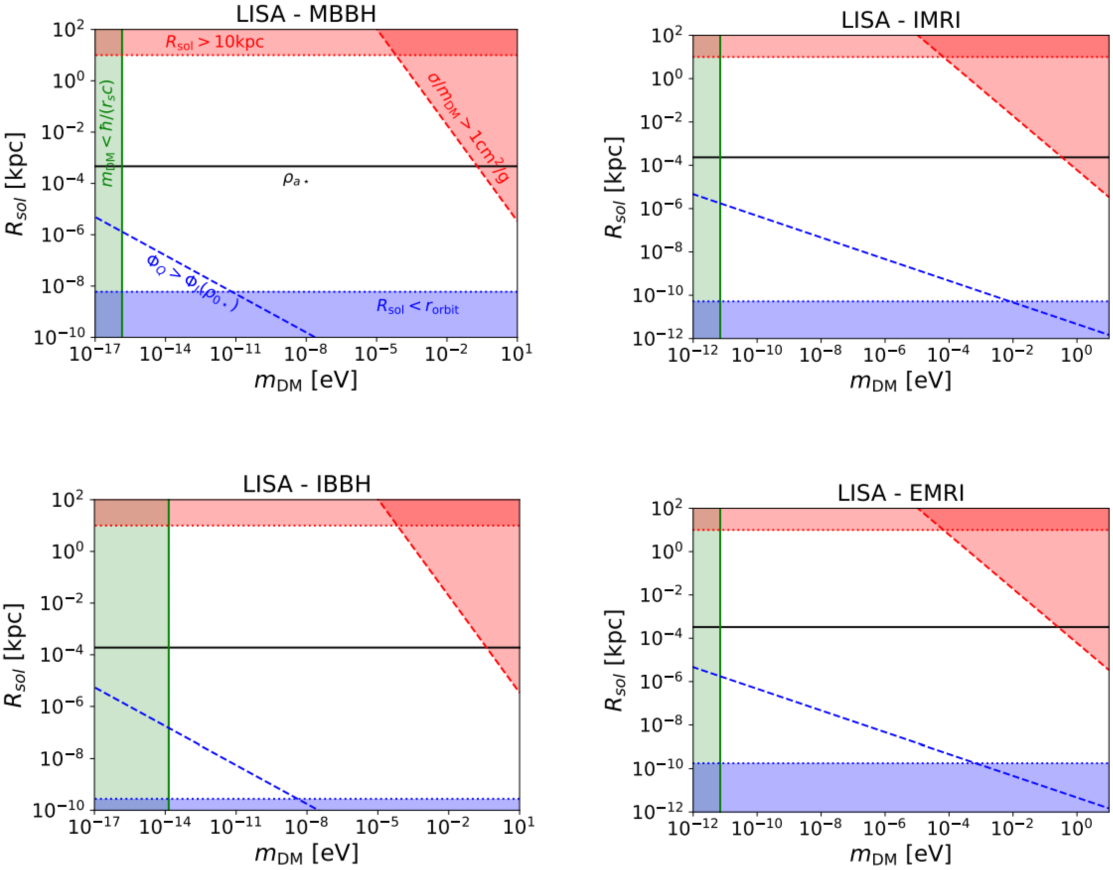

Figure 5.6: Domain over the parameter space ($m_{\rm DM}$, $R_{\rm sol}$) where our derivations are applicable and detection threshold, in the case of the LISA interferometer and assuming a bulk dark matter density $\rho_{0\star}$ as in Figure 5.4. The white area below the solid black line is the area where effects of drag force are detectable.

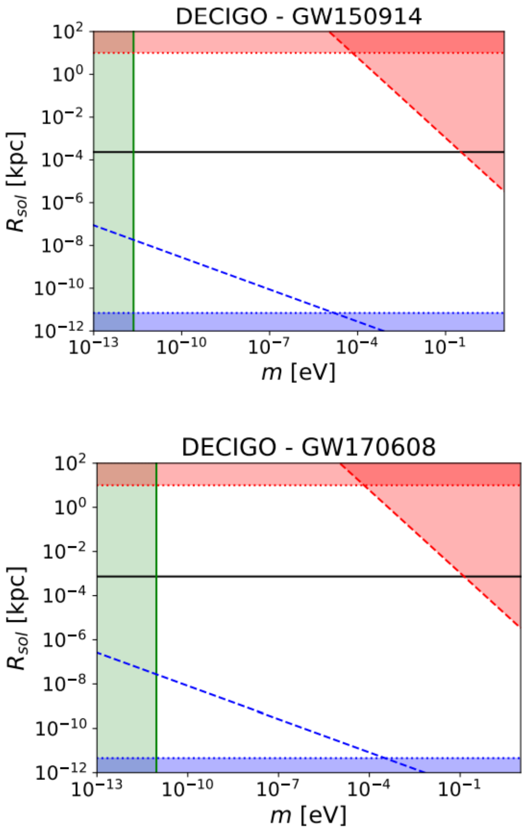

Figure 5.7: Domain over the parameter space ($m_{\rm DM}$, $R_{\rm sol}$) where our derivations are applicable and detection threshold, in the case of the B-DECIGO events, as in Figure 5.5.

5.6 . Summary of the chapter

The detection of gravitational waves has already provided significant results for fundamental physics, such as confirming the near equality between the speed of gravitational waves and the speed of light [220, 235, 244]. In this study, we propose that future experiments could shed light on key properties of dark matter. Specifically, we focus on scalar field dark matter models with quartic self-interactions and assume that the overall density of dark matter in the Universe arises from the misalignment mechanism of the scalar field. Within galaxies, these models can give rise to finite-sized solitons of dark matter, where gravity and the repulsive self-interaction pressure balance precisely. This regime is applicable when the size of the solitons is much larger than the de Broglie wavelength of the scalar particles. Consequently, these solitons could potentially exist throughout each galaxy, and black holes could naturally become embedded within these scalar clouds as they inspiral towards each other in binary systems.

The scalar clouds have two effects on the orbits of binary systems. First, the dark matter accretes onto the black holes, causing them to slow down. Second, in the supersonic regime, dynamical friction resulting from the gravitational interaction between the black holes and distant streamlines further decelerates the black holes. Both effects can introduce significant deviations in the binary orbits and, consequently, perturbations in the GW signals emitted by the black hole pair. The accretion effect contributes at the -4PN level in the low-velocity regime (subsonic regime and moderate Mach numbers) and at the -5.5PN level in the hig-velocity regime (high Mach numbers), while dynamical friction contributes at the -5.5PN level. Therefore, these effects are not degenerate with the relativistic corrections appearing at higher post-Newtonian orders.

For a significant portion of the parameter space in scalar field dark matter models, future experiments such as LISA, B-DECIGO, ET, or Adv-LIGO should be capable of observing the impact of these dark matter environments on gravitational waves, provided that binary systems are indeed embedded within such scalar clouds. This would provide valuable insights into the nature of dark matter. Within the framework of the scalar field models with quartic self-interactions explored here, these observations would yield indications regarding the values of the bulk dark matter density ρ_0 and the characteristic density ρ_a of (2.3), which corresponds to the combination $m_{\rm DM}^4/\lambda_4$. Additionally, this would indirectly provide an estimate of the size $R_{\rm sol}$ of the solitons, as given by (2.16). Measuring the bulk density of dark matter ρ_0 appears achievable with upcoming gravitational wave experiments within a substantial portion of the parameter space associated with these dark matter models. This is particularly evident for detection of events from LISA and B-DECIGO. As for ρ_a, forecasting this parameter poses challenges due to its primary association with peak dark matter density proximate to black holes. Nonetheless, the values discernible by LISA and B-DECIGO align with anticipated ranges, even though they considerably exceed the typical dark matter density observed on galactic scales. Such high densities could be reached in scenarios where the dark matter clumps are significantly smaller and denser than the average galactic halos, which would correspond to models where these clumps formed at high redshifts, resulting in a highly clumpy distribution of dark matter. The absence of detection of such dark matter effects in ET and LIGO events suggests that either these dark matter clouds are rare or absent, or that ρ_a is below 0.01 g/cm^3, as shown in Table 5.4.

Perturbations to the gravitational waveforms may arise from various environments, including gaseous clouds or dark matter halos associated with different dark matter models. In all cases where such environments are present, we can expect both accretion and dynamical friction to occur and slow down the orbital motion. It would be interesting to investigate whether one can distinguish between these different environments. As demonstrated in this paper, one could potentially utilize the magnitude of these two effects, as well as the regions in the data sequence where dynamical friction appears to be active or not, to discriminate between scenarios. Specifically, depending on the medium, dynamical friction is expected to be negligible in certain regimes, such as subsonic velocities. If it is possible to extract such conditions from the data, valuable information about the environment of the binary systems could be gained.

Conclusions

In this thesis, our primary aims were to calculate the mass accretion and dynamical friction experienced by a Schwarzschild black hole moving inside a self-interacting scalar field dark matter soliton. Additionally, we sought to investigate the subsonic and supersonic regimes and quantify the effects of mass accretion and dynamical friction in gravitational wave emissions by binary black holes, providing a possible probe for dark matter.

To achieve these aims, we first introduced the self-interacting scalar field dark matter model in chapter 2, providing an overview of its implications for large-scale structures, solitons, and interactions with black holes. We discussed the constraints on the self-interaction coupling constant derived from astrophysical observations and outlined the parameter space relevant to our computations.

In chapter 3, we focused on the subsonic regime, studying the behavior of dark matter flow in the presence of a Schwarzschild black hole and a self-interacting scalar field dark matter soliton. Our results demonstrated that the dark matter behaves as an isentropic potential flow, characterized by a polytropic index of $\gamma_{\rm ad} = 2$. Notably, we compared the accretion rate and drag force with those of collisionless particles [60–62] and fuzzy dark matter [63–65], revealing that our model exhibits null dynamical friction in the subsonic regime, resembling the behavior of a gas [277]. However, we found the accretion rate to be significantly smaller than that predicted by Bondi's result for a perfect gas [300].

In chapter 4, we explored the supersonic regime, which is characterized by conflicting boundary conditions. We examined the emergence of shock fronts in hyperbolic systems such as supersonic flows, as they play a crucial role in matching the upstream bulk flow (determined by initial conditions) with the downstream bulk flow (influenced by boundary conditions at the black hole horizon). The dynamics in the upstream and downstream regions require a more detailed treatment than that employed in the subsonic regime. Notably, we found that while the mass accretion exhibited similarities to previous results, a new regime similar to Hoyle-Lyttleton result for isentropic gas appeared in the case of high Mach number. Furthermore, a dynamical friction term analogous to Chandrasekhar's result [60] appeared in this regime, supplementing the drag force and introducing a discontinuity between the subsonic and supersonic regime forces.

In chapter 5, we explored the potential of gravitational wave detection for studying dark matter. Specifically, we investigated self-interacting scalar field dark matter models and their impact on binary black holes and gravitational wave signals. Our findings revealed that mass accretion and dynamical friction contribute to deviations in binary orbits and perturbations in emitted gravitational wave signals. While accretion drag force leave a -4PN signature on gravitational wave signals in low velocity regime and a -5.5PN signature in high velocity regime, dynamical friction leave a -5.5PN signature, hardly permitting to distinguish between both effects. Future experiments such as LISA, B-DECIGO, ET, or AdvLIGO [66, 67, 279, 280] hold promise in observing these effects, offering valuable insights into dark matter parameters and their influence on gravitational waves. Furthermore, we discussed the potential for distinguishing between different environments, such as gaseous clouds or alternative dark matter models, based on the magnitude and characteristics of these effects.

Several points warrant further investigation and serve as intriguing avenues for future research:

- Firstly, while our calculations focused on the nonrelativistic regime, incorporating relativistic effects would be valuable to provide a more comprehensive understanding of dark matter systems. This extension would allow us to study the effects of the drag force at higher frequencies, closer to the merging of black holes. Additionally, our study predominantly considered non-spinning Schwarzschild black holes. Incorporating Kerr black holes with angular momentum or spin would enhance the realism of our models, particularly considering the presence of spin in observed binary black hole systems [208, 218, 220, 221]. This work was done for ultralight dark matter [275].
- Expanding our scope beyond black holes to include other astrophysical objects, such as stars and neutron stars, is crucial. These objects offer unique characteristics that can provide valuable insights into testing dark matter models. However, accounting for the back reactions of dark matter becomes important for such objects, as mass accretion is typically not the dominant factor in the subsonic regime.
- Furthermore, it is essential to consider scenarios where black holes reside closer to the boundaries of a soliton or when the soliton itself is relatively small. Broadening our exploration to encompass a wider range of soliton sizes would expand our ability to detect and characterize solitons, enabling the identification of distinct signatures associated with scalar field dark matter models.

In summary, this thesis investigated the mass accretion, dynamical friction, and their combined effects on binary systems within self-interacting scalar field dark matter solitons. The findings contribute to our understanding of the dynamics of black holes in the presence of dark matter and open up avenues for future research. Incorporating relativistic effects, considering spinning black holes, exploring the influence of stars and neutron stars, and investigating a broader range of soliton sizes are all promising directions for advancing our knowledge and uncovering stronger signatures in the exploration of scalar field dark matter models.

Appendices

A . Subsonic regime

A.1 . Green functions

In the appendices that follow we drop the hats for simplicity of notation.

In order to go beyond the linear flow described in section 3.5.1, the nonlinear equation (3.20) is split into a system of two equations (3.56). This system is then solved using an iterative scheme. The source term S is obtained directly from the flow β using the second equation in the system. To determine the flow β from the source S, the first equation is solved with the aid of the appropriate Green function $G(\mathbf{r},\mathbf{r}')$, which satisfies $\nabla \cdot (k_+^2 \nabla G) = \delta_D(\mathbf{r}-\mathbf{r}')$. By solving the first equation in (3.56), the following expression for β is obtained

$$\beta = \beta^L + \int d\mathbf{r}' \; G(\mathbf{r},\mathbf{r}')S(\mathbf{r}') \,. \tag{A.1}$$

Here, β^L represents the linear flow (3.34). Expanding the Green function in terms of spherical harmonics and decomposing the phase β and the source S in terms of Legendre polynomials, the following expressions are obtained

$$\beta(r,\theta) = \sum_\ell \beta_\ell(r) P_\ell(\cos\theta) \,, \tag{A.2}$$

$$G(\mathbf{r},\mathbf{r}') = \sum_{\ell,m} G_\ell(r,r') Y_\ell^m(\theta',\varphi')^* Y_\ell^m(\theta,\varphi) \,. \tag{A.3}$$

Using these decompositions, the expression for β_ℓ becomes

$$\beta_\ell = \beta_\ell^L + \int_{r_\mathrm{m}}^\infty dr' \; r'^2 G_\ell(r,r') S_\ell(r') \,. \tag{A.4}$$

As β^L already satisfies the boundary conditions, the Green function must approach zero at both r_m and large radii. Therefore, the following expressions are used for the Green function:

$$\begin{aligned} r<r' : &\quad G_\ell(r,r') = w_\ell \, G_\ell^+(r)\, G_\ell^-(r') \,, \\ r>r' : &\quad G_\ell(r,r') = w_\ell \, G_\ell^-(r)\, G_\ell^+(r') \,, \end{aligned} \tag{A.5}$$

where

$$w_\ell = \frac{3}{2(r+\gamma r^2)[G_\ell^+(r) G_\ell^{-\prime}(r) - G_\ell^{+\prime}(r) G_\ell^-(r)]} \,. \tag{A.6}$$

This constant is determined by the Wronskian theorem. At the inner boundary r_m, the condition $\frac{\partial G_0}{\partial r}(r_\mathrm{m}) = 0$ is enforced, allowing for the recovery of the radial velocity. For modes $\ell \neq 0$, the radial and angular velocities are not exactly zero at r_m. However, it is sufficient for them to be negligible. This approximation is made because the numerical solution is truncated at the radius r_{m}, slightly above the Schwarzschild radius, where the flow is already dominated by radial accretion while angular velocities are not precisely zero. The accuracy of this approximation can be verified by referring to Figure 3.3.

A.2 . Odd multipoles

The cubic non-linearity in β given by (3.20) introduces mode coupling between Legendre multipoles. This effect can be estimated at large radii, where the velocity is nearly equal to $\mathbf{v}_0$ and β is dominated by the dipole term in expression (3.34). At large radii, the linear solution (3.34) behaves according to (3.49). As r approaches infinity, the source term S in (3.56) is primarily contributed by two powers of the leading term $v_0 r$ and one power of the subleading term $-v_0/2\gamma$ from β_1^L. This results in a contribution of order $1/r^2$ to S. Terms of order $1/r^2$ are also generated on the left-hand side of the first equation in (3.56) due to constant terms in β and the contribution from the leading $v_0 r$ term paired with the contribution $2/(3r)$ to the kernel k_+^2 in (3.25). Consequently, mode couplings produce a constant tail for all odd multipoles as the cubic non-linearity repeatedly transfers power from the dipole to higher-order odd multipoles. Therefore, we can express the odd part of the phase β_{odd} as a large-distance expansion of the form (3.50)-(3.51). In the linear flow, $a_1 = -v_0/(2\gamma)$, and all other multipoles are zero.

Collecting terms of order $1/r^2$ in (3.20), we obtain the following expression

$$
\begin{aligned}
-\frac{\gamma}{r^2}\sum_{n\ \mathrm{odd}} a_n n(n+1)P_n - \frac{v_0\cos\theta}{r^2} = -\frac{v_0^2}{r^2}\sum_{n\ \mathrm{odd}} a_n n(n+1)P_n + \frac{2v_0^2}{r^2}\sum_{n\ \mathrm{odd}} a_n n(n+1) \\
\times\left[\frac{(n+2)^2}{(2n+1)(2n+3)}P_{n+2} + \frac{(n-1)^2}{(2n-1)(2n+1)}P_{n-2} - \frac{2n^2+2n-1}{(2n-1)(2n+3)}P_n\right] ,
\end{aligned}
\tag{A.7}
$$

where P_n corresponds to the Legendre Polynomial of degree n. For the linear flow, neglecting the right-hand side, we recover $a_1 = -v_0/(2\gamma)$. By collecting the coefficient of each Legendre polynomial P_n, we obtain the recursion relation for odd integers $n \geq 1$

$$
\begin{aligned}
-3k_0^2 a_n - v_0\delta_{n,1} =& 4v_0^2\left[\frac{n(n-2)(n-1)}{(n+1)(2n-3)(2n-1)}a_{n-2}\right. \\
&\left. + \frac{(n+1)(n+2)(n+3)}{n(2n+3)(2n+5)}a_{n+2} - \frac{2n^2+2n-1}{(2n-1)(2n+3)}a_n\right] .
\end{aligned}
\tag{A.8}
$$

Consequently, due to the mode couplings induced by the cubic non-linearity, a nonzero a_1 generates nonzero values for all odd multipoles. By defining the parameter

$$
\xi = \frac{3k_0^2}{v_0^2} = 4\frac{c_{s,0}^2}{v_0^2} ,
\tag{A.9}
$$

where $c_{s,0}$ was defined in (3.42), the recursion relation simplifies at large n to

$$
n \gg 1 : \quad -\xi a_n = a_{n-2} + a_{n+2} - 2a_n .
\tag{A.10}
$$

This equation has two independent solutions of the form

$$a_n = y_+^{n/2} \quad \text{and} \quad a_n = y_-^{n/2} \,, \tag{A.11}$$

with

$$\begin{aligned} 0 < \xi < 4: \quad y_\pm &= \frac{-(\xi-2) \pm i\sqrt{4-(\xi-2)^2}}{2} \quad \text{hence} \quad y_\pm = e^{\pm i\zeta} \,, \\ \xi > 4: \quad y_\pm &= \frac{-(\xi-2) \pm \sqrt{(\xi-2)^2-4}}{2} \,, \end{aligned} \tag{A.12}$$

where we defined $\zeta = \arccos(1-\xi/2)$.

For small velocities, $\xi > 4$, corresponding to $v_0 < c_{s,0}$, where $c_{s,0}$ is defined in (3.42), the solution $y_+^{n/2}$ decays more rapidly compared to $y_-^{n/2}$. Therefore, in order to have a well-defined multipole expansion, the decaying solution $y_+^{n/2}$ is selected. The recursion relation (A.8), starting from the second equation at $n = 3$, determines all a_n with $n \geq 5$, while a_1 and a_3 remain undetermined. This recursion relation is a linear difference equation of second order, also known as a three-term recursion, with two independent solutions. The selection of the decaying solution $y_+^{n/2}$ then determines the ratio a_3/a_1. By substituting a_3 in terms of a_1 in the first equation of (A.8) with $n = 1$, the value of a_1 can be determined. Hence, all coefficients a_n are uniquely determined.

In the limit of $v_0 \to 0$, the amplitude of the coefficients a_n shows a rapid decrease with n, as $|a_n| \sim |y_+|^{n/2} \sim v_0^n$. In this limit, the right-hand side of the first equation in (A.8) becomes negligible. Thus, the linear flow given by (3.49) is recovered, which is expected. The expressions are as follows

$$v_0 \ll c_{s,0}: \quad a_1 \simeq -\frac{v_0}{3k_0^2} \simeq -\frac{v_0}{2\gamma} \,, \quad a_n \sim v_0^n \,. \tag{A.13}$$

These results are consistent with the explicit expression given in (3.44).

In contrast to the linear flow where multipoles beyond the dipole are exactly zero, the mode couplings induced by the cubic non-linearity lead to a constant value for these odd multipoles at large r. Consequently, the multipoles of the angular velocity decay only as $1/r$ and not with a power of $1/r$ that grows with n. This behavior differs from the large-distance behavior of the linear modes G_n^- in (3.32) of the operator $\nabla[k_+^2 \nabla(\cdot)]$. The difference arises because the source S is not strongly peaked at a specific scale, such as r_γ, resulting in the integral over the Green function in (A.4) not being peaked around a finite range of r'. Instead, significant contributions arise up to $r' \sim r$. As a result, the results given by (3.44) and (A.8) are robust, and the large-distance behavior of the phase β is not sensitive to its behavior at small radii.

Consistent with the change in flow properties from the subsonic to the supersonic regime, we note that the threshold $c_{s,0}$ can be recovered from the result given in (A.8). For velocities $v_0 > c_{s,0}$, at large values of n, the two independent real solutions are given by $\mathrm{Re}(y_+^{n/2}) = \cos(n\zeta/2)$ and $\mathrm{Im}(y_+^{n/2}) = \sin(n\zeta/2)$. In the limit of large n, the Legendre polynomials take the following asymptotic form

$$n \to \infty: \quad P_n(\cos\theta) = \sqrt{\frac{2}{\pi n \sin\theta}} \cos\left[\left(n+\frac{1}{2}\right)\theta - \frac{\pi}{4}\right] \,, \tag{A.14}$$

for $0 < \theta < \pi$. When $\theta = \zeta/2$, both solutions $\cos(n\zeta/2)$ and $\sin(n\zeta/2)$ lead to divergent series in n. This agrees with the singularity of (3.44) at the threshold $c_{s,0}$, specifically at $\mu = 0$. Therefore, for $v_0 > c_{s,0}$, a shock appears and the flow is no longer a smooth perturbation around the linear flow given by (3.34). The study of this regime is done in chapter 4.

A.3 . Even multipoles

As discussed in the previous appendix, at large radii, the nonlinear mode couplings generate contributions to all odd multipoles as long as the dipole is nonzero. This partial decoupling between odd and even multipoles arises from the properties of the linear operator and the cubic source term in the nonlinear system (3.56). The linear operator $\nabla[k_+^2\nabla\beta]$ preserves the parity of β, while the cubic source term $\nabla\cdot[(\nabla\beta)^2\nabla\beta]$ requires one or three odd multipoles to generate an odd multipole, and one or three even multipoles to generate an even multipole. Consequently, if we start with a phase β that has no even component, the cubic source term will never generate even multipoles. On the other hand, if there is an initial seed for even multipoles, all even-order multipoles will be generated by the cubic non-linearity and will mix with the odd multipoles through products of two odd terms with one even term. However, due to the partial decoupling, the final amplitude of the even terms will be proportional to the initial seed.

Since the linear flow (3.35) has an even component β_0 that decays as $1/r$ at large radii, we can write the even part of the phase β_{even} using a large-distance expansion in the form (3.50)-(3.51). The even components decay faster than the odd components (except for the leading growing dipole term) due to the partial decoupling explained earlier. For the linear flow, only b_0 is non-zero and proportional to $1/\gamma$, while all other multipoles are zero. By collecting all terms of order $1/r^3$ in (3.20), we obtain

$$-\frac{\gamma}{r^3}\sum_{n\ \text{even}} b_n n(n+1)P_n = -\frac{v_0^2}{r^3}\sum_{n\ \text{even}} b_n n(n+1)P_n\frac{2v_0^2}{r^3}\sum_{n\ \text{even}} b_n \\ \times\left[\frac{(n+1)^2(n+2)(n+3)}{(2n+1)(2n+3)}P_{n+2}+\frac{n^2(n-2)(n-1)}{(2n-1)(2n+1)}P_{n-2}-\frac{n(n+1)(2n^2+2n-1)}{(2n-1)(2n+3)}P_n\right]. \tag{A.15}$$

For the linear flow, neglecting the right-hand side, we find that $b_n = 0$ for $n \geq 2$, while b_0 can take any value determined by the small-radius boundary condition. Collecting the coefficient of each Legendre polynomial P_n, this gives the recursion for even integers $n \geq 2$

$$-3k_0^2 b_n = 4v_0^2\left[\frac{(n-1)^2}{(2n-3)(2n-1)}b_{n-2}+\frac{(n+2)^2}{(2n+3)(2n+5)}b_{n+2}-\frac{2n^2+2n-1}{(2n-1)(2n+3)}b_n\right]. \tag{A.16}$$

The equation obtained from (A.15) at $n = 0$ is automatically satisfied because all terms include the prefactor $n(n+1)$, which canceled out in (A.16) for $n \geq 2$. As a result, a nonzero b_0 generates nonzero values for all even multipoles. At large n, we recover the same recursion as in (A.10) and the two independent solutions given in (A.11).

At low velocities, $v_0 < c_{s,0}$, we recover the decaying solution $y_+^{n/2}$ from (A.12). However, because the relation (A.16) at $n = 0$ was automatically satisfied as $0 = 0$, the series of even multipoles is not uniquely determined and depends on the unconstrained monopole coefficient b_0, which is determined by the matching to the behavior at small radii. For $v_0 \to 0$, we recover the linear flow (3.35) with the even multipoles given by

$$v_0 \ll c_{s,0}: \quad b_n \sim \frac{v_0^n}{\gamma}. \tag{A.17}$$

Once again, this $1/r$ tail is not sensitive to the behavior of the phase β at small radii, except for its overall normalization.

At large velocities, $v_0 > c_{s,0}$, we recover the oscillating modes (A.12) and the singularity analyzed in Appendix A.2. This singularity agrees with the singularity at $\mu \to 0$ of the explicit expression (3.46) and indicates the appearance of a shock, as well as the fact that the flow is no longer a smooth perturbation of the linear flow.

B . Drag force calculation for different models

B.1 . Chandrasekhar's calculation of dynamical friction

In this appendix, we provide a step-by-step explanation of the Chandrasekhar's calculation of dynamical friction in the case of nonrelativistic collisionless particles. As a reminder, dynamical friction refers to the deceleration experienced by a massive object moving through a medium composed of lighter particles, resulting in its gradual orbital decay. We outline the main equations and elucidate the calculation process, starting from the gravitational force and culminating in the formulation of the dynamical friction equation.

The gravitational force acting on the test particle p due to one field particle ϕ is described by Newton's law of gravitation

$$F = \frac{\mathcal{G} M_p M_\phi}{r^2}, \tag{B.18}$$

where M_p and M_ϕ are the masses of the test particle and field particles, respectively, and $r = |\mathbf{r}| = |\mathbf{r}_p - \mathbf{r}_\phi|$ is the separation distance between them (with r_p and r_ϕ the positions of the test particle and the field particle respectively).

To account for the cumulative effect of all field particles on the test particle, we integrate the force over the velocity distribution of the field particles. In the case where $M_p \gg M_\phi$ and assuming a Maxwellian velocity distribution for the field particles, characterized by $f(v) = \frac{\mathcal{N}}{(2\pi\sigma^2)^{3/2}} \mathrm{e}^{-\frac{v^2}{2\sigma^2}}$, where σ represents the velocity dispersion of the field particles and $\mathcal{N}$ the total number of field particles, we obtain the following formula

$$\dot{\boldsymbol{v}}_p = -\frac{16\pi^2 \mathcal{G}^2 M_\phi (M_\phi + M_p)}{v_p^3} C \int_0^{v_p} f(v) dv \boldsymbol{v}_p . \tag{B.19}$$

In this last expression, v_p represents the velocity of the test particle and $C = \ln(\Lambda)$ is the so-called Coulomb logarithm accounting for the logarithmic divergence arising from considering both small-scale and large-scale gravitational interactions. It is usually defined as $\Lambda = b_{\max}/b_{\min}$ where $b_{\max}$ and $b_{\min}$ represent the maximum and minimum impact parameters for which gravitational interaction is considered significant. The determination of $b_{\max}$ depends on the specific context of the problem. In contrast, the minimum impact parameter, represented by $b_{\min}$, is typically set to the size of the test particle, although its precise definition may vary depending on the nature of the object under consideration (i.e. as black holes). To provide a concrete example, when dealing with a test particle situated within a dark matter halo, different peoples may adopt distinct approaches for defining $b_{\max}$. While some might encompass the entire extent of the halo, others may restrict themselves to considering the region within the light cone of the test particle.

To simplify the integration process in (B.19), we introduce a dimensionless quantity $X = v/(\sqrt{2}\sigma)$ Then, we use the error function $\mathrm{erf}(x)$ defined as

$$\mathrm{erf}(X) = \frac{2}{\sqrt{\pi}} \int_0^X \mathrm{e}^{-t^2} dt \,, \tag{B.20}$$

capturing the cumulative effect of all field particles on the test particle. By integrating the force over the velocity distribution, incorporating the Coulomb logarithm and the error function, we derive the equation for dynamical friction

$$\dot{\boldsymbol{v}}_p = -\frac{4\pi\mathcal{G}^2 M_p^2 \rho_\phi}{v_p^3} C \left(\mathrm{erf}(X) - \frac{2X}{\sqrt{\pi}} \mathrm{e}^{-X^2} \right) \boldsymbol{v}_p \,, \tag{B.21}$$

where ρ_ϕ is the density of the field particles. Solving this differential equation provides insights into the time evolution of the velocity of the test particle, allowing us to understand the orbital decay caused by dynamical friction. This last equation can be further simplified as

$$F \simeq \frac{\mathcal{G}^2 M_p^2 \rho_\phi}{v_p^2} C \,. \tag{B.22}$$

It is interesting to note that the calculation of dynamical friction can be complex, often requiring numerical techniques for accurate solutions. The steps outlined in this appendix offer a logical progression through the fundamental equations and principles underlying the Chandrasekhar's calculation. For a comprehensive mathematical treatment and further details, we recommend referring to the original works by Chandrasekhar [60].

B.2 . Calculation of drag force for fuzzy dark matter

In this Appendix, keeping the system of a black hole moving inside a dark matter cloud, we will calculate the drag force in the free case. To do so, we set $\lambda_4 = 0$ to eliminate the effects of self-interactions. Consequently, the potential term simplifies to $V(\phi) = m_{\rm dm}^2 \phi^2/2$.

To analyze the system in the absence of self-interaction, we adopt a similar approach as in [190]. From the madelung transformation (2.7), we obtain the scalar field

$\phi = \sqrt{2\rho}\cos(m_{\rm dm}t - s)/m_{\rm dm}$. The equations of motion, derived from the Euler-Lagrange equations, can be expressed as follows (2.8)

$$\dot{\rho} + \sqrt{\frac{f}{h^3}}\nabla\cdot\left(\sqrt{fh}\rho\frac{\nabla s}{m_{\rm dm}}\right) = 0\,, \quad \frac{\dot{s}}{m_{\rm dm}} + \frac{f}{m_{\rm dm}}\frac{(\nabla s)^2}{2m_{\rm dm}^2} = \frac{1-f}{2}\,. \tag{B.23}$$

These equations govern the evolution of the density ρ and the phase s of the scalar field, respectively. To find a stationary solution for s, we consider a planar system in (r,θ) and assume that s can be written as $s = -Et + \hat{s}$, where $\hat{s}$ is time-independent, the kinetic energy $E = k^2/(2m_{\rm dm})$, and the momentum $k = m_{\rm dm}v_0$ (v_0 being the relative velocity at $z \to -\infty$). After substituting this solution into the second equation of (B.23), and identifying it with the Hamilton-Jacobi equation $\frac{dS}{dt} + H(\mathbf{p},\mathbf{r}) = 0$ (giving $S \to \hat{s}$ and $H = f(\hat{s})$), we obtain

$$\frac{d\hat{s}}{dt} + \frac{(\nabla\hat{s})^2}{2m_{\rm dm}} - \frac{h}{f}\left(E + \frac{1-f}{2}m_{\rm dm}\right) = 0\,. \tag{B.24}$$

From this equation, we derive the equations of Hamilton

$$\dot{\mathbf{r}} = \frac{\partial H}{\partial \mathbf{p}} = \frac{\mathbf{p}}{m_{\rm dm}}\,, \quad \dot{\mathbf{p}} = -\frac{\partial H}{\partial \mathbf{r}} = -\frac{\partial V(\mathbf{r})}{\partial \mathbf{r}}\,. \tag{B.25}$$

These equations allow us to obtain the total time derivative of $\hat{s}$. Considering a central force potential, we can express the momentum components as

$$p_\theta = L = kb\,, \quad |p_r| = \sqrt{-\left(\frac{L^2}{m_{\rm dm}^2 r^2} + \frac{2}{m_{\rm dm}}V(r)\right)} = m_{\rm dm}\sqrt{\frac{h}{f}}\sqrt{1 - f + v_0^2\left(1 - \frac{b^2}{r^2}\frac{f}{h}\right)}\,, \tag{B.26}$$

where $b = \sqrt{x^2+y^2} = r\sin(\theta)$ is the impact parameter. With this, we can obtain a final expression for s as

$$s = \hat{s}_0 + (\theta - \theta_0)L + \int_{t_0}^{t} dt\dot{r}p_r\,, \tag{B.27}$$

where $\hat{s}_0 = kz_0$, and θ_0 and z_0 are the angle and position at initial time t_0.

To account for the transition of dark matter particles from $p_r = -|p_r|$ to $p_r = +|p_r|$ at the minimum radius $r_{\rm min}$ of their trajectories, we divide the phase s and the angle θ into two cases:

- $t \leq t_{\rm min}$:

$$s = \hat{s}_0 + (\theta - \theta_0)L - \int_{r_0}^{r} dr|p_r|\,, \tag{B.28}$$

$$\theta = \theta_0 - L\int_{r_0}^{r}\frac{dr}{r^2|p_r|}\,. \tag{B.29}$$

- $t > t_{\rm min}$:

$$s = \hat{s}_0 + (\theta - \theta_0)L - \int_{r_0}^{r_{\rm min}} dr|p_r| + \int_{r_{\rm min}}^{r} dr|p_r|\,, \tag{B.30}$$

$$\theta = \theta_0 - L\int_{r_0}^{r_{\rm min}}\frac{dr}{r^2|p_r|} + L\int_{r_{\rm min}}^{r}\frac{dr}{r^2|p_r|}\,. \tag{B.31}$$

Now, to evaluate the density at a certain time ρ relative to the soliton density ρ_0, we introduce the yield defined as

$$\frac{\rho}{\rho_0} = \frac{r_0^2 \sin(\theta_0)}{r^2 \sin(\theta)} J^{-1} , \tag{B.32}$$

where $J = \frac{\partial r}{\partial r_0}\frac{\partial \theta}{\partial \theta_0} - \frac{\partial r}{\partial \theta_0}\frac{\partial \theta}{\partial r_0}$ is the Jacobian. Considering the initial conditions $\theta_0 = \pi$ and $r_0 = \infty$, we can determine both $\theta_{\text{min}} = \theta(t_{\text{min}})$ and the deflection angle at infinity θ_{def} from (B.31))

$$\theta_{\text{min}} = \pi + L \int_{r_{\text{min}}}^{\infty} \frac{dr}{r^2 |p_r|} , \qquad \theta_{\text{def}} = \pi + 2L \int_{r_{\text{min}}}^{\infty} \frac{dr}{r^2 |p_r|} , \tag{B.33}$$

giving the relation $\theta_{\text{def}} - \pi = 2(\theta_{\text{min}} - \pi)$. For convenience, we can define $\tilde{J} = J/(r_0^2 \sin(\theta_0))$, that is giving at infinity, the Jacobian

$$\tilde{J}_\infty = \frac{1}{b} \frac{\partial \theta_{\text{def}}}{\partial b} , \tag{B.34}$$

where we introduced the impact parameter $b = \sqrt{x^2 + y^2} = r \sin(\theta)$, as the motion is one the z-axis. Using (B.34), we can rewrite (B.32) as

$$\left. \frac{\rho}{\rho_0} \right|_\infty = \left(\frac{r^2 \sin(\theta_{\text{def}})}{b} \frac{\partial \theta_{\text{def}}}{\partial b} \right)^{-1} . \tag{B.35}$$

As their is no internal pressure in the free case, the drag force formula (3.79) can be expressed as [63]

$$F_z = - \oint dS_j T_{jz} = - \oint dx dy T_{zz} , \tag{B.36}$$

where $d\mathbf{S} = dS_z \mathbf{e}_z = dxdy\mathbf{e}_z$. However, integrating over dx and dy is not convenient due to the deviation of trajectories. An alternative parameter correlated to x and y that follows the trajectories is the impact parameter b. We will evaluate this integral at infinity, far from the black hole, allowing us to use a Minkowski metric and Kepler's approximation. Using the hydrodynamics approximation ($v^4 \ll v_z^2$), we find the energy-momentum tensor component T_{zz} is

$$T_{zz} \approx \rho v_z^2 . \tag{B.37}$$

Initially, we have the relations $b = r \sin(\theta)$, $x = b \cos(\varphi)$ and $y = b \sin(\varphi)$, where we introduce the angle ϕ between the impact parameter and the x and y-axis. We can perform the change $(dx, dy) \rightarrow (db, d\varphi)$, which results in $dx \cdot dy = bdbd\varphi$. At an infinite radius after the black hole, we can define b in terms of θ_{def}. Indeed, we know that at infinity $v_z = v_0 \cos(\theta_{\text{def}})$, and the previous relations become $z_\infty = r \cos(\theta_{\text{def}})$, $x = z_\infty \tan(\theta_{\text{def}}) \cos(\varphi)$, $y = z_\infty \tan(\theta_{\text{def}}) \sin(\varphi)$. Thus, a natural change of units to do is $(dx, dy) \rightarrow (d\theta_{\text{def}}, d\varphi)$, resulting in

$$dx \cdot dy = z_\infty^2 \frac{\sin(\theta_{\text{def}})}{\cos^3(\theta_{\text{def}})} d\theta_{\text{def}} \cdot d\varphi . \tag{B.38}$$

Since the surface integral (B.36) can be evaluated at infinity both before and after the black hole, we can use Kepler's approximation

$$r \to \infty : |p_r| = \sqrt{k^2 + \frac{2\mathcal{G} m_{\mathrm{BH}} m_{\mathrm{dm}}}{r} - \frac{L^2}{r^2}}\,, \tag{B.39}$$

which, combined with (B.33), gives

$$\theta_{\mathrm{def}} = -2\sin^{-1}\left(\frac{1}{\sqrt{1+\alpha^2}}\right)\,, \tag{B.40}$$

where $\alpha = bv_0^2/(\mathcal{G} m_{\mathrm{BH}})$. Finally, the drag force can be expressed as

$$F_z = 2\pi\rho_0 v_0^2 \left[\left(\frac{\mathcal{G} m_{\mathrm{BH}}}{v_0^2}\right)^2 \ln\left(\frac{(b^+)^2 + \left(\frac{\mathcal{G} m_{\mathrm{BH}}}{v_0^2}\right)^2}{(b^-)^2 + \left(\frac{\mathcal{G} m_{\mathrm{BH}}}{v_0^2}\right)^2}\right) + \frac{(b^-)^2}{2}\right]\,, \tag{B.41}$$

where b^- represents the minimum impact parameter for a particle of mass m_{dm} to avoid being absorbed by the black hole, and b^+ is the chosen maximum impact parameter. This result matches the one from [63, 275]. In the equation (B.41), the first term can be likened to Chandrasekhar's classical result [60], whereas the second term is directly linked to the accretion drag force. This is because the value of b^- depends on the radius of the black hole (as it the the minimum impact parameter for which dark matter particles can escape the black hole), which is also determined by its mass by $r_s = 2\mathcal{G} m_{\mathrm{BH}}$.

C . Accretion Column Analysis

C.1 . Hoyle-Lyttleton Accretion Rate Framework

This appendix delves into the accretion behavior of black holes during high Mach number scenarios as denoted by (4.38). In this context, accretion occurs via a columnar structure situated on the trailing end of the black hole, consistent with the traditional Hoyle-Lyttleton model. Drawing from [308] as a basis, we employ dimensional coordinates to align with our study's specifics. In scenarios characterized by extreme speeds (hypersonic regime), the pressure upstream of the shock front is essentially inconsequential, leading the dynamics to adhere to Keplerian orbits typical of the collisionless model. Consequently, for a streamline with an impact parameter b, the hyperbolic orbit is represented by

$$r = \frac{b^2 v_0^2}{\mathcal{G} m_{\mathrm{BH}}(1+\cos\theta) + bv_0^2 \sin\theta}\,, \tag{C.42}$$

where the respective radial and angular velocities are given by

$$v_r = \pm\sqrt{v_0^2 + \frac{2\mathcal{G} m_{\mathrm{BH}}}{r} - \frac{b^2 v_0^2}{r^2}}\,, \tag{C.43}$$

$$v_\theta = -\frac{bv_0}{r}\,, \tag{C.44}$$

and the density is

$$\rho = \frac{\rho_0 b^2}{r\sin\theta(2b - r\sin\theta)}\,. \tag{C.45}$$

With high v_0 values, the accretion column approximates a slender conical structure, oriented around the downstream z-axis, positioned post the shock front. This structure, at extended distances, narrows to an angle $\theta_s \ll 1$, aligning with the Mach angle θ_c as expressed in Section 4.1.2. Based on (C.42), the orbit corresponding to the impact parameter b intersects the downstream z-axis ($\theta = 0$) at a radius of

$$r_1 = \frac{b^2 v_0^2}{2\mathcal{G} m_{\rm BH}}\,, \tag{C.46}$$

associated with the velocities

$$v_{r_1} = v_0, \tag{C.47}$$

$$v_{\theta_1} = -\frac{2\mathcal{G} m_{\rm BH}}{b v_0}\,. \tag{C.48}$$

Here, the boundary conditions, placed before the shock front, can be approximated by $\theta_s \simeq 0$. The density in this region is

$$\rho_1 = \frac{\rho_0 \mathcal{G} m_{\rm BH}}{\sin\theta_s b v_0^2}. \tag{C.49}$$

Post the shock front, continuity conditions necessitate consistent tangential velocities and transverse momentum. With an approximation of $\theta_s \simeq 0$, immediate conditions past the shock yield

$$v_{r_2} = v_0\,, \tag{C.50}$$

$$v_{\theta_2} = -\frac{c_{s,0}^2}{\sin\theta_s v_0}\,, \tag{C.51}$$

$$\rho_2 = \frac{\rho_a \mathcal{G} m_{\rm BH}}{r} \tag{C.52}$$

$$= \frac{\rho_0 2\mathcal{G}^2 m_{\rm BH}^2}{b^2 v_0^2 c_{s,0}^2}\,, \tag{C.53}$$

derived from the Bernoulli equation

$$\frac{v^2}{2} + \frac{\rho}{\rho_a} - \frac{\mathcal{G} m_{\rm BH}}{r} = \frac{v_0^2}{2} + \frac{\rho_0}{\rho_a}\,. \tag{C.54}$$

In a slower flow region situated directly behind the black hole, where $v^2 \ll c_{s,0}^2 = \rho/\rho_a$, the density approximation is given by $\rho \simeq \rho_a \mathcal{G} m_{\rm BH}/r$, valid for $r \lesssim \mathcal{G} m_{\rm BH}/v_0^2$. For θ_s comparable to θ_c, we deduce

$$\rho_1 \sim \frac{\rho_0 \mathcal{G} m_{\rm BH}}{b v_0 c_{s,0}}\,, \tag{C.55}$$

$$v_{\theta_2} \sim -c_{s,0}\,. \tag{C.56}$$

Assuming negligible $v_{\theta 2}$ and postulating that dark matter gets accreted when bound to the black hole (given by $v_0^2/2 - \mathcal{G} m_{\mathrm{BH}}/r < 0$), the resultant Hoyle-Lyttleton radius and impact parameter as proposed by [308] are

$$r_{\mathrm{HL}} = \frac{2\mathcal{G} m_{\mathrm{BH}}}{v_0^2}, \quad b_{\mathrm{HL}} = \frac{2\mathcal{G} m_{\mathrm{BH}}}{v_0^2}, \tag{C.57}$$

which subsequently defines the Hoyle-Lyttleton accretion rate as

$$\dot{M}_{\mathrm{HL}} = \rho_0 v_0 \pi b_{\mathrm{HL}}^2 , \tag{C.58}$$

corresponding to (4.36).

C.2 . Estimation of the Lower Limit for Accretion Rate

Recent detailed investigations into the accretion column hint that the accretion rate might be somewhat reduced compared to initial assumptions [308]. Given (C.46), the quantity of mass influx joining the accretion column via the shock within the radial interval r to $r + dr$ can be represented as

$$F dr = \rho_0 v_0 2\pi b db = 2\pi \frac{\mathcal{G} m_{\mathrm{BH}} \rho_0}{v_0} dr . \tag{C.59}$$

Consider μdr as the mass located in the accretion column between the radial intervals r and $r+dr$, and let v symbolize the average longitudinal speed in the column. The principle of mass conservation translates to

$$\frac{d}{dr}(\mu v) = F . \tag{C.60}$$

Simultaneously, longitudinal momentum conservation can be expressed as

$$\frac{d}{dr}(\mu v^2) = -\frac{\mathcal{G} m_{\mathrm{BH}} \mu}{r^2} + \frac{d}{dr}(\pi r_\perp^2 P) + F v_0, \tag{C.61}$$

Here, the gravitational pull of the black hole is depicted by the first term on the right, the second term illustrates the pressure force, and the momentum influx is represented by the third term since $v_2 = v_0$ on the shock. Given that $P = \rho^2/(2\rho_a)$, contrary to the Bondi-Hoyle framework [308, 320], it is evident that the pressure is potentially comparable to the gravitational energy, expressed as $r_\perp^2 P$. Nevertheless, for a cone-shaped shock with a fixed angle θ_s, the derivative of the pressure term becomes null due to the proportionalities $r_\perp$ to r and P to ρ^2. This causes the pressure term to diminish relative to the gravitational term, allowing the analysis to follow the approach in [308, 320]. From the mass conservation equation (C.60), we deduce

$$\mu v = F(r - r_0) , \tag{C.62}$$

where r_0 denotes the point of stagnation behind the black hole. The momentum conservation equation (C.61) can be restructured to

$$v \frac{dv}{dr} = -\frac{\mathcal{G} m_{\mathrm{BH}}}{r^2} + \frac{v(v_0 - v)}{r - r_0} . \tag{C.63}$$

A necessary condition for the velocity to vary consistently from -1 near the black hole to v_0 at infinity was recognized by [308]

$$r_0 > \frac{\mathcal{G} m_{\rm BH}}{v_0^2} \,. \tag{C.64}$$

Finally, the lowest possible accretion rate becomes

$$\dot{m}_{\rm BH} = \int_0^{r_0} dr F = F r_0 > \frac{2\pi \rho_0 \mathcal{G}^2 m_{\rm BH}^2}{v_0^3} \,. \tag{C.65}$$

This rate is half of the Hoyle-Lyttleton accretion rate (4.36).

C.3 . Determining the Accretion-Column Velocity Boundary

Within the accretion column, for radii approaching the Schwarzschild radius, the values for density and velocity converge to $\rho \approx \rho_a$ and $v \approx -1$, respectively. According to the Bernoulli equation (C.54), these values represent the maximum achievable density and velocity in the Newtonian frame. Notably, these limits are also evident in radial accretion scenarios. The accretion rate at this Schwarzschild radius is connected to the solid angle Ω of the accretion column as

$$\Omega r_s^2 \rho_a \approx \dot{m}_{\rm BH} \approx \rho_0 \mathcal{G}^2 m_{\rm BH}^2 / v_0^3 \,. \tag{C.66}$$

This relationship implies

$$\Omega \approx \frac{c_{s,0}^2}{v_0^3} \,, \tag{C.67}$$

from which we can deduce

$$\Omega \geq 1 \quad \text{when} \quad v_0 \leq c_{s,0}^{2/3} \,. \tag{C.68}$$

From here, we can identify the two regimes (4.37) and (4.38):

- In scenarios where $v_0 > c_{s,0}^{2/3}$, the accretion column narrows behind the black hole, and the accretion rate aligns closely with the forecast of Hoyle-Lyttleton.
- For $v_0 < c_{s,0}^{2/3}$, the accretion column broadens to envelop the black hole from every side. A prominent bow shock is now formed before the black hole, as visualized in Figure. 4.2. The resultant accretion rate drops significantly below the Bondi-Hoyle-Lyttleton projection. This decrease arises from the pronounced influence of self-interactions in the subsonic area.

In high Mach number settings, where $v_0 > c_{s,0}^{2/3}$, the analysis of equations (C.42) to (C.45) reveals that both density and velocity around $r \approx r_s$ on the leading edge of the black hole (at $\theta = \pi$) are

$$v_r \approx 1 \,, \quad \rho \approx \rho_a \frac{c_{s,0}^2}{v_0} < \rho_a c_{s,0}^{4/3} \ll \rho_a \,. \tag{C.69}$$

This outcome highlights the asymmetry of this regime. With reduced density and minimal self-interactions, the inflow rate on the forward face of the black hole is quite low. This allows matter to plunge directly into the black hole, maintaining its supersonic state without undergoing a shock for a vast portion of the surface of the black hole. However, the primary source of the accretion rate is the confined accretion column behind the black hole, which is coupled with an attached shock and a localized subsonic zone.

D . Calculation of the gravitational wave contribution

In this appendix, we will derive the expression for the rate of change of velocity, specifically the radiation-reaction acceleration, for binary black holes. The following discussion is based on chapter 12.7 of [326], and include possible mass accretion.

The expression for the radiation-reaction acceleration is given by

$$\ddot{r}^j[rr] \simeq \mathcal{G}\left[-\frac{\mathcal{G}M}{r^2}\left(3\,\dddot{I}^{pq}n^pn^q+\frac{1}{3}\,\dddot{I}^{pp}\right)n^j+2I^{(4)jk}v^k+\frac{3}{5}I^{(5)jk}r^k-\frac{1}{5}I^{(5)pp}r^j\right]\,. \tag{D.70}$$

Here, $r := |r|$ and $n := r/r$ and the mass quadrupole moment is $I^{jk} = \mu r^j r^k$. The change in in I^{jk} due to the change in masses is taken into account at order $\dot{\mu}$ by defining a function $g^{jk} = r^j r^k$. Thus,

$$\begin{aligned}
\dot{I}^{jk} &= \dot{\mu}g^{jk} + \mu\dot{g}^{jk}\,,\\
\ddot{I}^{jk} &= 2\dot{\mu}\dot{g}^{jk} + \mu\ddot{g}^{jk}\,,\\
\dddot{I}^{jk} &= 3\dot{\mu}\ddot{g}^{jk} + \mu\,\dddot{g}^{jk}\,,\\
I^{(4)jk} &= 4\dot{\mu}\,\dddot{g}^{jk} + \mu g^{(4)jk}\,,\\
I^{(5)jk} &= 5\dot{\mu}g^{(4)jk} + \mu g^{(5)jk}\,.
\end{aligned} \tag{D.71}$$

where $\mu := m_1m_2/(m_1+m_2)^2$. The initial terms of each derivative provide no change in the value of the radiation-reaction acceleration due to their parity. The second terms demonstrate the usual contribution of gravitational waves to the equation of motion $\ddot{r}^j = -\frac{\mathcal{G}M}{r^2}\hat{r}^j$ (normally utilized as a perturbation of Keplerian dynamics). To account for the terms in $\dot{\mu}$, one must alter the equation of motion to incorporate contributions from mass accretion and Chandrasekhar's force. However, since the hypothesis states that the contributions from mass accretion and Chandrasekhar's force are much less than the gravitational waves contribution, these terms can be considered negligible.

After considering these factors, the result for the rate of change of velocity is given by

$$\dot{\boldsymbol{v}} = \frac{8}{5}\mu\frac{\mathcal{G}^2M}{r^3}\left[\left(3v^2+\frac{17}{3}\frac{\mathcal{G}M}{r}\right)\dot{r}\hat{\boldsymbol{r}}-\left(v^2+3\frac{\mathcal{G}M}{r}\right)\boldsymbol{v}\right]\,. \tag{D.72}$$

This expression describes the radiation-reaction acceleration experienced by the binary black hole system due to the emission of gravitational waves, and does not depends on the mass rate of change of the black holes. Then, by using equations (5.30), (5.31) and (5.32), we recover the expressions (5.40) and (5.41).

E . Fisher analysis - principles and procedures

The Fisher analysis is a widely used statistical method in physics for estimating model parameters and assessing their uncertainties. Developed by Fisher [356], this approach allows to understand how variations in observed data impact the estimation of model parameters. In this appendix, we provide a comprehensive explanation of the Fisher analysis, emphasizing its fundamental principles, procedural steps, and the mathematical assumptions behind it.

In order to apply the Fisher analysis, we first establish a mathematical model that describes the relationship between the observed data and the parameters of interest. This model is typically based on a probabilistic framework, where the observed data is governed by a probability distribution conditioned on the model parameters. To quantify the likelihood of obtaining the observed data given specific parameter values, we define the likelihood function

$$L(\theta) = P(x|\theta)\,, \tag{E.73}$$

where x represents the observed data, θ denotes the model parameters and $P(D|\theta)$ the probability to have x knowing the parameters θ. It assumes that the likelihood function is approximately Gaussian in shape. This assumption is valid when the observed data follows a well-behaved distribution and the sample size is sufficiently large, as per the central limit theorem. The likelihood function can be expressed as

$$L(\theta) = \frac{1}{\sqrt{2\pi\sigma^2}} \exp\left(-\frac{(x-\mu)^2}{2\sigma^2}\right)\,, \tag{E.74}$$

where μ is the model prediction, and σ represents the standard deviation. The sensitivity of the likelihood function to changes in the model parameters is assessed through the computation of the score function. This function provides information about the gradient of the log-likelihood function with respect to the parameters, indicating the direction and magnitude of the parameter effects on the likelihood

$$\mathcal{S}(\theta) = \frac{\partial \ln L(\theta)}{\partial \theta}\,. \tag{E.75}$$

Additionally, the Fisher analysis assumes that the model is correctly specified and that the observed data is generated from the assumed probabilistic model. Deviations from the model assumptions can lead to biased parameter estimates and unreliable uncertainties. Therefore, it is crucial to carefully evaluate the appropriateness of the chosen model for the given data.

The Fisher information matrix is a key element in the Fisher analysis. It measures the precision or uncertainty associated with the parameter estimates. The Fisher information matrix is determined by taking the negative expected value of the Hessian matrix, which consists of the second-order partial derivatives of the log-likelihood function with respect to the parameters

$$\Gamma_{ij}(\theta) = -\mathbb{E}\left[\frac{\partial^2 \ln L(\theta)}{\partial\theta_i \partial\theta_j}\right]\,. \tag{E.76}$$

By examining the curvature of the log-likelihood function, the Fisher information matrix provides insights into the uncertainties in parameter estimation. The inverse of the Fisher information matrix $(\Gamma_{ij}(\theta))^{-1}$, known as the inverse Fisher information matrix, is particularly significant. It offers valuable information regarding the precision of the parameter estimates and facilitates the derivation of the variances and covariances for these estimates. To obtain the most likely values of the model parameters, we employ numerical optimization techniques to maximize the likelihood function or minimize the negative log-likelihood function. These optimal values, known as maximum likelihood estimates, represent the best estimates of the model parameters based on the observed data. In order to assess the statistical significance of the estimated parameters, we conduct hypothesis testing. This involves comparing the estimated parameters with their expected values under the null hypothesis or employing likelihood ratio tests to evaluate the significance of nested models. To quantify the uncertainty surrounding the estimated parameters, we calculate confidence intervals. These intervals provide a range of plausible values for the parameters based on the observed data. The standard errors of the parameter estimates, derived using the inverse Fisher information matrix, indicate the uncertainties associated with each parameter estimate.

The resulting parameter estimates represent the best estimates of the model parameters based on the observed data. To assess the statistical significance of the estimated parameters, hypothesis testing can be conducted. This involves comparing the estimated parameters with their expected values under the null hypothesis or employing likelihood ratio tests to evaluate the significance of nested models. Confidence intervals are used to quantify the uncertainty surrounding the estimated parameters. These intervals provide a range of plausible values for the parameters based on the observed data.

While the Fisher analysis is a widely used and computationally efficient method, it may not always be the most suitable approach, especially in complex models or situations with limited data. In such cases, more sophisticated techniques like Markov Chain Monte Carlo (MCMC) methods can be advantageous. These methods allow for the exploration of high-dimensional parameter spaces and provide a more complete characterization of the posterior distribution of parameters. However, they are computationally expensive and require significant computational resources and time. The choice of the appropriate statistical method depends on the specific requirements and characteristics of the problem at hand.

Bibliography

[1] Alexis Boudon, Philippe Brax, and Patrick Valageas. "Subsonic accretion and dynamical friction for a black hole moving through a self-interacting scalar dark matter cloud". In: *Phys. Rev. D* 106.4 (2022), p. 043507. doi: `10.1103/PhysRevD.106.043507`. arXiv: `2204.09401 [astro-ph.CO]`.

[2] Alexis Boudon, Philippe Brax, and Patrick Valageas. "Supersonic friction of a black hole traversing a self-interacting scalar dark matter cloud". In: (July 2023). arXiv: `2307.15391 [astro-ph.CO]`.

[3] Alexis Boudon et al. "Gravitational waves from binary black holes in a self-interacting scalar dark matter cloud". In: (May 2023). arXiv: `2305.18540 [astro-ph.CO]`.

[4] Jianglai Liu, Xun Chen, and Xiangdong Ji. "Current status of direct dark matter detection experiments". In: *Nature Phys.* 13.3 (2017), pp. 212–216. doi: `10.1038/nphys4039`. arXiv: `1709.00688 [astro-ph.CO]`.

[5] Julien Billard et al. "Direct Detection of Dark Matter – APPEC Committee Report". In: (Apr. 2021). arXiv: `2104.07634 [hep-ex]`.

[6] Leszek Roszkowski, Enrico Maria Sessolo, and Sebastian Trojanowski. "WIMP dark matter candidates and searches—current status and future prospects". In: *Rept. Prog. Phys.* 81.6 (2018), p. 066201. doi: `10.1088/1361-6633/aab913`. arXiv: `1707.06277 [hep-ph]`.

[7] Giorgio Arcadi et al. "The waning of the WIMP? A review of models, searches, and constraints". In: *Eur. Phys. J. C* 78.3 (2018), p. 203. doi: `10.1140/epjc/s10052-018-5662-y`. arXiv: `1703.07364 [hep-ph]`.

[8] David H. Weinberg et al. "Cold dark matter: Controversies on small scales". In: *Proc. Nat. Acad. Sci.* 112.40 (2015), pp. 12249–12255.

[9] Philip Bull et al. "Beyond ΛCDM: Problems, solutions, and the road ahead". In: *Phys. Dark Univ.* 12 (2016), pp. 56–99. doi: `10.1016/j.dark.2016.02.001`. arXiv: `1512.05356 [astro-ph.CO]`.

[10] James S. Bullock and Michael Boylan-Kolchin. "Small-Scale Challenges to the ΛCDM Paradigm". In: *Ann. Rev. Astron. Astrophys.* 55 (2017), pp. 343–387. doi: `10.1146/annurev-astro-091916-055313`. arXiv: `1707.04256 [astro-ph.CO]`.

[11] Antonino Del Popolo and Morgan Le Delliou. "Small scale problems of the ΛCDM model: a short review". In: *Galaxies* 5.1 (2017), p. 17. doi: `10.3390/galaxies5010017`. arXiv: `1606.07790 [astro-ph.CO]`.

[12] Leandros Perivolaropoulos and Foteini Skara. "Challenges for ΛCDM: An update". In: *New Astron. Rev.* 95 (2022), p. 101659. doi: 10.1016/j.newar.2022.101659. arXiv: 2105.05208 [astro-ph.CO].

[13] Alan R. Duffy et al. "Impact of baryon physics on dark matter structures: a detailed simulation study of halo density profiles". In: *Mon. Not. Roy. Astron. Soc.* 405 (2010), p. 2161. doi: 10.1111/j.1365-2966.2010.16613.x. arXiv: 1001.3447 [astro-ph.CO].

[14] Alyson M. Brooks et al. "A Baryonic Solution to the Missing Satellites Problem". In: *Astrophys. J.* 765 (2013), p. 22. doi: 10.1088/0004-637X/765/1/22. arXiv: 1209.5394 [astro-ph.CO].

[15] Shea Garrison-Kimmel et al. "Can Feedback Solve the Too Big to Fail Problem?" In: *Mon. Not. Roy. Astron. Soc.* 433 (2013), p. 3539. doi: 10.1093/mnras/stt984. arXiv: 1301.3137 [astro-ph.CO].

[16] Matthieu Schaller et al. "Baryon effects on the internal structure of ΛCDM haloes in the EAGLE simulations". In: *Mon. Not. Roy. Astron. Soc.* 451.2 (2015), pp. 1247–1267. doi: 10.1093/mnras/stv1067. arXiv: 1409.8617 [astro-ph.CO].

[17] Jose Oñorbe et al. "Forged in FIRE: cusps, cores, and baryons in low-mass dwarf galaxies". In: *Mon. Not. Roy. Astron. Soc.* 454.2 (2015), pp. 2092–2106. doi: 10.1093/mnras/stv2072. arXiv: 1502.02036 [astro-ph.GA].

[18] Andrew R. Wetzel et al. "Reconciling dwarf galaxies with ΛCDM cosmology: Simulating a realistic population of satellites around a Milky Way-mass galaxy". In: *Astrophys. J. Lett.* 827.2 (2016), p. L23. doi: 10.3847/2041-8205/827/2/L23. arXiv: 1602.05957 [astro-ph.GA].

[19] Aaron A. Dutton et al. "NIHAO XX: the impact of the star formation threshold on the cusp–core transformation of cold dark matter haloes". In: *Mon. Not. Roy. Astron. Soc.* 486.1 (2019), pp. 655–671. doi: 10.1093/mnras/stz889. arXiv: 1811.10625 [astro-ph.GA].

[20] Aaron A. Dutton et al. "NIHAO – XXV. Convergence in the cusp-core transformation of cold dark matter haloes at high star formation thresholds". In: (Nov. 2020). doi: 10.1093/mnras/staa3028. arXiv: 2011.11351 [astro-ph.GA].

[21] Jeremy Goodman. "Repulsive dark matter". In: *New Astron.* 5 (2000), p. 103. doi: 10.1016/S1384-1076(00)00015-4. arXiv: astro-ph/0003018.

[22] Hsi-Yu Schive, Tzihong Chiueh, and Tom Broadhurst. "Cosmic Structure as the Quantum Interference of a Coherent Dark Wave". In: *Nature Phys.* 10 (2014), pp. 496–499. doi: 10.1038/nphys2996. arXiv: 1406.6586 [astro-ph.GA].

[23] Hsi-Yu Schive et al. “Understanding the Core-Halo Relation of Quantum Wave Dark Matter from 3D Simulations”. In: *Phys. Rev. Lett.* 113.26 (2014), p. 261302. doi: 10.1103/PhysRevLett.113.261302. arXiv: 1407.7762 [astro-ph.GA].

[24] Alexandre Arbey, Julien Lesgourgues, and Pierre Salati. “Quintessential haloes around galaxies”. In: *Phys. Rev.* D64 (2001), p. 123528. doi: 10.1103/PhysRevD.64.123528. arXiv: astro-ph/0105564 [astro-ph].

[25] Pierre-Henri Chavanis. “Mass-radius relation of Newtonian self-gravitating Bose-Einstein condensates with short-range interactions: I. Analytical results”. In: *Phys. Rev.* D84 (2011), p. 043531. doi: 10.1103/PhysRevD.84.043531. arXiv: 1103.2050 [astro-ph.CO].

[26] P. H. Chavanis and L. Delfini. “Mass-radius relation of Newtonian self-gravitating Bose-Einstein condensates with short-range interactions: II. Numerical results”. In: *Phys. Rev.* D84 (2011), p. 043532. doi: 10.1103/PhysRevD.84.043532. arXiv: 1103.2054 [astro-ph.CO].

[27] David J. E. Marsh and Ana-Roxana Pop. “Axion dark matter, solitons and the cusp–core problem”. In: *Mon. Not. Roy. Astron. Soc.* 451.3 (2015), pp. 2479–2492. doi: 10.1093/mnras/stv1050. arXiv: 1502.03456 [astro-ph.CO].

[28] Erminia Calabrese and David N. Spergel. “Ultra-Light Dark Matter in Ultra-Faint Dwarf Galaxies”. In: *Mon. Not. Roy. Astron. Soc.* 460.4 (2016), pp. 4397–4402. doi: 10.1093/mnras/stw1256. arXiv: 1603.07321 [astro-ph.CO].

[29] Shu-Rong Chen, Hsi-Yu Schive, and Tzihong Chiueh. “Jeans Analysis for Dwarf Spheroidal Galaxies in Wave Dark Matter”. In: *Mon. Not. Roy. Astron. Soc.* 468.2 (2017), pp. 1338–1348. doi: 10.1093/mnras/stx449. arXiv: 1606.09030 [astro-ph.GA].

[30] Bodo Schwabe, Jens C. Niemeyer, and Jan F. Engels. “Simulations of solitonic core mergers in ultralight axion dark matter cosmologies”. In: *Phys. Rev.* D94.4 (2016), p. 043513. doi: 10.1103/PhysRevD.94.043513. arXiv: 1606.05151 [astro-ph.CO].

[31] Jan Veltmaat and Jens C. Niemeyer. “Cosmological particle-in-cell simulations with ultralight axion dark matter”. In: *Phys. Rev.* D94.12 (2016), p. 123523. doi: 10.1103/PhysRevD.94.123523. arXiv: 1608.00802 [astro-ph.CO].

[32] Alma X. González-Morales et al. “Unbiased constraints on ultralight axion mass from dwarf spheroidal galaxies”. In: *Mon. Not. Roy. Astron. Soc.* 472.2 (2017), pp. 1346–1360. doi: 10.1093/mnras/stx1941. arXiv: 1609.05856 [astro-ph.CO].

[33] Victor H. Robles and Tonatiuh Matos. “Flat Central Density Profile and Constant DM Surface Density in Galaxies from Scalar Field Dark Matter”. In: *Mon. Not. Roy. Astron. Soc.* 422 (2012), pp. 282–289. doi: `10.1111/j.1365-2966.2012.20603.x`. arXiv: `1201.3032 [astro-ph.CO]`.

[34] Tula Bernal et al. “Rotation curves of high-resolution LSB and SPARC galaxies with fuzzy and multistate (ultralight boson) scalar field dark matter”. In: *Mon. Not. Roy. Astron. Soc.* 475.2 (2018), pp. 1447–1468. doi: `10.1093/mnras/stx3208`. arXiv: `1701.00912 [astro-ph.GA]`.

[35] Philip Mocz et al. “Galaxy formation with BECDM – I. Turbulence and relaxation of idealized haloes”. In: *Mon. Not. Roy. Astron. Soc.* 471.4 (2017), pp. 4559–4570. doi: `10.1093/mnras/stx1887`. arXiv: `1705.05845 [astro-ph.CO]`.

[36] Kyohei Mukaida, Masahiro Takimoto, and Masaki Yamada. “On Longevity of I-ball/Oscillon”. In: *JHEP* 03 (2017), p. 122. doi: `10.1007/JHEP03(2017)122`. arXiv: `1612.07750 [hep-ph]`.

[37] Jorge Vicens, Jordi Salvado, and Jordi Miralda-Escudé. “Bosonic dark matter halos: excited states and relaxation in the potential of the ground state”. In: (2018). arXiv: `1802.10513 [astro-ph.CO]`.

[38] Nitsan Bar et al. “Galactic rotation curves versus ultralight dark matter: Implications of the soliton-host halo relation”. In: *Phys. Rev.* D98.8 (2018), p. 083027. doi: `10.1103/PhysRevD.98.083027`. arXiv: `1805.00122 [astro-ph.CO]`.

[39] Joshua Eby et al. “Classical nonrelativistic effective field theory and the role of gravitational interactions”. In: *Phys. Rev.* D99.12 (2019), p. 123503. doi: `10.1103/PhysRevD.99.123503`. arXiv: `1807.09795 [hep-ph]`.

[40] Ben Bar-Or, Jean-Baptiste Fouvry, and Scott Tremaine. “Relaxation in a Fuzzy Dark Matter Halo”. In: *Astrophys. J.* 871.1 (2019), p. 28. doi: `10.3847/1538-4357/aaf28c`. arXiv: `1809.07673 [astro-ph.GA]`.

[41] David J. E. Marsh and Jens C. Niemeyer. “Strong Constraints on Fuzzy Dark Matter from Ultrafaint Dwarf Galaxy Eridanus II”. In: (2018). arXiv: `1810.08543 [astro-ph.CO]`.

[42] Pierre-Henri Chavanis. “A predictive model of BEC dark matter halos with a solitonic core and an isothermal atmosphere”. In: (2018). arXiv: `1810.08948 [gr-qc]`.

[43] Razieh Emami et al. “A Soliton Solution for the Central Dark Masses in 47-Tuc Globular Cluster and Implications for the Axiverse”. In: (2018). arXiv: `1806.04518 [astro-ph.CO]`.

[44] D. G. Levkov, A. G. Panin, and I. I. Tkachev. “Gravitational Bose-Einstein condensation in the kinetic regime”. In: *Phys. Rev. Lett.* 121.15 (2018), p. 151301. doi: `10.1103/PhysRevLett.121.151301`. arXiv: `1804.05857 [astro-ph.CO]`.

[45] Tom Broadhurst et al. “Ghostly Galaxies as Solitons of Bose-Einstein Dark Matter”. In: (2019). arXiv: `1902.10488 [astro-ph.CO]`.

[46] Kohei Hayashi and Ippei Obata. “Non-sphericity of ultra-light axion dark matter halos in the Galactic dwarf spheroidal galaxies”. In: (2019). arXiv: `1902.03054 [astro-ph.CO]`.

[47] Nitsan Bar et al. “Ultralight dark matter in disk galaxies”. In: *Phys. Rev.* D99.10 (2019), p. 103020. doi: `10.1103/PhysRevD.99.103020`. arXiv: `1903.03402 [astro-ph.CO]`.

[48] Raquel Galazo García, Philippe Brax, and Patrick Valageas. “Solitons and halos for self-interacting scalar dark matter”. In: (Apr. 2023). arXiv: `2304.10221 [astro-ph.CO]`.

[49] Lam Hui. “Unitarity bounds and the cuspy halo problem”. In: *Phys. Rev. Lett.* 86 (2001), pp. 3467–3470. doi: `10.1103/PhysRevLett.86.3467`. arXiv: `astro-ph/0102349`.

[50] W. J. G. de Blok. “The Core-Cusp Problem”. In: *Adv. Astron.* 2010 (2010), p. 789293. doi: `10.1155/2010/789293`. arXiv: `0910.3538 [astro-ph.CO]`.

[51] Vid Iršič et al. “First constraints on fuzzy dark matter from Lyman-α forest data and hydrodynamical simulations”. In: *Phys. Rev. Lett.* 119.3 (2017), p. 031302. doi: `10.1103/PhysRevLett.119.031302`. arXiv: `1703.04683 [astro-ph.CO]`.

[52] Eric Armengaud et al. “Constraining the mass of light bosonic dark matter using SDSS Lyman-α forest”. In: *Mon. Not. Roy. Astron. Soc.* 471.4 (2017), pp. 4606–4614. doi: `10.1093/mnras/stx1870`. arXiv: `1703.09126 [astro-ph.CO]`.

[53] Jiajun Zhang et al. “The Importance of Quantum Pressure of Fuzzy Dark Matter on Lyman-Alpha Forest”. In: *Astrophys. J.* 863 (2018), p. 73. doi: `10.3847/1538-4357/aacf3f`. arXiv: `1708.04389 [astro-ph.CO]`.

[54] Helvi Witek et al. “Superradiant instabilities in astrophysical systems”. In: *Phys. Rev. D* 87.4 (2013), p. 043513. doi: `10.1103/PhysRevD.87.043513`. arXiv: `1212.0551 [gr-qc]`.

[55] Richard Brito, Vitor Cardoso, and Paolo Pani. “Black holes as particle detectors: evolution of superradiant instabilities”. In: *Class. Quant. Grav.* 32.13 (2015), p. 134001. doi: `10.1088/0264-9381/32/13/134001`. arXiv: `1411.0686 [gr-qc]`.

[56] Richard Brito, Vitor Cardoso, and Paolo Pani. “Superradiance: New Frontiers in Black Hole Physics”. In: *Lect. Notes Phys.* 906 (2015), pp.1–237. doi: `10.1007/978-3-319-19000-6`. arXiv: `1501.06570 [gr-qc]`.

[57] Valerio De Luca and Paolo Pani. "Tidal deformability of dressed black holes and tests of ultralight bosons in extended mass ranges". In: *JCAP* 08 (2021), p. 032. doi: `10.1088/1475-7516/2021/08/032`. arXiv: `2106.14428 [gr-qc]`.

[58] Valerio De Luca, Andrea Maselli, and Paolo Pani. "Modeling frequency-dependent tidal deformability for environmental black hole mergers". In: *Phys. Rev. D* 107.4 (2023), p. 044058. doi: `10.1103/PhysRevD.107.044058`. arXiv: `2212.03343 [gr-qc]`.

[59] Philippe Brax, Jose A. R. Cembranos, and Patrick Valageas. "Impact of kinetic and potential self-interactions on scalar dark matter". In: *Phys. Rev.* D100 (2019), p. 023526. doi: `10.1103/PhysRevD.100.023526`. arXiv: `1906.00730 [astro-ph.CO]`.

[60] Subrahmanyan Chandrasekhar. "Dynamical Friction. I. General Considerations: the Coefficient of Dynamical Friction". In: *Astrophys. J.* 97 (1943), p. 255. doi: `10.1086/144517`.

[61] J. Binney and S. Tremaine. *Galactic dynamics*. Princeton, N.J. : Princeton University Press, 1987.

[62] Fabio Antonini and David Merritt. "DYNAMICAL FRICTION AROUND SUPERMASSIVE BLACK HOLES". In: *The Astrophysical Journal* 745.24pp (2011), p. 83. doi: `10.1088/0004-637X/745/1/83`.

[63] Lam Hui et al. "Ultralight scalars as cosmological dark matter". In: *Phys. Rev. D* 95.4 (2017), p. 043541. doi: `10.1103/PhysRevD.95.043541`. arXiv: `1610.08297 [astro-ph.CO]`.

[64] Lachlan Lancaster et al. "Dynamical Friction in a Fuzzy Dark Matter Universe". In: *JCAP* 01 (2020), p. 001. doi: `10.1088/1475-7516/2020/01/001`. arXiv: `1909.06381 [astro-ph.CO]`.

[65] Lorenzo Annulli, Vitor Cardoso, and Rodrigo Vicente. "Response of ultralight dark matter to supermassive black holes and binaries". In: *Phys. Rev. D* 102.6 (2020), p. 063022. doi: `10.1103/PhysRevD.102.063022`. arXiv: `2009.00012 [gr-qc]`.

[66] Pau Amaro-Seoane et al. "Laser Interferometer Space Antenna". In: (Feb. 2017). arXiv: `1702.00786 [astro-ph.IM]`.

[67] Seiji Kawamura et al. "Current status of space gravitational wave antenna DECIGO and B-DECIGO". In: *PTEP* 2021.5 (2021), 05A105. doi: `10.1093/ptep/ptab019`. arXiv: `2006.13545 [gr-qc]`.

[68] Albert Einstein. "The Field Equations of Gravitation". In: *Sitzungsber. Preuss. Akad. Wiss. Berlin (Math. Phys.)* 1915 (1915), pp. 844–847.

[69] N. Aghanim et al. "Planck 2018 results. VI. Cosmological parameters". In: *Astron. Astrophys.* 641 (2020). [Erratum: Astron.Astrophys. 652, C4 (2021)], A6. doi: `10.1051/0004-6361/201833910`. arXiv: `1807.06209 [astro-ph.CO]`.

[70] C. Doux et al. “Dark Energy Survey Year 3 results: cosmological constraints from the analysis of cosmic shear in harmonic space”. In: (Mar. 2022). arXiv: `2203.07128 [astro-ph.CO]`.

[71] P. J. E. Peebles and Bharat Ratra. “The Cosmological Constant and Dark Energy”. In: *Rev. Mod. Phys.* 75 (2003). Ed. by Jong-Ping Hsu and D. Fine, pp. 559–606. doi: `10.1103/RevModPhys.75.559`. arXiv: `astro-ph/0207347`.

[72] R. B. Partridge and David T. Wilkinson. “Isotropy and Homogeneity of the Universe from Measurements of the Cosmic Microwave Background”. In: *Phys. Rev. Lett.* 18.14 (1967), p. 557. doi: `10.1103/PhysRevLett.18.557`.

[73] A. A. Penzias and R. W. Wilson. “A Measurement of Excess Antenna Temperature at 4080 Mc/s.” In: 142 (July 1965), pp. 419–421. doi: `10.1086/148307`.

[74] R. A. Sunyaev. “The Thermal History of the Universe and the Spectrum of Relic Radiation”. In: *Confrontation of Cosmological Theories with Observational Data*. Ed. by M. S. Longair. Dordrecht: Springer Netherlands, 1974, pp. 167–173. isbn: 978-94-010-2220-0. doi: `10.1007/978-94-010-2220-0_14`. url: `https://doi.org/10.1007/978-94-010-2220-0_14`.

[75] John D. Barrow and Michael S. Turner. “Baryosynthesis and the Origin of Galaxies”. In: *Nature* 291 (1981), pp. 469–472. doi: `10.1038/291469a0`.

[76] *LambdaCDM Model of Cosmology*, *`https://lambda.gsfc.nasa.gov/education/graphic_history/univ_evol.html`*, *Accessed:* 2023-07-15.

[77] Shadab Alam et al. “The clustering of galaxies in the completed SDSS-III Baryon Oscillation Spectroscopic Survey: cosmological analysis of the DR12 galaxy sample”. In: *Mon. Not. Roy. Astron. Soc.* 470.3 (2017), pp. 2617–2652. doi: `10.1093/mnras/stx721`. arXiv: `1607.03155 [astro-ph.CO]`.

[78] H. Hildebrandt et al. “KiDS-450: Cosmological parameter constraints from tomographic weak gravitational lensing”. In: *Mon. Not. Roy. Astron. Soc.* 465 (2017), p. 1454. doi: `10.1093/mnras/stw2805`. arXiv: `1606.05338 [astro-ph.CO]`.

[79] A. Friedmann. “Über die Krümmung des Raumes”. In: *Zeitschrift fur Physik* 10 (Jan. 1922), pp. 377–386. doi: `10.1007/BF01332580`.

[80] A. Friedmann. “On the Possibility of a world with constant negative curvature of space”. In: *Z. Phys.* 21 (1924), pp. 326–332. doi: `10.1007/BF01328280`.

[81] Georges Lemaitre. “A Homogeneous Universe of Constant Mass and Growing Radius Accounting for the Radial Velocity of Extragalactic Nebulae”. In: *Annales Soc. Sci. Bruxelles A* 47 (1927), pp. 49–59. doi: `10.1007/s10714-013-1548-3`.

[82] H. P. Robertson. “Kinematics and World-Structure”. In: *Astrophys. J.* 82 (1935), pp. 284–301. doi: `10.1086/143681`.

[83] H. P. Robertson. “Kinematics and World-Structure. 2”. In: *Astrophys. J.* 83 (1935), pp. 187–201. doi: `10.1086/143716`.

[84] H. P. Robertson. “Kinematics and World-Structure. 3”. In: *Astrophys. J.* 83 (1936), pp. 257–271. doi: `10.1086/143726`.

[85] A. G. Walker. “On Milne’s Theory of World-Structure”. In: *Proceedings of the London Mathematical Society* 42 (Jan. 1937), pp. 90–127. doi: `10.1112/plms/s2-42.1.90`.

[86] P. J. E. Peebles. “Large scale background temperature and mass fluctuations due to scale invariant primeval perturbations”. In: *Astrophys. J. Lett.* 263 (1982). Ed. by M. A. Srednicki, pp. L1–L5. doi: `10.1086/183911`.

[87] Marc Davis et al. “The Evolution of Large Scale Structure in a Universe Dominated by Cold Dark Matter”. In: *Astrophys. J.* 292 (1985). Ed. by M. A. Srednicki, pp. 371–394. doi: `10.1086/163168`.

[88] Julio F. Navarro, Carlos S. Frenk, and Simon D. M. White. “The Structure of cold dark matter halos”. In: *Astrophys. J.* 462 (1996), pp. 563–575. doi: `10.1086/177173`. arXiv: `astro-ph/9508025 [astro-ph]`.

[89] Julio F. Navarro, Carlos S. Frenk, and Simon D. M. White. “A Universal density profile from hierarchical clustering”. In: *Astrophys. J.* 490 (1997), pp. 493–508. doi: `10.1086/304888`. arXiv: `astro-ph/9611107`.

[90] F. Zwicky. “Die Rotverschiebung von extragalaktischen Nebeln”. In: *Helv. Phys. Acta* 6 (1933), pp. 110–127. doi: `10.1007/s10714-008-0707-4`.

[91] F. Zwicky. “On the Masses of Nebulae and of Clusters of Nebulae”. In: *Astrophys. J.* 86 (1937), pp. 217–246. doi: `10.1086/143864`.

[92] Vera C. Rubin and W. Kent Ford Jr. “Rotation of the Andromeda Nebula from a Spectroscopic Survey of Emission Regions”. In: *Astrophys. J.* 159 (1970), pp. 379–403. doi: `10.1086/150317`.

[93] Eric Hayashi and Simon D. M. White. “How Rare is the Bullet Cluster?” In: *Mon. Not. Roy. Astron. Soc.* 370 (2006), pp. L38–L41. doi: `10.1111/j.1745-3933.2006.00184.x`. arXiv: `astro-ph/0604443`.

[94] Douglas Clowe et al. “A direct empirical proof of the existence of dark matter”. In: *Astrophys. J. Lett.* 648 (2006), pp. L109–L113. doi: `10.1086/508162`. arXiv: `astro-ph/0608407`.

[95] Garry W. Angus et al. “On the Law of Gravity, the Mass of Neutrinos and the Proof of Dark Matter”. In: *Astrophys. J. Lett.* 654 (2007), pp. L13–L16. doi: `10.1086/510738`. arXiv: `astro-ph/0609125`.

[96] Douglas Clowe, S. W. Randall, and M. Markevitch. “Catching a bullet: Direct evidence for the existence of dark matter”. In: *Nucl. Phys. B Proc. Suppl.* 173 (2007). Ed. by David B. Cline, pp. 28–31. doi: `10.1016/j.nuclphysbps.2007.08.150`. arXiv: `astro-ph/0611496`.

[97] Jonathan L. Feng, Huitzu Tu, and Hai-Bo Yu. "Thermal Relics in Hidden Sectors". In: *JCAP* 10 (2008), p. 043. doi: 10.1088/1475-7516/2008/10/043. arXiv: 0808.2318 [hep-ph].

[98] Dan Hooper. "Particle Dark Matter". In: *Theoretical Advanced Study Institute in Elementary Particle Physics: The Dawn of the LHC Era*. 2010, pp. 709–764. doi: 10.1142/9789812838360_0014. arXiv: 0901.4090 [hep-ph].

[99] Dominik J. Schwarz. "The first second of the universe". In: *Annalen Phys.* 12 (2003), pp. 220–270. doi: 10.1002/andp.200310010. arXiv: astro-ph/0303574.

[100] Spencer Chang et al. "Effective WIMPs". In: *Phys. Rev. D* 89.1 (2014), p. 015011. doi: 10.1103/PhysRevD.89.015011. arXiv: 1307.8120 [hep-ph].

[101] Marcos A. G. Garcia et al. "Freeze-in from preheating". In: *JCAP* 03.03 (2022), p. 016. doi: 10.1088/1475-7516/2022/03/016. arXiv: 2109.13280 [hep-ph].

[102] Jonathan L. Feng. "The WIMP Paradigm: Theme and Variations". In: *Les Houches summer school on Dark Matter*. Dec. 2022. doi: 10.21468/SciPostPhysLectNotes.71. arXiv: 2212.02479 [hep-ph].

[103] D. S. Akerib et al. "The Large Underground Xenon (LUX) Experiment". In: *Nucl. Instrum. Meth. A* 704 (2013), pp. 111–126. doi: 10.1016/j.nima.2012.11.135. arXiv: 1211.3788 [physics.ins-det].

[104] D. S. Akerib et al. "First results from the LUX dark matter experiment at the Sanford Underground Research Facility". In: *Phys. Rev. Lett.* 112 (2014), p. 091303. doi: 10.1103/PhysRevLett.112.091303. arXiv: 1310.8214 [astro-ph.CO].

[105] D. S. Akerib et al. "Results from a search for dark matter in the complete LUX exposure". In: *Phys. Rev. Lett.* 118.2 (2017), p. 021303. doi: 10.1103/PhysRevLett.118.021303. arXiv: 1608.07648 [astro-ph.CO].

[106] E. Aprile et al. "Physics reach of the XENON1T dark matter experiment". In: *JCAP* 04 (2016), p. 027. doi: 10.1088/1475-7516/2016/04/027. arXiv: 1512.07501 [physics.ins-det].

[107] E. Aprile et al. "First Dark Matter Search Results from the XENON1T Experiment". In: *Phys. Rev. Lett.* 119.18 (2017), p. 181301. doi: 10.1103/PhysRevLett.119.181301. arXiv: 1705.06655 [astro-ph.CO].

[108] E. Aprile et al. "Dark Matter Search Results from a One Ton-Year Exposure of XENON1T". In: *Phys. Rev. Lett.* 121.11 (2018), p. 111302. doi: 10.1103/PhysRevLett.121.111302. arXiv: 1805.12562 [astro-ph.CO].

[109] Daniel A. Camargo, Yann Mambrini, and Farinaldo S. Queiroz. "XENON1T takes a razor to a dark E_6-inspired model". In: *Phys. Lett. B* 786 (2018), pp. 337–341. doi: 10.1016/j.physletb.2018.09.057. arXiv: 1805.12162 [hep-ph].

[110] D. S. Akerib et al. “LUX-ZEPLIN (LZ) Conceptual Design Report”. In: (Sept. 2015). arXiv: 1509.02910 [physics.ins-det].

[111] D. S. Akerib et al. “Projected WIMP sensitivity of the LUX-ZEPLIN dark matter experiment”. In: *Phys. Rev. D* 101.5 (2020), p. 052002. doi: 10.1103/PhysRevD.101.052002. arXiv: 1802.06039 [astro-ph.IM].

[112] R. Agnese et al. “Search for Low-Mass Weakly Interacting Massive Particles with SuperCDMS”. In: *Phys. Rev. Lett.* 112.24 (2014), p. 241302. doi: 10.1103/PhysRevLett.112.241302. arXiv: 1402.7137 [hep-ex].

[113] R. Agnese et al. “New Results from the Search for Low-Mass Weakly Interacting Massive Particles with the CDMS Low Ionization Threshold Experiment”. In: *Phys. Rev. Lett.* 116.7 (2016), p. 071301. doi: 10.1103/PhysRevLett.116.071301. arXiv: 1509.02448 [astro-ph.CO].

[114] A. Abada et al. “FCC-ee: The Lepton Collider: Future Circular Collider Conceptual Design Report Volume 2”. In: *Eur. Phys. J. ST* 228.2 (2019), pp. 261–623. doi: 10.1140/epjst/e2019-900045-4.

[115] Anatoly A. Klypin et al. “Where are the missing Galactic satellites?” In: *Astrophys. J.* 522 (1999), pp. 82–92. doi: 10.1086/307643. arXiv: astro-ph/9901240.

[116] Louis E. Strigari et al. “Redefining the Missing Satellites Problem”. In: *Astrophys. J.* 669 (2007), pp. 676–683. doi: 10.1086/521914. arXiv: 0704.1817 [astro-ph].

[117] Qi Guo et al. “From dwarf spheroidals to cDs: Simulating the galaxy population in a LCDM cosmology”. In: *Mon. Not. Roy. Astron. Soc.* 413 (2011), p. 101. doi: 10.1111/j.1365-2966.2010.18114.x. arXiv: 1006.0106 [astro-ph.CO].

[118] Jorge Penarrubia et al. “The coupling between the core/cusp and missing satellite problems”. In: *Astrophys. J. Lett.* 759 (2012), p. L42. doi: 10.1088/2041-8205/759/2/L42. arXiv: 1207.2772 [astro-ph.GA].

[119] Michael Boylan-Kolchin, James S. Bullock, and Manoj Kaplinghat. “Too big to fail? The puzzling darkness of massive Milky Way subhaloes”. In: *Mon. Not. Roy. Astron. Soc.* 415 (2011), p. L40. doi: 10.1111/j.1745-3933.2011.01074.x. arXiv: 1103.0007 [astro-ph.CO].

[120] Shea Garrison-Kimmel et al. “Too Big to Fail in the Local Group”. In: *Mon. Not. Roy. Astron. Soc.* 444.1 (2014), pp. 222–236. doi: 10.1093/mnras/stu1477. arXiv: 1404.5313 [astro-ph.GA].

[121] Manoj Kaplinghat, Mauro Valli, and Hai-Bo Yu. “Too Big To Fail in Light of Gaia”. In: *Mon. Not. Roy. Astron. Soc.* 490.1 (2019), pp. 231–242. doi: 10.1093/mnras/stz2511. arXiv: 1904.04939 [astro-ph.GA].

[122] Marcel S. Pawlowski et al. “On the persistence of two small-scale problems in ΛCDM”. In: *Astrophys. J.* 815.1 (2015), p. 19. doi: 10.1088/0004-637X/815/1/19. arXiv: 1510.08060 [astro-ph.GA].

[123] Se-Heon Oh et al. “The central slope of dark matter cores in dwarf galaxies: Simulations vs. THINGS”. In: *Astron. J.* 142 (2011), p. 24. doi: 10.1088/0004-6256/142/1/24. arXiv: 1011.2777 [astro-ph.CO].

[124] Romain Teyssier et al. “Cusp-core transformations in dwarf galaxies: observational predictions”. In: *Mon. Not. Roy. Astron. Soc.* 429 (2013), p. 3068. doi: 10.1093/mnras/sts563. arXiv: 1206.4895 [astro-ph.CO].

[125] J. I. Read, O. Agertz, and M. L. M. Collins. “Dark matter cores all the way down”. In: *Mon. Not. Roy. Astron. Soc.* 459.3 (2016), pp. 2573–2590. doi: 10.1093/mnras/stw713. arXiv: 1508.04143 [astro-ph.GA].

[126] Gianfranco Bertone and Tim Tait M. P. “A new era in the search for dark matter”. In: *Nature* 562.7725 (2018), pp. 51–56. doi: 10.1038/s41586-018-0542-z. arXiv: 1810.01668 [astro-ph.CO].

[127] Leanne D. Duffy and Karl van Bibber. “Axions as Dark Matter Particles”. In: *New J. Phys.* 11 (2009), p. 105008. doi: 10.1088/1367-2630/11/10/105008. arXiv: 0904.3346 [hep-ph].

[128] David J. E. Marsh. “Axion Cosmology”. In: *Phys. Rept.* 643 (2016), pp. 1–79. doi: 10.1016/j.physrep.2016.06.005. arXiv: 1510.07633 [astro-ph.CO].

[129] Jihn E. Kim and Gianpaolo Carosi. “Axions and the Strong CP Problem”. In: *Rev. Mod. Phys.* 82 (2010). [Erratum: Rev.Mod.Phys. 91, 049902 (2019)], pp. 557–602. doi: 10.1103/RevModPhys.82.557. arXiv: 0807.3125 [hep-ph].

[130] Peter W. Graham et al. “Experimental Searches for the Axion and Axion-Like Particles”. In: *Ann. Rev. Nucl. Part. Sci.* 65 (2015), pp. 485–514. doi: 10.1146/annurev-nucl-102014-022120. arXiv: 1602.00039 [hep-ex].

[131] Igor G. Irastorza and Javier Redondo. “New experimental approaches in the search for axion-like particles”. In: *Prog. Part. Nucl. Phys.* 102 (2018), pp. 89–159. doi: 10.1016/j.ppnp.2018.05.003. arXiv: 1801.08127 [hep-ph].

[132] Luca Di Luzio et al. “The landscape of QCD axion models”. In: *Phys. Rept.* 870 (2020), pp. 1–117. doi: 10.1016/j.physrep.2020.06.002. arXiv: 2003.01100 [hep-ph].

[133] Wayne Hu, Rennan Barkana, and Andrei Gruzinov. “Cold and fuzzy dark matter”. In: *Phys. Rev. Lett.* 85 (2000), pp. 1158–1161. doi: 10.1103/PhysRevLett.85.1158. arXiv: astro-ph/0003365 [astro-ph].

[134] Simon Knapen, Tongyan Lin, and Kathryn M. Zurek. “Light Dark Matter: Models and Constraints”. In: *Phys. Rev. D* 96.11 (2017), p. 115021. doi: 10.1103/PhysRevD.96.115021. arXiv: 1709.07882 [hep-ph].

[135] Elisa G. M. Ferreira. "Ultra-light dark matter". In: *Astron. Astrophys. Rev.* 29.1 (2021), p. 7. doi: 10.1007/s00159-021-00135-6. arXiv: 2005.03254 [astro-ph.CO].

[136] Lam Hui. "Wave Dark Matter". In: *Ann. Rev. Astron. Astrophys.* 59 (2021), pp. 247–289. doi: 10.1146/annurev-astro-120920-010024. arXiv: 2101.11735 [astro-ph.CO].

[137] Scott Dodelson and Lawrence M. Widrow. "Sterile-neutrinos as dark matter". In: *Phys. Rev. Lett.* 72 (1994), pp. 17–20. doi: 10.1103/PhysRevLett.72.17. arXiv: hep-ph/9303287.

[138] Xiang-Dong Shi and George M. Fuller. "A New dark matter candidate: Nonthermal sterile neutrinos". In: *Phys. Rev. Lett.* 82 (1999), pp. 2832–2835. doi: 10.1103/PhysRevLett.82.2832. arXiv: astro-ph/9810076.

[139] Alexey Boyarsky, Oleg Ruchayskiy, and Mikhail Shaposhnikov. "The Role of sterile neutrinos in cosmology and astrophysics". In: *Ann. Rev. Nucl. Part. Sci.* 59 (2009), pp. 191–214. doi: 10.1146/annurev.nucl.010909.083654. arXiv: 0901.0011 [hep-ph].

[140] Alexander Kusenko. "Sterile neutrinos: The Dark side of the light fermions". In: *Phys. Rept.* 481 (2009), pp. 1–28. doi: 10.1016/j.physrep.2009.07.004. arXiv: 0906.2968 [hep-ph].

[141] Jonathan L. Feng. "Dark Matter Candidates from Particle Physics and Methods of Detection". In: *Ann. Rev. Astron. Astrophys.* 48 (2010), pp. 495–545. doi: 10.1146/annurev-astro-082708-101659. arXiv: 1003.0904 [astro-ph.CO].

[142] K. N. Abazajian et al. "Light Sterile Neutrinos: A White Paper". In: (Apr. 2012). arXiv: 1204.5379 [hep-ph].

[143] P. Ivanov, P. Naselsky, and I. Novikov. "Inflation and primordial black holes as dark matter". In: *Phys. Rev. D* 50 (1994), pp. 7173–7178. doi: 10.1103/PhysRevD.50.7173.

[144] Sébastien Clesse and Juan García-Bellido. "Massive Primordial Black Holes from Hybrid Inflation as Dark Matter and the seeds of Galaxies". In: *Phys. Rev. D* 92.2 (2015), p. 023524. doi: 10.1103/PhysRevD.92.023524. arXiv: 1501.07565 [astro-ph.CO].

[145] Bernard Carr, Florian Kuhnel, and Marit Sandstad. "Primordial Black Holes as Dark Matter". In: *Phys. Rev. D* 94.8 (2016), p. 083504. doi: 10.1103/PhysRevD.94.083504. arXiv: 1607.06077 [astro-ph.CO].

[146] Bernard Carr and Florian Kuhnel. "Primordial Black Holes as Dark Matter: Recent Developments". In: *Ann. Rev. Nucl. Part. Sci.* 70 (2020), pp. 355–394. doi: 10.1146/annurev-nucl-050520-125911. arXiv: 2006.02838 [astro-ph.CO].

[147] Anne M. Green and Bradley J. Kavanagh. "Primordial Black Holes as a dark matter candidate". In: *J. Phys. G* 48.4 (2021), p. 043001. doi: 10.1088/1361-6471/abc534. arXiv: 2007.10722 [astro-ph.CO].

[148] Robert H. Sanders and Stacy S. McGaugh. "Modified Newtonian dynamics as an alternative to dark matter". In: *Ann. Rev. Astron. Astrophys.* 40 (2002), pp. 263–317. doi: 10.1146/annurev.astro.40.060401.093923. arXiv: astro-ph/0204521.

[149] Jacob D. Bekenstein. "Relativistic gravitation theory for the MOND paradigm". In: *Phys. Rev. D* 70 (2004). [Erratum: Phys.Rev.D 71, 069901 (2005)], p. 083509. doi: 10.1103/PhysRevD.70.083509. arXiv: astro-ph/0403694.

[150] Benoit Famaey and James Binney. "Modified Newtonian dynamics in the Milky Way". In: *Mon. Not. Roy. Astron. Soc.* 363 (2005), pp. 603–608. doi: 10.1111/j.1365-2966.2005.09474.x. arXiv: astro-ph/0506723.

[151] Benoit Famaey and Stacy McGaugh. "Modified Newtonian Dynamics (MOND): Observational Phenomenology and Relativistic Extensions". In: *Living Rev. Rel.* 15 (2012), p. 10. doi: 10.12942/lrr-2012-10. arXiv: 1112.3960 [astro-ph.CO].

[152] Gonzalo J. Olmo. "Palatini Approach to Modified Gravity: f(R) Theories and Beyond". In: *Int. J. Mod. Phys. D* 20 (2011), pp. 413–462. doi: 10.1142/S0218271811018925. arXiv: 1101.3864 [gr-qc].

[153] Salvatore Capozziello and Mariafelicia De Laurentis. "Extended Theories of Gravity". In: *Phys. Rept.* 509 (2011), pp. 167–321. doi: 10.1016/j.physrep.2011.09.003. arXiv: 1108.6266 [gr-qc].

[154] S. Nojiri, S. D. Odintsov, and V. K. Oikonomou. "Modified Gravity Theories on a Nutshell: Inflation, Bounce and Late-time Evolution". In: *Phys. Rept.* 692 (2017), pp. 1–104. doi: 10.1016/j.physrep.2017.06.001. arXiv: 1705.11098 [gr-qc].

[155] Marco Battaglieri et al. "US Cosmic Visions: New Ideas in Dark Matter 2017: Community Report". In: *U.S. Cosmic Visions: New Ideas in Dark Matter*. July 2017. arXiv: 1707.04591 [hep-ph].

[156] Justin Khoury. "Dark Matter Superfluidity". In: *SciPost Phys. Lect. Notes* 42 (2022), p. 1. doi: 10.21468/SciPostPhysLectNotes.42. arXiv: 2109.10928 [astro-ph.CO].

[157] John Preskill, Mark B. Wise, and Frank Wilczek. "Cosmology of the Invisible Axion". In: *Phys. Lett. B* 120 (1983). Ed. by M. A. Srednicki, pp. 127–132. doi: 10.1016/0370-2693(83)90637-8.

[158] L. F. Abbott and P. Sikivie. "A Cosmological Bound on the Invisible Axion". In: *Phys. Lett. B* 120 (1983). Ed. by M. A. Srednicki, pp. 133–136. doi: 10.1016/0370-2693(83)90638-X.

[159] Michael Dine and Willy Fischler. “The Not So Harmless Axion”. In: *Phys. Lett. B* 120 (1983). Ed. by M. A. Srednicki, pp. 137–141. doi: `10.1016/0370-2693(83)90639-1`.

[160] Asimina Arvanitaki et al. “Large-misalignment mechanism for the formation of compact axion structures: Signatures from the QCD axion to fuzzy dark matter”. In: *Phys. Rev. D* 101.8 (2020), p. 083014. doi: `10.1103/PhysRevD.101.083014`. arXiv: `1909.11665 [astro-ph.CO]`.

[161] Matthew C. Johnson and Marc Kamionkowski. “Dynamical and Gravitational Instability of Oscillating-Field Dark Energy and Dark Matter”. In: *Phys. Rev.* D78 (2008), p. 063010. doi: `10.1103/PhysRevD.78.063010`. arXiv: `0805.1748 [astro-ph]`.

[162] Jai-chan Hwang and Hyerim Noh. “Axion as a Cold Dark Matter candidate”. In: *Phys. Lett.* B680 (2009), pp. 1–3. doi: `10.1016/j.physletb.2009.08.031`. arXiv: `0902.4738 [astro-ph.CO]`.

[163] Chan-Gyung Park, Jai-chan Hwang, and Hyerim Noh. “Axion as a cold dark matter candidate: low-mass case”. In: *Phys. Rev.* D86 (2012), p. 083535. doi: `10.1103/PhysRevD.86.083535`. arXiv: `1207.3124 [astro-ph.CO]`.

[164] Renée Hlozek et al. “A search for ultralight axions using precision cosmological data”. In: *Phys. Rev.* D91.10 (2015), p. 103512. doi: `10.1103/PhysRevD.91.103512`. arXiv: `1410.2896 [astro-ph.CO]`.

[165] J. A. R. Cembranos, A. L. Maroto, and S. J. Núñez Jareño. “Cosmological perturbations in coherent oscillating scalar field models”. In: *JHEP* 03 (2016), p. 013. doi: `10.1007/JHEP03(2016)013`. arXiv: `1509.08819 [astro-ph.CO]`.

[166] L. Arturo Ureña-López and Alma X. Gonzalez-Morales. “Towards accurate cosmological predictions for rapidly oscillating scalar fields as dark matter”. In: *JCAP* 1607.07 (2016), p. 048. doi: `10.1088/1475-7516/2016/07/048`. arXiv: `1511.08195 [astro-ph.CO]`.

[167] L. Arturo Ureña-López. “Brief Review on Scalar Field Dark Matter Models”. In: *Front. Astron. Space Sci.* 6 (2019), p. 47. doi: `10.3389/fspas.2019.00047`.

[168] James Halverson et al. “Dark Glueballs and their Ultralight Axions”. In: *Phys. Rev. D* 98.4 (2018), p. 043502. doi: `10.1103/PhysRevD.98.043502`. arXiv: `1805.06011 [hep-ph]`.

[169] Michele Cicoli et al. “Fuzzy Dark Matter candidates from string theory”. In: *JHEP* 05 (2022), p. 107. doi: `10.1007/JHEP05(2022)107`. arXiv: `2110.02964 [hep-th]`.

[170] Manuel Wittner. “The universe from a string-theoretic and cosmological perspective.” PhD thesis. Heidelberg U., Aug. 2022. doi: `10.11588/heidok.00032036`.

[171] Michele Cicoli, Kuver Sinha, and Robert Wiley Deal. “The dark universe after reheating in string inflation”. In: *JHEP* 12 (2022), p. 068. doi: 10.1007/JHEP12(2022)068. arXiv: 2208.01017 [hep-th].

[172] Michele Cicoli et al. “String Cosmology: from the Early Universe to Today”. In: (Mar. 2023). arXiv: 2303.04819 [hep-th].

[173] Philippe Jetzer. “Boson stars”. In: *Phys. Rept.* 220 (1992), pp. 163–227. doi: 10.1016/0370-1573(92)90123-H.

[174] Jens C. Niemeyer. “Small-scale structure of fuzzy and axion-like dark matter”. In: (Dec. 2019). doi: 10.1016/j.ppnp.2020.103787. arXiv: 1912.07064 [astro-ph.CO].

[175] Mohammadtaher Safarzadeh and David N. Spergel. “Ultra-light Dark Matter is Incompatible with the Milky Way’s Dwarf Satellites”. In: (June 2019). doi: 10.3847/1538-4357/ab7db2. arXiv: 1906.11848 [astro-ph.CO].

[176] S. T. H. Hartman, H. A. Winther, and D. F. Mota. “Dynamical friction in Bose-Einstein condensed self-interacting dark matter at finite temperatures, and the Fornax dwarf spheroidal”. In: *Astron. Astrophys.* 647 (2021), A70. doi: 10.1051/0004-6361/202039865. arXiv: 2011.00116 [astro-ph.CO].

[177] Jae-Weon Lee. “Is dark matter a BEC or scalar field?” In: *J. Korean Phys. Soc.* 54 (2009), p. 2622. doi: 10.3938/jkps.54.2622. arXiv: 0801.1442 [astro-ph].

[178] P. Sikivie and Q. Yang. “Bose-Einstein Condensation of Dark Matter Axions”. In: *Phys. Rev. Lett.* 103 (2009), p. 111301. doi: 10.1103/PhysRevLett.103.111301. arXiv: 0901.1106 [hep-ph].

[179] Abril Suárez, Victor H. Robles, and Tonatiuh Matos. “A Review on the Scalar Field/Bose-Einstein Condensate Dark Matter Model”. In: *Astrophys. Space Sci. Proc.* 38 (2014). Ed. by Claudia Moreno González, José Edgar Madriz Aguilar, and Luz Marina Reyes Barrera, pp. 107–142. doi: 10.1007/978-3-319-02063-1_9. arXiv: 1302.0903 [astro-ph.CO].

[180] JiJi Fan. “Ultralight Repulsive Dark Matter and BEC”. In: *Phys. Dark Univ.* 14 (2016), pp. 84–94. doi: 10.1016/j.dark.2016.10.005. arXiv: 1603.06580 [hep-ph].

[181] M. P. Silverman and Ronald L. Mallett. “Dark matter as a cosmic Bose-Einstein condensate and possible superfluid”. In: *Gen. Rel. Grav.* 34 (2002), pp. 633–649. doi: 10.1023/A:1015934027224.

[182] Lasha Berezhiani and Justin Khoury. “Dark Matter Superfluidity and Galactic Dynamics”. In: *Phys. Lett. B* 753 (2016), pp. 639–643. doi: 10.1016/j.physletb.2015.12.054. arXiv: 1506.07877 [astro-ph.CO].

[183] M. C. Bento et al. “Selfinteracting dark matter and invisibly decaying Higgs”. In: *Phys. Rev. D* 62 (2000), p. 041302. doi: `10.1103/PhysRevD.62.041302`. arXiv: `astro-ph/0003350`.

[184] Antonio Riotto and Igor Tkachev. “What if dark matter is bosonic and self-interacting?” In: *Phys. Lett.* B484 (2000), pp. 177–182. doi: `10.1016/S0370-2693(00)00660-2`. arXiv: `astro-ph/0003388 [astro-ph]`.

[185] Douglas Fregolente and Mauro D. Tonasse. “Selfinteracting dark matter from an SU(3)(L) x U(1)(N) electroweak model”. In: *Phys. Lett. B* 555 (2003), pp. 7–12. doi: `10.1016/S0370-2693(03)00037-6`. arXiv: `hep-ph/0209119`.

[186] Bohua Li, Tanja Rindler-Daller, and Paul R. Shapiro. “Cosmological Constraints on Bose-Einstein-Condensed Scalar Field Dark Matter”. In: *Phys. Rev.* D89.8 (2014), p. 083536. doi: `10.1103/PhysRevD.89.083536`. arXiv: `1310.6061 [astro-ph.CO]`.

[187] Abril Suárez and Pierre-Henri Chavanis. “Hydrodynamic representation of the Klein-Gordon-Einstein equations in the weak field limit: General formalism and perturbations analysis”. In: *Phys. Rev.* D92 (2015), p. 023510. doi: `10.1103/PhysRevD.92.023510`. arXiv: `1503.07437 [gr-qc]`.

[188] Abril Suárez and Pierre-Henri Chavanis. “Cosmological evolution of a complex scalar field with repulsive or attractive self-interaction”. In: *Phys. Rev.* D95.6 (2017), p. 063515. doi: `10.1103/PhysRevD.95.063515`. arXiv: `1608.08624 [gr-qc]`.

[189] Abril Suárez and Pierre-Henri Chavanis. “Jeans type instability of a complex self-interacting scalar field in general relativity”. In: *Phys. Rev.* D98.8 (2018), p. 083529. doi: `10.1103/PhysRevD.98.083529`. arXiv: `1710.10486 [gr-qc]`.

[190] Philippe Brax, Patrick Valageas, and Jose A. R. Cembranos. “Fate of scalar dark matter solitons around supermassive galactic black holes”. In: (2019). arXiv: `1909.02614 [astro-ph.CO]`.

[191] Andi Tan et al. “Dark Matter Results from First 98.7 Days of Data from the PandaX-II Experiment”. In: *Phys. Rev. Lett.* 117.12 (2016), p. 121303. doi: `10.1103/PhysRevLett.117.121303`. arXiv: `1607.07400 [hep-ex]`.

[192] Xiangyi Cui et al. “Dark Matter Results From 54-Ton-Day Exposure of PandaX-II Experiment”. In: *Phys. Rev. Lett.* 119.18 (2017), p. 181302. doi: `10.1103/PhysRevLett.119.181302`. arXiv: `1708.06917 [astro-ph.CO]`.

[193] Yue Meng et al. “Dark Matter Search Results from the PandaX-4T Commissioning Run”. In: *Phys. Rev. Lett.* 127.26 (2021), p. 261802. doi: `10.1103/PhysRevLett.127.261802`. arXiv: `2107.13438 [hep-ex]`.

[194] Nitsan Bar, Kfir Blum, and Chen Sun. “Galactic rotation curves versus ultralight dark matter: A systematic comparison with SPARC data”. In: *Phys. Rev. D* 105.8 (2022), p. 083015. doi: `10.1103/PhysRevD.105.083015`. arXiv: `2111.03070 [hep-ph]`.

[195] S. T. H. Hartman, H. A. Winther, and D. F. Mota. “Constraints on self-interacting Bose-Einstein condensate dark matter using large-scale observables”. In: *JCAP* 02.02 (2022), p. 005. doi: `10.1088/1475-7516/2022/02/005`. arXiv: `2108.07496 [astro-ph.CO]`.

[196] Caio F. B. Macedo et al. “Into the lair: gravitational-wave signatures of dark matter”. In: *Astrophys. J.* 774 (2013), p. 48. doi: `10.1088/0004-637X/774/1/48`. arXiv: `1302.2646 [gr-qc]`.

[197] Enrico Barausse, Vitor Cardoso, and Paolo Pani. “Can environmental effects spoil precision gravitational-wave astrophysics?” In: *Phys. Rev. D* 89.10 (2014), p. 104059. doi: `10.1103/PhysRevD.89.104059`. arXiv: `1404.7149 [gr-qc]`.

[198] Leor Barack et al. “Black holes, gravitational waves and fundamental physics: a roadmap”. In: *Class. Quant. Grav.* 36.14 (2019), p. 143001. doi: `10.1088/1361-6382/ab0587`. arXiv: `1806.05195 [gr-qc]`.

[199] Vitor Cardoso and Paolo Pani. “Testing the nature of dark compact objects: a status report”. In: *Living Rev. Rel.* 22.1 (2019), p. 4. doi: `10.1007/s41114-019-0020-4`. arXiv: `1904.05363 [gr-qc]`.

[200] Pierre Auclair et al. “Cosmology with the Laser Interferometer Space Antenna”. In: (Apr. 2022). arXiv: `2204.05434 [astro-ph.CO]`.

[201] E. O. Nadler et al. “Milky Way Satellite Census. III. Constraints on Dark Matter Properties from Observations of Milky Way Satellite Galaxies”. In: *Phys. Rev. Lett.* 126 (2021), p. 091101. doi: `10.1103/PhysRevLett.126.091101`. arXiv: `2008.00022 [astro-ph.CO]`.

[202] Mona Dentler et al. “Fuzzy dark matter and the Dark Energy Survey Year 1 data”. In: *Mon. Not. Roy. Astron. Soc.* 515.4 (2022), pp. 5646–5664. doi: `10.1093/mnras/stac1946`. arXiv: `2111.01199 [astro-ph.CO]`.

[203] J. Weber. “Detection and Generation of Gravitational Waves”. In: *Phys. Rev.* 117 (1960), pp. 306–313. doi: `10.1103/PhysRev.117.306`.

[204] Richard L. Arnowitt, Stanley Deser, and Charles W. Misner. “Wave zone in general relativity”. In: *Phys. Rev.* 121 (1961), p. 1556. doi: `10.1103/PhysRev.121.1556`.

[205] Asher Peres. “Classical Radiation Recoil”. In: *Phys. Rev.* 128 (1962), pp. 2471–2475. doi: `10.1103/PhysRev.128.2471`.

[206] J. Weber. “Anisotropy and polarization in the gravitational-radiation experiments”. In: *Phys. Rev. Lett.* 25 (1970), pp. 180–184. doi: 10.1103/PhysRevLett.25.180.

[207] J. Weber. “Evidence for discovery of gravitational radiation”. In: *Phys. Rev. Lett.* 22 (1969), pp. 1320–1324. doi: 10.1103/PhysRevLett.22.1320.

[208] B. P. Abbott et al. “GW151226: Observation of Gravitational Waves from a 22-Solar-Mass Binary Black Hole Coalescence”. In: *Phys. Rev. Lett.* 116.24 (2016), p. 241103. doi: 10.1103/PhysRevLett.116.241103. arXiv: 1606.04855 [gr-qc].

[209] *Two black holes merging, https://www.ligo.caltech.edu/image/ligo20160211f, Accessed: 2023-07-15.*

[210] H. Bondi, M. G. J. van der Burg, and A. W. K. Metzner. “Gravitational waves in general relativity. 7. Waves from axisymmetric isolated systems”. In: *Proc. Roy. Soc. Lond. A* 269 (1962), pp. 21–52. doi: 10.1098/rspa.1962.0161.

[211] J. B. Hartle and S. W. Hawking. “Wave Function of the Universe”. In: *Phys. Rev. D* 28 (1983). Ed. by Li-Zhi Fang and R. Ruffini, pp. 2960–2975. doi: 10.1103/PhysRevD.28.2960.

[212] Alex Abramovici et al. “LIGO: The Laser interferometer gravitational wave observatory”. In: *Science* 256 (1992), pp. 325–333. doi: 10.1126/science.256.5055.325.

[213] B. P. Abbott et al. “LIGO: The Laser interferometer gravitational-wave observatory”. In: *Rept. Prog. Phys.* 72 (2009), p. 076901. doi: 10.1088/0034-4885/72/7/076901. arXiv: 0711.3041 [gr-qc].

[214] T. Accadia et al. “Virgo: a laser interferometer to detect gravitational waves”. In: *JINST* 7 (2012), P03012. doi: 10.1088/1748-0221/7/03/P03012.

[215] F. Acernese et al. “Increasing the Astrophysical Reach of the Advanced Virgo Detector via the Application of Squeezed Vacuum States of Light”. In: *Phys. Rev. Lett.* 123.23 (2019), p. 231108. doi: 10.1103/PhysRevLett.123.231108.

[216] S. Kawamura et al. “The Japanese space gravitational wave antenna DECIGO”. In: *Class. Quant. Grav.* 23 (2006). Ed. by N. Mio, S125–S132. doi: 10.1088/0264-9381/23/8/S17.

[217] Seiji Kawamura et al. “The Japanese space gravitational wave antenna: DECIGO”. In: *Class. Quant. Grav.* 28 (2011). Ed. by Sasha Buchman and Ke-Xun Sun, p. 094011. doi: 10.1088/0264-9381/28/9/094011.

[218] B. P. Abbott et al. “GW170817: Observation of Gravitational Waves from a Binary Neutron Star Inspiral”. In: *Phys. Rev. Lett.* 119.16 (2017), p. 161101. doi: 10.1103/PhysRevLett.119.161101. arXiv: 1710.05832 [gr-qc].

[219] B. P. Abbott et al. “Multi-messenger Observations of a Binary Neutron Star Merger”. In: *Astrophys. J. Lett.* 848.2 (2017), p. L12. doi: 10.3847/2041-8213/aa91c9. arXiv: 1710.05833 [astro-ph.HE].

[220] Benjamin P. Abbott et al. “GW170104: Observation of a 50-Solar-Mass Binary Black Hole Coalescence at Redshift 0.2”. In: *Phys. Rev. Lett.* 118.22 (2017). [Erratum: Phys.Rev.Lett. 121, 129901 (2018)], p. 221101. doi: 10.1103/PhysRevLett.118.221101. arXiv: 1706.01812 [gr-qc].

[221] B. P. Abbott et al. “GWTC-1: A Gravitational-Wave Transient Catalog of Compact Binary Mergers Observed by LIGO and Virgo during the First and Second Observing Runs”. In: *Phys. Rev. X* 9.3 (2019), p. 031040. doi: 10.1103/PhysRevX.9.031040. arXiv: 1811.12907 [astro-ph.HE].

[222] Vitor Cardoso and Andrea Maselli. “Constraints on the astrophysical environment of binaries with gravitational-wave observations”. In: *Astron. Astrophys.* 644 (2020), A147. doi: 10.1051/0004-6361/202037654. arXiv: 1909.05870 [astro-ph.HE].

[223] Gen-Liang Li, Yong Tang, and Yue-Liang Wu. “Probing Dark Matter Spikes via Gravitational Waves of Extreme Mass Ratio Inspirals”. In: (Dec. 2021). arXiv: 2112.14041 [astro-ph.CO].

[224] Clemente Smarra et al. “The second data release from the European Pulsar Timing Array: VI. Challenging the ultralight dark matter paradigm”. In: (June 2023). arXiv: 2306.16228 [astro-ph.HE].

[225] Daniel J. Reardon et al. “Search for an Isotropic Gravitational-wave Background with the Parkes Pulsar Timing Array”. In: *Astrophys. J. Lett.* 951.1 (2023), p. L6. doi: 10.3847/2041-8213/acdd02. arXiv: 2306.16215 [astro-ph.HE].

[226] Heng Xu et al. “Searching for the Nano-Hertz Stochastic Gravitational Wave Background with the Chinese Pulsar Timing Array Data Release I”. In: *Res. Astron. Astrophys.* 23.7 (2023), p. 075024. doi: 10.1088/1674-4527/acdfa5. arXiv: 2306.16216 [astro-ph.HE].

[227] Gabriella Agazie et al. “The NANOGrav 15 yr Data Set: Evidence for a Gravitational-wave Background”. In: *Astrophys. J. Lett.* 951.1 (2023), p. L8. doi: 10.3847/2041-8213/acdac6. arXiv: 2306.16213 [astro-ph.HE].

[228] J. Antoniadis et al. “The second data release from the European Pulsar Timing Array: V. Implications for massive black holes, dark matter and the early Universe”. In: (June 2023). arXiv: 2306.16227 [astro-ph.CO].

[229] Yann Gouttenoire. “First-order Phase Transition interpretation of PTA signal produces solar-mass Black Holes”. In: (July 2023). arXiv: 2307.04239 [hep-ph].

[230] Yu-Mei Wu, Zu-Cheng Chen, and Qing-Guo Huang. "Cosmological Interpretation for the Stochastic Signal in Pulsar Timing Arrays". In: (July 2023). arXiv: 2307.03141 [astro-ph.CO].

[231] Daniel G. Figueroa et al. "Cosmological Background Interpretation of Pulsar Timing Array Data". In: (July 2023). arXiv: 2307.02399 [astro-ph.CO].

[232] Caner Unal, Alexandros Papageorgiou, and Ippei Obata. "Axion-Gauge Dynamics During Inflation as the Origin of Pulsar Timing Array Signals and Primordial Black Holes". In: (July 2023). arXiv: 2307.02322 [astro-ph.CO].

[233] Bo-Qiang Lu and Cheng-Wei Chiang. "Nano-Hertz stochastic gravitational wave background from domain wall annihilation". In: (July 2023). arXiv: 2307.00746 [hep-ph].

[234] C. J. Moore, R. H. Cole, and C. P. L. Berry. "Gravitational-wave sensitivity curves". In: *Class. Quant. Grav.* 32.1 (2015), p. 015014. doi: 10.1088/0264-9381/32/1/015014. arXiv: 1408.0740 [gr-qc].

[235] B. P. Abbott et al. "Tests of General Relativity with the Binary Black Hole Signals from the LIGO-Virgo Catalog GWTC-1". In: *Phys. Rev. D* 100.10 (2019), p. 104036. doi: 10.1103/PhysRevD.100.104036. arXiv: 1903.04467 [gr-qc].

[236] R. Abbott et al. "Tests of general relativity with binary black holes from the second LIGO-Virgo gravitational-wave transient catalog". In: *Phys. Rev. D* 103.12 (2021), p. 122002. doi: 10.1103/PhysRevD.103.122002. arXiv: 2010.14529 [gr-qc].

[237] R. Abbott et al. "Tests of General Relativity with GWTC-3". In: (Dec. 2021). arXiv: 2112.06861 [gr-qc].

[238] Dimitrios Psaltis et al. "Gravitational Test Beyond the First Post-Newtonian Order with the Shadow of the M87 Black Hole". In: *Phys. Rev. Lett.* 125.14 (2020), p. 141104. doi: 10.1103/PhysRevLett.125.141104. arXiv: 2010.01055 [gr-qc].

[239] R. Abbott et al. "Population of Merging Compact Binaries Inferred Using Gravitational Waves through GWTC-3". In: *Phys. Rev. X* 13.1 (2023), p. 011048. doi: 10.1103/PhysRevX.13.011048. arXiv: 2111.03634 [astro-ph.HE].

[240] Michele Bosi, Nicola Bellomo, and Alvise Raccanelli. "Constraining extended cosmologies with GW$\times$LSS cross-correlations". In: (June 2023). arXiv: 2306.03031 [astro-ph.CO].

[241] B. P. Abbott et al. "Tests of General Relativity with GW170817". In: *Phys. Rev. Lett.* 123.1 (2019), p. 011102. doi: 10.1103/PhysRevLett.123.011102. arXiv: 1811.00364 [gr-qc].

[242] Neil Cornish, Diego Blas, and Germano Nardini. “Bounding the speed of gravity with gravitational wave observations”. In: *Phys. Rev. Lett.* 119.16 (2017), p. 161102. doi: `10.1103/PhysRevLett.119.161102`. arXiv: `1707.06101 [gr-qc]`.

[243] Alexander Bonilla et al. “Forecasts on the speed of gravitational waves at high z”. In: *JCAP* 03 (2020), p. 015. doi: `10.1088/1475-7516/2020/03/015`. arXiv: `1910.05631 [gr-qc]`.

[244] Xiaoshu Liu et al. “Measuring the speed of gravitational waves from the first and second observing run of Advanced LIGO and Advanced Virgo”. In: *Phys. Rev. D* 102.2 (2020), p. 024028. doi: `10.1103/PhysRevD.102.024028`. arXiv: `2005.03121 [gr-qc]`.

[245] William Giarè and Fabrizio Renzi. “Propagating speed of primordial gravitational waves”. In: *Phys. Rev. D* 102.8 (2020), p. 083530. doi: `10.1103/PhysRevD.102.083530`. arXiv: `2007.04256 [astro-ph.CO]`.

[246] Konstantin Leyde et al. “Current and future constraints on cosmology and modified gravitational wave friction from binary black holes”. In: *JCAP* 09 (2022), p. 012. doi: `10.1088/1475-7516/2022/09/012`. arXiv: `2202.00025 [gr-qc]`.

[247] Shreya Banerjee, Sayantani Bera, and David F. Mota. “Prospects of probing dark matter condensates with gravitational waves”. In: *JCAP* 03 (2023), p. 041. doi: `10.1088/1475-7516/2023/03/041`. arXiv: `2211.13988 [gr-qc]`.

[248] Ryuichi Takahashi and Takashi Nakamura. “Wave effects in gravitational lensing of gravitational waves from chirping binaries”. In: *Astrophys. J.* 595 (2003), pp. 1039–1051. doi: `10.1086/377430`. arXiv: `astro-ph/0305055`.

[249] C. G. Boehmer and T. Harko. “Can dark matter be a Bose-Einstein condensate?” In: *JCAP* 06 (2007), p. 025. doi: `10.1088/1475-7516/2007/06/025`. arXiv: `0705.4158 [astro-ph]`.

[250] Pedro V. P. Cunha and Carlos A. R. Herdeiro. “Shadows and strong gravitational lensing: a brief review”. In: *Gen. Rel. Grav.* 50.4 (2018), p. 42. doi: `10.1007/s10714-018-2361-9`. arXiv: `1801.00860 [gr-qc]`.

[251] Paolo Cremonese, David Fonseca Mota, and Vincenzo Salzano. “Characteristic Features of Gravitational Wave Lensing as Probe of Lens Mass Model”. In: *Annalen Phys.* 535.6 (2023), p. 2300040. doi: `10.1002/andp.202300040`. arXiv: `2111.01163 [astro-ph.CO]`.

[252] Mihael Petač, Julien Lavalle, and Karsten Jedamzik. “Microlensing constraints on clustered primordial black holes”. In: *Phys. Rev. D* 105.8 (2022), p. 083520. doi: `10.1103/PhysRevD.105.083520`. arXiv: `2201.02521 [astro-ph.CO]`.

[253] Valeria Rodriguez-Fajardo et al. “Einstein beams and the diffractive aspect of gravitationally-lensed light”. In: (June 2023). arXiv: 2306.11852 [astro-ph.IM].

[254] Anuj Mishra et al. “Exploring the Impact of Microlensing on Gravitational Wave Signals: Biases, Population Characteristics, and Prospects for Detection”. In: (June 2023). arXiv: 2306.11479 [astro-ph.CO].

[255] R. Abbott et al. “Search for gravitational-lensing signatures in the full third observing run of the LIGO-Virgo network”. In: (Apr. 2023). arXiv: 2304.08393 [gr-qc].

[256] Ankit Beniwal et al. “Gravitational wave, collider and dark matter signals from a scalar singlet electroweak baryogenesis”. In: *JHEP* 08 (2017), p. 108. doi: 10.1007/JHEP08(2017)108. arXiv: 1702.06124 [hep-ph].

[257] John Ellis, Marek Lewicki, and José Miguel No. “On the Maximal Strength of a First-Order Electroweak Phase Transition and its Gravitational Wave Signal”. In: *JCAP* 04 (2019), p. 003. doi: 10.1088/1475-7516/2019/04/003. arXiv: 1809.08242 [hep-ph].

[258] Chiara Caprini et al. “Detecting gravitational waves from cosmological phase transitions with LISA: an update”. In: *JCAP* 03 (2020), p. 024. doi: 10.1088/1475-7516/2020/03/024. arXiv: 1910.13125 [astro-ph.CO].

[259] Misao Sasaki et al. “Primordial black holes—perspectives in gravitational wave astronomy”. In: *Class. Quant. Grav.* 35.6 (2018), p. 063001. doi: 10.1088/1361-6382/aaa7b4. arXiv: 1801.05235 [astro-ph.CO].

[260] Z. Arzoumanian et al. “The NANOGrav 11-year Data Set: Pulsar-timing Constraints On The Stochastic Gravitational-wave Background”. In: *Astrophys. J.* 859.1 (2018), p. 47. doi: 10.3847/1538-4357/aabd3b. arXiv: 1801.02617 [astro-ph.HE].

[261] Bernard Carr et al. “Constraints on primordial black holes”. In: *Rept. Prog. Phys.* 84.11 (2021), p. 116902. doi: 10.1088/1361-6633/ac1e31. arXiv: 2002.12778 [astro-ph.CO].

[262] Kazunari Eda et al. “Gravitational waves as a probe of dark matter minispikes”. In: *Phys. Rev. D* 91.4 (2015), p. 044045. doi: 10.1103/PhysRevD.91.044045. arXiv: 1408.3534 [gr-qc].

[263] L. Gabriel Gómez and J. A. Rueda. “Dark-matter dynamical friction versus gravitational-wave emission in the evolution of compact-star binaries”. In: *Phys. Rev. D* 96.6 (2017), p. 063001. doi: 10.1103/PhysRevD.96.063001. arXiv: 1706.06801 [astro-ph.GA].

[264] Bradley J. Kavanagh et al. “Detecting dark matter around black holes with gravitational waves: Effects of dark-matter dynamics on the gravitational waveform”. In: *Phys. Rev. D* 102.8 (2020), p. 083006. doi: `10.1103/PhysRevD.102.083006`. arXiv: `2002.12811 [gr-qc]`.

[265] Anish Ghoshal and Alessandro Strumia. “Probing the Dark Matter density with gravitational waves from super-massive binary black holes”. In: (June 2023). arXiv: `2306.17158 [astro-ph.CO]`.

[266] V. P. Dokuchaev. “Emission of Magnetoacoustic Waves in the Motion of Stars in Cosmic Space.” In: *SvA* 8 (1964), p. 23.

[267] M. A. Ruderman and E. A. Spiegel. “Galactic Wakes”. In: 165 (Apr. 1971), p. 1. doi: `10.1086/150870`.

[268] Y. Rephaeli and E. E. Salpeter. “Flow past a massive object and the gravitational drag”. In: *ApJ* 240 (Aug. 1980), pp. 20–24.

[269] Eve C. Ostriker. “Dynamical friction in a gaseous medium”. In: *Astrophys. J.* 513 (1999), p. 252. doi: `10.1086/306858`. arXiv: `astro-ph/9810324`.

[270] Lasha Berezhiani, Benjamin Elder, and Justin Khoury. “Dynamical Friction in Superfluids”. In: *JCAP* 10 (2019), p. 074. doi: `10.1088/1475-7516/2019/10/074`. arXiv: `1905.09297 [hep-ph]`.

[271] Lorenzo Annulli, Vitor Cardoso, and Rodrigo Vicente. “Response of ultralight dark matter to supermassive black holes and binaries”. In: *Phys. Rev. D* 102.6 (2020), p. 063022. doi: `10.1103/PhysRevD.102.063022`. arXiv: `2009.00012 [gr-qc]`.

[272] Yourong Wang and Richard Easther. “Dynamical Friction From Ultralight Dark Matter”. In: (Oct. 2021). arXiv: `2110.03428 [gr-qc]`.

[273] Dina Traykova et al. “Dynamical friction from scalar dark matter in the relativistic regime”. In: *Phys. Rev. D* 104.10 (2021), p. 103014. doi: `10.1103/PhysRevD.104.103014`. arXiv: `2106.08280 [gr-qc]`.

[274] Dhruba Dutta Chowdhury et al. “On the Random Motion of Nuclear Objects in a Fuzzy Dark Matter Halo”. In: *Astrophys. J.* 916.1 (2021), p. 27. doi: `10.3847/1538-4357/ac043f`. arXiv: `2105.05268 [astro-ph.GA]`.

[275] Rodrigo Vicente and Vitor Cardoso. “Dynamical friction of black holes in ultralight dark matter”. In: (Jan. 2022). arXiv: `2201.08854 [gr-qc]`.

[276] Dina Traykova et al. “Relativistic drag forces on black holes from scalar dark matter clouds of all sizes”. In: (May 2023). arXiv: `2305.10492 [gr-qc]`.

[277] Aaron T. Lee and Steven W. Stahler. “Dynamical Friction in a Gas: The Subsonic Case”. In: *Mon. Not. Roy. Astron. Soc.* 416 (2011), p. 3177. doi: `10.1111/j.1365-2966.2011.19273.x`. arXiv: `1106.4820 [astro-ph.GA]`.

[278] Alessandra De Rosa et al. "The quest for dual and binary supermassive black holes: A multi-messenger view". In: *New Astron. Rev.* 86 (2019), p. 101525. doi: `10.1016/j.newar.2020.101525`. arXiv: `2001.06293 [astro-ph.GA]`.

[279] J. Aasi et al. "Advanced LIGO". In: *Class. Quant. Grav.* 32 (2015), p. 074001. doi: `10.1088/0264-9381/32/7/074001`. arXiv: `1411.4547 [gr-qc]`.

[280] M. Punturo et al. "The Einstein Telescope: A third-generation gravitational wave observatory". In: *Class. Quant. Grav.* 27 (2010). Ed. by Fulvio Ricci, p. 194002. doi: `10.1088/0264-9381/27/19/194002`.

[281] Vincent Desjacques, Alex Kehagias, and Antonio Riotto. "Impact of ultralight axion self-interactions on the large scale structure of the Universe". In: *Phys. Rev.* D97.2 (2018), p. 023529. doi: `10.1103/PhysRevD.97.023529`. arXiv: `1709.07946 [astro-ph.CO]`.

[282] J. A. R. Cembranos et al. "Constraints on anharmonic corrections of Fuzzy Dark Matter". In: *JHEP* 08 (2018), p. 073. doi: `10.1007/JHEP08(2018)073`. arXiv: `1805.08112 [astro-ph.CO]`.

[283] L. Arturo Ureña-López. "Scalar field dark matter with a cosh potential, revisited". In: *JCAP* 06 (2019), p. 009. doi: `10.1088/1475-7516/2019/06/009`. arXiv: `1904.03318 [astro-ph.CO]`.

[284] Vicente Delgado and Antonio Muñoz Mateo. "Self-interacting superfluid dark matter droplets". In: *Mon. Not. Roy. Astron. Soc.* 518.3 (2022), pp. 4064–4072. doi: `10.1093/mnras/stac3386`. arXiv: `2201.12418 [astro-ph.CO]`.

[285] Sayan Chakrabarti et al. "Constraints on the mass and self-coupling of ultra-light scalar field dark matter using observational limits on galactic central mass". In: *JCAP* 09 (2022), p. 074. doi: `10.1088/1475-7516/2022/09/074`. arXiv: `2202.11081 [astro-ph.CO]`.

[286] Pierre-Henri Chavanis. "Jeans mass-radius relation of self-gravitating Bose-Einstein condensates and typical parameters of the dark matter particle". In: *Phys. Rev. D* 103.12 (2021), p. 123551. doi: `10.1103/PhysRevD.103.123551`. arXiv: `2011.01038 [gr-qc]`.

[287] P. S. Bhupal Dev, Manfred Lindner, and Sebastian Ohmer. "Gravitational waves as a new probe of Bose–Einstein condensate Dark Matter". In: *Phys. Lett.* B773 (2017), pp. 219–224. doi: `10.1016/j.physletb.2017.08.043`. arXiv: `1609.03939 [hep-ph]`.

[288] Nitsan Bar et al. "Looking for ultralight dark matter near supermassive black holes". In: (2019). arXiv: `1905.11745 [astro-ph.CO]`.

[289] Elliot Yarnell Davies and Philip Mocz. "Fuzzy Dark Matter Soliton Cores around Supermassive Black Holes". In: (2019). arXiv: `1908.04790 [astro-ph.GA]`.

[290] Hooman Davoudiasl and Peter B Denton. “Ultra Light Boson Dark Matter and Event Horizon Telescope Observations of M87*”. In: *Phys. Rev. Lett.* 123.2 (2019), p. 021102. doi: `10.1103/PhysRevLett.123.021102`. arXiv: `1904.09242 [astro-ph.CO]`.

[291] Pierre-Henri Chavanis. “Growth of perturbations in an expanding universe with Bose-Einstein condensate dark matter”. In: *Astron. Astrophys.* 537 (2012), A127. doi: `10.1051/0004-6361/201116905`. arXiv: `1103.2698 [astro-ph.CO]`.

[292] E. Madelung. “Quantentheorie in hydrodynamischer Form”. In: *Zeitschrift für Physik* 40.3-4 (Mar. 1927), pp. 322–326.

[293] T. Harko. “Evolution of cosmological perturbations in Bose-Einstein condensate dark matter”. In: *Mon. Not. Roy. Astron. Soc.* 413 (2011), pp. 3095–3104. doi: `10.1111/j.1365-2966.2011.18386.x`. arXiv: `1101.3655 [gr-qc]`.

[294] L. H. Thomas. “The calculation of atomic fields”. In: *Mathematical Proceedings of the Cambridge Philosophical Society* 23.5 (1927), pp. 542–548. doi: `10.1017/S0305004100011683`.

[295] E. Fermi. “Un Metodo Statistico per la Determinazione di alcune Priopriètà dell’Atomo”. In: *Rend. Accad. Naz. Lincei.* 6 (1927), pp. 602–607.

[296] Keir K. Rogers and Hiranya V. Peiris. “Strong Bound on Canonical Ultralight Axion Dark Matter from the Lyman-Alpha Forest”. In: *Phys. Rev. Lett.* 126.7 (2021), p. 071302. doi: `10.1103/PhysRevLett.126.071302`. arXiv: `2007.12705 [astro-ph.CO]`.

[297] Ivana Kovacic and Michael Brennan. *The Duffing Equation: Nonlinear Oscillators and their Behaviour*. Wiley, Mar. 2011. doi: `10.1002/9780470977859`.

[298] I. S. Gradshteyn and I. M. Ryzhik. *Table of integrals, series, and products*. 4th ed. prepared by Yu. V. Geronimus [and] M. Yu. Tseytlin. Translated from the Russian by Scripta Technika, inc. Translation edited by Alan Jeffrey. New York Academic Press, 1965.

[299] P.F Byrd and M.D. Friedman. *Handbook of Elliptic Integrals for Engineers and Scientists*. Springer, Berlin, Heidelberg, 1971.

[300] H. Bondi. “On spherically symmetrical accretion”. In: *Mon. Not. Roy. Astron. Soc.* 112 (1952), p. 195.

[301] F. C. Michel. “Accretion of Matter by Condensed Objects”. In: *Astrophysics and Space Science* 15 (1972), p. 153.

[302] W. G. Unruh. “Absorption cross section of small black holes”. In: 14.12 (Dec. 1976), pp. 3251–3259. doi: `10.1103/PhysRevD.14.3251`.

[303] Lam Hui et al. “Black Hole Hair from Scalar Dark Matter”. In: *JCAP* 1906.06 (2019), p. 038. doi: `10.1088/1475-7516/2019/06/038`. arXiv: `1904.12803 [gr-qc]`.

[304] R. Hunt. “A Fluid Dynamical Study of the Accretion Process”. In: *Monthly Notices of the Royal Astronomical Society* 154.2 (Oct. 1971), pp. 141–165.

[305] Loren I. Petrich et al. “Accretion onto a Moving Black Hole: A Fully Relativistic Treatment”. In: *ApJ* 336 (Jan. 1989), p. 313.

[306] S. L. Shapiro and S. A. Teukolsky. *Black holes, white dwarfs, and neutron stars: The physics of compact objects*. New York, USA: Wiley, 1983. isbn: 9780471873167.

[307] F. Hoyle and R. A. Lyttleton. “The effect of interstellar matter on climatic variation”. In: *Mathematical Proceedings of the Cambridge Philosophical Society* 35.3 (1939), pp. 405–415.

[308] Richard G. Edgar. “A Review of Bondi-Hoyle-Lyttleton accretion”. In: *New Astron. Rev.* 48 (2004), pp. 843–859. doi: `10.1016/j.newar.2004.06.001`. arXiv: `astro-ph/0406166`.

[309] W. A. Mulder. “Dynamical friction on extended objects”. In: *Astron. Astrophys.* 117.1 (1983), pp. 9–16.

[310] Michael K. H. Kiessling. “Mathematical Vindications of the Jeans Swindle”. In: *Adv. Appl. Math.* 31 (2003), pp. 132–149. doi: `10.1016/S0196-8858(02)00556-0`. arXiv: `astro-ph/9910247`.

[311] Hyosun Kim and Woong Tae Kim. “Nonlinear dynamical friction in a gaseous medium”. In: *Astrophysical Journal* 703.2 (2009), pp. 1278–1293.

[312] Nevill Francis Mott and Harrie Stewart Wilson Massey. *The theory of atomic collisions*. Vol. 35. Clarendon Press Oxford, 1965.

[313] Nitsan Bar et al. “Assessing the Fornax globular cluster timing problem in different models of dark matter”. In: *Phys. Rev. D* 104.4 (2021), p. 043021. doi: `10.1103/PhysRevD.104.043021`. arXiv: `2102.11522 [astro-ph.GA]`.

[314] F. Hoyle and R. A. Lyttleton. “The effect of interstellar matter on climatic variation”. In: *Proceedings of the Cambridge Philosophical Society* 35.3 (Jan. 1939), p. 405. doi: `10.1017/S0305004100021150`.

[315] Rony Keppens et al. “MPI-AMRVAC: A parallel, grid-adaptive PDE toolkit”. In: *Computers & Mathematics with Applications* 81 (2021). Development and Application of Open-source Software for Problems with Numerical PDEs, pp. 316–333. issn: 0898-1221. doi: `https://doi.org/10.1016/j.camwa.2020.03.023`. url: `https://www.sciencedirect.com/science/article/pii/S0898122120301279`.

[316] Keppens, R. et al. “MPI-AMRVAC 3.0: Updates to an open-source simulation framework”. In: *A&A* 673 (2023), A66. doi: `10.1051/0004-6361/202245359`. url: `https://doi.org/10.1051/0004-6361/202245359`.

[317] Ileyk El Mellah and Fabien Casse. “Numerical simulations of axisymmetric hydrodynamical Bondi–Hoyle accretion on to a compact object”. In: *Mon. Not. Roy. Astron. Soc.* 454.3 (2015), pp. 2657–2667. doi: `10.1093/mnras/stv2184`. arXiv: `1509.07700 [astro-ph.HE]`.

[318] C. Xia et al. “MPI-AMRVAC 2.0 for Solar and Astrophysical Applications”. In: *The Astrophysical Journal Supplement Series* 234.2 (Feb. 2018), p. 30. doi: `10.3847/1538-4365/aaa6c8`. url: `https://dx.doi.org/10.3847/1538-4365/aaa6c8`.

[319] Hank Childs et al. “VisIt: An End-User Tool For Visualizing and Analyzing Very Large Data”. In: *High Performance Visualization–Enabling Extreme-Scale Scientific Insight*. Oct. 2012, pp. 357–372. doi: `10.1201/b12985`.

[320] H. Bondi and F. Hoyle. “On the Mechanism of Accretion by Stars”. In: *Monthly Notices of the Royal Astronomical Society* 104.5 (Oct. 1944), pp. 273–282. issn: 0035-8711. doi: `10.1093/mnras/104.5.273`. eprint: `https://academic.oup.com/mnras/article-pdf/104/5/273/8072203/mnras104-0273.pdf`. url: `https://doi.org/10.1093/mnras/104.5.273`.

[321] M. A. Ruderman and E. A. Spiegel. “Galactic Wakes”. In: *The Astrophysical Journal* 165 (Apr. 1971), p. 1. doi: `10.1086/150870`. url: `https://doi.org/10.1086%2F150870`.

[322] F. J. Sánchez-Salcedo and A. Brandenburg. “Deceleration by Dynamical Friction in a Gaseous Medium”. In: *The Astrophysical Journal* 522.1 (Aug. 1999), p. L35. doi: `10.1086/312215`. url: `https://dx.doi.org/10.1086/312215`.

[323] Cristian G. Bernal and F. J. Sanchez-Salcedo. “The gravitational drag force on an extended object moving in a gas”. In: *Astrophys. J.* 775 (2013), p. 72. doi: `10.1088/0004-637X/775/1/72`. arXiv: `1308.4370 [astro-ph.CO]`.

[324] Hyosun Kim and Woong-Tae Kim. “Dynamical Friction of a Circular-Orbit Perturber in a Gaseous Medium”. In: *Astrophys. J.* 665 (2007), pp. 432–444. doi: `10.1086/519302`. arXiv: `0705.0084 [astro-ph]`.

[325] Robin Buehler and Vincent Desjacques. “Dynamical friction in fuzzy dark matter: Circular orbits”. In: *Phys. Rev. D* 107.2 (2023), p. 023516. doi: `10.1103/PhysRevD.107.023516`. arXiv: `2207.13740 [astro-ph.CO]`.

[326] Eric Poisson and Clifford M. Will. *Gravity: Newtonian, Post-Newtonian, Relativistic*. Cambridge University Press, 2014. doi: `10.1017/CBO9781139507486`.

[327] Ákos Szölgyén, Morgan MacLeod, and Abraham Loeb. “Eccentricity evolution in gaseous dynamical friction”. In: *Monthly Notices of the Royal Astronomical Society* 513.4 (May 2022), pp. 5465–5473. issn: 0035-8711. doi: `10.1093/mnras/stac1294`. eprint: `https://academic.oup.com/mnras/article-pdf/513/4/5465/45904611/stac1294.pdf`. url: `https://doi.org/10.1093/mnras/stac1294`.

[328] Riccardo Catena and Piero Ullio. “A novel determination of the local dark matter density”. In: *JCAP* 08 (2010), p. 004. doi: `10.1088/1475-7516/2010/08/004`. arXiv: `0907.0018 [astro-ph.CO]`.

[329] Markus Weber and Wim de Boer. “Determination of the Local Dark Matter Density in our Galaxy”. In: *Astron. Astrophys.* 509 (2010), A25. doi: `10.1051/0004-6361/200913381`. arXiv: `0910.4272 [astro-ph.CO]`.

[330] P. Salucci et al. “The dark matter density at the Sun’s location”. In: *Astron. Astrophys.* 523 (2010), A83. doi: `10.1051/0004-6361/201014385`. arXiv: `1003.3101 [astro-ph.GA]`.

[331] Jo Bovy and Scott Tremaine. “On the local dark matter density”. In: *Astrophys. J.* 756 (2012), p. 89. doi: `10.1088/0004-637X/756/1/89`. arXiv: `1205.4033 [astro-ph.GA]`.

[332] Miguel Pato, Fabio Iocco, and Gianfranco Bertone. “Dynamical constraints on the dark matter distribution in the Milky Way”. In: *JCAP* 12 (2015), p. 001. doi: `10.1088/1475-7516/2015/12/001`. arXiv: `1504.06324 [astro-ph.GA]`.

[333] P. F. de Salas et al. “On the estimation of the Local Dark Matter Density using the rotation curve of the Milky Way”. In: *JCAP* 10 (2019), p. 037. doi: `10.1088/1475-7516/2019/10/037`. arXiv: `1906.06133 [astro-ph.GA]`.

[334] Hai-Nan Lin and Xin Li. “The Dark Matter Profiles in the Milky Way”. In: *Mon. Not. Roy. Astron. Soc.* 487.4 (2019), pp. 5679–5684. doi: `10.1093/mnras/stz1698`. arXiv: `1906.08419 [astro-ph.GA]`.

[335] Marius Cautun et al. “The Milky Way total mass profile as inferred from Gaia DR2”. In: *Mon. Not. Roy. Astron. Soc.* 494.3 (2020), pp. 4291–4313. doi: `10.1093/mnras/staa1017`. arXiv: `1911.04557 [astro-ph.GA]`.

[336] Yoshiaki Sofue. “Rotation Curve of the Milky Way and the Dark Matter Density”. In: *Galaxies* 8.2 (2020), p. 37. doi: `10.3390/galaxies8020037`. arXiv: `2004.11688 [astro-ph.GA]`.

[337] Eric Poisson and Clifford M. Will. “Gravitational waves from inspiraling compact binaries: Parameter estimation using second postNewtonian wave forms”. In: *Phys. Rev. D* 52 (1995), pp. 848–855. doi: `10.1103/PhysRevD.52.848`. arXiv: `gr-qc/9502040`.

[338] Lorenzo Annulli, Vitor Cardoso, and Rodrigo Vicente. “Stirred and shaken: Dynamical behavior of boson stars and dark matter cores”. In: *Phys. Lett. B* 811 (2020), p. 135944. doi: 10.1016/j.physletb.2020.135944. arXiv: 2007.03700 [astro-ph.HE].

[339] Hyungjin Kim et al. “Adiabatically compressed wave dark matter halo and intermediate-mass-ratio inspirals”. In: *Phys. Rev. D* 107.8 (2023), p. 083005. doi: 10.1103/PhysRevD.107.083005. arXiv: 2212.07528 [astro-ph.GA].

[340] Michele Vallisneri. “Use and abuse of the Fisher information matrix in the assessment of gravitational-wave parameter-estimation prospects”. In: *Phys. Rev. D* 77 (2008), p. 042001. doi: 10.1103/PhysRevD.77.042001. arXiv: gr-qc/0703086.

[341] P. Ajith et al. “Inspiral-Merger-Ringdown Waveforms for Black-Hole Binaries with Nonprecessing Spins”. In: *Phys. Rev. Lett.* 106 (24 2011), p. 241101. doi: 10.1103/PhysRevLett.106.241101. url: https://link.aps.org/doi/10.1103/PhysRevLett.106.241101.

[342] L. Barsotti et al. “The updated Advanced LIGO design curve”. In: (2018). url: https://dcc.ligo.org/LIGO-T1800044/public.

[343] S. Hild et al. “Sensitivity Studies for Third-Generation Gravitational Wave Observatories”. In: *Class. Quant. Grav.* 28 (2011), p. 094013. doi: 10.1088/0264-9381/28/9/094013. arXiv: 1012.0908 [gr-qc].

[344] K. G. Arun et al. “New horizons for fundamental physics with LISA”. In: *Living Rev. Rel.* 25.1 (2022), p. 4. doi: 10.1007/s41114-022-00036-9. arXiv: 2205.01597 [gr-qc].

[345] Soichiro Isoyama, Hiroyuki Nakano, and Takashi Nakamura. “Multiband Gravitational-Wave Astronomy: Observing binary inspirals with a decihertz detector, B-DECIGO”. In: *PTEP* 2018.7 (2018), 073E01. doi: 10.1093/ptep/pty078. arXiv: 1802.06977 [gr-qc].

[346] Emanuele Berti, Alessandra Buonanno, and Clifford M. Will. “Estimating spinning binary parameters and testing alternative theories of gravity with LISA”. In: *Phys. Rev. D* 71 (8 2005), p. 084025. doi: 10.1103/PhysRevD.71.084025. url: https://link.aps.org/doi/10.1103/PhysRevD.71.084025.

[347] B. P. Abbott et al. “Observation of Gravitational Waves from a Binary Black Hole Merger”. In: *Phys. Rev. Lett.* 116.6 (2016), p. 061102. doi: 10.1103/PhysRevLett.116.061102. arXiv: 1602.03837 [gr-qc].

[348] B. . P. . Abbott et al. “GW170608: Observation of a 19-solar-mass Binary Black Hole Coalescence”. In: *Astrophys. J. Lett.* 851 (2017), p. L35. doi: 10.3847/2041-8213/aa9f0c. arXiv: 1711.05578 [astro-ph.HE].

[349] D. Syer. “Relativistic dynamical friction in the weak scattering limit”. In: *Mon. Not. Roy. Astron. Soc.* 270 (1994), p. 205. doi: `10.1093/mnras/270.1.205`. arXiv: `astro-ph/9404063`.

[350] Enrico Barausse. “Relativistic dynamical friction in a collisional fluid”. In: *Mon. Not. Roy. Astron. Soc.* 382 (2007), pp. 826–834. doi: `10.1111/j.1365-2966.2007.12408.x`. arXiv: `0709.0211 [astro-ph]`.

[351] Thomas P. K. Martinsson et al. “The DiskMass Survey. VII. The distribution of luminous and dark matter in spiral galaxies”. In: *Astron. Astrophys.* 557 (2013), A131. doi: `10.1051/0004-6361/201321390`. arXiv: `1308.0336 [astro-ph.CO]`.

[352] Paolo Salucci. “The distribution of dark matter in galaxies”. In: *Astron. Astrophys. Rev.* 27.1 (2019), p. 2. doi: `10.1007/s00159-018-0113-1`. arXiv: `1811.08843 [astro-ph.GA]`.

[353] V. S. Berezinsky, V. I. Dokuchaev, and Yu N. Eroshenko. “Small-scale clumps of dark matter”. In: *Phys. Usp.* 57 (2014), pp. 1–36. doi: `10.3367/UFNe.0184.201401a.0003`. arXiv: `1405.2204 [astro-ph.HE]`.

[354] Philippe Brax, Jose A. R. Cembranos, and Patrick Valageas. “Nonrelativistic formation of scalar clumps as a candidate for dark matter”. In: *Phys. Rev. D* 102.8 (2020), p. 083012. doi: `10.1103/PhysRevD.102.083012`. arXiv: `2007.04638 [astro-ph.CO]`.

[355] Scott W. Randall et al. “Constraints on the Self-Interaction Cross-Section of Dark Matter from Numerical Simulations of the Merging Galaxy Cluster 1E 0657-56”. In: *Astrophys. J.* 679 (2008), pp. 1173–1180. doi: `10.1086/587859`. arXiv: `0704.0261 [astro-ph]`.

[356] R. A. Fisher. “Statistical Methods for Research Workers”. In: *Breakthroughs in Statistics: Methodology and Distribution*. Ed. by Samuel Kotz and Norman L. Johnson. New York, NY: Springer New York, 1992, pp. 66–70. isbn: 978-1-4612-4380-9. doi: `10.1007/978-1-4612-4380-9_6`. url: `https://doi.org/10.1007/978-1-4612-4380-9_6`.